PROCEEDINGS OF SPIE

SPIE—The International Society for Optical Engineering

F61775-98-WE027

CSP98-1028

Laser Optics '98
Nonlinear and Coherent Optics

Vladimir E. Sherstobitov
Editor

22–26 June 1998
St. Petersburg, Russia

SPIE
P
PROCEEDINGS
SERIES

Volume 3684

19990702 026

DTIC QUALITY INSPECTED 4

AQF99-10-1697

PROCEEDINGS OF SPIE

SPIE—The International Society for Optical Engineering

Laser Optics '98

Nonlinear and Coherent Optics

Vladimir E. Sherstobitov
Editor

22–26 June 1998
St. Petersburg, Russia

SPIE

P

PROCEEDINGS
SERIES

Volume 3684

Contents

Conference Committees

V.I. **Kovalev,** P.N. Lebedev Physical Institute
I.B. Kovsh, Laser Association
V.V. Lyubimov, Institute for Laser Physics, S.I. Vavilov State Optical Institute
A.A. Manenkov, General Physics Institute
Yu.T. Mazurenko, S.I. Vavilov State Optical Institute
A.P. Napartovich, TRINITI
A.N. Oraevsky, P.N. Lebedev Physical Institute
V.Ya. Panchenko, NICTL Laser Research Center
P.P. Pashinin, General Physics Institute
G.T. Petrovskiy, S.I. Vavilov State Optical Institute
L.A. Rivlin, Moscow State Institute of Radio Engineering, Electronics
  and Automation
N.N. Rosanov, Institute for Laser Physics, S.I. Vavilov State Optical Institute
A.S. Rubanov, B.I. Stepanov Institute of Physics (Belarus)
V.A. Serebryakov, Institute for Laser Physics, S.I. Vavilov State Optical Institute
I.A. Shcherbakov, General Physics Institute
V.E. Sherstobitov, Institute for Laser Physics, S.I. Vavilov State Optical Institute
A.P. Shkadarevith, Peleng (Belarus)
V.B. Smirnov, St. Petersburg State University
M.S. Soskin, Institute of Physics (Ukraine)
A.P. Sukhorukov, M.V. Lomonosov Moscow State University
V.I. Ustyugov, Institute for Laser Physics, S.I. Vavilov State Optical Institute
V.V. Valuev, GPO Almaz
E.A. Viktorov, Institute for Laser Physics, S.I. Vavilov State Optical Institute
G.M. Zverev, Polyus Research and Development Institute

American Local Committee

Howard Lowdermilk, *Chair,* Lawrence Livermore National Laboratory (USA)
Sherene Goulart, *Secretary,* Lawrence Livermore National Laboratory (USA)

Asian Local Committee

Sadao Nakai, *Chair,* Osaka University (Japan)
Tomoo Fujioka, *Cochair and Scientific Secretary,* Tokai University (Japan)

European Local Committee

Erich Spitz, *Chair,* Thomson SA (France)
Arnaud Brignon, *Scientific Secretary,* Thomson-CSF (France)
Henri Rajbenbach, *Scientific Secretary,* European Commission (Belgium)

Dynamic Correction for Distortions in Imaging Optical Systems using Liquid Crystal SLMs

V.A.Berenberg, A.A.Leshchev, M.V.Vasil'ev, V.Yu.Venediktov, A.P.Onokhov

Institute for Laser Physics, SC "Vavilov State Optical Institute"
199034, Birzhevaya, 12, St.-Petersburg, Russia

L.A.Beresnev

Technical University, Darmstadt, Germany

ABSTRACTS

Given are the results of experimental study on the quasi real time holographic correction for the lens distortions in the passive observational telescope in the visible range of spectrum, using the liquid crystal optically addressed spatial light modulator.

Keywords: dynamic hologram, holographic corrector, liquid crystal spatial light modulator, passive imaging telescope.

1. INTRODUCTION

The method of holographic correction for distortions, imposed by the primary mirror (lens) of the telescope, was first proposed and realized in the experiment in [1,2]. The holographic corrector was recorded by the coherent radiation, and its chromatism (grating disperse) was corrected for by use of the auxiliary diffraction grating, providing thus the possibility of imaging in the comparatively wide spectral range. These works, as well as much later investigations in USA[3-5] were realized with the use of static holographic media, providing thus correction only for the static distortions.

The principle of the holographic correction for the telescope lens distortions is illustrated by the Fig.1. Let the telescope is comprised by the distorted lens 1 and the eye-piece 2. This system is imaging the remote self-luminous object 4 in the registration plane 3. In the case of the high optical quality of the elements 2 and 3 the system resolution is determined by the properties of the lens 1. One can compensate for the lens distortions by the holographic corrector 5, mounted in the plane to which the eye-piece 2 images the pupil of the lens 1[1,2]. The hologram is recorded by the coherent radiation as the interference pattern of the plain reference wave and the object wave, emitted by the point source, mounted in the plane of the object 4.

The light wave from this point source which has passed through the distorted lens bears the information on its distortions. This information is encoded in the hologram. On the stage of the hologram reconstruction the radiation, emitted by the point source and distorted on its path through the telescope will diffract on the hologram into the plain wave, coinciding with the reference wave, used for the hologram recording. Any luminous object can be treated as a set of the point sources. Hence the radiation from the object, distorted by the telescope, will diffract to the set of plain waves. These waves will reconstruct in the plane 3 the non-distorted image of the object notwithstanding the arbitrary distortions of the telescope lens 1.

The non-monochrome radiation from the object would be expanded by the hologram to the spectrum. This chromatism is to be corrected by the auxiliary static diffraction grating whose spatial frequency is equal to the spatial carrier of the holographic corrector.

2. THE CHOICE FOR THE CORRECTING ELEMENT

One can use the nonlinear optical phase conjugation for the dynamic correction for the primary lens (mirror) distortions[6]. In particular, in [7,8] it was realized with the use of the stimulated Brillouin scattering. In this case, however, the imaged object is either to emit the coherent radiation or to be illuminated by such a radiation.

The highest efficiency among the nonlinear-optical media for holograms recording, providing dynamic correction for distortions in the wide spectral range, is revealed by the liquid crystal spatial light modulators (LC SLM)[9] and by the photorefractive crystals[10]. For example, in [11], the use of LC SLM made it possible to correct for distortions in the spectral band with the width 10 nm, separated from the hologram recording wavelength in 90 nm. In the experiment[17] similar schematics was realized with the use of the auxiliary static holographic grating, compensating for the dynamic hologram chromatism. In [12] the correction for the distortions of the optical elements was realized with the use of the photorefractive crystals BSO and NBS with the hologram record at the wavelength 514 nm. The holograms were reconstructed by the Ar-ion laser radiation at several discrete wavelength in the range of 476..514 nm.

Not that for the correction for distortions, imposed by the lens into the image of the distant and spatially-incoherent radiation it is sensible to use the thin holograms. The use of the volume (thick) holograms will result in extra limitations due to their angular and spectral selectivity[12], resulting in most cases in the impossibility to realize the most important advantage of this class of holograms - the high diffraction efficiency. So, to our opinion, the LC SLM medium is more prospective from the point of view of dynamic correction than the photorefractive media. The comparison of the combination of such a basic parameters, as the sensitivity, response time, reversibility, resolution and depth of phase modulation, realized in these two media, also puts the LC SLM ahead.

This paper is devoted to the experimental results on thermal object imaging in the wide spectral range by the model telescope with the dynamic holographic correction for its primary lens and auxiliary correction for the hologram chromatism. The dynamic hologram was recorded in LC SLM, using the polymer photoconductor[13,14] or the photoconductor on the base of silicon carbide[18-21]. The S-effect was used for the holograms record in SLM with the nematic LC, and in the case of ferroelectric LC we have used the DHF-effect[22,23]. The holograms were recorded in pulsed mode[15,16].

Variation of the voltage pulse, feeding the SLM, duration and of its synchronization with respect to the light pulse provides the control of the temporal delay from the hologram recording to the moment of its highest diffraction efficiency. In our experiments we could vary this delay from 100 msec to several dozen seconds.

The diffraction efficiency of the realized holographic correctors equaled 20-25%. The holograms, recorded in FLC SLM, revealed very weak dependence of their diffraction efficiency on the polarization of reconstructing radiation. So in the case of imaging of test-object, illuminated by the incoherent (thermal) radiation, the effective efficiency was two times higher.

3. EXPERIMENTAL SETUP

The experimental setup is shown in the Fig.2. The thermal source at the infinity was simulated by the standard test object 1, illuminated by the light of the tungsten lamp. The imaged test-object was mounted in the focal plane of the auxiliary lens 2. The absolute angular dimension of the object was equal 0.02 radian. This object was imaged by the lens telescope, comprised by the primary lens 3 to be corrected and the eye-piece 4. Two identical achromatic lenses with the focal length of 230 mm were used as the elements 3 and 4. The corrector unit comprised the LC SLM 5, the transparent phase (holographic) diffraction grating 6 for the dynamic hologram chromatism compensation and the scheme for the corrector recording.

The hologram-corrector was recorded by the pulsed radiation of second harmonics (0.54 μm) of Nd:YAP laser 7 as the interference pattern of the plain reference wave and the object wave, transmitted via the telescope. The telescope 8 (10^x) improved the spatial homogeneity of the recording beams. The useful clear aperture of the SLM was determined by the apertures 9 and 10 and equaled 15 mm. Beam split cube 11 (transparency 50 %) separated the recording beams and, in a time, combined the radiation from the imaged object 1 and the probe beam of laser radiation.
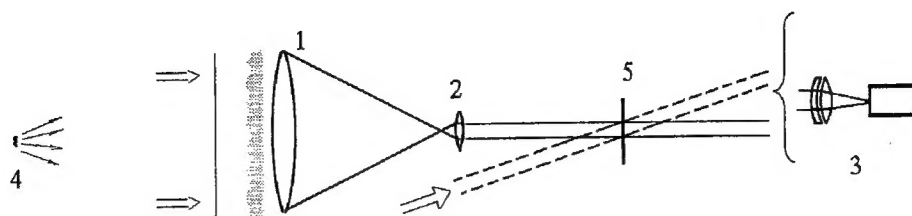
Fig.1. Principle scheme of holographic correction for telescope lens distortion
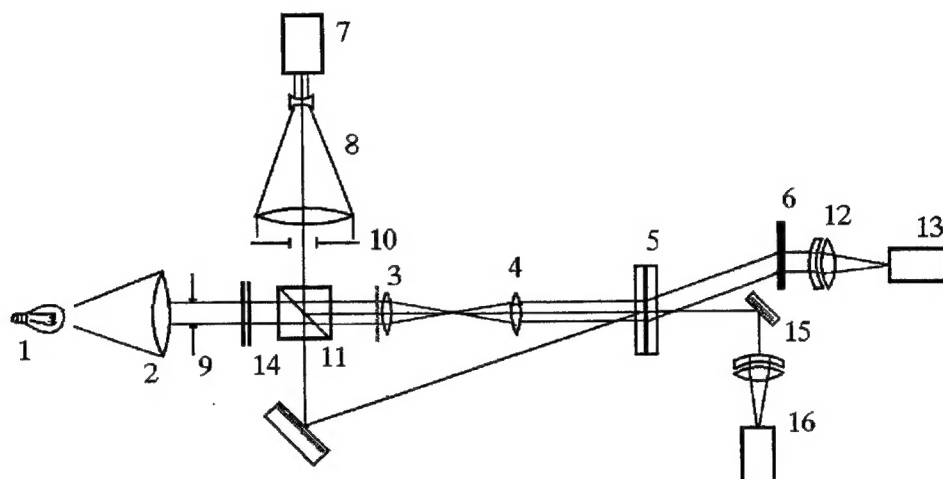
Fig.2. Experimental setup
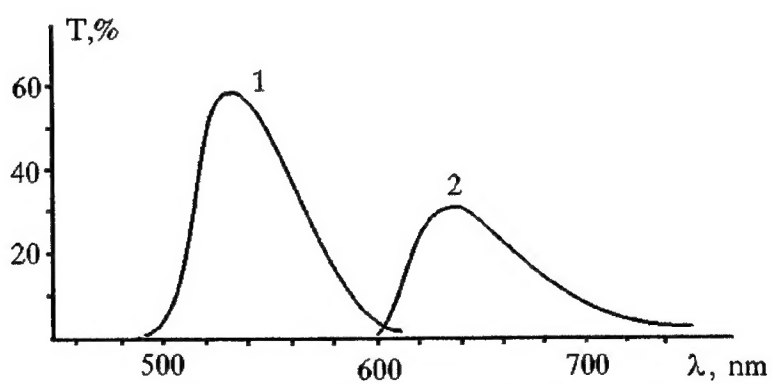
Fig.3. Spectral dependence of the colored filters transparency:
1 — colored filters GS-18 + SZS-22 (ЖС-18 + СЗС-22);
2 — colored filters KS-10 + SZS-23(KC-10+C3C-23)

The eye-piece 4 imaged the pupil of the lens 3 in the plane of the corrector 5. The spatial carrier frequency of the dynamic hologram was equal to the spatial frequency of the grating 6 and was equal 95 mm^{-1}. Such a value was chosen as the trade-off value, providing both spatial separation of the object images in different diffraction orders and sufficiently high diffraction efficiency.

The radiation from the thermal source, diffracted from the grating 6, was caught by the lens 12 and focused to the CCD-matrix 13. The spectral range, used for the object imaging, was varied by the colored filters 14. We have used the filters made of standard colored glasses (the spectral characteristics of the filters transparency are shown in the Fig.3), and the band interference filter with the width of the transparency band 10 nm centered at 0.53 µm.. The zero order diffraction on element 5 radiation from the thermal object was caught by the plain mirror 15 and used for control non-corrected image of the object, registered by the system 16.

4. EXPERIMENTAL RESULTS

The various distorters were mounted in the signal beam. Small-scale distortions of the lens were simulated with the use of glass plates etched in hydrofluoric acid. For an example, in the Fig.4 the interferogram is shown of the "strongest" distorter of this kind, providing beam divergence of ~ 0.006 radian (FWHM). The Fresnel bi-prism was used for simulation of the local wedge-like distortions, which in practice can be caused, for example, by the mutual tilt of the primary mirror segments; the angular misalignment of "images" in our case was ~ 0.01 radian. We have used the tungsten wire of lamp, the sharp edge and the standard test object as the objects of imaging. The latter two kinds of test-objects provided the application of standard methods of the quantitative evaluation of the correction fidelity and its dependence on the spectral range of imaging radiation.

The following results were obtained with the NLC SLM.

We have measured the frequency-contrast characteristics of the optical system under correction with the imitation of the small-scale scattering distorter with the angular divergence of ~ 0.006 radian. It was measured for the green range of spectrum (see filter transparency - curve 1 in the Fig.3), for the red range of spectrum (curve 2 in the Fig.3) and for the "white" light of tungsten lamp. In the Fig.5 the results are shown of this characteristic measuring as $K = \{I_{max} - I_{min}\}/\{I_{max} + I_{min}\}$. One can see from the Fig.5, that in the case of imaging in the green range of spectrum (the width of spectral range ~ 50 nm), whose maximum approximately coincides with the wavelength of laser radiation used for the hologram recording, the system performance is close to the diffraction limited. The use of "white" light also provides rather good quality of image. Significant deterioration of the image is observed only while imaging in red spectral band whose maximum is shifted in ~ 100 nm with respect to the recording wavelength. In the Fig.6-10 are shown the photographs of the standard test object, which confirm the above said. In the case of the wedge-like distortions the shift of imaging spectrum to the red range or use of "white" light the image was "expanded" in the "wedge" direction.

Additional information on the correction fidelity was got from the analysis of the photographs of the sharp edge (Fig.11,12). One can see that in the case of spectral band shift with respect to the recording wavelength, and of the strong distortions of the probe beam, the wings in the edge spread function (ESF) are observed. These wings are responsible for the decrease of the complicated image contrast, and they are resulted from non-sufficient correction for the chromatism distortions. One can also see from these photographs that the point spread function (PSF) consists of two components: the narrow core, resulting of nearly diffraction limited performance of the OS, and of the wings, caused by the non-sufficient chromatic correction for the optical distortions. According to evaluations, in the absence of the distortions in the probe beam the image core contains ~ 65 % of total energy for reading out both in the green and in the red spectral ranges (Fig.11). Distortions of the probe beam by the etched plate with the distortions rate of 0.006 rad result, in the green range, in preservation of the core energy, while in the red range of spectrum it is reduced down to ~ 35% (Fig.12).

4
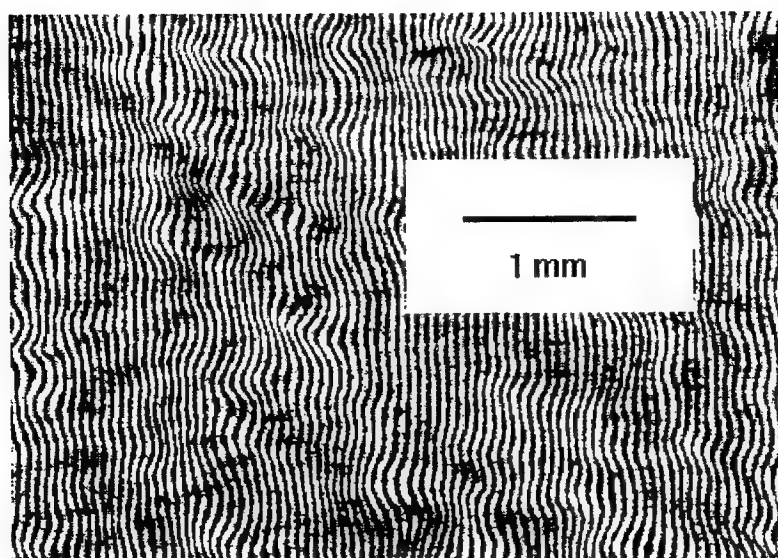
Fig.4. The part of interferogram of the distorting plate, providing beam divergence of 0.006 radian.
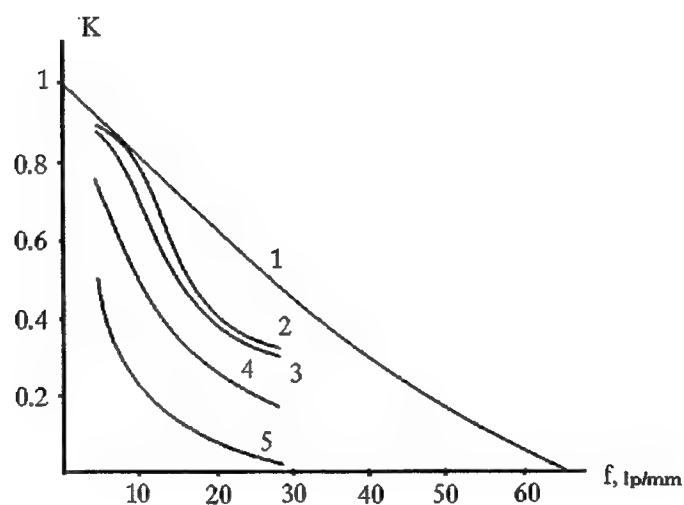
Fig.5. Frequency-contrast characteristics of the optical system under correction in the absence (curves 1, 2) and in the presence (curves 3, 4, 5) of small-scale distortions. Curve 1 - the ideal lens, curve 2 – optical system used in our experiment, 3 - correction in the green range of spectrum, 4 - correction in the "white" and 5 - light correction in the red range of spectrum.
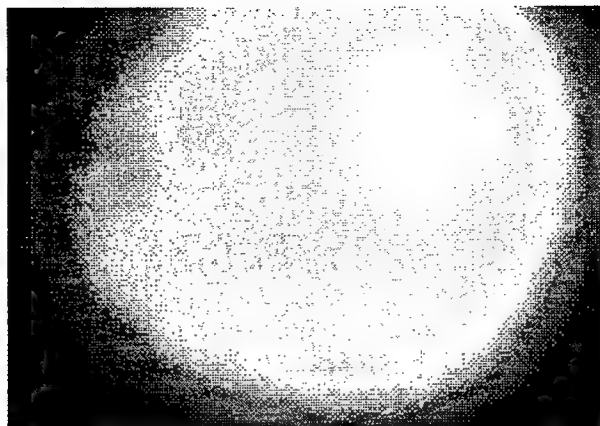
Fig.6. Image of standard test-object without correction for lens distortions.
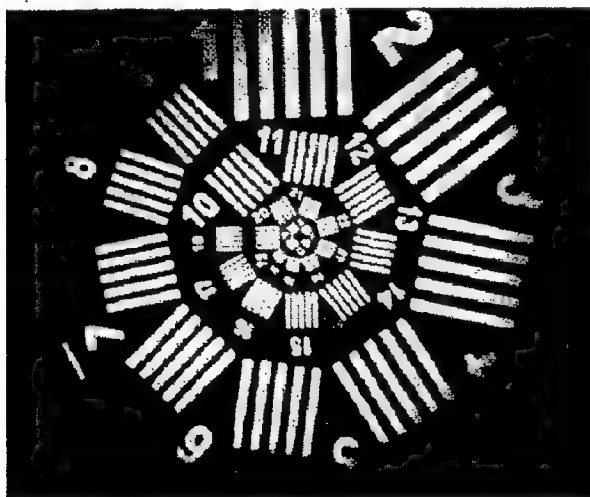
Fig.7. Image of test object in green light with correction for distortions.
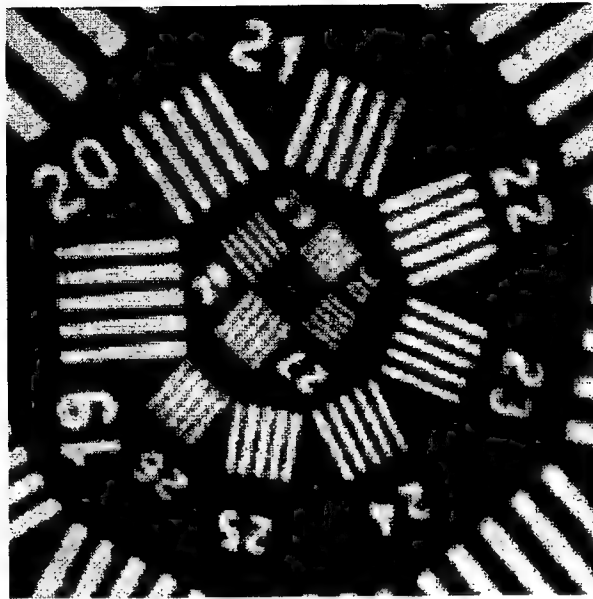
Fig.8. Central zone of standard test object image in green light with the correction for distortions.
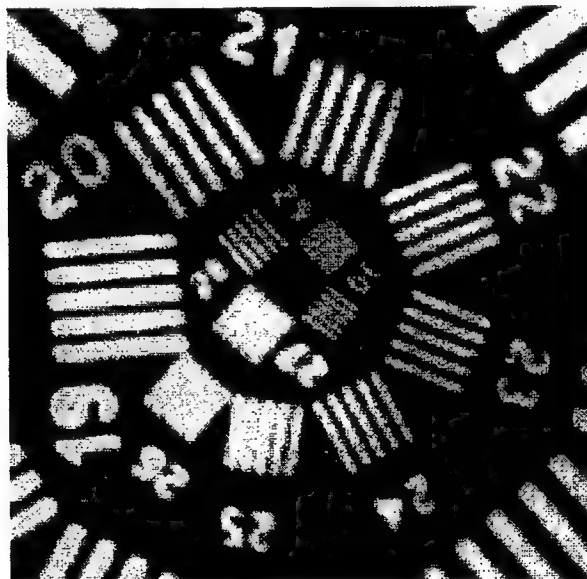
Fig.9. Central zone of standard test object image in "white" light with the correction for distortions.
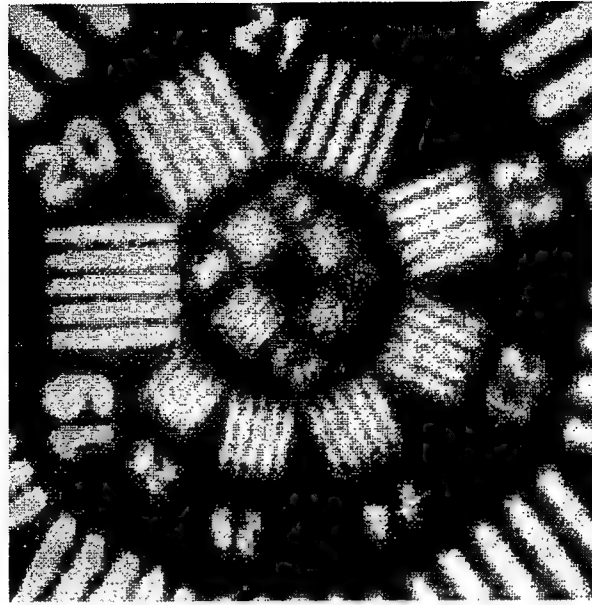
Fig.10. Central zone of standard test object image in red light with the correction for distortions.

(a)   (b)
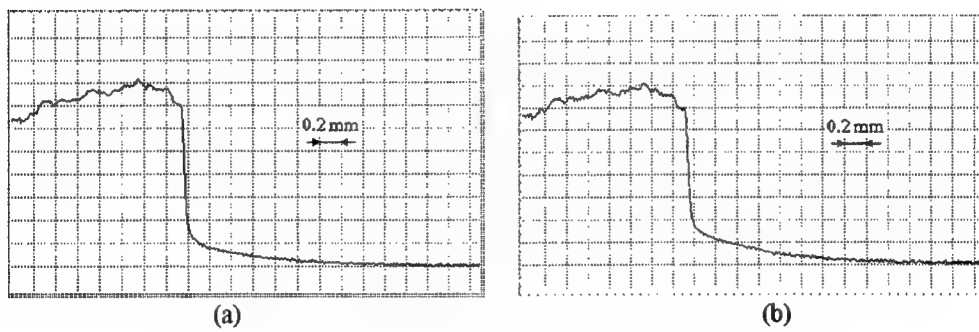
Fig.11. Reconstructed image of the sharp edge without distortions,
read out in green (a) and red (b) spectral bands (see Fig.3.).

(a)   (б)
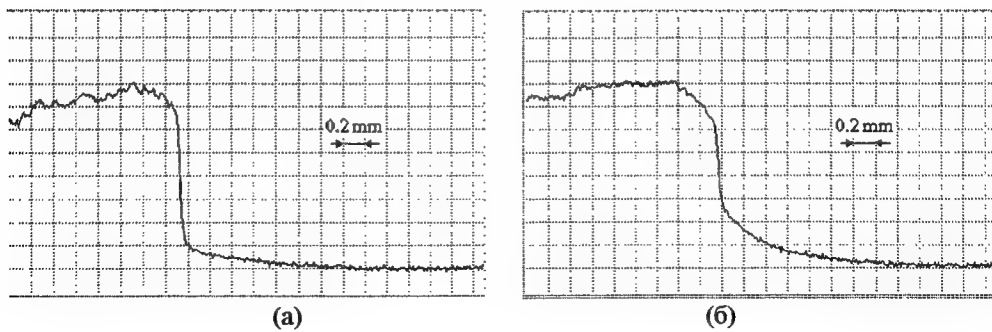
Fig.12. Reconstructed image of the sharp edge with distorter 0.006 rad,

read out in green (a) and red (b) spectral bands.
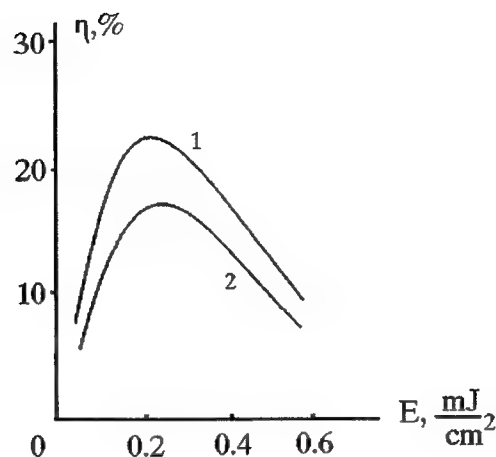
Fig.13. Peak values of DE vs. radiation energy fluency without distorter (1)

and with the distorter 0.006 radian (2).

It was found out that the influence of the small-scale distortions onto the absolute value of the hologram-correctors DE reveals itself for the etched glass distorters providing random divergence of more than 0.004-0.005 radian. These values are approximately in an order of magnitude smaller than the angular separation of neighboring orders of diffraction. Corresponding results, obtained by reading out by He-Ne laser radiation, are shown in the Fig.13.

In course of the experiments we have also tried the image correction with the use of SLM, based on the ferroelectric LC. Visual correction ability was not worse that in the case of nematic LC application. Image brightness, however, was much higher: in this case the radiation from thermal object is used much better, for the FLC SLM performance is almost polarization independent.

5. CONCLUSION

In the reported experiment the source of coherent radiation, used for the corrector record, was mounted in the plane of the object (or, generally speaking, optically conjugate plane). In practice of imaging of the remote object it is impossible. In the so called bypass optical schemes[7] the source of the radiation, used for reading out of the primary lens (mirror) distortions can be mounted nearby this lens or mirror, say, in the latter center of curvature. In this case the distortions are compensated (corrected) not completely, but down to some residual error. However, depending on the telescope design the surplus can be some dozen or hundred times[7,8].

Hence the results of the reported experiment promise the successful use of the optically addressed LC SLM as the dynamic holographic media for the record of the holographic correctors to be used in the passive bypass imaging telescopes.

REFERENCES

1. Denisuk Yu.N., Soskin S.I. Holographic correction of deformational aberrations of the primary mirror of the telescope. Opt. Spektrosk., 1971, Vol. 31. No. 6, p. 991-997, (in Russian).
2. Denisuk Yu.N., Soskin S.I. Holographic correction of deformational aberrations of the primary mirror of the telescope. Opt. Spektrosk., 1972, Vol. 33, No. 5, p. 994-996, (in Russian).
3. Munch J., Wuerker R. Holographic technique for correcting aberrations in a telescope//Appl. Opt. - 1989. - Vol. 28, No. 7. - P. 1312-1317.
4. Munch J., Wuerker R., Heflinger L. Wideband holographic correction of an aberrted telescope objective//Appl. Opt. - 1990. - Vol. 29, No. 16. - P. 2440-2445.
5. Andersen G., Munch J.,Veitch P. "Holographic correction of large telescope primaries by proximal, off-axis beacons// Appl. Opt. -1996-V.35, No.4 P. 603-608.
6. Zel'dovich B.Ya., Pilipetsky N.F., Shkunov V.V. Phase conjugation. - Moscow, 1985, 240 p. (in Russian).
7. Leshchev A.A, Pasmanik G.A.,.Sidorovich V.G, Vasil'ev M.V., Venediktov V.Yu.. Compensation for distortions in the imaging systems, using phase conjugation technique. Izvestiya Academii Nauk SSSR, v.55, 2, p.260-266, 1991. (In Russian).
8. Leshchev A. A., Sidorovich V. G., Vasil'ev M. V., Venedictov V.Yu., Pasmanik G.A. Nonreciprocal optical systems with phase-conjugating mirrors - a new class of optical imaging systems. International Journal of Nonlinear Optical Physics. - 1994. - Vol. 3, No. 1. - p. 89-100.
9. Vasil'ev A.A.. Casasent D., Kompanets I.N., Parfenov A.V. Spatial light modulators. Moscow, Radio i Svyaz. 1987. 320 p. (in Russian)
10. Petrov M.P., Stepanov S.I., Khomenko A.V. Photorefractive crystals in coherent optics. St.-Petersburg. Nauka. 1992. 320 p. (in Russian)
11. Kramer M. A., Wetterer .C. J., Martinez Ty. One-way imaging through an aberrator with spatially incoherent light by using an optically addressed spatial light modulator// Appl. Opt. - 1991. - Vol. 30, No. 23. - P. 3319-3323.
12. Dimakov S.A., Klimentiev S.I., Sventsitskaya N.A., Sherstobitov V.E. Compensation for optical elements distortions by means of dynamic holography in "white light". Opt. Spektr., 1996, Vol.80. No 4, p. 699-704 (in Russian).
13. Groznov M.A., Myl'nikov V.S., Soms L.N., Tarasov A.A. Liquid crystal spatial light modulator with the resolution of more than 1000 lines per mm. Zh. Tekh. Fiz.. 1987, Vol . 57. No. 10. p. 2041-2042, (in Russian).
14. Myl'nikov V.S. Liquid crystal spatial light modulators with the organic polymer photoconductor. Optical Journal, 1993, #7, p.41-45 (in Russian).
15. Kamanina N.V., Soms L.N., Tarasov A.A. Holographic correction for distortions using the liquid crystal phase light modulators. Opt. Spektrosk., 1990. Vol. 68. No. 3, p. 691-693 (in Russian).
16. Berenberg V.A., Kamanina N.V., Soms L.N. Holographic correction for distortions using the liquid crystal phase light modulators under different frequencies of recording and reconstructing radiation. Izv. Akad. Nauk SSSR, Ser. Fiz.. 1991, Vol. 55. No. 2. p. 236-238, (in Russian).
17. Berenberg V.A., Vasil'ev M.V., Venediktov V.Yu., Leshchev A.A., Soms L.N. Journal of Optical Technology, Vol.64, No.9, p.73-74, 1997.
18. Ahiyama K., Takimoto A., Ogivara A., Ogawa H. Jpn.J.Appl. Phys., 1993, Part 1, Vol. 32, p. 590.
19. Feoktistov N.A., Morozova L.E. Pisma v ZhTF, 1994, Vol.20, No.5, p.12-16, (in Russian).
20. Ahiyama K., Takimoto A., Ogawa H. Appl.Opt., 1993, Vol.32, No.32, p. 6493-6500.
21. Ivanova N.L., Morozova L.E., Onokhov A.P., Pevtsov A.B., Feoktistov N.A. Pisma v ZhTF, 1996, Vol.22, No.4, p.7-11, (in Russian).
22. Beresnev L.A., Blinov L.M., Dergachev D.I., Loseva M.V., Chernova N.I. Pisma v ZhTF, 1988. Vol. 14, No. 3, p. 260-263. (in Russian).
23. Abdulhalim I., Moddel G. Mol. Cryst. Liq. Cryst., 1991, Vol.200, p.79-101.

White Light Imaging Using Large Numerical Aperture Telescope with Dynamic Holographic Correction for Primary Mirror Distortions

M.V.Vasil'ev, V.A.Berenberg, A.A.Leshchev, P.M.Semenov, V.Yu.Venediktov

199034, Birzhevaya, 12, Institute for Laser Physics,
Scientific Center "Vavilov State Optical Institute" St.-Petersburg, Russia

ABSTRACTS

Large numerical aperture telescope with nonlinear optical correction for distortions, designed for the remote self-luminous object imaging, was realized in experiment and investigated. Dynamic hologram, recorded in optically addressed liquid crystal spatial light modulator, was used as the corrector. Nearly diffraction limited performance of the system was demonstrated.

Keywords: telescope, dynamic correction, dynamic hologram

INTRODUCTION

Just after the very holography invention it was proposed[1,2] to apply the holographic methods for the non-distorted imaging through the media with the phase distortions (the so called one way image correction technique). Later on the base of these first ideas there was elaborated the proposal to apply the holographic correction technique to the distortions, imposed the primary mirror (PM) of the telescope, imaging the remote objects[3,4]. In these works the successful holographic correction was realized on the base of the static hologram of the PM distortions, recorded from this PM center of curvature in the Twyman-Greene interferometer. The hologram was processed and then mounted in the focal unit of the telescope, imaging the remote object. Later similar experiments were carried out in the USA[5-7]. This method, obviously, can be applied only to the static distortions. At the same time the difficulties due to the necessity to take the hologram out for the processing and then to put it to the proper position with the high accuracy prevented the wide application of the method.

Later the progress in the development of the methods of the dynamic correction for distortions, using the nonlinear-optical technique of the phase conjugation has resulted in elaboration[8-12] of the so called bypass (nonreciprocal) telescopes, where the effect of phase conjugation compensation was applied to the telescope PM and other elements. This schematics, which was elaborated first of all for the purposes of laser beam direction, well fits also with the problem of the remote object imaging. Of course, the use of phase conjugation technique implied the application of the coherent radiation for the object illumination and imaging.

Such a technique was realized in several experiments. In particular, in the work[11] there was realized the diffraction limited imaging with the use of the bypass telescope with the PM (diameter 300 mm, curvature radius 2400 mm), comprised by six poor quality and non-coaligned segments. The remote point object was illuminated by the coherent radiation of second harmonics of Nd-laser ($\lambda=0.54$ μm). In the Fig.1 are shown the photographs, published first in paper[11]. One can see in one and the same angular scale the images of the point source, reconstructed by the "conventional" telescope, whose segmented PM was not coaligned (the relative piston shift of the segments was at least 10 μm), and by the bypass telescope with the phase conjugation compensation for the same PM distortions. In the latter case the system performance was practically diffraction limited.

Soon it became clear that the schematics of such systems and the methods of their design well fits, in particular, with the task of remote object imaging with the use of the dynamic nonlinear-optical correctors, in particular, of the dynamic holographic corrector. The first to our knowledge realization of the system of such a kind was demonstrated in the work[13]. This work was realized on the base of the bypass telescope, elaborated primarily for the intense CO$_2$-laser beam ($\lambda=10.6$ μm) direction[14], using the phase conjugation for the correction for the distortions of the PM (diameter 400 mm,

curvature radius 4000 mm, comprised by six segments); in the paper[14] such a system has demonstrated the nearly diffraction limited performance for the severely disaligned (relative piston shift of the segments exceeded 1 mm!). In the demonstration experiment[13] just the same telescope was used for the imaging of the remote object. The phase conjugation mirror was replaced by the dynamic holographic corrector, recorded in the thermal medium by the radiation of the CO_2-laser. This hologram was used for the correction for the distortions imposed by the PM into the image of the point object, illuminated by the radiation of another CO_2-laser, mutually incoherent with the first one.

Recent several years has brought fast progress in the technique of the dynamic holographic correction, using various nonlinear optical media. The most spectacular results were demonstrated with the use of the optically addressed liquid crystal spatial light modulators (OA LC SLM). The elements of such a kind[15-18] as well as some other[19,20] were successfully applied for the one-way dynamic holographic correction for the severe distortions of the lenses, imaging the complicated test objects in the incoherent radiation. In the paper[21] there was demonstrated the application of the OA LC SLM as the dynamic holographic corrector in the bypass telescope, imaging the monochrome point source of radiation.

This paper is devoted to the studies of the non-monochrome complicated test-object imaging with the use of the bypass telescope with the large numerical aperture and dynamic holographic correction for its PM distortions, using the OA LC SLM as the medium for the dynamic hologram recording. The above mentioned bypass telescope[11] (PM diameter 300 mm, curvature radius 2400 mm, focal length 1200 mm) served as the prototype for this telescope design (general composition and secondary lenses were the same as in the experiment with the phase conjugation compensation). In the paper[22], published in the same book, are given the details of the system optical design and the results of its performance numerical simulation. According to the results of the paper[22], in the case of the bypass schematics application for the imaging in the comparatively wide spectral range the requirements to the PM quality are closer than in the case of monochrome radiation. So in this case the segmented PM of paper[11] was replaced by the poor quality solid mirror with the same geometry parameters. The experiments with the poor quality PM were accompanied by the control experiments with the high-quality PM.

EXPERIMENTAL SETUP

Optical scheme of the experimental setup is shown in the Fig.2. Imaged test object was mounted at the distance of 16500 mm from the telescope PM. The radiation from the test object is collected by the PM nearby its focal plane. The three component lens of special design[11,22] (clear aperture 30 mm) images the object to the infinity. In the assumption of the nondistorted PM this image quality is to be practically diffraction limited. Beam splitting cube sends the beam to the corrector unit (special relay telescope reduces this beam diameter twice down to 15 mm so as to obtain the optimal radiation energy at the element and to fill within the experimental facility dimensions; the overall clear aperture of the OA LC SLM available in this experiment was 30 mm) and to the registering system (lens and CCD-camera or photocamera). The system design made it possible to record both the zero and first diffraction (at the dynamic hologram) orders without the system re-adjustment. The zero diffraction order was used while system adjusting and provided the control for the images, recorded without application of the correction technique (see further).

In the mode of correction for distortions the system action consists of two stages. On the first stage the distortions of PM are read out by the pulsed radiation (second harmonics of single mode Q-switched Nd-laser, $\lambda=0.54\mu m$). This radiation records the hologram of these distortions. After some delay, when the pulsed radiation is absent, the test-object is imaged with the correction.

The hologram of PM distortions is recorded in the following way. Laser radiation enters the system as the beam with the plain wavefront through the beam splitting cube. Two component lens of special design[11,22] (clear aperture 30 mm) focuses it to the PM center of curvature. The radiation, reflected by the PM, goes back through the lens. The beam, whose wavefront bears the information on the PM distortions, is sent by the beam splitting cube to the relay telescope and to the corrector unit. The dynamic hologram was recorded as the interference pattern of the distorted beam with some part of primary laser beam with the non-distorted plain wavefront. The angle between two beams equaled 3°, so the spatial carrier frequency of the dynamic grating equaled 95 mm^{-1}. Special shutter protected image registration system off the laser radiation. The performance and parameters of the dynamic holographic corrector were rather similar to that described in the papers[17,18], published in this book. In this work we have also used the OA LC SLM with both nematic and ferroelectric LC layers.

10^{-5} rad
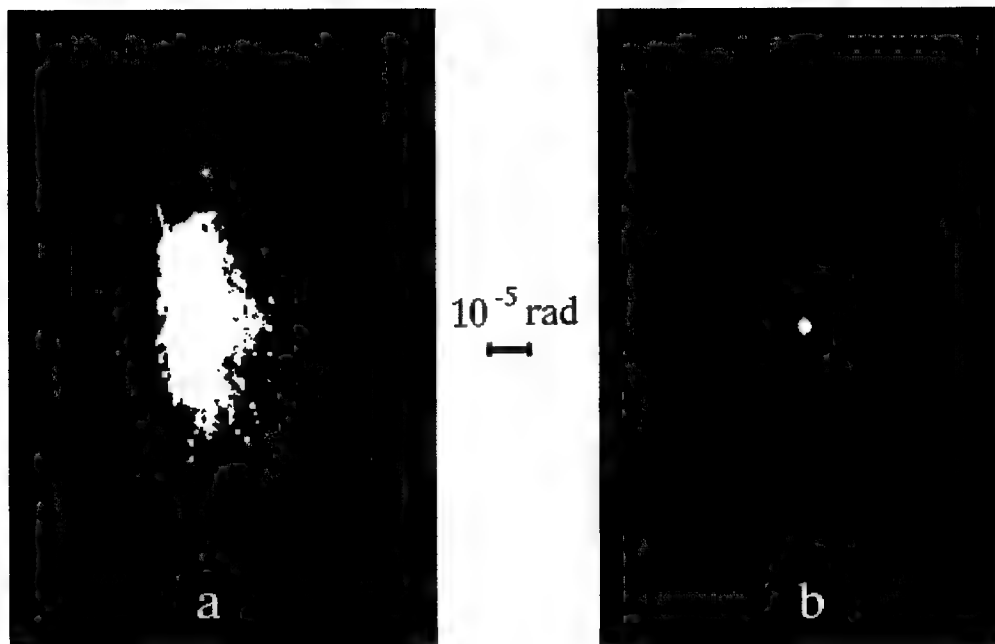
Fig.1. Experimental (paper[11]) point spread function, recorded for one and the same PM distortions in the telescope without correction for distortions (a) and with correction (b).
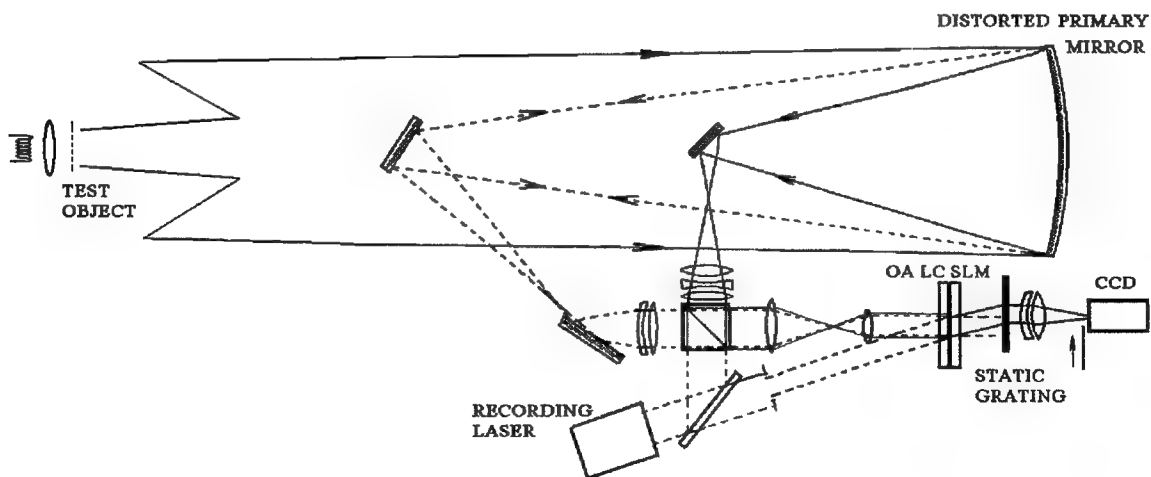
Fig.2. Scheme of the experiment on the dynamic holographic correction for the PM distortions.
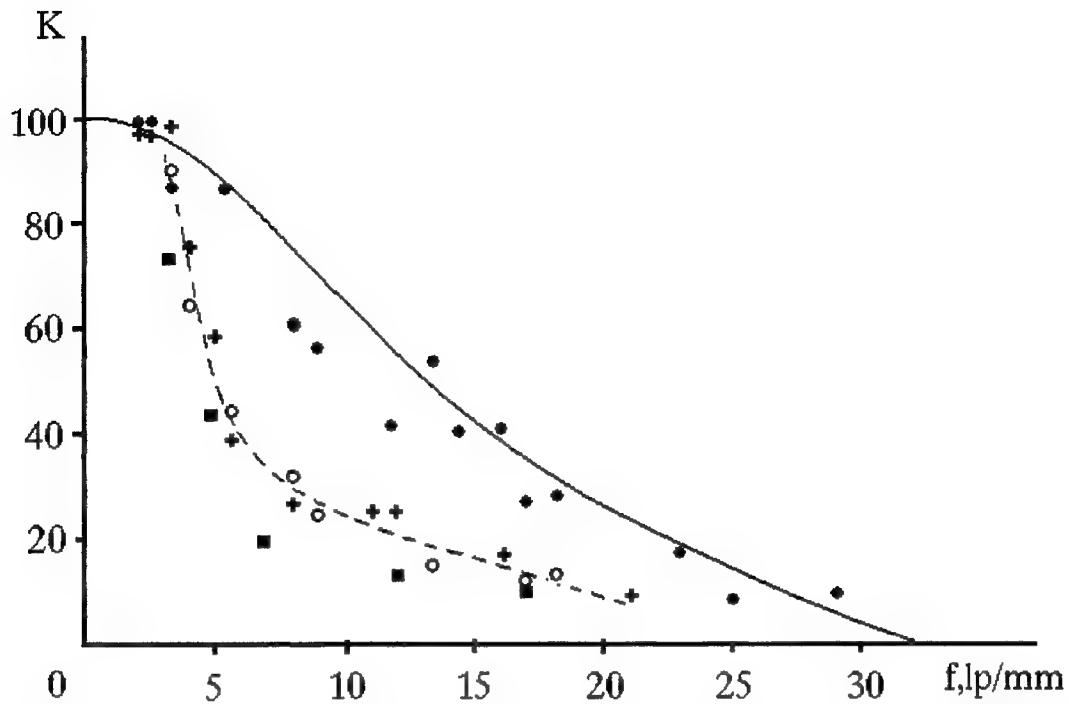
Fig.3. Measured values of frequency - contrast characteristics of telescopes. Solid line stays for the theoretical limit, calculated for the ideal system, solid dots correspond to the image, recorded in zero diffraction order with non-distorted PM; hollow circles correspond to the system with "correction" and non-distorted PM, crosses - to the system with distorted PM and correction (green radiation, centered at 540 nm) and squares - to the system with distorted PM and correction at the shifted in 25 nm wavelength.

Fig.4. Interferogram of the deformed mirror, recorded at λ=0.54 μm

Fig.5.Test-object, imaged by conventional kind telescope (without correction) with the distorted PM.
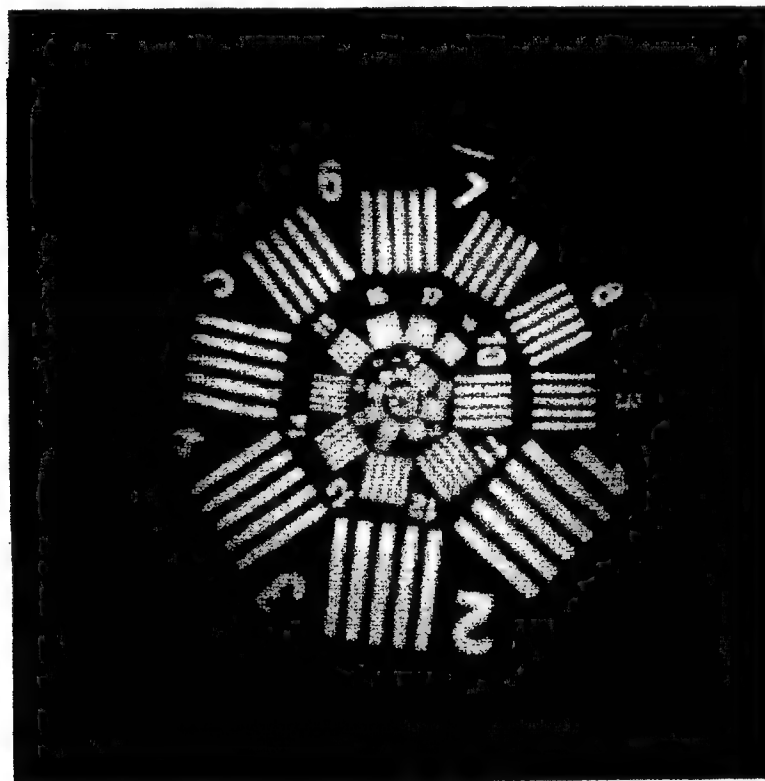
Fig.6. Test-object, imaged by the telescope with correction with the distorted PM.

On the stage of image reconstruction the radiation from the test object reaches the dynamic hologram, which corrects in the first order for diffraction for the distortions, imposed by the PM. Auxiliary static diffraction grating[6,17,18] with the same spatial frequency of 95 mm^{-1} works in the minus first order of diffraction and thus compensates for the dynamic grating chromatism. Now the registering system entrance is open and the reconstructed image can be recorded (while recording the corrected image in the diffraction order, the non-corrected image, going in the zero order of diffraction was shut off). In the reported cycle of studies we have realized only imaging in the single flash mode, but, in principle, in the future such a system can be used in pulse repetitive mode of action.

Standard stroke test object with the spiral arrangement of the strokes[23] was used in the experiment. The transverse size of the test-object was 9 mm, fitting to the design aberration-free field of system vision (~ 2 minutes in the angular measure). This test object was illuminated either by the halogen lamp (power ~ 50 W) or by the photographic flashlamp. Colored filters with the transmission maximum in green band were mounted between the lamp and test-object so as to provide necessary spectral content of imaging radiation. Images of test-object, recorded under various conditions of the experiment were subject of frequency vs. contrast analysis. The measured dependencies of the image contrast vs. spatial frequency of strokes are summarized in the Fig.3.

SYSTEM PERFORMANCE WITH THE HIGH-QUALITY PM

The evaluation of the system with the correction performance was preceded by the evaluations of ideal system performance. On the very first stage of the experiment the high-quality spherical mirror was mounted in the telescope. The image of the test-object was first recorded in the zero diffraction order, i.e. in the mode of the common type telescope. The measured parameters of frequency vs. contrast parameter are shown in the Fig.3 as solid dots. The solid line corresponds to the theory limit of the same characteristics, calculated for the system parameters for the rectangular test object and for the ideal PM quality. One can see, that the optical performance of the very telescope was practically diffraction limited.

On the next stage we have evaluated the performance of the system with the "correction" (i.e. with the record of the corrector and image reconstruction in the first order of diffraction) for the case of ideal PM. The corresponding values of the frequency vs. contrast characteristics are shown in the Fig.3 as the hollow circles. One can see that in this case the system performance is somewhat worse than in the first case. Possible reasons are the large number of auxiliary elements in the beamlet of corrector and the non-ideal quality of the very corrector unit. Obviously, these results, indicated in the Fig.3 also by the dotted line, are to be treated as the best possible parameters, available in the case of realization of the system with the correction for real distortions.

SYSTEM PERFORMANCE IN THE MODE OF CORRECTION FOR PM DISTORTIONS

On the next stage of experiment the ideal PM was replaced by the intentionally poor quality PM, realized as the thin (15 mm thickness) and slightly flexible mirror. This mirror was intentionally distorted by means of longitudinal stress. In the Fig.4 is shown the interferogram of the poor quality PM, mounted in the telescope. This interferogram was recorded in the plane of the holographic corrector; the proper spatial frequency of the interference fringes was realized by means of choosing of the proper angle between the probe and reference beams. One can see that the global deformation of the PM surface with respect to the spherical shape equals some 5-8 fringes.

In the Fig.5 is shown the severely distorted image of the test object, recorded in the zero diffraction order (i.e., without correction for distortions) in the system with such a distorted PM. In the Fig.6 is shown the corrected image, recorded for the same distortions of PM with the use of the colored filter (bandwidth 50 nm, centered at the recording wavelength of 540 nm). In the Fig.3 the corresponding values of frequency vs. contrast characteristics are shown by crosses. One can see that this system performance was quite identical to that with the use of ideal quality PM, i.e. the distortions were completely eliminated.

At the shifted wavelength one has to observe the deterioration[17,18,22] of the correction fitness. In experiment we have used the colored filter, whose band center was shifted in 25 nm with respect to recording wavelength (bandwidth 75 nm). The corresponding values of frequency vs. contrast characteristics are shown in the Fig.3 by squares. One can see some deterioration of the system performance. However, it can be explained not only by the effect of non-fitting to the distortions while hologram reconstruction at the shifted wavelength, but also by the incomplete achromatization of the auxiliary optics, used in this experiment.

CONCLUSION

We have shown in the experiment that one can use the bypass telescopes with the dynamic holographic correction for the PM distortions in the mode of complicated object imaging in the sufficiently wide spectral band. The quality of the corrected image is rather high.

REFERENCES

1. J.Upatnieks, A.VanderLugt, E.Leith, "Correction of Lens Aberrations by Means of Holograms", pl.Opt., v.5, p.589, (1966)
2. H.Kogelnik, K.S.Pennington, " Holographic Imaging Through a Random Medium", JOSA, v.58, p.273, (1968).
3. Yu.N.Denisuk, S.I.Soskin. Holographic correction of deformation aberrations of the primary mirror of a telescope. Opt. Spektrosc. (USSR), Vol. 31. p. 535-541 (1971).
4. Yu.N.Denisuk, S.I.Soskin. Holographic correction of the aberrations of an optical system caused by deformations of the primary mirror. Opt. Spektrosc. (USSR), Vol. 33, p. 544-546 (1972).
5. J.Munch, R. Wuerker, Holographic technique for correcting aberrations in a telescope, Appl.Opt., v.28, n.7, p.1312 - 1317, (1989).
6. J.Munch, R. Wuerker, L.Heflinger, Appl. Opt., Wideband holographic correction of an aberrated telescope objective, v.29, n.16., p.2440 -2445, (1990).
7. G.Andersen, J.Munch, P.Veitch, Appl.Opt., Compact, holographic correction of aberrated telescopes, v.36, n.7, p.1427-1432, (1997).
8. O.V.Kulagin, A.A.Leshchev, G.A.Pasmanik, V.G.Sidorovich. Patent USSR 1729221, priority May, 21, 1985, published in «Bulleten izobreteniyi i otkritiyi SSSR», 15, 1992. (In Russian).
9. J.Menders, R.Aprahamian, J.Godden. Proc. of SPIE v.1044, , p.256, 1989.
10. A.A.Leshchev, G.A.Pasmanik, V.G.Sidorovich, M.V.Vasil'ev, V.Yu.Venediktov. Compensating the distortions of imaging optical systems using phase conjugation. Izv. Acad. Nauk SSSR, Ser.Fiz., v.55, No.2, p.260-266, 1991. (In Russian).
11. A.A.Leshchev, P.M.Semenov, V.G.Sidorovich, O.V.Solodyankin, M..V.Vasil'ev, V.Yu.Venediktov, Kvantovaya electronika, V.18, 12, p.1405-1406, 1991. (In Russian).
12. A.A.Leshchev, V.G.Sidorovich, M.V.Vasil'ev, V.Yu.Venediktov, G.A.Pasmanik, Int..J.of Nonl.Opt.Phys.,v.3, No.1, p.89-100, 1994.
13. A.A.Ageichik, S.A.Dimakov, O.G.Kotayev, A.A.Leshchev, Yu.A.Rezunkov, A.L.Safronov, V.E.Sherstobitov, V.V.Stepanov, "Use of dynamic holography technique for correction of aberrations in telescopes", SPIE, v.2771, p.156-163, (1996).
14. A.A.Leshchev, P.M.Semenov, M.V.Vasil'ev, V.Yu.Venediktov, Kvantovaya electronika, v.20, 4, p.317-318, 1993. (In Russian).
15. M.A.Kramer, C.J.Wetterer, T.Martinez, Appl.Opt., One-way imaging through an aberrator with spatialy incoherent light by using an optically addressed spatial light modulator, v.30, n.23,p.3319 - 3323, (1991).
16. S.Fukushima, T.Kurokawa, M.Ohno, Appl.Phys.Lett., Real-time hologram construction and reconstruction using a high-resolution spatial light modulator, v.58, p.787-789, (1991).
17. V.A.Berenberg, M.V.Vasil'ev, V.Yu.Venediktov, A.A.Leshchev, L.N.Soms. Correcting the aberrations of an objective in a wide spectral range of a liquid-crystal light-controlled spatial light modulator. J.Opt.Technol, v.64, no.9, p.863-864, 1997
18. V.A.Berenberg, A.A.Leshchev, M.V.Vasil'ev, V.Yu.Venediktov. Polychromatic correction for aberration in lenses of telescopic systems using liquid crystal optically addressed spatial light modulator.SPIE,vol.3353,paper145 (this book)
19. J.D.Downie, "Real-time holographic image correction using bacteriorhodopsin", Appl.Opt.,v.33,n.20, p.4353, (1994).
20. S.A.Dimakov, S.I.Kliment'ev, N.A.Sventiskaya, V.E.Sherstobitov. Compensating the distortions of optical elements by the methods of dynamic holography in white light. Opt. Spektrosc., v.80, p.628-632 (1996).
21. M.T.Gruneisen, K.W.Peters, J.M.Wilkes, Compensated imaging by real-time holography with optically addressed liquid-crystal spatial light modulators, Proceedings SPIE, v.3143, p.171-181, (1997).
22. N.A.Bezina, A.A.Leshchev, M.V.Vasil'ev, V.Yu.Venediktov. Numerical Simulation of Observational Telescope with the Dynamic Holographic Correction. SPIE vol.3353, paper 95 (this book).
23. K.V.Vendrovsky, A.I.Weitzman. Photographic structurometery. Moscow, Iskusstvo, 1982, p.194 (in Russian).

Cylindrical and spherical adaptive liquid crystal lenses

Alexander Naumov[a], Mikhail Loktev[a], Igor Guralnik[b], Gleb Vdovin[c]

[a]P.N. Lebedev Physical Institute of Russian Academy of Sciences, Samara Branch, 443011, Novo-Sadovaya St., 221, Samara, Russia; e-mail: naumov@ssu.samara.ru
[b]Department of Physics, Samara State University, 443011, Acad. Pavlov St., 1, Samara, Russia; e-mail: guralnik@ssu.samara.ru
[c]General Physics Institute of Russian Academy of Sciences, 117942, Moscow, Russia

ABSTRACT

A novel approach to the liquid crystal modulators design is suggested under which the liquid crystal is treated as a distributed capacitor. To control the capacitor, we introduced a distributed high resistance control electrode. We devised methods of control and investigated modal liquid crystal modulators that can be used as adaptive cylindrical and spherical lenses. Analytical derivations, computer and experimental results are presented and discussed.

Keywords: liquid crystals, spatial light modulators, adaptive lenses

1. INTRODUCTION

Multi-element liquid crystal (LC) phase modulators hold great promise because of their light-transmitting operation, simple control, and reliability. They can be applied for suppressing phase aberrations in the atmosphere[1] or in optical systems[2] and for the light beams focusing in complex patterns[3] as well. To solve these problems, LC modulators with direct electrical or optical addressing are used. In many current and feasible applications, such as autofocus in bar code readers and compact disk players, zoomfocus image in capturing systems and 3D-scanners, semiconductor lasers astigmatism correction, and human vision correction, it is the low order space aberrations that one has to deal with, such as defocusing and astigmatism, i.e., adaptive spherical or cylindrical lenses are necessary.

Two major approaches to an adaptive LC lens design have been suggested. Kowel et al.[4] produced a given shape of the LC refractive index gradient by a set of individually controlled electrodes using zonal correction principle. Precision control in these modulators requires that a large number of discrete control electrodes be used. In the simplest configuration, the electrodes are linear and equidistant to shape a cylindrical wavefront. A circular electrode configuration is impractical because of the difficult mask fabrication. Spherical phase correction is achieved by combining two crossed modulators. Developing this concept, Riza and DeJule[5] used the same parallel electrode geometry with the high-resistance coating between the neighboring electrodes that are interconnected with electrical biasing resistors network. Cylindrical index variation of the LC is induced by distribution of control voltage applied to the top and bottom electrodes of the LC lens. The central electrode is biased near the threshold value for the LC molecular activation and top cover-glass electrode is grounded. Thus, the authors actually realized modal control principle through zonal control.

The second approach is based on modal control principle. This approach makes use of a non-uniformity of electric field produced by two hole-patterned electrodes or one hole-patterned electrode and a ground electrode. In both cases, there is a strong limitation on the hole diameter to the LC layer thickness ratio, to produce nearly quadratic index perturbation across the LC cell area. The lens focusing properties deteriorate when this ratio increases. Typically, for a good alignment, the LC thickness should not exceed 50 μm, limiting the lens aperture to several hundred micrometers. Hence, this approach is only suitable for microlenses fabrication[6,7].

Both concepts described allow for the voltage amplitude control of an adaptive LC lens but the voltage frequency is not taken into account. We propose a novel approach to form a smooth continuous near-quadratic distribution of the refractive index in the nematic LC layer, realizing pure modal control principle in a wide aperture modal liquid crystal lens (MLCL). This is achieved by introducing a high-resistance control electrode (CE) and regarding the CE-LC combination as a system with distributed resistance (control electrode) and distributed capacitance (LC layer). Along with regular amplitude control, reactive nature of this system enables a frequency control of the LC lens performance[8]. Spatial modulation of the wavefront is specified by the geometry of contacts located at the periphery of the modulator aperture. Ultimately, we need a single circular control contact for a spherical MLCL lens and two linear equidistant contacts for a cylindrical MLCL.

2. BASIC THEORY

Let us consider a LC cell configuration shown in Fig. 1. The LC layer is sandwiched between two transparent plate electrodes deposited on glass substrates. The distributed resistance of the CE is much higher than that of the ground electrode. Control voltage is applied to the contacts deposited at the periphery of the highly resistive electrode. Initial homogeneous LC layer alignment is determined by the alignment coating, and the dielectric spacers set the LC's thickness. Active impedance of the high resistance CE and reactive impedance of the LC layer form a distributed voltage divider. When an AC control voltage is applied to the peripheral contacts, the voltage at the center of the CE lags behind the voltage variation at the contacts because of the reactive nature of the device. At higher frequencies, this delay increases, reducing the *rms.* voltage at the aperture center. Another factor contributing to this voltage drop is leakage currents through the LC layer. For certain frequencies and amplitudes of the control voltage, resulting *rms.* voltage distribution over the LC layer is close to parabolic. Additionally, if we ensure a linear working range on the LC birefringence *vs.* voltage curve, a plane lightwave passing through the MLCL becomes cylindrical or spherical.

Fig. 1. General schematic for MLCL (a) and the contacts layout for cylindrical (b) and spherical (c) lenses.

To enable prediction and optimization of the MLCL focusing properties, we performed a theoretical analysis of the voltage distribution across its aperture. We treat the LC layer as a parallel-plate capacitor, one plate of which carries a non-uniform free carriers distribution and another one is an equipotential surface. We found the LC conductance to have strong effect on the MLCL electrical properties, so we also took into account leakage currents in the LC. Quantitatively, the voltage distribution in the LC adaptive lens is described by the following equation of the MLCL (see Appendix for its derivation):

$$\nabla_s^2 U = \rho_s C_s \frac{\partial U}{\partial t} + \rho_s g_s U, \tag{1}$$

where ρ_s is the CE sheet resistance, C_s and g_s are specific capacitance and conductance of the LC layer, respectively. The nature of Eq. (1) can be clarified by a lumped-parameter electrical analogue shown in Fig. (2). Deriving from Kirchhoff's rules the voltage distribution for this model, we also obtain Eq. (1).

Equation (1) is applicable to any contact configuration and to arbitrary temporal dependence of U. However, in this paper we focus on a harmonic-type applied voltage. For a single harmonic of frequency ω, the MLCL equation is reduced to
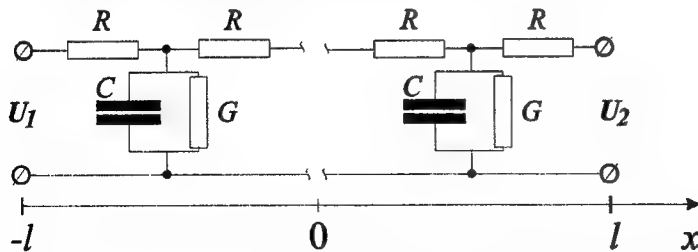
Fig. 2. One-dimensional lumped-parameter electrical analog for a MLCL.

$$\nabla_s^2 U = \chi^2 U \tag{2}$$

where $\chi^2 = \rho_s (g_s - i\omega C_s)$. Note that mathematically the voltage distribution is governed by a single complex-valued parameter χ, measured in m^{-1}. Therefore, we should expect distinctly different voltage profiles for large and small values of χl, respectively, where l is the characteristic aperture size. Alternatively, introducing the LC specific impedance as $Z_s = (g_s - i\omega C_s)^{-1}$, we find the parameter χ^2 to equal the ratio ρ_s/Z_s. Frequency dependence of χl

enables the MLCL control through applied voltage frequency variation, along with traditional voltage amplitude control.

The LC specific conductivity g_s and capacitance C_s are determined by the real and imaginary parts of the complex dielectric constant $\varepsilon = \varepsilon' + i\varepsilon''$ (see Ref. 9). Generally speaking, they are fairly complex functions of *rms.* and frequency of the applied voltage, rendering analytical solution of Eq. (2) practically impossible. Below we consider a special case of voltage-independent Z_s, which is important for the insight into the physics of the MLCL work, as well as initial approximation for computer simulations.

2.1 Cylindrical lens

The contact geometry is shown in Fig. 1(b). The linear symmetry for the 2D potential distribution in this case greatly simplifies the analysis. Instead of Eq. (2) we have

$$\frac{d^2 U}{dx^2} = \chi^2 U .$$ (3)

Equation (3) should be completed by a set of boundary conditions (BC). In general form the single-harmonic BC can be written as follows:

$$U(-l) = U_{01}\sin(\omega t), \quad U(l) = U_{02}\sin(\omega t + \varphi),$$ (4)

where φ is the contact voltage phase shift, i.e., the phase shift between the control voltages applied to the contacts relative to the ground plate. The following special case BCs can be realized experimentally:

(a)	Symmetric	$U_{01} = U_{02}$, $\varphi = 0$
(b)	Anti-symmetric	$U_{01} = U_{02}$, $\varphi = \pi$
(c)	Asymmetric,	Open-circuit at $x = l$
(d)	Asymmetric,	Short-circuit at $x = l$
(e)	Asymmetric,	$U_{01} = U_{02}$, $\varphi \neq 0$ and $\varphi \neq k\pi$, $k = 1, 2, \ldots$
(f)	Asymmetric,	$U_{01} \neq U_{02}$, $\varphi = 0$

(5)

First, we consider the (a)-type BC. These are available both for cylindrical and spherical MLCL's. Other cases can be realized only in a cylindrical lens and are dealt with later. From Eq. (3) we obtain

$$U = U_0 \frac{\cosh(\chi x)}{\cosh(\chi l)} .$$ (6)

By introducing the LC impedance $Z = Z_s/2la$ and the CE resistance $R = \rho_s 2l/a$, we present this parameter in the form $\chi l = \sqrt{R(G - i\omega C)}/2$. Here a is the aperture width along the contacts. It is instructive to consider limiting cases of small and large magnitudes of $|\chi l|$, respectively:

$$|\chi l|^2 << 1$$ (7)

and

$$|\chi l|^2 >> 1.$$ (8)

For small values of $|\chi l|$, Eq. (6) gives

$$U(x) \approx U_0 \left[1 - \frac{\chi^2}{2}(l^2 - x^2) \right].$$ (9)

Equation (9) shows that for small bends the voltage distribution is essentially parabolic. The voltage in the aperture center is equal to

$$U(0) \approx U_0 \left(1 - \frac{R}{2Z}\right). \tag{10}$$

It is necessary to keep the *rms.* voltage $U(0)$ above the threshold electrooptic voltage U_{th}. Then for $U<(2\div3)U_{th}$ the variation of the LC refraction index *vs.* U is linear and the required quadratic index perturbation of the LC for formation of a cylindrical lens occurs.

In the opposite case of large $|\chi l|$ we obtain

$$U(x) = U_0 e^{-\chi \ (l-|x|)}. \tag{11}$$

The voltage drops exponentially from contacts to the central area and is noticeably different from zero only in narrow regions next to the contacts. The width of these regions is of the order of $(\text{Re}\chi)^{-1}$ and, according to (8), is much smaller than l. This regime is not desirable for the LC lens, as the bulk of the lens is not involved in focusing.

Now let us consider the (b)-type BC. Similarly to the previous analysis, we obtain

$$U = U_0 \frac{\sinh(\chi x)}{\sinh(\chi l)}. \tag{12}$$

Unlike the symmetric distribution, in case of anti-symmetric distribution the voltage in the MLCL center is always zero. The focusing properties of the MLCL in this case are important for the design of adaptive cylindrical axicon.

Finally, for both (e) and (f)-type BC, the voltage minimum shifts away from the MLCL center but optically these types are different. Coupled with criterion (7), the (e)-type BC causes the MLCL optical axis to shift from the center, while for (f)-type BC optical axis is deflected from the center.

2.2 Spherical Lens

Introducing the polar coordinates in the center of the MLCL aperture (see Fig. 1(c)), Eq. (2) can be modified as

$$\frac{d^2U}{dr^2} + \frac{1}{r}\frac{dU}{dr} - \chi^2 U = 0. \tag{13}$$

Particular solution of this equation, finite at $r=0$ and complying the BC

$$U(r = l) = U_0, \tag{14}$$

has a form

$$U = U_0 \frac{I_0(\chi r)}{I_0(\chi l)}. \tag{15}$$

Here I_0 is the modified Bessel function of zero order. From Eq. (15) for small values of χl we obtain

$$U \approx U_0 \left[1 - \frac{\chi^2}{4}\left(l^2 - r^2\right)\right]. \tag{16}$$

Similar to cylindrical MLCL, the voltage varies quadratically with the distance from the center of the spherical MLCL. For large values of $|\chi l|$ we obtain exponential voltage decay from the contact to the lens aperture center. Indeed, expansion of the Bessel function in this zone contains exponents $\exp(\pm r\chi)$. Assuming $\text{Re}\chi>0$, we can ignore the exponents with $-\chi r$. Then for $r > (2\div3)(\text{Re}\chi)^{-1}$

$$U = U_0 \sqrt{l/r} \ e^{-\chi \ (l-r)}. \tag{17}$$

Thus, only thin ring-shaped area at the aperture periphery is involved in focusing so that the MLCL regime with $|\chi l|\gg1$ is impractical.

2.3. Focal lengths

In Fresnel's approximation the focal length of the MLCL is given by

$$F = \frac{\pi l^2}{(\Delta\Phi_c - \Delta\Phi_e)\lambda},$$

(18)

where $\Delta\Phi_c = \Delta\Phi(0)$ and $\Delta\Phi_e = \Delta\Phi(l)$ are the phase delays between ordinary and extraordinary light waves with the wavelength λ in the center and at the edges of the device, correspondingly. Phase delay for arbitrary point on the MLCL aperture can be written as

$$\Delta\Phi = 2\pi \Delta n d / \lambda,$$

(19)

where Δn is the LC birefringence:

$$\Delta n = \int_{-d/2}^{d/2} \left(\frac{n_\parallel n_\perp}{\sqrt{n_\perp^2 \cos^2 \theta + n_\parallel^2 \sin^2 \theta}} - n_\perp \right) dz.$$

(20)

As it follows from the analysis in Section 2, in case of small values of $|\chi|$ the phase distribution in a MLCL has a desired quadratic form. However, in this regime the voltage bend in the lens center is small (of the order of $(\chi l)^2$), resulting in small values of $\Delta\Phi_c$-$\Delta\Phi_e$. Hence, the MLCL should exhibit good focusing properties at large focal lengths. For many applications, though, the short focuses are preferable, in which case we must move from condition (7) to larger values of χl. We have already noted, however, in connection with Eq. (11), that it is impractical to increase the value of $|\chi l|$ much above the unit, as only small portion of the MLCL aperture becomes involved in focusing. Thus, the best MLCL performance criterion is (χl)~1, i.e.,

$$l^2 \rho_s \sqrt{g_s^2 + \omega^2 C_s^2} \sim 1.$$

(21)

The phase shift distribution in this case is not parabolic, inducing phase aberrations. To alleviate the problem of short focal length phase aberrations, we developed two special techniques. The first one consists in optimizing the MLCL focusing properties by appropriate choice of the control voltage frequency and amplitude for a single harmonic. The second technique is based on the use of multiple harmonics in the applied voltage spectrum. Let us consider more closely the best performance criterion (21). The range of the focal distances is mainly determined by the aperture size. The value of $(\Delta\Phi_c$-$\Delta\Phi_e)$ in Eq. (18) is limited by $\Delta\Phi_{max} = 2\pi(n_e-n_o)d/\lambda$, where n_e, n_o are refractive indices for extraordinary and ordinary light, correspondingly. The value of $\Delta\Phi_{max}$ is determined by the LC layer thickness, which is normally less than 50 μm to provide a good LC alignment. The limit value of birefringence for visible light is about 0.3. To obtain a short-focus MLCL, it is necessary to decrease the aperture size l. Though in this case the relation (21) can be destroyed and we face the risk of obtaining a simple LC cell instead of a lens, we can rescue the criterion (21) by increasing the control voltage frequency.

Thus, for the steady-state regimes the LC material for a MCLC should meet the following requirements:

(a) a high birefringence Δn to obtain maximum $(\Delta\Phi_c$-$\Delta\Phi_e)$,

(b) high dielectric constants $\varepsilon_\perp'$ and $\varepsilon_\parallel'$ to enhance the MLCL reactive impedance, enabling low frequency voltage control (important for maintaining low g_s),

(c) low dielectric constants $\varepsilon_\perp''$ and $\varepsilon_\parallel''$ to guarantee small g_s, preventing by-passing of the LC capacitance by its conductance.

3. EXPERIMENTAL RESULTS

We used two types of nematic LC with positive dielectric anisotropy: LC1348 and LC616 (from NIOPIK, Moscow). The LC 1348B has a relatively high birefringence 0.224 for $\lambda=0.633$ μm and high electrical conductivity. The birefringence of the LC 616 is 0.101 but its conductance is twice as little. We produced initial homogeneous alignment of the LC by rubbing polyvinylalcohol film coating on the CE layer and the ground electrode. Polymer spacers determined the LC layer thickness to be 25 μm. Dielectric constants $\varepsilon_\perp'$ and $\varepsilon_\parallel'$ and the ratio of elastic constants K_{11}/K_{33} were pointed out in the LC's certificates. The absolute value of splay constant K_{11} was found from the threshold voltage, which for electrooptic S-effect[9] is

$$U_{th} = \pi \sqrt{\frac{4\pi K_{11}}{\Delta \varepsilon'}} \; . \tag{22}$$

To evaluate $\varepsilon_\perp''$ and $\varepsilon_\parallel''$ and to find the specific capacitance and conductance of the LC layer, we investigated their integral values of $C=C_sS$ and $G=g_sS$ for a simple LC cell[10].

We assembled modulators with ground plates coated by highly conductive indium-tin-oxide films. The high resistance CE's of titanium films were deposited on glass substrates at ~10^{-3} Pa and subsequently heated in atmosphere. These electrodes have good transparency in visible region but it was difficult to obtain a desired surface resistance because of its degradation. We selected the deposition regime under which the resistance between 15-mm-long linear highly conductive titanium contacts spaced by a 4-mm distance stabilized at the level of ~2 MΩ after a period of degradation. The line contacts were fabricated by evaporation of the titanium film through the steel mask. We also fabricated circle contacts for spherical MLCL's with the diameter 6.5 mm. Computer simulations show that the value of ρ_s has no immediate effect on the focusing performance but may lead to contravention of the criterion (21).

3.1. Amplitude-frequency lens control

Theoretical analysis of Section 2 shows that by adjusting the applied voltage frequency we can control the MLCL focal length even at fixed voltage amplitudes. Figure 3 shows intensity distribution at 1 m away from the spherical MLCL

← Frequency				*Rms.* voltage →		
2.56V	2.56V	2.56V		1.32V	2.56V	3.61V
6.2kHz	4.8kHz	2.7kHz		4.8kHz	4.8kHz	4.8kHz
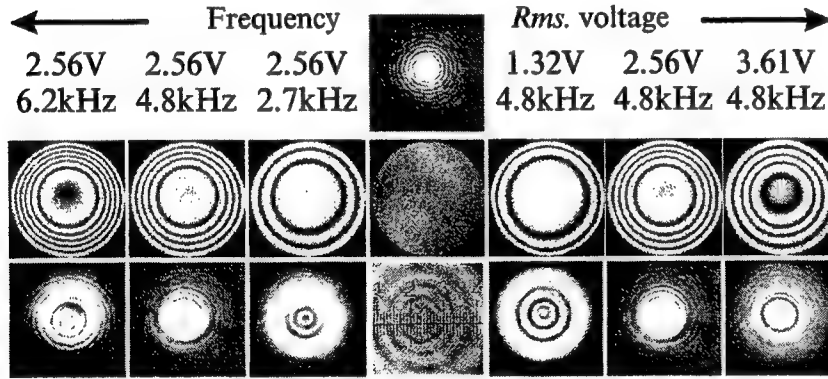
Fig. 3. Interference fringe patterns obtained by positioning the spherical MLCL (based on Merck LC) between crossed polarizers (middle row) for different AC frequencies and rms. voltage values (top row). Bottom row is corresponding intensity distributions 1 m away from the MLCL. For comparison we present also focusing by ordinary glass lens of the same aperture and focal length (in the middle of the top row). Numbers on the scale are mm.

and corresponding interference pattern between ordinary and extraordinary waves in the MLCL positioned between two crossed polarizers. To reduce RMS deviation from an ideal parabolic phase profile, one can optimize both frequency and *rms.* voltage. From computer simulations we found that variation of R has practically no effect on the optimal control voltage but affects the optimal frequency, and that only for different focal distances. On the contrary, variation of ε'' changes the optimum voltage amplitude but not its frequency. Experimental results of focusing by means of the cylindrical MLCL are shown in Fig. 4. These curves were obtained by scanning a coupled photodiode and adjusting 0.3 mm slit diaphragm. To avoid laser power fluctuation influence and to increase measurement sensitivity, we modulated the laser beam by a mechanical chopper and used a selective millivoltmeter tuned to the chopper frequency.

Up to now we regarded the MLCL amplitude-frequency control through variation of the LC capacitance. However, due to dispersion of nematic LC's dielectric constant, at certain frequencies its imaginary part ε'' can display a resonance behavior[9] which results in the similar resonance of g_s vs. f dependence. We believe this sudden rise in g_s to be responsible for the focusing by the MLCL based on relatively low resistance CE ($R=4$ kΩ) with LC 1348B, that we observed at high frequencies 850..900 kHz. Figure 5 shows the interference pattern for *rms.* voltage 4 V and $f=870$ kHz. Reduction of the picture contrast is explained by the dynamic scattering at the MLCL aperture periphery. To prove the active nature of the LC impedance in this frequency range, we measured the phase shift between the throughput current (a-type BC) and the applied voltage, and obtained values of about 11°. Voltage distribution was unstable for the similar MLCL with the LC 616.
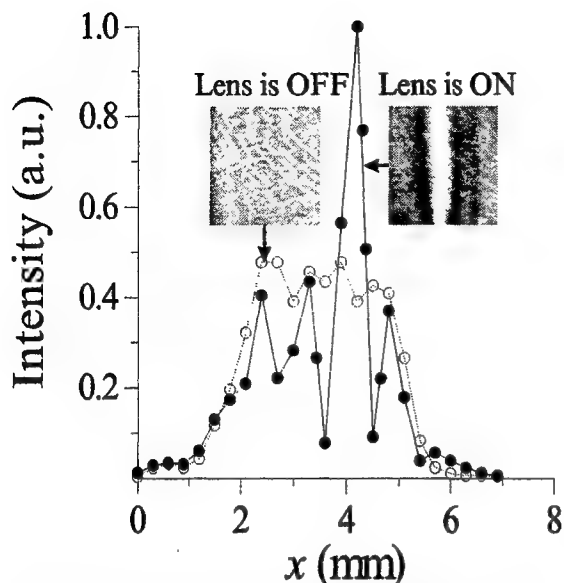
Fig. 4. Plots represent focal line intensity distributions of cylindrical MLCL at 1.5 m for U=0 V and U=7V, f=5 kHz. Inserts show corresponding imaging by MLCL.

Fig. 5. MLCL interferogram for frequency corresponding to dielectric constant dispersion: f=870 kHz, U=4V.

3.2. Lens control through contact voltages phase shift

As it follows from (e)- and (b)-type BC's in Eq. 5, cylindrical wavefront profile can be produced in the cylindrical MLCL by adjusting the phase shift φ between control voltages U_1 and U_2. In this case, the maximum value of $(\Delta\Phi_c-\Delta\Phi_e)$ is independent of the MLCL parameters and control voltage frequency. Figure 6 shows interferograms obtained by the Michelson interferometer adjusted on the equal slope fringes perpendicular to the line contacts. In this experiment, we used the same cylindrical MLCL as for the electrooptic reply visualization (paragraph A of the current Section). We fixed the *rms.* voltage (5 V) and frequency (100 Hz) and varied φ from 0 to π. For φ=2.2 rad and φ=π interferograms have vertical "furrowing" that we attribute to amplitude-phase modulation caused by the usual kink in $\Delta\Phi(x)$ distribution due to the threshold nature of the electrooptic effect. These distortions can still be seen at the shut off of the interferometer reference aim. Theoretical curves in Fig. 7 show the voltage and phase delay distributions which were calculated according to the experimental result at φ=π. The $\Delta\Phi$ fracture can be eliminated by pretilted initial alignment of the LC molecules or by additional voltage bias. The latter can be realized through dual-harmonic voltage control. The first harmonic has no contact voltages phase shift and serves as a tool for biasing out of the threshold, the second harmonic having the phase shift of π. We use similar method to realize adaptive cylindrical axicon, i.e., the optical element providing long beam waist in its focus. Computed voltage distribution and phase profiles of the corresponding axicon are presented in Fig. 8(a). Figure 8(b) shows intensity distributions near the focal distance of the axicon versus the ideal equivalent cylindrical lens.

According to computer simulations, the RMS error of phase approximation by the MLCL increases with the optical power and for F=0.5 m its theoretical value reaches 1.26 rad. This situation can be somewhat improved by introducing addi-

Fig. 6. Interferograms for different contact phase shift (top) and correspondent amplitude transmission of MLCL (bottom). *Rms.* voltage 7 V, frequency is 100 Hz.

Fig. 7. Voltage and phase delay distributions for φ=π.

Fig. 8. Axicon voltage and phase profiles (a) and computer simulated intensity distributions near the focal distance of the axicon (solid lines) and of the equivalent ideal cylindrical lens (dotted lines) (b).

tional harmonics into the control voltage and further by introducing phase shifts between some of these harmonics. To examine this possibility, we combined the Monte-Carlo method with the descent search, and for 5 harmonics obtained the RMS 22% less . To save symmetry in the phase delay distribution, $\Delta\Phi(x)$, the phase shift φ between harmonics of the same order should be equal to π. In this particular case, the computer introduced the phase shift π between the 3-rd, the 4-th and the 5-th harmonics.

4. CONCLUSION

We proposed and developed a novel method of the LC space modulator control in applications to a given wavefront shape formation. The method was realized in adaptive cylindrical and spherical MLCL's. The main distinction of the suggested approach is that the LC modulator is treated as a system with distributed electric parameters. The modulator is driven by controlling its distributed reactive parameters, which causes optical reply redistribution across the modulator aperture. We demonstrated that the time profile (Fourier spectrum) of the control voltage determines the spatial profile of the phase transmission through the modulator. We used this circumstance to reduce phase aberrations at short focal lengths of the cylindrical MLCL.

5. APPENDIX

This appendix outlines the derivation of Eq. (1). Electric field along the CE layer, produced by the AC voltage applied to the contacts (see Fig. 1), induces AC current parallel to the CE layer. As the AC current destroys the local charge neutrality in the CE layer, the excess charge produces electric field and local potential difference $U(x,y)$ across the LC layer. Now we derive the equation governing the distribution of $U(x,y)$ along the aperture. We start with equations for electric fields and currents in the LC layer:

$$\nabla \mathbf{D} = 0 , \tag{A1}$$

$$D_z = \varepsilon_0 \varepsilon E_z , \tag{A2}$$

$$\mathbf{j} = \sigma \mathbf{E} , \tag{A3}$$

$$U = - \int_{-d/2}^{d/2} E_z dz \approx -E_z d . \tag{A4}$$

Here $\mathbf{D}$ and $\mathbf{E}$ are electric displacement and field strength, respectively, $\mathbf{j}$ is electric current density, ε and σ are effective dielectric constant and conductivity of the LC, respectively, d is the LC layer thickness. As we use pure LC materials, we can assume the conductivity to be due to dielectric losses only and ignore space charge density in the Eq. (A1). We also assume that only z-components of vectors $\mathbf{D}$ and $\mathbf{E}$ are nonzero and ε can be considered constant throughout the LC layer. Only in this case Eq. (A4) remains valid. The total current continuity equation and Ohm's law describe space charge generation in a thin layer of the CE:

$$\frac{\partial \rho_{CE}}{\partial t} + \nabla \mathbf{j}_{CE} = 0 , \tag{A5}$$

$$\mathbf{j}_{CE} = \sigma_{CE} \mathbf{E}_{CE} = -\sigma_{CE} \nabla_s U , \tag{A6}$$

where ρ_{CE} is the space charge density and σ_{CE} is the conductivity of the CE layer, respectively, and

$$\nabla_s = N_x \frac{\partial}{\partial x} + N_y \frac{\partial}{\partial y}.$$ (A7)

As we used high conductivity coatings for CE, all AC voltage frequencies comply with the condition

$$\omega \tau_M \ll 1,$$ (A8)

where $\tau_M = \varepsilon_0 \varepsilon_{CE}/\sigma_{CE}$ is the CE material Maxwell relaxation time. The inequality (A8) implies that the frequency is low enough for the space charge in the CE layer to follow the voltage variation. The outer regions then are effectively screened out from the field in the LC layer, i.e., outside the lens z-component of the displacement is essentially zeroed. Then from the boundary jump of the displacement on the CE layer

$$D_z(d) - D_{LCz}(d) = \delta_{CE},$$ (A9)

where δ_{CE} is the surface charge density, we obtain

$$\delta_{CE} = -D_z(d).$$ (A10)

Combining Eqs. (A2), (A4), and (A10), we find a local relation between the applied voltage and the electric charge:

$$\delta_{CE}(x,y) = \frac{\varepsilon_0 \varepsilon}{d} U(x,y).$$ (A11)

Physically, Eq. (A11) describes the distributed capacitor recharge with $C_s = \varepsilon_0 \varepsilon/d$ as the capacitance per unit area. On the other hand, the surface charge density δ_{CE} is itself determined by the currents in the CE layer which, in turn, are driven by the distribution of $U(x,y)$. To express δ_{CE} in terms of $U(x,y)$, we integrate Eq. (A5) across the CE layer:

$$\frac{\partial \delta_{CE}}{\partial t} = -\left(\frac{\partial i_{CEx}}{\partial x} + \frac{\partial i_{CEy}}{\partial y} \right) - \int_{d/2}^{d/2+h} \frac{\partial j_{CEz}}{\partial z} dz = -\nabla_s i_{CE} + j_z,$$ (A12)

where $\delta_{CE} = h \langle \rho_{CE} \rangle$, $i_{CE} = h \langle j_{CE} \rangle$ are average surface CE charge and current density, correspondingly, h is the CE thickness. In Eq. (A11) we put $j_{CEz}(d/2+h) = 0$ and $j_{CEz}(d/2) = j_z(d/2) = j_z$ due to the current density boundary condition on the CE-LC interface. From Eqs. (A6), (A10) and (A11) the required equation follows:

$$\nabla_s^2 U = \rho_s C_s \frac{\partial U}{\partial t} + \rho_s g_s U,$$ (A13)

where $\rho_s = (\sigma_{CE} h)^{-1}$ is the CE sheet resistance, $g_s = \sigma/d$ is the specific surface conductance of the CE layer.

6. ACKNOWLEDGEMENT

7. REFERENCES

1. J.Gourlay, G.D.Love, P.M.Birch, R.M.Sharples, and A.Purvis, "A real-time closed-loop liquid crystal adaptive optics system: first results", *Opt. Commun. 137*, pp. 17-21, 1997
2. M.A.Vorontsov, V.A.Katulin, and A.F.Naumov, "Wavefront control by an optical-feedback interferometer," *Opt. Commun. 71*, pp. 35-38, 1989
3. A.A.Vasil'ev, M.A.Vorontsov, A.V.Korjabin, A.F.Naumov, and V.I.Shmal'gauzen, "A computer-controlled wavefront corrector," *Sov. J. Quant. Electr. 16*, pp. 599-603, 1989
4. W.W.Chan and S.T.Kowel, "Imaging performance of the liquid-crystal-adaptive lens with conductive ladder meshing," *Appl. Opt. 36*, pp. 8958-8969, 1997
5. N.A.Riza and M.C.DeJule, "Three-terminal adaptive nematic liquid-crystal lens device," *Opt. Lett. 19*, pp. 1013-1015, 1994

6. T.Nose, S.Masuda and S.Sato, "Optical properties of a hybrid-aligned liquid crystal microlens," *Mol. Cryst. Liq. Cryst. 199*, pp. 27-35. 1991

7. T.Nose, S.Masuda and S.Sato, "A liquid crystal microlens with hole-pattern electrodes on both substrates," *Jpn. J. Appl. Phys. 31*, pp. 1643-1646. 1992

8. A.F.Naumov, "Modal wavefront correctors," *Proc. of P.N. Lebedev Physical Institute 217*, pp. 177-182. 1993

9. L.M.Blinov, *Electro-Optical and Magneto-Optical Properties of Liquid Crystals,* Wiley, New York, 1983

10. I.R.Guralnik, A.F.Naumov, and V.N.Belopukhov, "Optic and electric characteristics of phase modulators based on nematic liquid crystals" in the current issue of SPIE Proceedings

11. D.I.Dergachev, A.F.Naumov, I.S.Klimenko, and V.G.Chigrinov "About one method of investigation of liquid crystal electrooptic properties", *Lett. to J. of Techn. Phys. 14*, pp. 394-396. 1988

Optic and electric characteristics of phase modulators based on nematic liquid crystals

Igor Guralnik[a], Alexander Naumov[b], and Valentin Belopukhov[b]

[a]Department of Physics, Samara State University, 443011, Acad. Pavlov St., 1, Samara, Russia; guralnik@ssu.samara.ru
[b]P.N. Lebedev Physical Institute of Russian Academy of Sciences, Samara Branch, 443011, Novo-Sadovaya St., 221, Samara, Russia; naumov@ssu.samara.ru

ABSTRACT

We used a combined approach, investigating capacitance, resistance, and electrooptic reply of nematic liquid crystals within the same experimental framework, which enabled us to plot the phase delay as a function of electric parameters. Phase delay vs. capacitance curves are almost linear, but the slope is frequency dependent for the liquid crystal with the low-frequency dispersion of the dielectric anisotropy. To interpret the results, equivalent electric parameters definition, consistent with the AC current measurement techniques, is presented and phenomenological theory of the RC-parameters is developed. When completed by the Ericksen-Leslie equation for the liquid crystal molecules realignment in the external electric field, the theory is in good agreement with the experiment.

Keywords: liquid crystals, equivalent resistance and capacitance, birefringence

1. INTRODUCTION

Recent applications of electrically controlled liquid crystal (LC) phase modulators in adaptive optics[1] require deeper insight in and more accurate determination of their equivalent electric parameters - capacitance C and resistance R. Particularly, in a novel adaptive LC lens that we proposed[2-3], the distributed capacitance and conductance of the LC layer have critical effect on the lens focusing performance.

Equivalent capacitance and resistance of pure nematic LC cells was usually investigated by way of small-signal techniques[4-5], with the AC voltage about 1 V. Maze[6] used over-threshold C-V curves for LC's parameters measurements, and Hirabayashi[7] demonstrated correlation between capacitance-voltage and phase delay-voltage characteristics for a nematic LC. In these experiments, the equivalent resistance of the LC cell was not taken into account. However, depending on the measuring technique, the cell resistance may lead to different interpretations of the experimental C-V curves.

In this paper, we introduce consistent definition of capacitance, based on AC throughput current measurements. Experimentally, we report the results of combined investigations including simultaneous measurements of conductance, capacitance, and electrooptic reply in nematic LC cells with positive anisotropy and planar initial alignment. We studied nematics both with and without low-frequency inversion of initially positive anisotropy. Low frequency inversion is particularly important in speeding up the LC adaptive systems by means of dual-frequency control.

2. THEORETICAL

We consider a LC material pure enough, so that we can ignore free carrier currents. Then the total current density contains only displacement current component:

$$j_i = \frac{1}{4\pi} \frac{\partial D_i}{\partial t}, \tag{1}$$

where $i=x,y,z$, x and y are the coordinates along the LC layer, and z is the coordinate normal to the layer. When electric field $\mathbf{E}$ is directed along z-axis, electric displacement is given by

$$D_z = \varepsilon E_z, \quad \varepsilon = \varepsilon_\perp \cos^2\theta + \varepsilon_\parallel \sin^2\theta, \tag{2}$$

where $\varepsilon_\perp$ and $\varepsilon_\parallel$ are the dielectric tensor components normal and parallel to the LC director, respectively; θ is the director's deformation angle.

From the microscopic viewpoint, the permittivity ε is determined by averaging individual molecular dipoles over a physically small volume. The LC molecules alignment is perturbed by the applied AC electric field. Then, according to Eq. (2), there exists a twofold dependence of ε on the amplitude and frequency of the applied voltage. The first dependence is the direct effect of the alignment of the LC molecules on the dielectric relaxation. Rotation of a molecule around its long axis contributes mainly into $\varepsilon_\perp$ and is independent of the nematic interaction. As a result, $\varepsilon_\perp$ demonstrates traditional Debye-type relaxation with relatively short characteristic times. On the other hand, rotation around its short axis, contributing into $\varepsilon_\parallel$, is impeded by such interaction, resulting in much longer relaxation times (low frequency dispersion). Thus, in Eq. (2) ε may depend on the frequency ω via $\varepsilon_\parallel$ and $\varepsilon_\perp$. Because of the dielectric losses, these are the complex quantities: $\varepsilon_\gamma = \varepsilon_\gamma' + \varepsilon_\gamma''$, where $\gamma = \perp, \parallel$. Secondly, due to electrooptic S-effect observed in the positive anisotropy LC's, ε is influenced by the LC molecules alignment through the director deformation angle θ. For high enough frequencies, however, the deformation angle in nematic LC's lags behind the time variation of the electric field. Ultimately, θ depends only on the *rms.* (but not instantaneous) value of the applied voltage, so that in Eq. (2) ε also depends only on the AC *rms.* voltage. We see that for time-dependent applied voltage, dielectric constant of the nematic LC can be time-independent, controlled only by the voltage *rms.* as parameter. This circumstance is important, enabling correct introduction of the equivalent electric parameters of the LC cell.

From Eqs. (1)-(2), for harmonic temporal behavior of applied voltage we obtain the current density in the form (phase exponents omitted):

$$j_z = \frac{i\omega\varepsilon}{4\pi} E_z .$$

(3)

Integration across the cell with $j_z = const$ (charge conservation) gives

$$U = \int_{-d/2}^{d/2} E dz = \frac{I}{i\omega C_0} \frac{1}{d} \int_{-d/2}^{d/2} \frac{dz}{\varepsilon(z)} = \frac{I\langle \varepsilon^{-1} \rangle}{i\omega C_0},$$

(4)

where $I = j_z S$ is the total current amplitude, $C_0 = S/(4\pi d)$ is the so called geometric capacitance of the cell, S and d are the LC cell area and thickness, correspondingly.

As we have mentioned before, the definition of equivalent parameters should reflect the experimental technique they are measured with. Many experimental procedures are based on the AC current measurements (e.g., in Ref. 7 the capacitance is measured by comparing the voltage drop across the LC cell with that across the known capacitor). Then the equivalent parallel circuit conductance and capacitance may be defined in terms of the real and imaginary parts of the complex admittance, respectively:

$$Z^{-1} = \frac{I}{U} = \frac{1}{R} + i\omega C .$$

(5)

Substituting the voltage amplitude from Eq. (4) into Eq. (5) and separating the real and imaginary parts, we find the following set of equations for the parallel RC-circuit parameters:

$$\frac{R}{1 + (\omega RC)^2} = \frac{1}{\omega C_0 d} \int_{-d/2}^{d/2} \frac{\varepsilon'' dz}{\varepsilon'^2 + \varepsilon''^2},$$

$$\frac{\omega R^2 C}{1 + (\omega RC)^2} = \frac{1}{\omega C_0 d} \int_{-d/2}^{d/2} \frac{\varepsilon' dz}{\varepsilon'^2 + \varepsilon''^2}.$$

(6)

To obtain explicit solution for R and C, θ vs. z dependence is to be known. The latter can be found from the steady-state Ericksen-Leslie's equation[4] and in general case is available only in numerical form.

Phase delay between extraordinary and ordinary components of the light wave passing through the LC layer is also determined by the LC molecules alignment:

$$\Delta\Phi = \frac{2\pi}{\lambda} \int_{-d/2}^{d/2} \left\{ \frac{n_\perp n_\parallel}{\left[n_\perp^2 \cos^2 \theta(z) + n_\parallel^2 \sin^2 \theta(z) \right]^{1/2}} - n_\perp \right\} dz ,$$

(7)

where $n_\parallel$ and $n_\perp$ are refractive indices measured along and normal to the LC director. Equations (6) and (7) provide a basis for interpretation of experimental results below.

3. EXPERIMENTAL RESULTS AND DISCUSSION

We studied typical nematic liquid crystals LC1348 and LC1001, available from NIOPIC (Moscow). LC1001 exhibits low frequency inversion of the anisotropy, LC1348 has no such inversion.

To ensure the absence of impurity ions, we measured direct current through the cell with 20 V DC bias and observed no exponential decrease of the current, which is characteristic for the electrolytic purification[4]. On the contrary, for some samples the current increased due to electric dissociation, for the others it remained constant. With the AC voltage applied, the current increased with the voltage amplitude U and its frequency ω.

We used AC bridge circuit to measure the equivalent RC-parameters, with the studied LC cell in one arm of the bridge and adjustable capacitor and resistor connected in parallel in the other. A sinusoidal generator was connected across one of the bridge diagonals and a selective millivoltmeter tuned to the generator frequency across the other. It was necessary to use the selective millivoltmeter because of the strong non-linearity of the LC current-voltage characteristic. The phase delay was measured with the standard interferometer technique.

(a) **(b)**
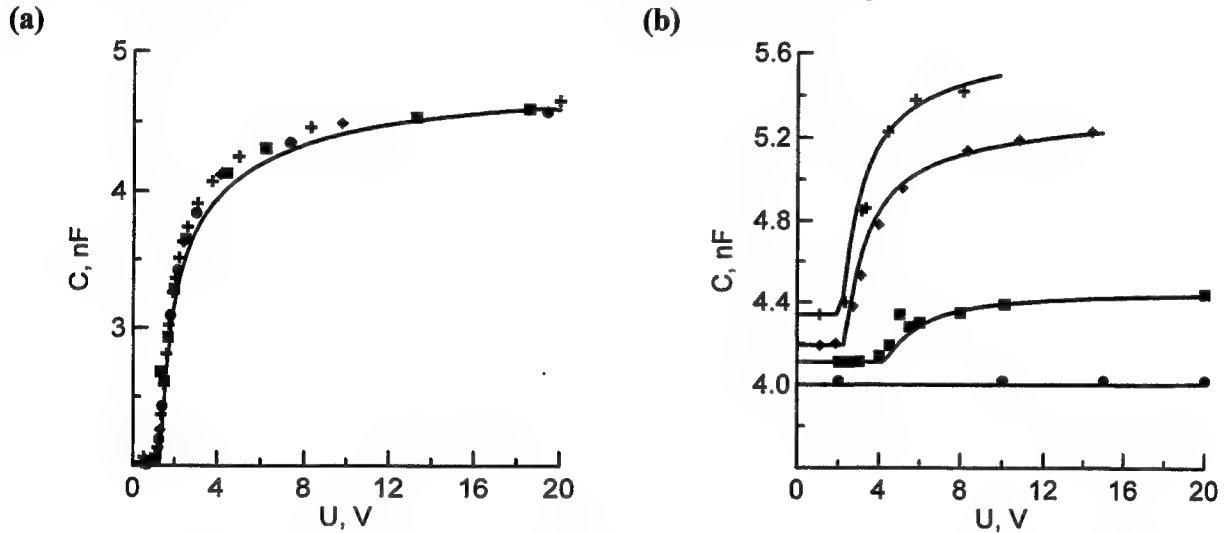
Fig. 1. AC voltage dependence of the cell capacitance for (a) LC1348 and (b) LC1001 at different frequencies: + 0.5 kHz, ◆ 1 kHz, ■ 4 kHz, ● 8 kHz.

Experimental C-U characteristics for different frequencies $f=\omega/2\pi$ are plotted in Fig. 1. For the LC1348 with the voltage passing over the threshold (about 2 V for both samples), the capacitance increases. This is as it should be, considering the positive anisotropy ($\varepsilon_\parallel' > \varepsilon_\perp'$) of this crystal. To demonstrate this, we simplify Eqs. (6) for small and large voltages, respectively. Then for voltages below S-effect threshold voltage U_S, the LC director is not realigned, and $\varepsilon=\varepsilon_\perp$. For $U>>U_S$ the director is everywhere along the field lines, except for narrow regions beside the cell walls, giving $\varepsilon=\varepsilon_\parallel$. We also note that for LC1348 in the working frequency range, the active reactance R is negligible as compared to its capacitive reactance $(\omega C)^{-1}$, suggesting that ε'' is much smaller than ε'. Then Eqs. (6) yield

$$R=\left(\omega C_0\varepsilon_\gamma''\right)^{-1}, \quad C=\varepsilon_\gamma'C_0, \quad \gamma=\begin{cases} \perp \text{ for } U<U_S \\ \parallel \text{ for } U>>U_S \end{cases}. \tag{8}$$

The high-voltage behavior of the capacitance in Fig. 1b corresponds to low frequency dispersion of $\varepsilon_\parallel'$ for LC1001. $\varepsilon_\parallel'$ falls off with frequency growth and equals $\varepsilon_\perp'$ at approximately 7 kHz. At higher frequencies the capacitance retains its pre-threshold magnitude since S-effect vanishes at zero anisotropy.

Figure 2 shows the cell equivalent resistance R as a function of applied voltage. Compared to the capacitance, the change in resistance at the threshold transition is more pronounced. The ratio of the values of R below and above the threshold is never less than 2 and exceeds 6 for LC1348 at 8 kHz, whereas the corresponding ratio for capacitance is never more than 2 and is less than 1.4 for LC1001. Thus, monitoring capacitance, and especially resistance, of an LC cell can provide alternative method of the threshold voltage measurement.
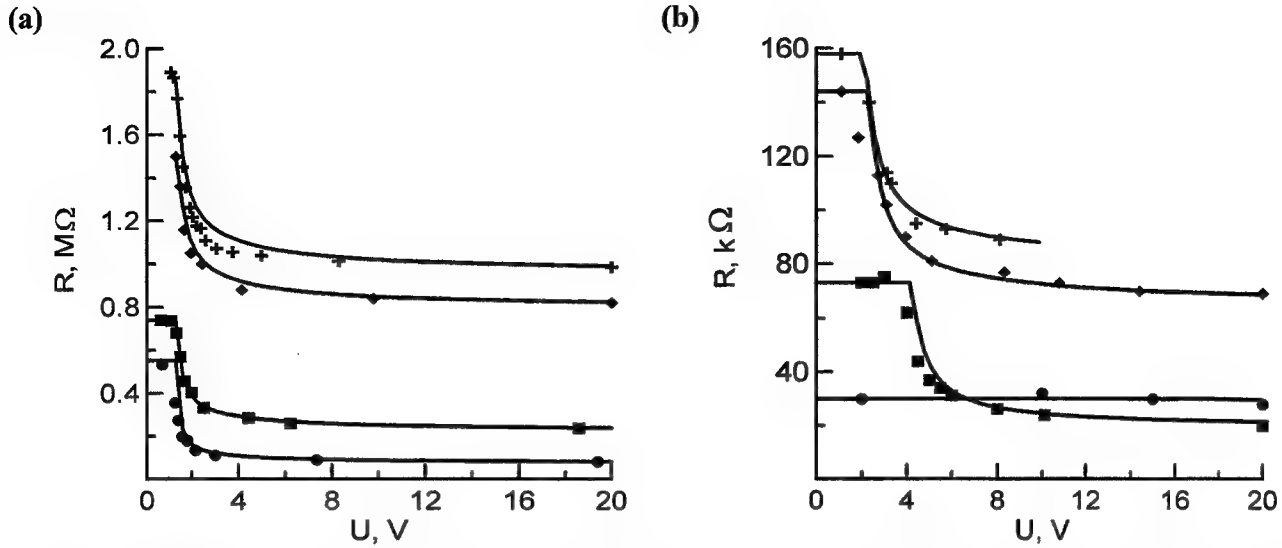
Fig. 2. AC voltage dependence of the cell resistance for (a) LC1348 and (b) LC1001 at different frequencies: + 0.5 kHz, ◆ 1 kHz, ■ 4 kHz, ● 8 kHz.

Electric quality $Q=\omega RC$, indicating the relative magnitude of the leakage current due to the dielectric losses, is readily obtained from the graphs above. As expected, $Q \gg 1$ for non-dispersive LC1348, and $Q \leq 1$ for dispersive LC1001 cell. On the other hand, we have mentioned before that it is the low frequency dispersion that is used for speeding up LC modulators through dual-frequency control techniques. Our results reinforce the necessity of considering the leakage currents for such LC cells.

According to Eqs. (6) and (7), both optical ($\Delta\Phi$) and electrical (R and C) voltage dependencies are caused by the LC molecules alignment. This suggests for non-dispersive cells the existence of a simple correlation between $\Delta\Phi$ on one hand, and R and C, on the other hand. Beyond the dispersion region, the dielectric losses are negligible and we can ignore ε'' in the denominators of both formulas (6), like we did to arrive at Eqs. (8). Assuming also the quality ωRC to be greater than unit, we obtain

$$\frac{1}{\omega R} = \frac{C^2}{C_0 d} \int_{-d/2}^{d/2} \frac{\varepsilon'' dz}{\varepsilon'^2}, \quad \frac{1}{C} = \frac{1}{C_0 d} \int_{-d/2}^{d/2} \frac{dz}{\varepsilon'}. \tag{9}$$

It can be seen that the angle dependence of the reciprocal of the capacitance is similar to this dependence of the phase delay. Thus, with the voltage passing over the threshold, the capacitance of the cell, but not its resistance, must repeat the phase delay as the function of the voltage in Eq. (7). Besides, the inverse of ωR should be frequency dependent through ε'' even for a non-dispersive LC. We used data similar to that in Figs. 1, 2 and experimental $\Delta\Phi$ vs. U curves, shown in Fig. 3., to plot $\Delta\Phi$ as a function of C and R. The results are shown in Figs. 4 and 5. For the LC1348 (Fig. 4), $\Delta\Phi$ vs. C curves are almost linear, whereas $\Delta\Phi$ vs. ωR relationships are more complicated and frequency dependent. Contrary to Fig. 4, $\Delta\Phi$ vs. C relationships for LC1001 are more sensitive to the frequency changes, as indicated by Fig. 5.

Solid lines in Figs. 1-5 represent theoretical fits from Ericksen-Leslie equation coupled with Eqs. (6), (7) for $\lambda=0.633$ μm, and $d=25$ μm, $S=8$ cm² for LC1348, and $d=5$ μm, $S=10$ cm² for LC1001. The elastic modulus K_{11} was found from the threshold voltage, the real and imaginary parts of the dielectric constants were determined for each frequency by fitting the theoretical curves to the experimental data at minimum and maximum applied voltages. A good agreement can be seen, as the discrepancies *within* the measuring voltage interval are fairly small.

It is instructive to consider the so called *Cole-Cole* diagram for this cell which is plotted in Fig. 6 for $U=10$ V and so features the dispersion of $\varepsilon_{\parallel}$. The portion of the plot that forms a semicircle corresponds to the Debye relaxation. However, there is also present a relatively strong low frequency losses tail that we attribute to energy dissipation accompanying the frequency realignment of the LC director caused by the applied AC voltage.

31

(a)

(b)
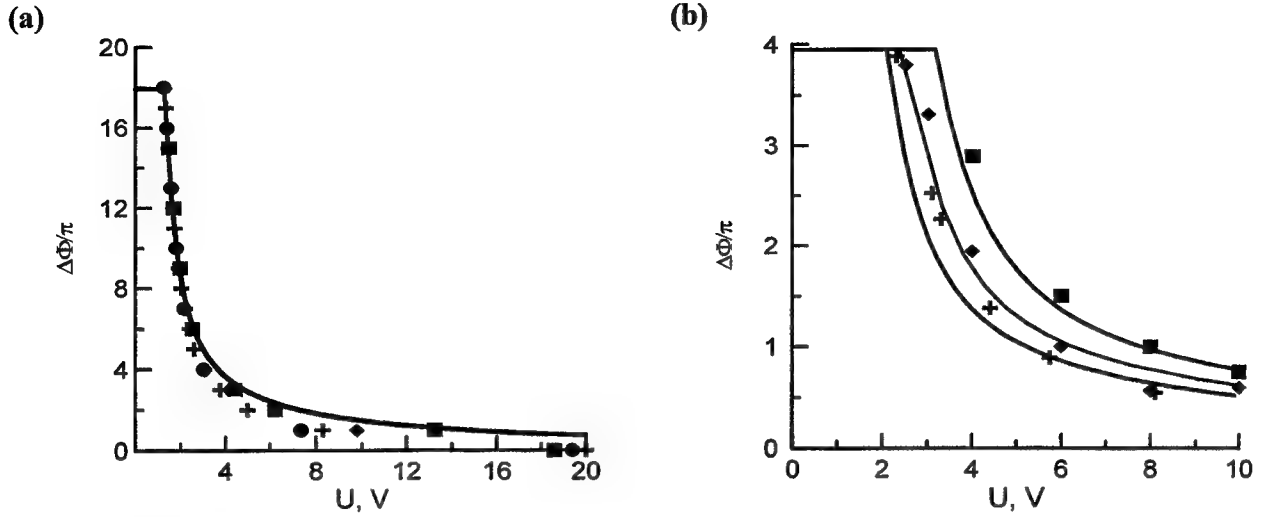
Fig. 3. Phase delay, $\Delta\Phi$, for LC1348 (a) and LC1001 (b). Symbols correspond to frequencies + 0.5 kHz, ◆ 1 kHz, ■ 4 kHz, ● 8 kHz (a); + 0.5 kHz, ◆ 2 kHz, ■ 4 kHz (b).

(a)

(b)
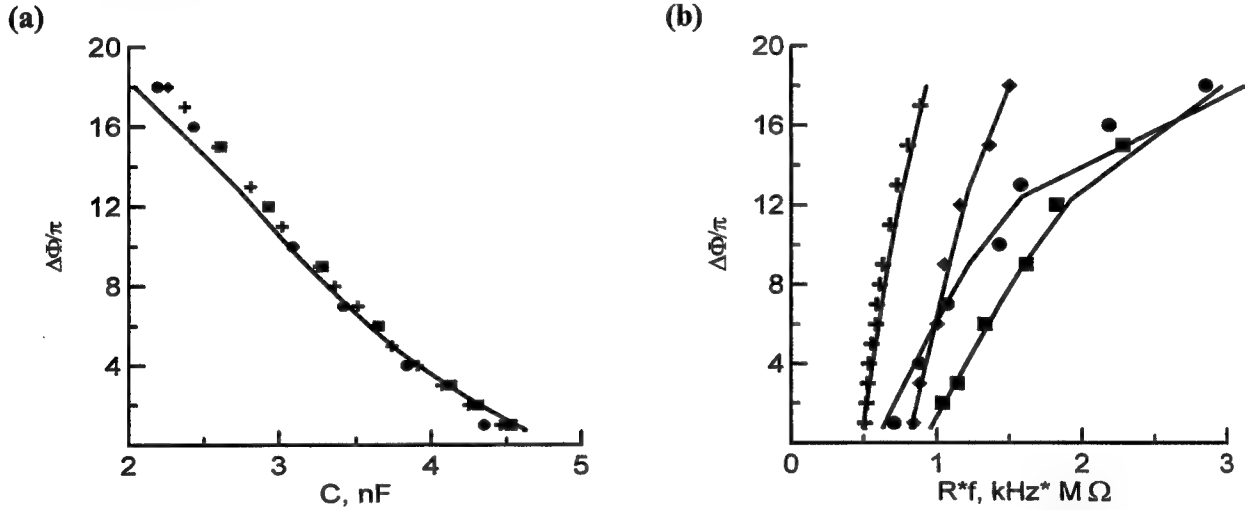
Fig. 4. Phase delay, $\Delta\Phi$, for LC1348 as a function of (a) cell capacitance and (b) cell resistance at different frequencies: + 0.5 kHz, ◆ 1 kHz, ■ 4 kHz, ● 8 kHz.

4. SUMMARY

We measured both *RC* parameters and phase delay in pure LC cell for AC voltages up to 20 V. We demonstrated that *RC* parameters can be useful for providing information about phase delay. In particular, *C-U* plots follow closely the non-linear $\Delta\Phi$ vs. *U* dependencies. Alternatively, *R-U* plots enables more precise determination of the threshold voltage of electrooptic S-effect, and saturation voltage for $\Delta\Phi$. The latter dependencies are also self-important as they affect stability and the speed of adaptive optics systems based on the LC modulators.

5. ACKNOWLEDGEMENTS

(a)

(b)
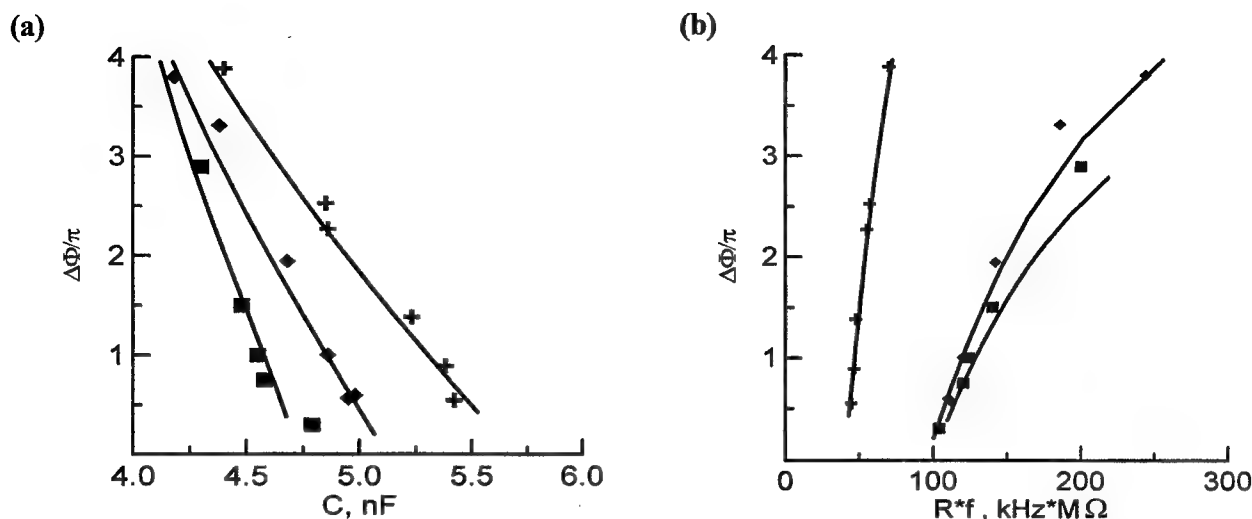
Fig. 5. Phase delay, $\Delta\Phi$, for LC1001 as a function of (a) cell capacitance and (b) cell resistance at different frequencies: + 0.5 kHz, ◆ 2 kHz, ■ 4 kHz.
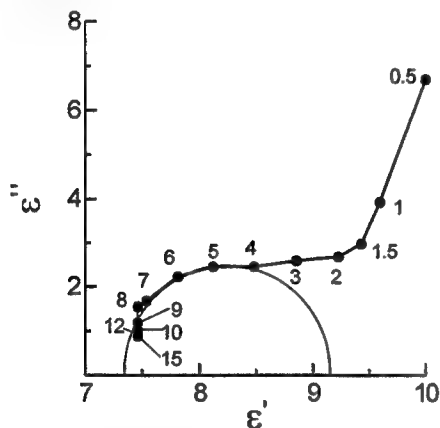
Fig. 6. Cole-Cole diagram for LC1001. Numbers besides the labels are AC voltage frequencies in kHz..

6. REFERENCES

1. G.D. Love, J.C. Fender and S. Restaino, "Adaptive wavefront shaping with liquid crystals", *Opt. & Photon. News 6, No 10*, pp. 16-20. 1995

2. A.F. Naumov, "Modal wavefront correctors", *Proceedings of P.N. Lebedev Physical Institute 217*, pp. 177-182. 1993 (in Russian)

3. A.F. Naumov, M.Yu. Loktev, I.R. Guralnik, and G.V. Vdovin, Liquid crystal adaptive lenses with modal control, *Opt. Lett. 23*, pp. 992-994

4. L.M. Blinov, *Electro-Optical and Magneto-Optical Properties of Liquid Crystals,* Wiley, New York, 1983

5. W.H. De Jeu, *Physical Properties of Liquid Crystalline Materials,* Gordon and Breach Science Publishers, New York London Paris, 1980

6. C. Maze, "Determination of nematic liquid crystals elastic and dielectric properties from the shape of capacitance-voltage characteristics", *Mol. Cryst. Liq. Cryst. 48*, pp. 273-287, 1978

7. K. Hirabayashi, "Relationship between optical and electrical properties of liquid crystal optical devices, *Opt. Lett. 21*, pp. 1484-1486, 1996

8. V.G. Chigrinov, "Alignment effects in nematic liquid crystals in electric and magnetic fields, *Crystallography 26,* pp. 404-430, 1981

Experimental verification of a bright-speckle algorithm of compensation for turbulent wandering of a repetitively-pulsed CO_2 laser beam

V.E.Sherstobitov, V.I.Kuprenyuk, D.A.Goryachkin, V.P.Kalinin, V.M.Irtuganov, V.V.Sergeev, A.Yu.Rodionov, N.A.Romanov, S.A.Dimakov, Yu.A.Rezunkov[a]

Research Institute for Laser Physics, Science Center "S.I.Vavilov State Optical Institute", St.Petersburg, 199034, Russia
Institute for Testing Optoelectronic Devices[a], Science Center "S.I.Vavilov State Optical Institute", Sosnovyi Bor, Leningrad region, Russia

ABSTRACT

A novel algorithm of compensation for repetitively-pulsed laser beam wandering at propagation paths, caused by the atmospheric turbulence and mirror vibrations has been proposed and verified in experiments with a TE-CO_2 laser. The algorithm is based on the precise temporal control of triggering each of the TE-laser pulses at the moments when the auxiliary probe cw-laser beam modified by a modal-type adaptive optics system and having exactly the same wavefront profile, as the pulsed radiation, hits the remote object (retroreflector in the pre-set point at the path exit) by its brightest speckle.

1. INTRODUCTION

It is well known that during propagation of radiation of a high power repetitively-pulsed laser along an extended near-land atmospheric range the initial optical quality of a beam is deteriorated by the action of turbulence and thermal blooming. In turn, the initial quality of the beam at the laser output is degraded by internal distortions within the laser caused by gas flow inhomogeneities, acoustic waves etc. It is known that both the atmospheric distortions and phase distortions within the optical train of lasers can be corrected to some extent by using adaptive optics techniques or phase conjugation[1-3]. As for adaptive optics, its application for correction of distortions inherent in repetitively-pulsed lasers is limited by a relatively slow response time of existing adaptive mirrors (milliseconds), finite number of actuators (hundreds), system complexity and cost. In turn, phase conjugation techniques are capable of compensating fast and small-scale distortions within the laser, because their time response is much faster (up to nanoseconds) and spatial resolution is limited usually only by the field of view of a laser amplifier. However, application of phase conjugation techniques to the task of atmospheric correction encounters serious difficulties connected with a too low energy level of the coherent signal, reflected from the remote object, and the necessity to have a very high gain of the system comprising a laser amplifier and a phase conjugate mirror (10^9-10^{10} and more). Thus separate use of the adaptive optics or nonlinear phase conjugation techniques can be hardly efficient if there is a necessity to compensate simultaneously for phase distortions in the turbulent atmosphere and in the optical train of the repetitively-pulsed laser.

We propose an algorithm of compensation, further reffered as a "bright-speckle algorithm", which is based on the use of the both concepts:
- modal-type adaptive optics to compensate for relatively slow atmospheric distortions by measuring the intensity of an auxiliary low-power cw-laser beam, reflected from the object, which intensity reaches its maximum when the brightest speckle of the cw-laser beam covers the point-wise object;
- nonlinear phase conjugation to control the wavefront profile of a high-energy repetitively-pulsed radiation, to adjust this profile to that of the cw-probe beam at the entrance of the atmospheric path, and to compensate for fast distortions and vibrations inside the amplifier.

This separation of compensation techniques by a time scale of typical distortions can allow, in our opinion, to make use of advantages of the both correction methods, to relax requirements for the reflected signal level and to make a system as a whole less complicated and expensive.

In this paper, the bright-speckle algorithm is considered in more detail and is verified in simple model experiments as applied to the first-order wedge-like distortions (beam turbulent wandering and jitter), but basically it can be implemented in more sophisticated adaptive optics systems as well.

2. CONCEPT OF THE ALGORITHM PERFORMANCE

The algorithm performance is illustrated in Fig.1. The system, shown in the figure, consists of a cw-probe and TEA-repetitively-pulsed laser modules, which are placed in a common resonator, a repetitively-pulsed preamplifier and high-power double-pass amplifier with a phase conjugate mirror (PCM), scanning mirrors, a beam director telescope, an atmospheric path, a reflecting object (shown as a triple-prism), a detector for measuring the energy of the reflected probe beam, and a system for controlling the moments of triggering the amplifiers.

The system operates as follows. In the searching mode, only the cw-probe laser module operates in the "dual-mode resonator" and a part of its radiation, reflected by the coupling plate, is directed to the atmospheric path via the scanning mirrors, beam expanding telescope, and then is focused onto the object triple-prism of about 1/4 diffraction size. The energy of the probe radiation, reflected from the triple-prism, is measured by a high-sensitive detector with a collecting lens, which is placed in the vicinity of a transmitting equipment. The probe beam is continuously scanned over the object plane by a system of two mirrors, oscillating in a prescribed fashion in mutually perpendicular planes (frames and lines). In this case, the reflected signal is modulated in intensity (see the left bottom in Fig.1) with a line frequency, and high-amplitude peaks correspond to the moments when the beam spot passes the object triple-prism by its bright speckles. The scanning system parameters can be chosen from data on average variation rates and typical values of wedge-like distortions, caused by the atmospheric turbulence (up to 10 Hz and $\pm 2(\lambda/D)$, respectively).

To choose properly the amplifier triggering time, which must correspond to the moment when the brightest speckle of the probe radiation spot covers the object, it is necessary to have at least one calibration frame before the operation one, to read out the amplitudes of all of the reflected signal peaks and to select the maximum one. When the same amplitude is obtained in the subsequent operation frame (or somewhat smaller to make the system more reliable), the pulsed TEA module in the dual-mode resonator, preamplifier, and final amplifier are triggered. The pulse radiation of the dual-mode laser is emitted from the same resonator as the probe cw-radiation, their wavefront profiles being precisely coincident and, therefore, the beam of the pulsed radiation will also cover the object by its brightest speckle.

A part of the pulsed radiation of the dual-mode laser, reflected by the coupling plate (polarizer) to the right (see Fig.1), is amplified in the high-power double-pass amplifier with the phase conjugation mirror and propagates to the object. Phase conjugation ensures compensation for vibrations and errors of intermediate optical components and fast phase distortions in the gas-flow amplifier medium. Another part of the dual-mode laser radiation after amplification in the preamplifier is used for pumping the PCM, based on degenerate four-wave mixing.

Each of the successive pulses in the repetitively pulse mode is triggered at the moment of hitting the triple-prism by the brightest speckle of the cw-laser radiation, which is random to a certain extent, so the sequence of pulses becomes somewhat nonequidistant. The important element in the system operation is the detector unit, which, in fact, is an analogous electronic device ensuring detection of signals, their processing and controlling the algorithm operation. In addition, this unit is intended for excluding the amplifiers triggering if the reflected signal of the required amplitude was not obtained as well as for protecting the high-sensitive detector when the high-power pulsed radiation comes from the object. The latter function is provided by synchronous blocking the reflected signal.

In this paper we consider in more detail the results of model experiments (without amplifiers), aimed at verification of the bright-speckle algorithm as well as at testing its key components: the dual-mode laser and the analog unit, controlling the system operation by the reflected signal.

3. EXPERIMENTAL SET-UP

An optical schematic of the experimental set-up is shown in Fig.2. The main units and their performance are similar to those discussed above. Therefore, we briefly note only the main features of the experiment. The algorithm has been verified at a short-length (L=120 m in two passes with an intermediate mirror) inclined atmospheric path. As the beam distortions at the path were fairly small, we had to develop a special imitator to simulate the beam speckling, which was a four-segment plane mirror with variable (up to $\lambda/2$) piston shifts between the segments, brought in by piezoceramic actuators (see Fig.3). A single beam, impinged symmetrically four or two segments, was splitted down in the far field into the corresponding number of spots with variable intensities (imitating the speckles).

The beam of a 0.5 atm-pulsed TE CO_2 laser with a repetition rate of 10-15 pps and a pulse energy up to several Joules was stabilized, and a cw-low pressure TE CO_2 laser of about 100W-power was used as a source of the probe radiation. These laser modules were placed in the common stable resonator with a length of about 34 m and a Frensel number close to 1 and formed a dual-mode laser. Instead of a totally reflecting mirror the resonator comprised a so-called "cat-eye" reflector[4], which significantly simplified the cavity alignment and enhanced the beam axis stability. The beams of cw and pulsed radiation (when the gain modules operated separately) had the same near-Gaussian intensity profile, and their angular divergence corresponded to the diffraction limit. The dual-mode operation gave rise to certain specific features of lasing in both modules. After a pulse ceased, the cw-oscillation was blocked during about 200 μs, and then recovered for 300-400 μs with pulsations, because of the action of inhomogeneities in the pulsed active media (this time was the "dead time" for the system operation, see the oscillogram in Fig.4). The time behavior of the radiation from the pulsed module (about several microseconds), in turn, became almost smooth in the presence of the cw-oscillation, which was evidence of a spectral selection similar to that which takes place in hybrid CO_2 lasers[5].

A key prerequisite of the bright-speckle algorithm performance is the precise coincidence of the wavefront profiles of the probe and operation beams. It was tested by recording and comparing their spot patterns at various points along the optical path when the speckle imitator was switched on. For any mode of the imitator operation (see Fig.3 in the bottom), the spot patterns of the pulse and cw-radiation were always exactly the same.

In addition to the dual-mode laser and speckle imitator, the optical scheme of the experiment included the following elements (see Fig.2):
- two oscillating mirrors, which provided the beam scanning in vertical (frame) and horizontal (line) planes with frequencies of 31 and 310 Hz, respectively within a frame with angular size of ~6(λ/D);
- a mirror telescope, which expanded the output beam of the dual mode laser before it left the path up to diameter D~100 mm and focused the beam onto the triple-prism, placed inside the laboratory at the end of the path;
- an object triple-prism limited by the aperture with diameter ($\lambda/2D$)×L=6 mm, and systems for measuring the emitted and delivered energy of the repetitively-pulsed radiation (wedges 1,2, detectors D2, D3) and for recording the number of hits of the radiation at the triple-prism (a mirror diaphragm $\varnothing$10 mm and a thermosensitive disk 350 mm in diameter rotating at a velocity of 20 rps, with 4-fold reduction imaging optics);
- a measuring unit, which processed the radiation of the probe cw-laser reflected by the triple-prism and controlled the repetitively-pulsed TE module triggering at the moments when the reflected energy achieved its maximum (the brightest speckle was on the triple-prism).

The reflected signal was measured within the angle of view of the main optical path by splitting a part of the reflected energy by wedge 2 and collecting the signal onto high-sensitive HgCdTe photodetector D1. The operation of the analog controlling unit was considered above. Note here that a fast rotating disk with holes was placed as a

chopper in front of the photodetector, and the detector was opened only when the reflected pulsed radiation could not hit it. Typical time sweeps of the measured reflected signal are illustrated in Fig.5. Separate peaks within a line (see Fig.5b, c) correspond to the pulses transmitted by the chopper. It is seen that pulse trains were different in the cases of a single and two-speckle spots. The speed of disk rotation could be varied, that enabled variation of the duration and number of peaks within every line. The threshold level of the pulsed laser triggering could also be varied from 0.7 to 0.95 of the maximum signal measured in the calibration frames preceding the operation ones.

4. MAIN RESULTS AND DISCUSSION

The considered model experiments were aimed at the first verification of the laser beams stabilization algorithm and its key components. Nevertheless, the obtained results, which are presented below, appeared to be rather instructive and promising. The beam stabilization was proved by measuring the probability of hitting the triple-prism by repetitively-pulsed beam spots (or their brightest speckles) and by the efficiency of the radiation delivery. Typical static patterns of the two-speckle and single spots (the imitator was on or off, respectively) at the plane in front of the mirror diaphragm are illustrated in Fig 6a. Similar patterns, but obtained after reflection from the mirror diaphragm are shown in Fig.6b,c. White circular "holes" on the spots correspond to the 10 mm-mirror diaphragm diameter (a part of energy passing through it hits the triple-prism), and smaller 6 mm-circles, coaxial to the former ones, are drawn in the figure to point the triple-prism position and size. Thus, those cases can be assumed as good hits when the spot (or its brightest speckle in the two-speckle case) completely covers these circles. It corresponds to the maximum deviation of the beam not exceeding $\pm\lambda/2D$ (or 1/4 of the diffraction angle). The patterns of a such kind are shown in Fig.6b.

Typical sweep traces of radiation spots, obtained in a repetitively-pulsed mode on the rotating disk with and without the speckle imitator, are shown in Fig.7b,d and Fig.7a,c respectively. The upper traces (a, b) correspond to the case when the stabilization algorithm was switched off. It is clearly seen that only occasional radiation spots cover the white holes. The spots are positioned randomly (within the scanning range) on each side of the large-diameter circle, which corresponds to the trajectory of the image of the triple-prism center on the rotating disk. On the contrary, when the stabilization algorithm was switched on 100% percent of the spots covered the triple-prism, as it is seen from the lower traces in Fig 7c, d. Note that during a burst (of 5-10 s duration) the rotating disk was able to make a large number of full revolutions, hence the positioning of spots in azimutal direction is random in the figure.

The probability of hitting and the efficiency of the repetitively-pulsed radiation delivery were estimated quantitatively as well. Fig.8 shows typical fragments of trains of negative pulses corresponding to an energy emitted and delivered in each pulse of the same bursts by detectors D2 and D3 respectively (see Fig.2). These sweeps were obtained when imitating a dual-speckle spot with and without switching on the stabilization algorithm (the left and right ones, respectively). The amplitudes in the sweeps are expressed in arbitrary units. It is seen that in the mode of stabilization, each of the emitted pulses corresponds to the delivered one (9 signs "+" in the left sweeps). The pulses were not equidistant which is evidence of the external control of the laser triggering. When the stabilization algorithm was off, the delivered pulses were typically of smaller amplitudes or absent at all. When processing the results (see Fig.8b), we considered only those pulses as "hits" (signs "+" in the figure), which amplitudes (energies) exceeded the e^{-1} level of the maximal value, obtained for the precise static hitting. The gain in the number of hits in the fragment, shown in the figure, is 4.6-fold.

The most proper parameter to verify the beam stabilization is the achievable gain in energy, delivered onto the object (the triple-prism) in a burst of pulses. A computer processing of the measured results was done to estimate the delivery efficiency. The processing involved (see Fig.8c) summarizing the delivered and emitted energy over pulse trains, calculating a delivery ratio *DEL* (as a ratio of the mentioned sums) and a delivery efficiency *Eff*, defined as *DEL* normalized to the best static value of *DEL* observed. The gain in the delivery efficiency, achieved due to using the algorithm in the fragment shown in Fig. 8, was 4.8-fold. The results obtained from processing a large number of

experimental bursts show, that the bright-speckle algorithm was capable of providing on the average the 15-20-fold gain in the number of hits and 5-6-fold gain in the delivery efficiency for two-speckle spots.

The experimental results presented above prove that the bright-speckle algorithm can be considered as a simple and reliable way of stabilizing a repetitively-pulsed laser beam against wedge-like distortions. Recently, the first encouraging results have also been obtained when using the algorithm in a full-scale optical scheme including a high-power repetitively-pulsed CO_2 amplifier. The experiments have been performed at an indoor range with imitating the strong turbulent wandering and speckling. At present, we also have at our disposal the completely developed phase conjugate mirrors, based on both conventional four-wave mixing[6] and on a loop-type self-phase conjugation[7]. Thus, all the components as well as the required experience have been accumulated to continue the algorithm investigations at a real near-land atmospheric path of 2-3 km in length. We believe, that incorporation into the optical schematic of a more sophisticated modal-type adaptive system will allow to compensate using the bright-speckle algorithm not only wedge-like distortions but the distortions of higher orders in atmospheric propagation paths.

5. ACKNOWLEDGEMENTS

6. REFERENCES

1. C.A.Primmerman, T.R.Price, R.A.Humphreys, D.A.Zollars, H.T.Barclay, J.Herrmann, "Atmospheric compensation experiments in strong-scintillation conditions", *Appl.Opt.*, Vol. 34, pp. 2081-2088, 1995.

2. H.Bruesselbach, D.C.Jones, D.A.Rockwell and R.C.Lind, "Real-time atmospheric compensation by Stimulated Brillouin-Scattering phase conjugation", *J.Opt.Soc.Am.B.*, Vol. 12, No. 8, pp. 1434-1447, 1995.

3. V.E.Sherstobitov, A.A.Ageichik, V.D.Bulaev, S.A.Dimakov, M.N.Gerke, D.A.Goryachkin, V.P.Kalinin et al, «Phase Conjugation in a high-power E-beam-sustained CO_2 laser», *Proc. SPIE*, Vol. 1841, pp. 135-145, 1991.

4. S.A.Dimakov, S.I.Kliment'ev, V.I.Kuprenyuk, I.B.Orlova, V.V.Sergeev, V.E.Sherstobitov, "Low-sensitive to misalignments resonator", *Proc. SPIE*, Vol. 2257, pp. 187-192, 1997.

5. N.R.Heckenberg, J.Meyer, "Residual mode beating in a high-pressure-low-pressure hybrid CO_2 laser system", *Optics Communs*, Vol.16, pp. 54-57, 1976.

6. V.E.Sherstobitov, V.P.Kalinin, D.A.Goryachkin, N.A.Romanov, S.A.Dimakov, V.I.Kuprenyuk, "CO_2 lasers and phase conjugation", *Proc. SPIE*, Vol. 1415, pp. 79-89, 1991.

7. D.A.Goryachkin, V.P.Kalinin, I.M.Kozlovskaya, V.E.Sherstobitov, "An experimental study of phase self-conjugation of the CO_2-laser radiation", Kvantovaya Elektronika, Vol. 17, pp. 1349-1355, 1990 (in Russian).
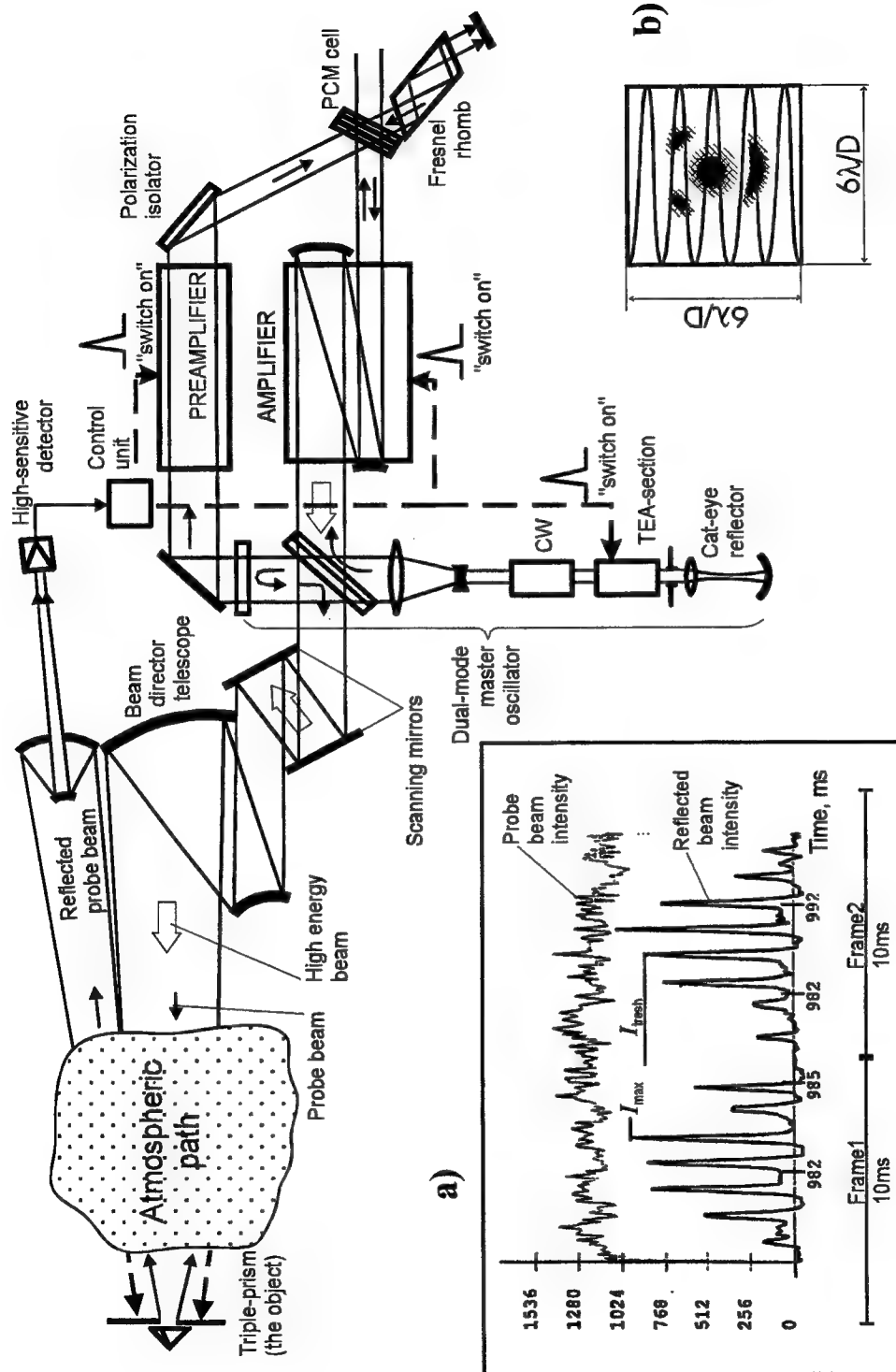
Fig. 1. Basic concept of beam stabilisation using a bright-speckle algorithm with illustrations of time sweeps of the probe and reflected signals (a) and of a beam scanning frame in the triple-prism plane (b).

Fig. 2. Optical schematic of the experimental set-up.

a)

b)

Near-field patterns

four segments

two segments

two-segment mirror

Far-field patterns

c)
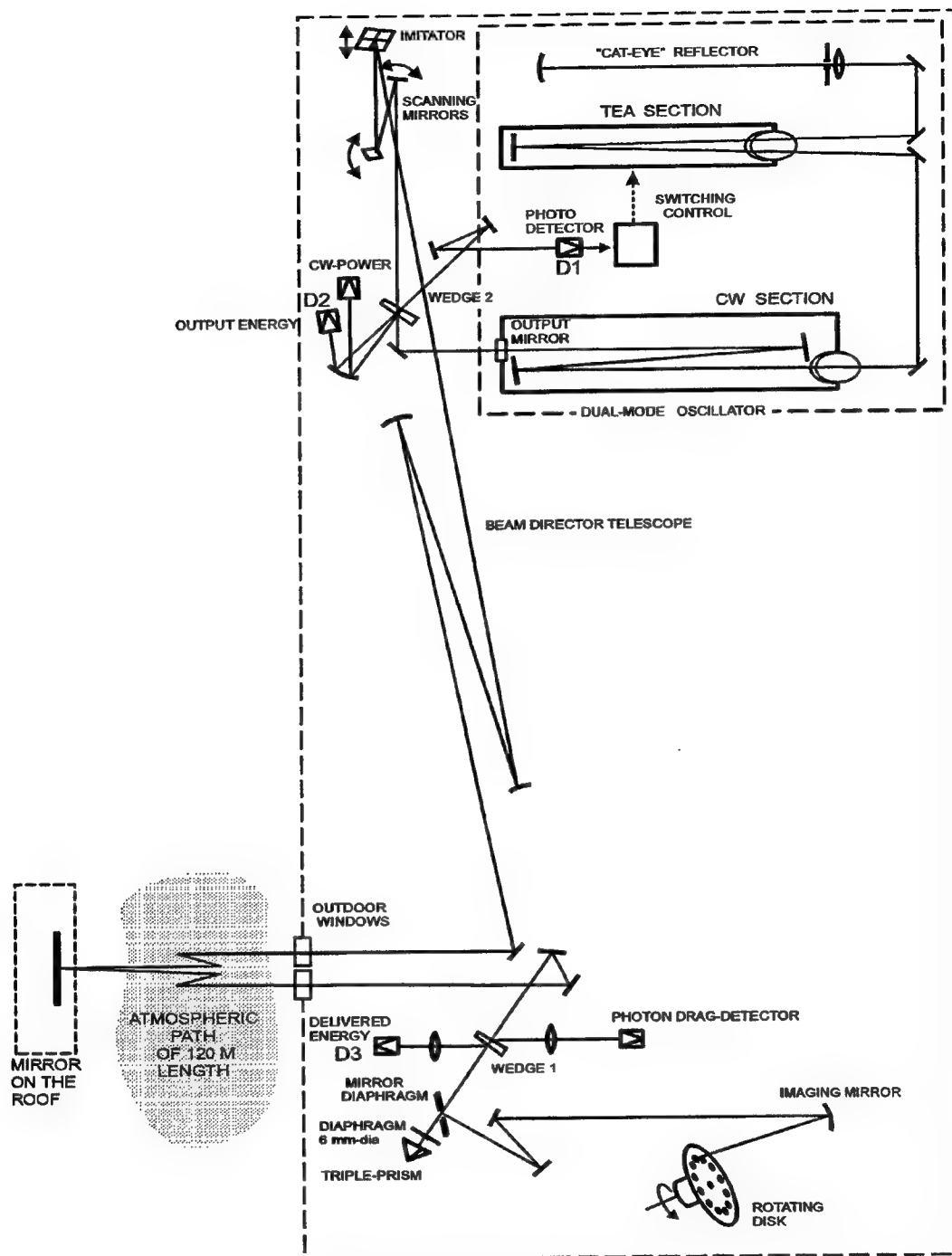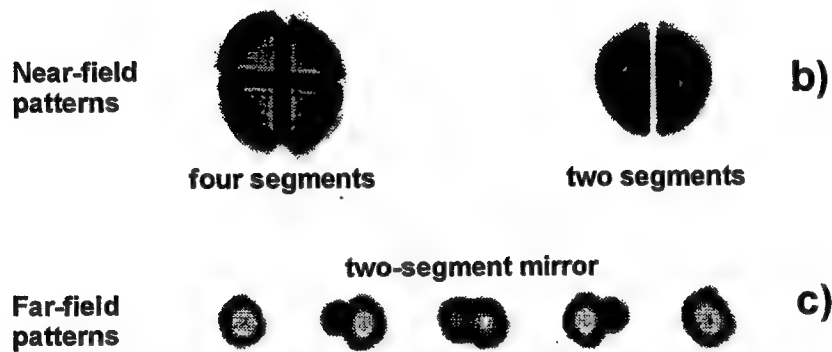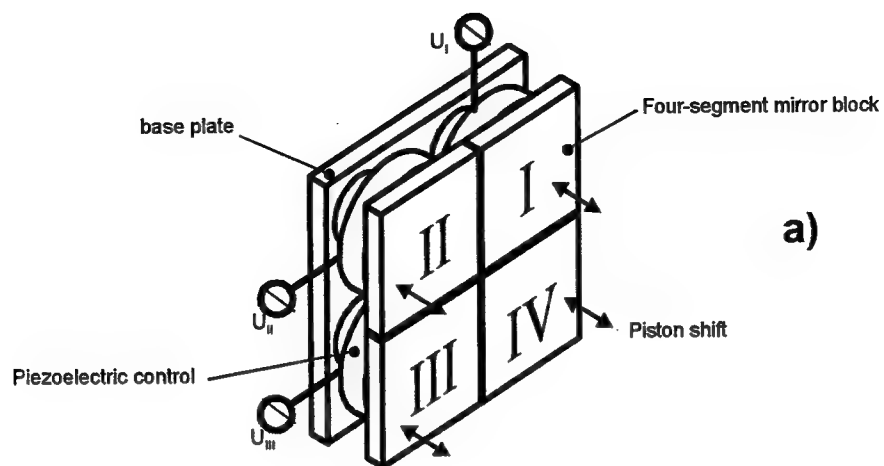
Fig.3. General wiew of the imitator of distortions (a) and typical patterns of radiation spots at various beam positions on the segmented mirror (b) and various voltages between two segments (c).

2 v/div

0.2 ms/div
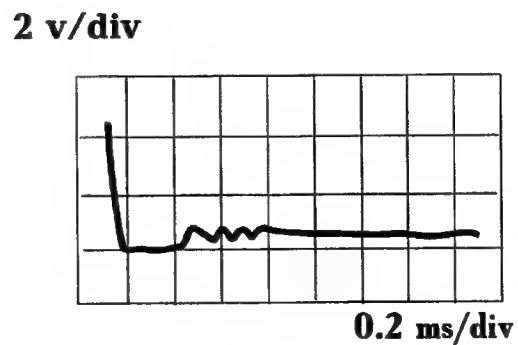
Fig.4. Typical oscillogram of the dual-mode laser output radiation at joint action of the pulse and cw-sections.
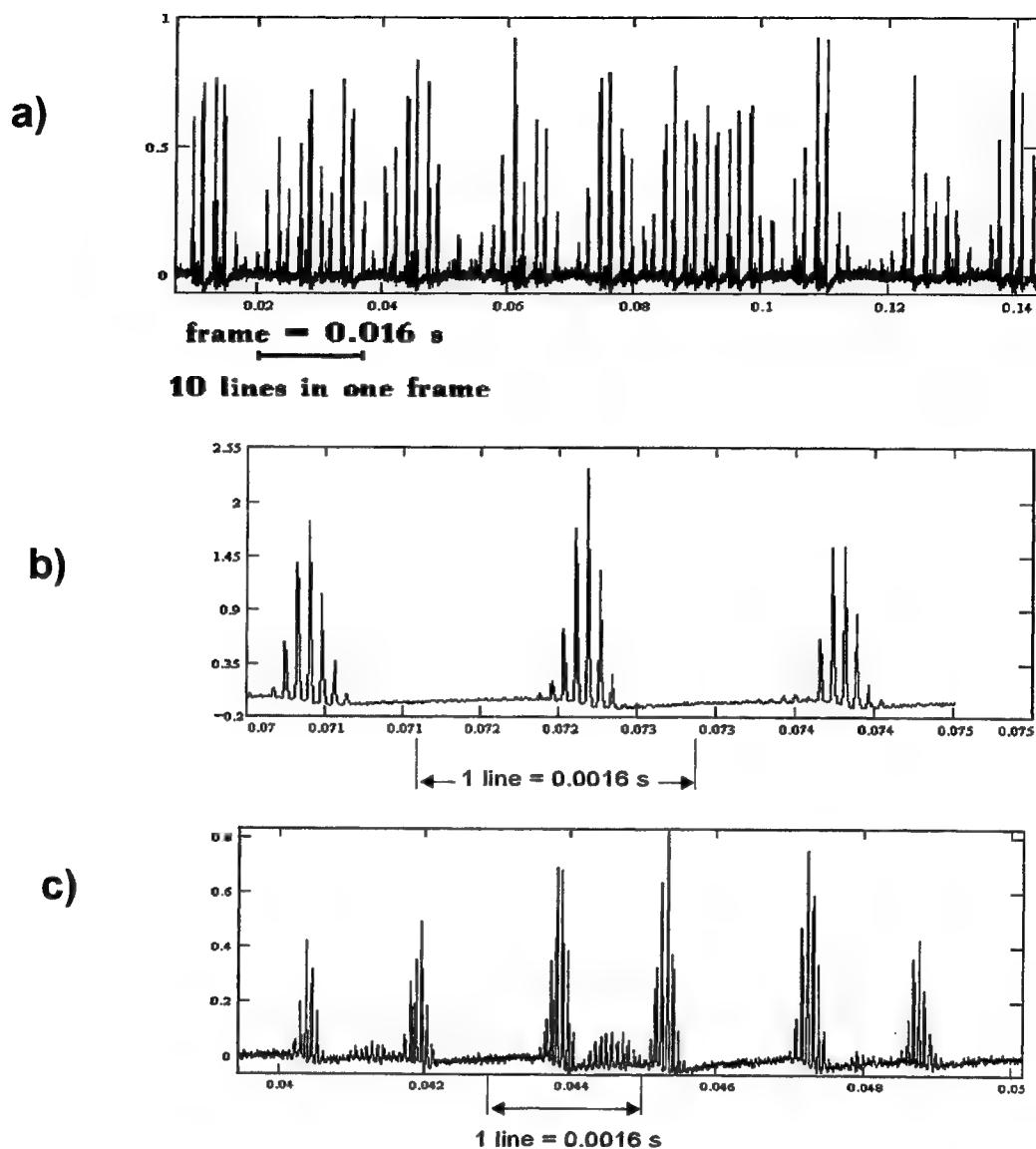
Fig.5. Typical traces of reflected signals during system operation at low-resolution (a) and high-resolution (b,c) time scales obtained without the imitator (b) and with simulating a two-speckle spot (c).
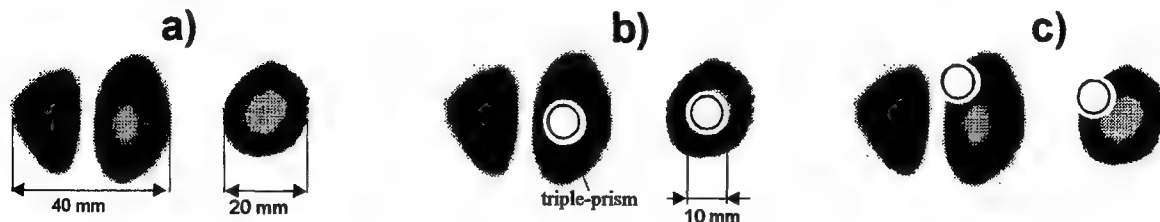
Fig6. Typical patterns of pulse radiation spots on the mirror diaphragm (a) and after reflection from it (b,c) in cases of presice (b) and bad (c) hitting the triple-prism..
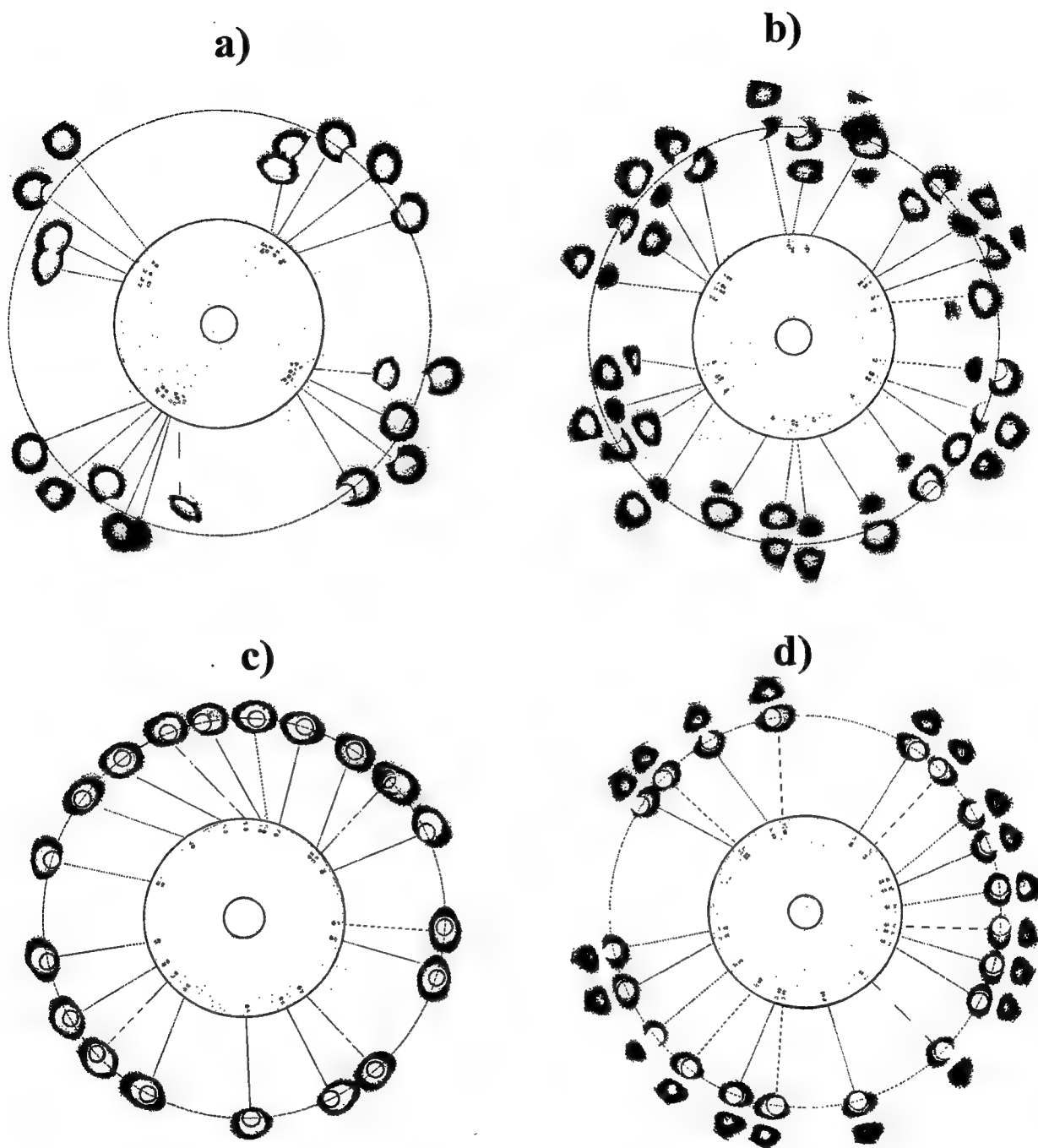
Fig.7. Typical sweep traces of radiation spots, obtained in a repetitively pused mode on the rotating disk without stabilisation (a,b) and with the use of the bright-speckle algorithm (c,d). In cases (a,c) the imitator of speckles was switched off, in cases (b,d) two-speckle spots were simulated. General views of disks are shown in the figure in inner areas of each of four fragments, and all the spot patterns are magnified in outer areas.

a)

With the algorithm   **Without the algorithm**

Delivered energy in a pulse, $E_{del1...N}$

0, 1, 2, 3

e^{-1} level of delivered energy achievable for precise static hitting

NO   YES

$\oplus \oplus \oplus \oplus \oplus \oplus \oplus \oplus \oplus$ $\ominus \ominus \ominus \ominus \oplus \oplus \ominus \ominus \ominus$

Output energy in a pulse, $E_{out1...N}$

0, 1, 2

Time, 0.5 s/div
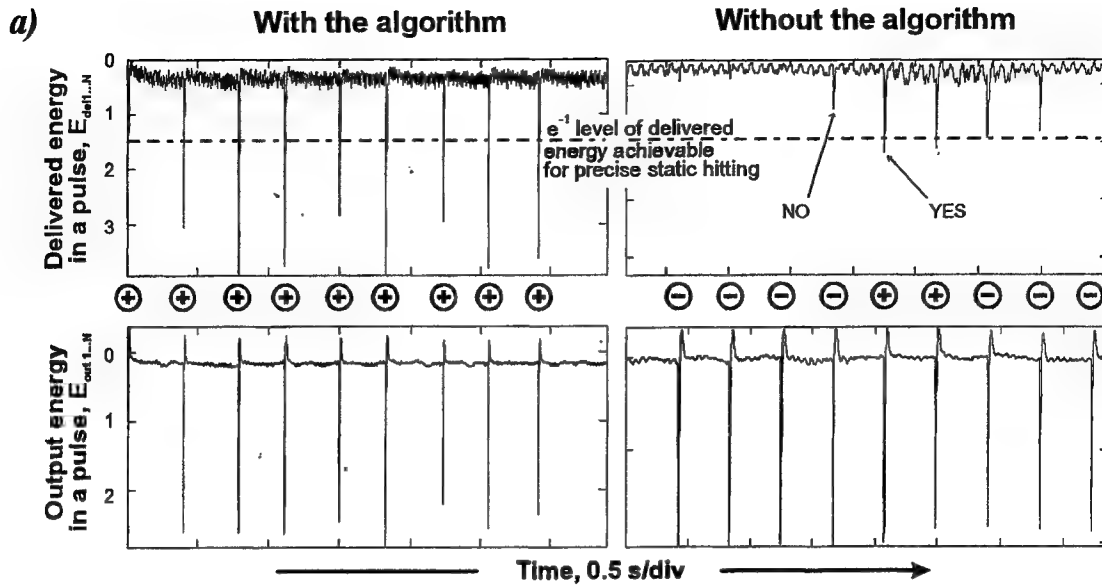
b)

$$\text{Probability of hitting the triple-prism} = \frac{\text{Number of } \oplus}{\text{Total number of pulses}}$$

$$\frac{9 \ \oplus}{9 \ \text{pulses}} = 1.00 \qquad \frac{2 \ \oplus}{9 \ \text{pulses}} = 0.22$$

$$\text{Gain in hitting} = \frac{1.00}{0.22} = 4.6$$

c)

Energy delivered in a burst, $E_{del} = E_{del1} + E_{del2} + ... + E_{delN}$;

Total output energy in a burst, $E_{out} = E_{out1} + E_{out2} + ... + E_{outN}$;

Delivery ratio, $DEL = \dfrac{E_{del}}{E_{out}}$;   Delivery efficiency, $Eff = \dfrac{DEL}{DEL_{max}}$

where DEL_{max} - achievable delivery ratio for precise static hitting

Eff with algorithm = 0.91   Eff without algorithm = 0.19

$$\text{Gain in efficiency} = \frac{0.91}{0.19} = 4.8$$

Fig.8. Typical trains of emitted and delivered pulses (a), and procedures of processing the data for estimating gains in probability of hitting the triple-prism (b) and delivery efficiency (c), obtained at using the beam stabilisation.

Novel scheme of dynamic correction using negative optical feedback

V.Yu.Venediktov, V.A.Berenberg, N.A.Bezina, A.A.Leshchev, M.V.Vasil'ev, F.L.Vladimirov

Institute for Laser Physics, SC "Vavilov State Optical Institute",

199034, St.-Petersburg, Russia

ABSTRACTS

Proposed is the novel method of dynamic nonlinear-optical correction for distortions in wide spectral band. The method is based on combining of the negative optical feedback correction and dynamic holography correction in the system, using optically addressed phase modulators. State-of-the-art of key technologies is evaluated.

Keywords: negative optical feedback, dynamic holography, optically addressed liquid crystal modulator, dynamic holographic converter.

1. BACKGROUND AND STATE-OF-THE-ART

In mid-80es there was proposed[1] and realized in several experiments[2,3] the scheme of the nonlinear-optical correction for distortions of optical radiation wavefront, using the optically addressed spatial phase modulator, introduced into the negative optical feedback (NOF) loop (see Fig.1).

In such a scheme the probe beam of radiation of the auxiliary laser source passes via the aberrated optical beamlet and through the layer with the controlled optical thickness (the layer of liquid crystal, LC, in the optically addressed spatial light modulator, SLM[4]). The optical thickness of this layer, i.e. phase retardation of the probe beam, depends on the intensity of controlling optical signal coming to the corresponding zone of photoconductor of the SLM. In our case such a signal is the interference pattern of the probe beam with the coherent and coaxial nondistorted reference beam. So in the system there is realized the optical feedback. In the case of appropriate phase shift between the probe and reference beams this feedback reveals itself as the negative feedback, and the system as a whole drifts to the state, in which the wavefront distortions, imposed by the induced relief of optical thickness of LC layer, add approximately to those imposed by the aberrated beamlet and thus correct for them. Note, that such a corrector works not only at the wavelength of the auxiliary probelaser source, but can be (with the accuracy of spectral dispersion of the LC refraction index) used across the overall spectral range of LC transparency.

The basic limitation, preventing this technique use for practical purposes is the so called 2π-problem (see Fig.2). In any scheme of output signal stabilization, using the negative feedback, the maximal magnitude of the error corrected is limited by the width of monotonous range of variation of the signal, used for the control of actuator with this error variation. In our case the control signal is produced by the dual beam interference in the Michelson, Mach-Zander etc. interferometer. Correspondingly, the range of monotonous variation of the intensity at the output of such an interferometer vs. relative phase shift between the reference and probe wave (i.e., the magnitude of the corrected distortion of wavefront) can not exceed the wavelength of the auxiliary laser source radiation.

In the case of larger distortions, exceeding these limits, the aperture of the corrector splits into several independent domains with the abrupt phase shift at the edge. Such a system is not stable, the acute edges of the domains result in significant diffraction losses of radiation. But the most important disadvantage is that the regions of the corrected wavefront, corresponding to different domains, obtain the relative phase shift in several wavelengths. Such a "broken" corrector can be efficiently used not in the whole range of LC transparency, but only in the rather narrow spectral zone $\Delta\lambda \ll \lambda$.
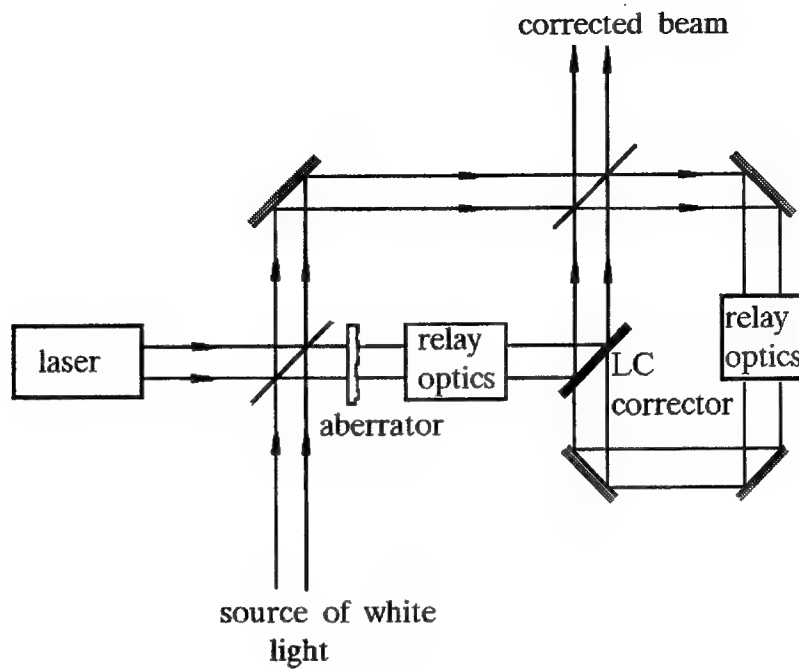
Fig.1. Usual scheme of NOF-correction for distortions
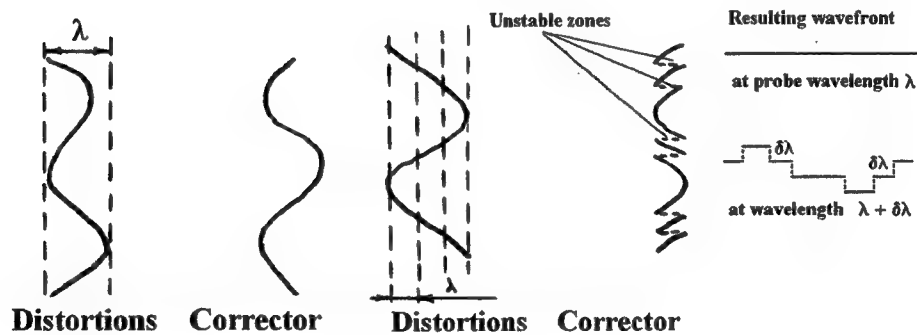
Fig.2. 2π−problem in NOF correction: phase retardation
in the corrector for small (left) and large (right) magnitudes of distortions.

There are several possibilities of the system performance improvement so as to enlarge the range of magnitudes of the corrected distortions with the preservation of wide spectral range of the corrected radiation wavelengths. For example, some improvement can be obtained just by enlargement of the auxiliary laser source radiation wavelength. However, the significant shift to the mid-IR range of spectrum (several microns) is limited by the reduce of LC media transparency and by the lack of sensitive photoelectric media.

D.M.Pepper[5] has suggested to use the spectrum-zonal approach. One can split the spectral range of correction into several narrow ranges and to use separate corrector for each of these ranges. This approach, however, is very complicated and results in significant energy losses due to the necessity of complicated spectral separation.

2. INTERFEROMETER WITH THE ENCOARSED SENCITIVITY

Recently we have proposed[6] another approach to this problem solution, which seems now to be the most prospective. The simple dual beam interferometer, forming the NOF signal in the discussed schematics, can be replaced by the sophisticated interferometery scheme, in which the variation of the output intensity from minimum to maximum will be smooth and monotonous along the phase shift range, whose magnitude equals several wavelengths of probe radiation.

Such an interferometer can, in particular, implement the following property of the thin (plain, non-Bragg) dynamic hologram (Fig.3). Let us record such a hologram as the interference pattern of the nondistorted plain wave and probe wave with some phase modulation of its wavefront (both waves have the wavelength λ_1). Let us then reconstruct this hologram at the shifted wavelength λ_2. In this case we shall obtain the reconstructed probe wave with the phase modulation of its wavefront, equal to that of the primary probe wave, measured in terms of wavelength of radiation. I.e., the reconstructed probe wave would have the phase modulation of its wavefront, scaled in the ratio (λ_2/λ_1) with the respect to that of primary probe wave. The use of this feature, in particular, makes it possible to obtain the mutually coherent light beams with the similar, but scaled wavefront distortions, which can be, in turn, used in the above mentioned sophisticated interferometer.

3. NOF CORRECTION SCHEMATICS FOR THE EXTENDED RANGE OF DISTORTIONS

One of variants of the NOF-correction schematics[6], using the interferometer with the reduced sensitivity and the extended range of the output signal monotonous behavior, is shown in the Fig.4.

In this case the auxiliary laser system has to emit the radiation at two wavelengths λ and λ'; the difference of these wavelengths has to be small: $\Delta\lambda = \lambda - \lambda' = \lambda / m << \lambda,\lambda'$; $m >> 1$. The probe beams at both wavelengths read out the wavefront distortions, imposed by the aberrant beamlet and momentary profile of the corrector. Than the probe beam at the wavelength λ' interferes with the coherent nondistorted reference beam in the medium, providing recording of the thin dynamic hologram. This hologram is read out by another reference beam at the wavelength λ and reconstructs the distorted probe beam with the scaled distortions. This beam is combined coaxial with the distorted probe beam at the same wavelength. The intensity in the interference pattern of these two beams varies monotonously from minimum to maximum at the range of phase shifts, imposed by the aberrant beamlet and corrector, m times exceeding that in usual scheme and thus providing the possibility of their correction. As to the medium for recording of the thin dynamic hologram, the optically addressed LC SLM, similar to that used as NOF-corrector, seems to be the most promising medium[7].

However, this schematics is not the best one. The main limitation is that in this case one has to organize several paths, where propagate light beams with the significantly distorted wave front (darkened in the Figure), and the information on these distortions is to be preserved in rather precise manner. In practice it means the necessity to use the various methods of optical relay and thus in extra sources of energy losses and of the extra errors.

There are possible other optical schematics, based on the same principles. One of such schematics is shown in the Fig.5. In this case the dynamic hologram is recorded by the distorted wave and reference wave at one wavelength and reconstructed by the distorted wave at another wavelength, producing thus directly the wave front with the reduced (scaled) distortions. Such an element can be called the *dynamic holographic converter* of the distortions' scale. In this case the propagation of the severely distorted wave front is limited by only one path. Such a system is also simpler and has the smaller number of the elements.
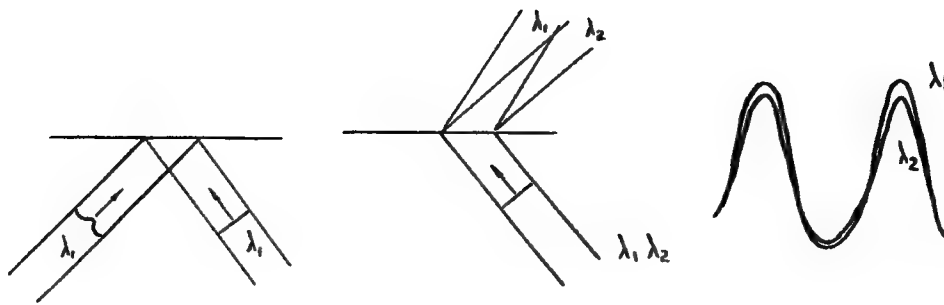
Fig.3. Writing-in of the thin dynamic hologram, its reconstruction
on two wavelengths and scaling of wavefront distortions
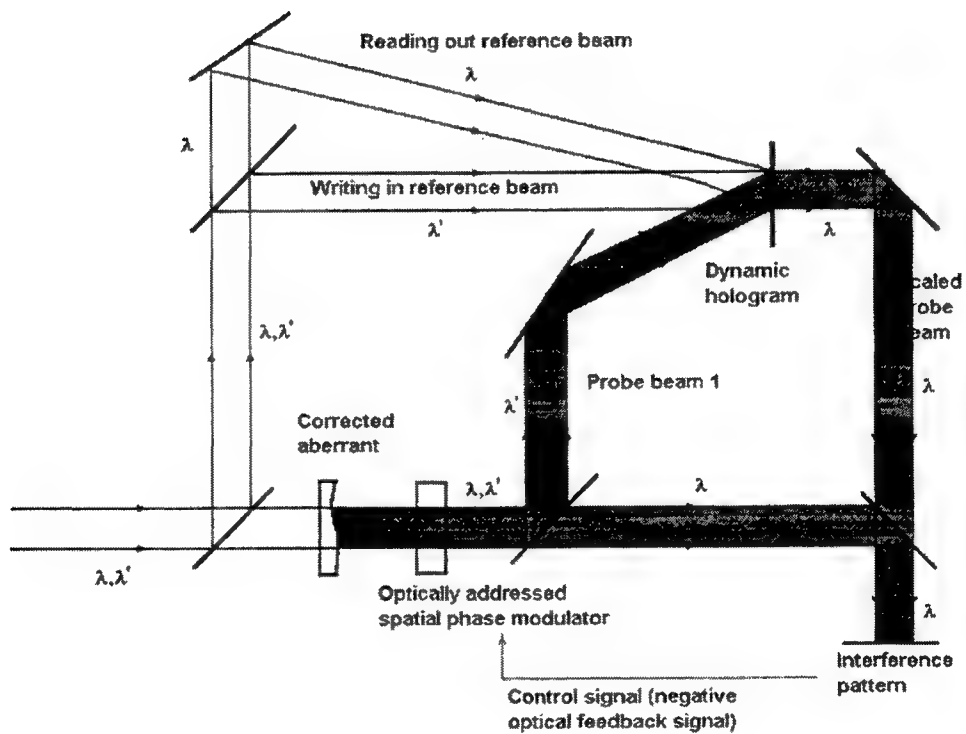
Fig.4. The use of interferometer with the encoarsed sensitivity in the scheme of NOF-correction. Dark region corresponds
to the path of strongly distorted beams.
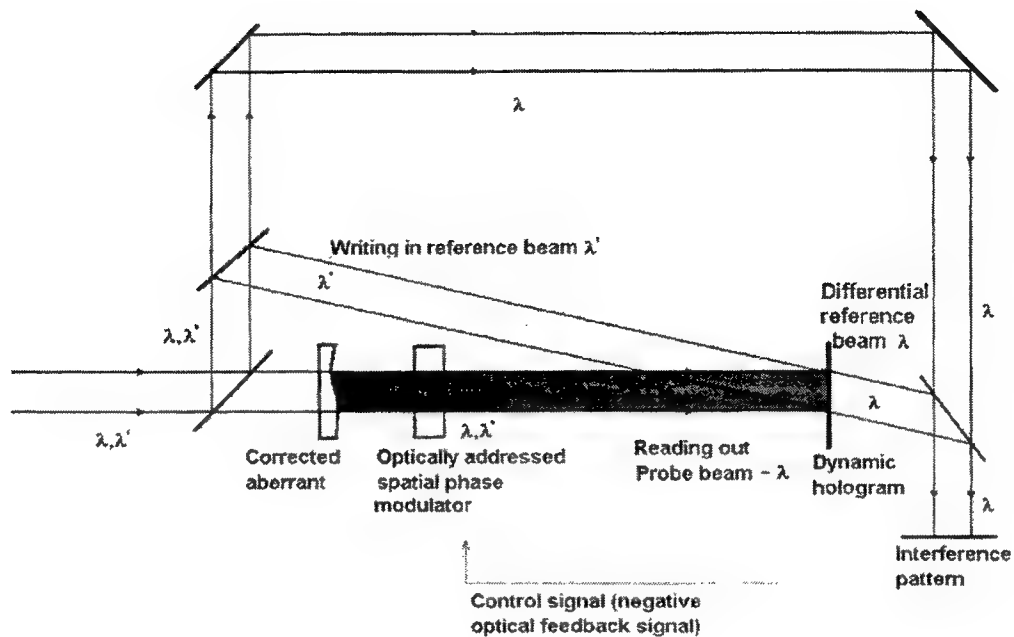
Fig.5. Improved NOF-correction schematics, using the dynamic holographic converter. Dark region corresponds to the path of strongly distorted beams.
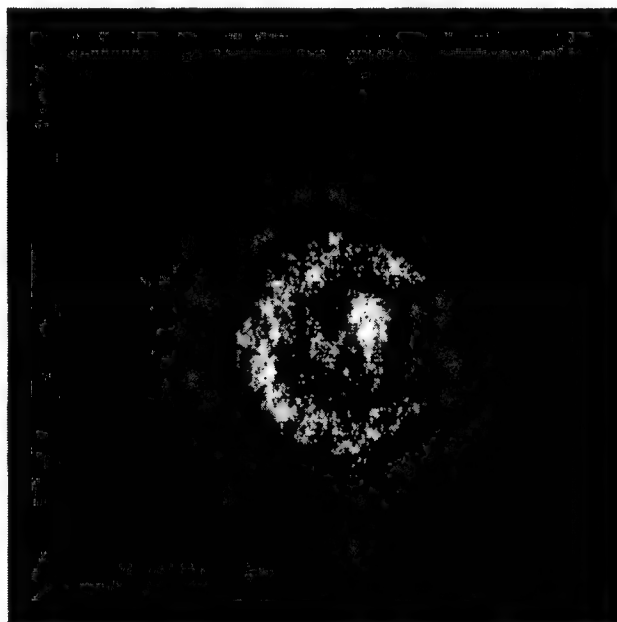
Fig.6. Spatial distribution of the gaussian beam after the self-action in the OA LC SLM, mounted between two polarizers.

4. LC SLM ELEMENTS WITH DEEP PHASE MODULATION

The proposed schematics requires the experimental feasibility study. As we have said already, there are possible several variants of the interferometer with the reduced sensitivity; one has to choose the optimal. Even more important seems to be the problem of residual non-corrected error. Similarly to any schematics of stabilization , using the negative feedback, the point of dynamic equilibrium of the system is somewhat shifted with respect to the minimal error signal. In our case it means, that the profile of the dynamic corrector does not completely correspond to the profile of the distortions, imposed by the aberrant beamlet.

The magnitude of the residual distortions of the output wavefront, imposed by the summary action of this beamlet and corrector, has to be sufficient for provision of the required distorted profile of the corrector. This problem was not yet analyzed, for the magnitude of the distortions, coped with by the traditional scheme of NOF-correction, was not large and one could neglect these residual error.

Anyhow, there is simple, at least in principle, solution of this problem. One can mount afterwards the first contour of NOF-correction, using the encoarsed interferometer, the second one of the similar schematics or the one, based on the traditional NOF-correction schematics. However, the evaluation of the necessity of such a complication of the system has to be based on more detailed analysis and numerical simulation.

As to the technological problems in realization of NOF-corrector with the expanded range of corrected magnitudes, the most important seems to be that of fabrication of the "thick" optically addressed LC SLM. The depth of modulation of LC refraction index equals 0.1 - 0.2, so the correction for distortions with the magnitude of dozen wavelength requires the use of LC layer with the thickness of $\sim10^{-1}$ mm or LC SLM of the sophisticated design. The problem of fabrication of the elements of such a class was already discussed with respect, in particular, of their use as the actuator in the linear adaptive systems[8]. This problem, however, requires much more thorough study, because, in particular, this very element will determine the response time of the overall system.

In fact, it is known[9] that the possibility to realize the optically addressed LC SLM with the comparatively deep (several wavelengths of visible light) phase modulation meets significant difficulties. It can be simply explained in the following way. Enlargement of the LC layer thickness result in growth of its electric resistance. At the same time, most of the photoconductors, which are used as the photosensitive layer in OA LC SLM production, reveal not very high dark resistance. So for some, not very high, thickness of LC layer the dark resistance of both layers become comparable. As a result, in the dark condition the relative value of the feeding voltage, applied to the LC layer, reduces. So the modulation of optical thickness of the layer after photoconductor illumination also reduces. As a result, in most of available today combinations of liquid crystal — photoconductor the dependence of phase shift vs. LC layer thickness soon saturates. We have checked this hypothesis in the experiment. It is known that the chalcogenide photosensitive layer reveals much higher dark resistance than the most widely used today layers, such as modified silicon etc. On the base of this photosensitive layer have realized the optically addressed transparent LC SLM element with the nematic LC layer thickness of 20 μm. In the Fig.6 is shown the intensity distribution of the gaussian beam of He-Ne laser after transmission through this element, mounted between the crossed polarizers. The influence of radiation have modulated the phase retardation; one can see at least three fringes. More accurate measurements have shown that in such an element it is possible to obtain phase retardation of $\sim7\pi$ at 0.63 μm, i.e. of more than 2 μm. If one uses such an element in the mirror geometry, he can realize hence the retardation of at least 4-5 μm, which would be sufficient for most practical implementations of the method under consideration.

In addition to shortening the response time, one of the basic problems in design of the "thick" modulators is the problem of fabrication of the elements of the high and reproducible optical quality. Note that in the case of NOF-correction this factor has much lower importance, than in, say, case of linear adaptive actuator, for in our case the correcting LC layer is itself introduced into the correction loop.

REFERENCES

1. Vorontzov M.A., Shmalgauzen V.I. Izvestiya VUZov. Seria Radiofizika, Vol.25, #10, p.1179-1187, in Russian
2. Vorontzov M.A., Kirakosyan M.E., Larichev A.V. Kvantovaya Elektronika, Vol.18, #1, p.117-126, 1991, in Russian
3. Pepper D.M. et al. Innovative adaptive optics and compensated imaging using a liquid crystal light valve. CLEO'93, Technical Digest, paper CThO2, p.464-466.
4. Warde C., Fisher A.D., Spatial light modulators: applications and functional capabilities. In "Optical Signal Processing", J.L.Homer, ed., Academic Press, NY, 1987, p.477-523.
5. Pepper D.M., private communication.
6. Venediktov V.Yu. Negative optical feedback correction for the extended range of distortions. Proceedings of SPIE, Vol.3219, p.133-137, 1997.
7. Berenberg V.A., Kamanina N.V., Soms L.N. Holographic correction of distortions using the liquid crystal light modulator for differing frequencies of recording and reading radiation. Izvestiya AN SSSR, Ser.Fizicheskaya, 1991, v.55, #2, p.236-238, in Russian.
8. Onokhov A.P. et al. Optical wavefront corrector based on liquid crystal concept. Proceedings of SPIE, Vol.2201, pp.1020-1026, 1994.
9. Onokhov A.P., private communication

Adaptive correlation filtering of time-varying speckle pattern using photorefractive fanning effect

Erik Raita, Alexei A. Kamshilin, Kimmo Paivasaari, Yuri N. Kulchin[*], and Timo Jaaskelainen

Väisälä Laboratory, Department of Physics, University of Joensuu,
P.O. Box 111, FIN-80101, Joensuu, Finland
e-mail: erik.raita@joensuu.fi

ABSTRACT

Novel technique of object's vibration monitoring is proposed. It is based on self-diffraction of the speckle pattern on adaptive correlation filter recorded in photorefractive crystal owing to the fanning effect. The technique provides linear response on the displacement amplitude and high sensitivity. Both sensitivity and dynamic range of measurements can be adjusted varying the average speckle size on the input face of crystal.

KEYWORDS

Photorefraction, fanning effect, vibration monitoring, remote sensing.

1. INTRODUCTION

A number of optical techniques based on both holographic and speckle interferometry have been proposed for the detection of transient surface motion and for monitoring of objects vibrations.[1,2] Recently, the introduction of digital image processing methods has led to new possibilities in this field, especially in the application of the speckle interferometry.[3,4] Unfortunately, the high cost of the set-up and influence of environmental changes on the measurement accuracy restrict wide application of these techniques in the industry. Simpler methods for object vibration monitoring were proposed and studied as well. These are based on spatial filtering of the dynamic speckle pattern that occurs when coherent light is scattered from a vibrating object's surface.[5-7] However, the spatial filtering is usually implemented either by computer post-processing of the recorded speckle-patterns or by using a small-aperture filtering with significant losses of the light energy. Korneev and Stepanov have proposed to use self-diffraction of a speckle pattern recorded in a photorefractive crystal for vibrations monitoring.[8] Unfortunately, like in a small-aperture-technique, only a small portion of the light power can be exploited in their method.

In this letter, we propose a new simple and cost-effective technique of the speckle-pattern spatial-correlation filtering, which is continuously self-adapted to slowly varying environmental changes and serves for monitoring of the object's vibrations. This technique is based on the high sensitivity of a holographic filter to any decorrelation of the readout speckle pattern caused by its homogeneous shift or reconfiguration.[9,10] We propose to record novelty correlation holographic filter in a dynamic photorefractive crystal without any reference wave but using light-induced scattering named the fanning effect. This effect is known as a self-diffraction process in photorefractive media, in which a single light beam self generates scattering in asymmetrical way.[11,12] It is now well established that this effect is mainly caused by energy-exchange beam coupling between the incident beam and radiation scattered by inhomogeneities in the entrance face or within the bulk of the crystal.[11] Any light beam introduced into a photorefractive crystal with a high two-wave coupling gain generates a number of initially weak beams scattered in a broad angular spectrum. These scattered beams interfere with the incident beam, recording a number of volume phase gratings. The incident beam is self-diffracted from

---

these gratings, enhancing the scattered light if the phase-matching conditions are fulfilled.[13] The most power (up to 90%) of the incident light can be transferred to the scattered light, significantly diminishing the power of the beam transmitted through the crystal.

Owing to the holographic origin of the fanning effect, any fast change of either structure or position of the incident beam results in instantaneous diminishing of the fanning light intensity until a new set of the fanning holograms is recorded in the crystal. This feature of the fanning effect has been exploited as a novelty filter in optical image processors for the time-differentiation of the input images.[14,15] Here we propose to utilize the intensity of the whole transmitted beam as a parameter to measure variations in time of laser speckles and, consequently, vibrations of a rough object.

2. EXPERIMENTAL SETUP

The experimental set-up is depicted on Fig.1. We study vibrations of a piezo-ceramic plate with a rough surface, which diffusely scatters the incident light in a wide volume angle of 1.3 steradians. The plate was illuminated by a non-expanded laser beam (beam diameter is about 1 mm) from a He-Ne laser ($\lambda = 0.63$ μm) with power of 20 mW. The angle of incidence was 45° to ensure a lateral displacement of the vibration surface. The light scattered from the plate at the direction of specular reflection was collected by a lens $L1$ onto the photorefractive crystal of bismuth titanium oxide ($Bi_{12}TiO_{20}$). The crystal has dimensions of $0.9 \times 4.4 \times 9.8$ mm^3. To produce both fanning and the linear phase transformation we apply to the crystal alternating unipolar electric field of a square-wave. Mutual orientation of the vector of applied electric field and crystallographic axis of the crystal is shown in Fig. 1. The rising time of the voltage switching was 0.5 ms and the repetition rate can be varied from 0.2 Hz to 200 Hz. An average size of the speckles on the crystal's input face could be modified by changing the optical system, which collects light into the crystal (lens $L1$). The light transmitted through the crystal has been collected by the lens $L2$ into the photo-diode and its current was measured by a digital oscilloscope.
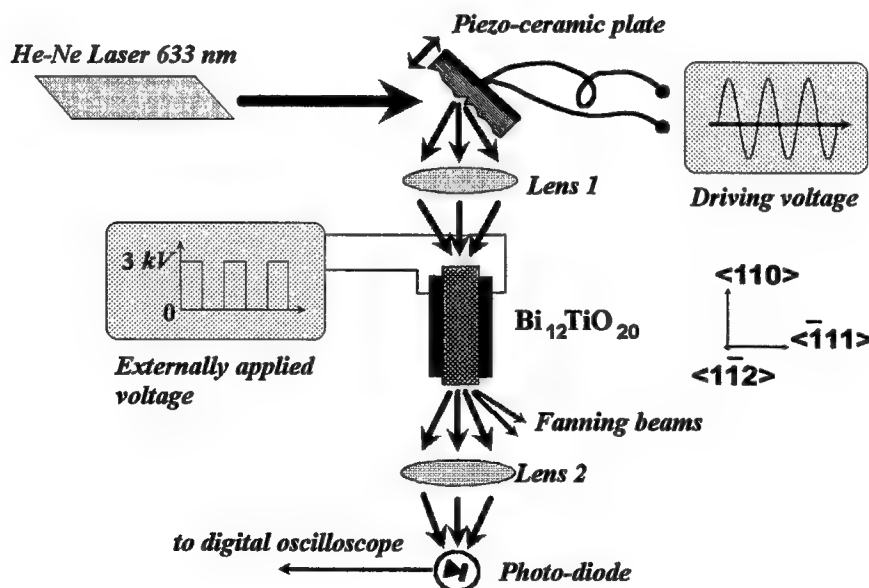
Fig.1. Schematic of the experimental set-up for vibrations monitoring of the diffusely scattered objects. Light scattered by objects surface is collected by lens $L1$. Lens $L2$ serves for collecting the light transmitted through the crystal.

3. ADAPTIVE CORRELATION FILTERING OF THE SPECKLE PATTERN

As we have recently demonstrated,[16] the intensity of the fanning light is proportional to the correlation function between an unperturbed speckle pattern launched into the photorefractive crystal and that one corresponding to the instant position of the scattering surface. The dynamic characteristics of this correlation function have been investigated in details by Asakura and Takai.[5] It was shown that if the scattering object vibrates harmonically at a frequency ω with a lateral component of the displacement vector, then the speckle pattern, caused by the object, oscillates with the same frequency. Let us suppose that the amplitude of the speckle's shift is smaller than the speckle's average size at the input face of the crystal. Then, as a first approximation, we can consider the movement of the speckle pattern to be similar to the movement of an interference pattern created by two plane waves when one of them is phase-modulated at the frequency ω. The latter problem of photorefractive two-wave mixing has been extensively treated both experimentally and theoretically.[17-21] It was shown that the periodical movement of the interference pattern is transferred into the intensity modulation of the transmitted beam, which oscillates in general case at both ω and 2ω. The ratio of the first and second harmonics amplitudes is determined by the relative phase shift ϕ between the interference pattern maxima and space-charge maxima, which, in turn, depends on the mechanism of the photorefractive recording. For example, diffusion recording (without external electric field) produces $\phi = \pi/2$ and results in the transmitted intensity modulation at the frequency of 2ω. In contrast, $\phi = \pi$ is achieved for drift-dominating recording producing first-harmonic intensity modulation (linear phase-to-intensity transformation). Naturally, a linear sensor is much preferable for practical applications, but $\phi = \pi$ does not allow efficient energy exchange between the interacting beams, and, consequently, the fanning effect is significantly suppressed. However, recent theoretical consideration of two-wave mixing allowing the pump beam depletion (which is just a case the of strong fanning effect) shows that the energy exchange may exist even for $\phi = \pi$.[21] Moreover, it was experimentally proved that both absorption and phase type of gratings are simultaneously recorded in sillenite crystals.[22] Each type of grating variously affects diffraction of a phase-modulated beam. Therefore, varying external conditions of the grating formation, one has a chance to find a situation, when strong energy exchange and linear transformation of the phase modulation coexist.

The application of the bipolar ac-field to sillenite crystals leads to most effective beam coupling and consequently to strongest fanning scattering.[23] The fanning effect is not so strong when the unipolar electric field is applied to the crystal but it is much stronger than under dc-electric field at the steady state. Due to the fanning effect, intensity of the light transmitted through the crystal was much smaller than without any external field. However, if we rapidly shift the speckle pattern, the intensity of fanning light is instantaneously decreasing resulting in respective increasing of the transmitted beam intensity. Figure 2 shows the typical reaction of the fanning light intensity on the fast lateral shift of the speckle pattern.
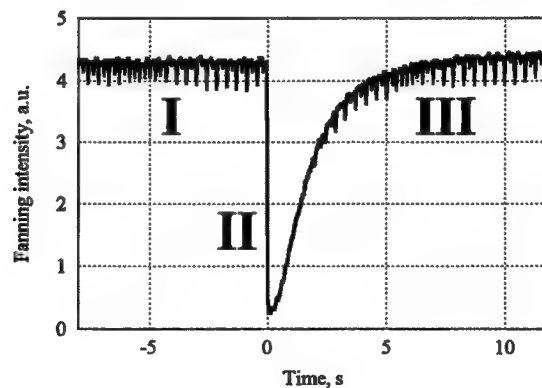
Fig. 2. Evolution of the fanning intensity after the rapid lateral displacement of the speckle pattern for 10 µm. Alternating electric field of 30 kV/cm is applied at the moment t=0. Stage I: steady-state fanning is produced by initial speckle-pattern. Stage II: the intensity of fanning is instantaneously decreasing because of the rapid displacement of the speckle pattern. Stage III: new set of gratings is recorded by shifted speckle pattern.

As one can see, fanning scattering is growing up with the response time τ_R after the initial drop. This increasing occurs because the new set of fanning holograms is recording in the crystal. Therefore, the photo-diode's current will change only if the speckle pattern varies faster than τ_R. Otherwise, all slower changes (with $\tau > \tau_R$) will not affect the transmitted beam power. For a chosen wavelength, the recording time τ_R depends on the crystal type, external electric field, and intensity of the input beam. Therefore, proper choice of the material and experimental conditions allows us to exclude harmful influence of environmental instability. The basic idea for the correlation filtering of time-varying speckle pattern is schematically depicted in Fig. 3.
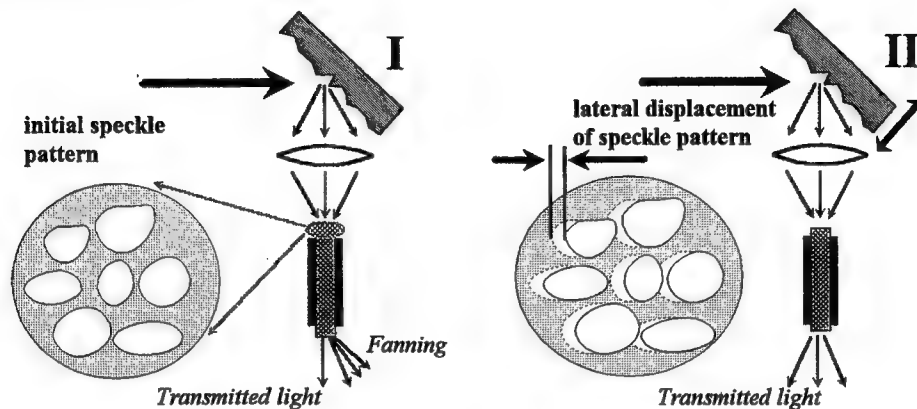
Fig. 3. Schematical illustration of the correlation filtering of time-varying speckle pattern using fanning effect. Parts I and II show the corresponding stages I and II in Fig. 2.

4. LINEAR PHASE DEMODULATION OF THE SPECKLE PATTERN

External dc-electric field produces linear transformation of the speckle-pattern displacement to the intensity variation. It means that sinusoidal vibrations of the piezo-ceramic plate in our set-up result in the intensity modulation of the transmitted beam at the first harmonic of the vibration frequency. We experimentally observed that switching on the dc-electric field leads to the sinusoidal modulation at the frequency ω just after switching. However, the modulation depth is diminishing with the time owing to not favourable conditions for fanning scattering under dc-electric field. In contrast, unipolar alternating voltage produces a steady-state modulation at the first harmonic. Note that the bipolar electric field results in further increasing of the fanning scattering but immediately leads to the intensity modulation at frequency 2ω.
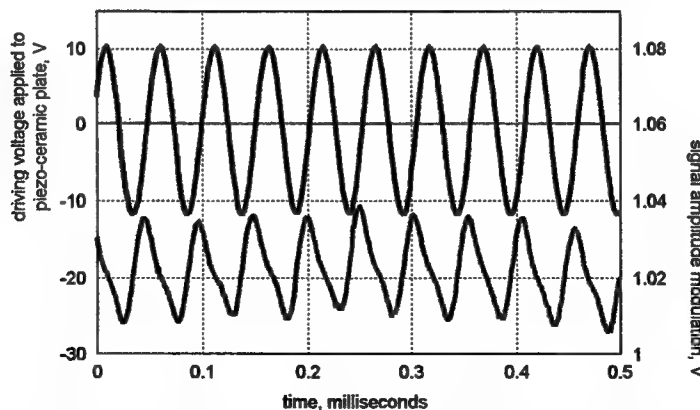
Fig. 4. Amplitude modulation of the signal in response to the periodic displacement of the illuminating speckle pattern.

Figure 5 demonstrates the ability of the proposed technique to adapt itself to changing frequency of the vibration of object. Initially, the piezo-ceramic plate was excited to oscillate at the frequency 4.4 kHz. Then, at the moment $t = 0$, the frequency was switched to 440 Hz as shown by an oscilloscope trace (a) in Fig. 5. A simultaneous record of the photo-diode current is shown by trace (b) in Fig. 5. One can see that the modulation with new frequency can be recognised immediately after the switching of the driving voltage. However, due to the mechanical inertia of the piezo-ceramic plate, it continues to oscillate during few milliseconds at the higher frequency as well.
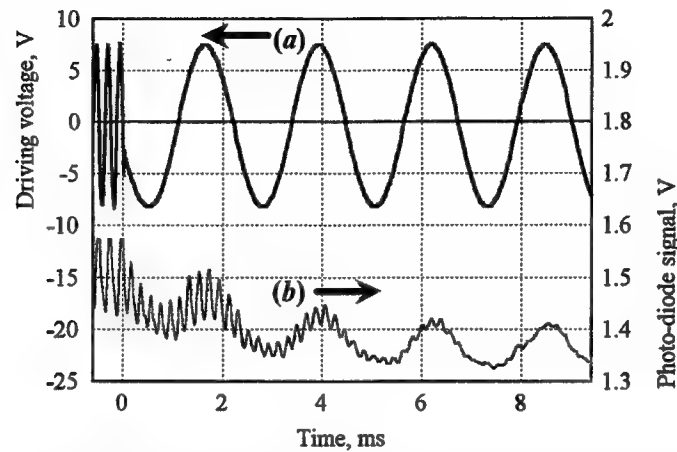
Fig. 5. Simultaneously recorded oscillogramms of the voltage driving the piezo-ceramic plate (a) and the photo-diode signal (b) showing the adaptiveness of the vibrometer to changing experimental conditions. At the moment t=0 the frequency of vibration is switched from 4.4 kHz to 440 Hz.

5. SENSITIVITY OF MEASUREMENTS

To estimate sensitivity of the proposed technique, we carried out preliminary measurements of the piezo-ceramic's vibration amplitude at various excitation frequencies. It was done by using the time-average holographic interferometer exploiting anisotropic diffraction in a photorefractive crystal.[24] Another $Bi_{12}TiO_{20}$ sample measuring $8.0 \times 12.0 \times 8.0$ mm^3 was used in this interferometer. After the calibration, we measured the response of the proposed system on sinusoidal vibrations of the rough object. Figure 6 shows the modulation depth of the photo-diode's current as a function of the piezo-ceramic's amplitude measured at different excitation frequencies. The modulation depth was defined as a ratio of the modulation amplitude to the photodiode's current at the steady-state for non-vibrating object. The group of curves marked as (a) in Fig. 6 has been obtained with optical set-up producing average size of the speckles of 45 μm at the input face of the photorefractive crystal. Alternatively, the group (b) has been obtained for 90-μm average size of speckles.

One can see from Fig. 6 that all dependencies are linear and sensitivity of the measurement system depends on the speckle size: the smaller speckle, the higher sensitivity. Therefore, both sensitivity and dynamic range of the measurements can be readily changed by modifying the optical projection system. It is worth noting that absolute value of sensitivity for the 45-μm speckle pattern reaches 0.15 V/μm, which is two orders of value higher than that reported in Ref.7. The dependence of the signal amplitude on an external electric field is linear up to the value of 35 kV/cm, which is the strongest field applicable to the particular photorefractive sample.

All the experiments reported here were carried out with a He-Ne laser (λ=632.8 nm). However, the proposed technique works also if a laser-diode (λ=682 nm) is used as a light source. In addition, there is no strong requirement for the coherence length of the light source. It may be about 1 mm or smaller, which is enough to create the speckle pattern and produce photorefractive fanning effect. Moreover, the optical projection system can be replaced by a multimode optical fiber that opens up a possibility to design compact, flexible, and stable vibration sensors.
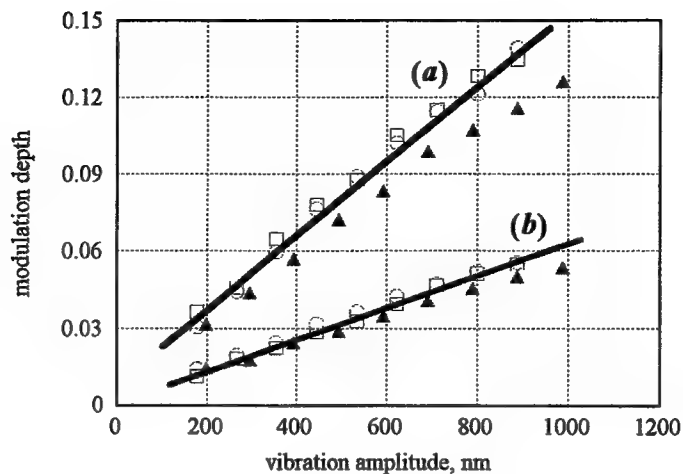
Fig. 6. Dependence of the photo-diode-current modulation depth on the vibration amplitude of the piezo-ceramic plate obtained for the average speckle size of 45 μm {set (a)}and for 90 μm speckles {set (b)} for different vibration frequencies. Open squares indicate experimental points measured for vibrations at the frequency of 500 Hz, open circles are for 1000 Hz, and triangles are for 2000 Hz. Unipolar electric field of 35 kV/cm with the repetition rate of 45 Hz is applied to the photorefractive BTO crystal.

6. CONCLUSIONS

Novel technique of the vibration monitoring based on the photorefractive fanning effect is proposed. Principle of the operation is the correlation analysis of the speckle pattern scattered by a rough surface in motion. The technique is very simple in the implementation and easily self-adapted to environmental changes. There is no need for any special reference or readout beams. It effectively uses most of the light power scattered by the object. The technique provides linear response on the displacement amplitude and its sensitivity is comparable with that of an interferometer. Both sensitivity and dynamic range of the measurements can be easily changed varying the average speckle size on the input face of the photorefractive crystal.

7. ACKNOWLEDGMENTS

REFERENCES

[1] C. M. Vest, *Holographic interferometry* (Wiley, New York, 1979).

[2] P. Hariharan, *Optical holography: principles, techniques, and applications*, 2nd ed. (Cambridge University Press, Cambridge, 1984).

[3] L. Wang and S. Krishnaswamy, Opt. Eng. **35**, 794 (1996).

[4] A. J. Moore and C. Perez-Lopez, Opt. Eng. **35**, 2641 (1996).

[5] T. Asakura and N. Takai, Appl. Phys. **25**, 179 (1981).

[6] H. Fujii, T. Asakura, K. Nohira, Y. Shintomi, and T. Ohura, Opt. Lett. **10**, 104 (1985).

[7] J. L. Remo, Opt. Eng. **35**, 2798 (1996).

[8] N. A. Korneev and S. I. Stepanov, Optik, **91**, 61 (1992).

[9] Y. A. Bykovskii, O. B. Vitrik, Y. N. Kulchin, and A. I. Larkin, Sov. J. Quantum. Electron. **20**, 83 (1990).

[10] Y. A. Bykovskii, O. B. Vitrik, Y. N. Kulchin, and A. I. Larkin, Opt. Spectrosc. **68**, 677 (1998).

[11] V. V. Voronov, I. R. Dorosh, Y. S. Kuzminov, and N. V. Tkachenko, Sov. J. Quantum. Electron. **10**, 1346 (1980).

[12] J. Feinberg, J. Opt. Soc. Am. **72**, 46 (1982).

[13] M. Cronin-Golomb and A. Yariv, J. Appl. Phys. **57**, 4906 (1985).

[14] M. Cronin-Golomb, A. M. Biernacki, C. Lin, and H. Kong, Opt. Lett. **12**, 1029 (1987).

[15] J. E. Ford, Y. Fainman, and S. H. Lee, Opt. Lett. **13**, 856 (1988).

[16] A. A. Kamshilin, T. Jaaskelainen, and Y. N. Kulchin, Adaptive correlation filter for stabilization of interference-fiber-optic sensors, to be published in Appl. Phys. Lett.

[17] T. J. Hall, M. A. Fiddy, and M. S. Ner, Opt. Lett. **5**, 485 (1980).

[18] A. A. Kamshilin, J. Frejlich, and L. Ceskato, Appl. Opt. **25**, 2376 (1986).

[19] C. T. Field and F. M. Davidson, Appl. Opt. **32**, 5285 (1993).

[20] S. Breugnot, M. Defour, and J. P. Huignard, Opt. Commun. **134**, 599 (1997).

[21] Y. Li, Z. Zhou, X. Sun, Y. Jiang, and K. Xu, Opt. Commun. **136**, 160 (1997).

[22] A. A. Kamshilin, Opt. Commun. **93**, 350 (1992).

[23] S. I. Stepanov and M. P. Petrov, Opt. Commun. **53**, 292 (1985).

[24] A. A. Kamshilin and M. P. Petrov, Opt. Commun. **53**, 23 (1985).

Single-mode Nd:YAG laser with cavity formed by population gratings

Oleg L. Antipov [+], Alexander S. Kuzhelev [+], Andrey P. Zinov'ev [+],
Andrey V. Gavrilov [++], Alexander.V. Fedin [++], Sergey N. Smetanin [++],
Tasoltan T. Basiev [+++]

[+] *Institute of Applied Physics of the Russian Academy of Science,*
603600, 46 Uljanov St., Nizhnii Novgorod, Russia.
[++] *Kovrov State Technology Academy,*
601910, 19 Mayakovsky Str., Kovrov, Vladimir region, Russia
[+++] *General Physics Institute of the Russian Academy of Science,*
117942, 38 Vavilov Str., Moscow, Russia.

ABSTRACT

Q–switched regimes of the nanosecond pulse–periodic *Nd:YAG* laser with dynamic cavity formed with participation of dynamics holographic gratings in laser elements have been investigated. A Sagnac interferometer was applied as a laser cavity mirror for angular selection of initial radiation. As a passive Q–switch, we used saturable absorber crystal $LiF:F_2^-$, which increased total intracavity diffraction efficiency of dynamic gratings completing the cavity. Self-pumped phase conjugation in *Nd:YAG* amplifier and $LiF:F_2^-$ absorber provided adaptive properties of the cavity. The peak power of generated beam with diffraction quality exceeded 17.5 MW and the average power achieved 50W.

Keywords: Dynamic holographic gratings; Refractive index and gain gratings in active media; High average power Nd:YAG laser.

1. INTRODUCTION

The methods of adaptive and nonlinear-optical corrections are actively investigated due to possibilities to improve the spatially - energetic parameters of a laser radiation [1-4]. One of the most perspective methods in this direction is the dynamic holography using effects of a phase conjugation (PC) and optical waves mixing. To the present time the set of effects of interaction of light waves in various nonlinear mediums is investigated, a lot of methods and schemes of the PC of laser beams with concrete parameters (intensity, spectral breadth, degree of polarization, duration of pulses etc.) is developed. The present work is directed to development of new physical principles of a construction of lasers using nonlinear mirrors based on the dynamic holograms, and research of their unique potential possibilities (such as self-adapting to intracavity distortions, etc.). The main goal of the work is the research of the lasers, which cavities are formed with participation of dynamic gratings of an index of refraction and amplification (or absorption), accompanying with gratings of population, induced in inverted laser crystals and saturated absorbers by an interference field of generated beams.

The stationary unstable cavity of a telescopic type and a passive Q–switcher (PQS) on a $LiF:F_2^-$ crystal were applied in [5,6] to reduce thermal phase distortions and realize of single–mode lasing. It has allowed to receive pulse–periodic single–mode radiation with peak power of a separate pulse up to 100 kW and spatial brightness $2 \cdot 10^9$ W/sm²sr at divergence of 2 mrad and coherence length of 10 sm. However beam quality of modern high-power lasers (having a broad spectrum of applications in a process engineering, communication, medicine) remains low - the divergence of their beams usually exceeds a diffraction limit in several orders of magnitude.

O.L. Antipov et.al.: Tel.:+7(8312)384547; Fax:+7(8312)363792; e-mail: antipov@appl.sci-nnov.ru

2. EXPERIMENTS

We present the study of a laser system which included a passive Q–switch by a $LiF:F_2^-$ crystal, dynamic cavity formed by holograms induced both in active (Nd:YAG)[4,7] and passive ($LiF:F_2^-$)[8] elements by generated beams themselves providing self–pumped phase conjugation (SPPC) and Sagnac interferometer as a transverse mode selector .

The optical scheme of the laser is shown in (fig. 1). The laser consists of two AEs (1 and 2), PQS (3), mirrors and the Sagnac interferometer, formed by beam splitter (8) and mirrors. Lasing starts from amplified spontaneous emission of AEs, reflected from the Sagnac interferometer ensuring initial spatial–angular selection. The different dynamic gratings induced by generating beams themselves are shown in the fig.1. These holographic gratings playing a role of nonlinear mirrors completed self–adaptive laser cavity.
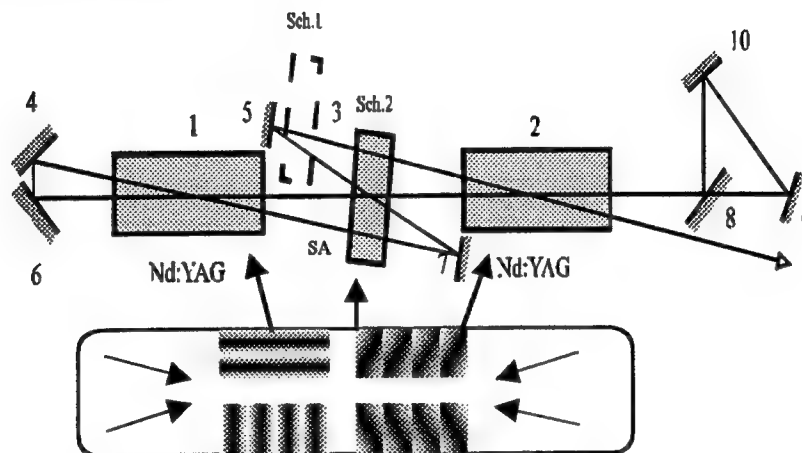
Fig. 1. Optical scheme of Nd:YAG laser with dynamic cavity: 1, 2 – AE; 3 – $LiF:F_2^-$ crystal; 4, 5, 6, 7 –mirrors; 8 – beam splitter; 9, 10 – Sagnac interferometer mirrors

The free running regime was realized in the scheme without $LiF:F_2^-$ crystal. The energy of generation pulses achieved 1.62 J at pulse repetition rate 30 Hz, pump pulse energy of 127 J and their duration of 200 μs (it corresponded to average power of single-mode radiation of 49 W). The divergence of the generated beam was 0.42 mrad. The coherence length exceeded 10 m, that corresponds to the oscillation spectrum width of 0.11 pm.

To increase the diffraction efficiency of the dynamic holographic gratings formed in the Nd:YAG crystals and to realize the passive Q–switch, the $LiF:F_2^-$ crystal was used. The crystal initial transmittance was varied from 20 % to 76 %. It allowed us to realize a Q–switch regime providing the equidistant huge pulses.

We investigated two schemes of passive Q–switch of the laser dynamic cavity:
 – the $LiF:F_2^-$ crystal was placed close to the mirrors 5 and 7 (scheme 1);
 – the $LiF:F_2^-$ crystal was placed between AEs (scheme 2) at the point of intersection of the internal beams, as shown in fig. 1.

The Q–switch provided a series of equidistant nanosecond pulses. The pulse duration was 20–80 ns. It did not depend on the scheme of PQS arrangement, and was defined both by cavity length, and initial transmittance of the $LiF:F_2^-$ crystal. PQS initial transmittance was changed by moving the $LiF:F_2^-$ crystal perpendicularly to the optical axis. It allowed us to change smoothly the duration of generated pulses, their number and pulse repetition period in the pulse train and hence to operate the average power and pulse energy of the beam.

The dependencies of power and temporary radiation parameters on PQS initial transmittance are shown in fig. 2 at total pump energy of 127 J and pump pulses repetition rate of 30 Hz. The $LiF:F_2^-$ crystal was placed according to the scheme 2. The given dependencies demonstrated that the duration of a separate pulse was reduced, and its energy and peak power was increased at reduction of initial transmittance of the crystal. The duration of generated beam pulses was $\tau = 20$ ns at PQS initial transmittance of $T_0 = 20$ %. The energy of a separate pulse in the series of pulses achieved $W_i = 350$ mJ, and the peak power exceeded $P_m = 17$ MW. The increase of power parameters was caused by increase of PQS optical den-

sity, losses on its enlightenment also grow. It resulted in increase of a time of achievement of threshold population inversion and increase of the reserved energy in AEs. And, as a consequence, it resulted in generation of pulses with large energy and peak power. On the other hand, the increase of PQS initial transmittance caused the decrease of losses on its enlightenment and decrease of the time of achievement of threshold population inversion in AEs. It resulted in growth of pulse quantity and decrease of pulse repetition period in the pulse train. For these reasons the generation pulse energy and their peak power was reduced. The energy of the pulse train was increased and at $T_0 = 50$ % exceeded the energy of free generation pulses (shaped line in a fig. 2).
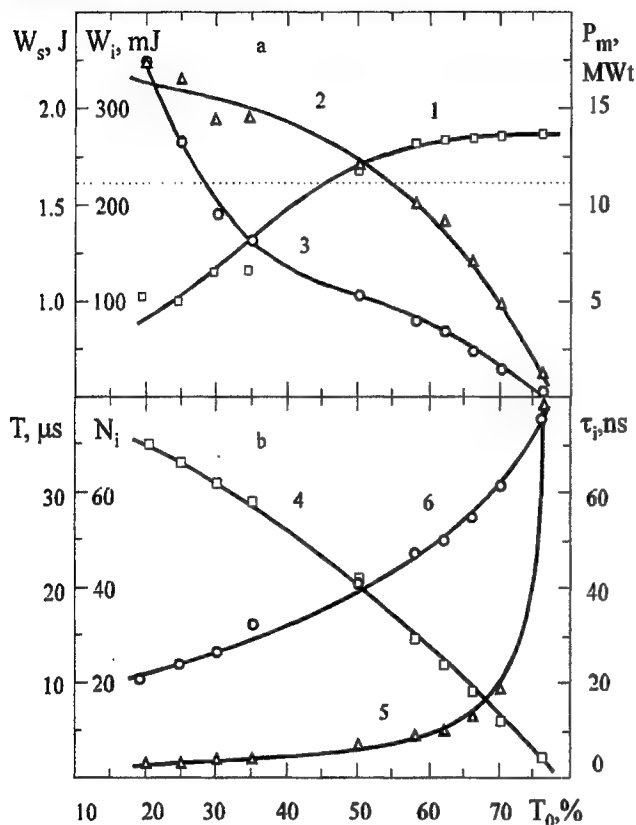
Fig. 2. Dependences of Nd: YAG laser radiation power parameters at 30 Hz pulse–periodical pump with 127 J energy on the initial transmittance of PQS: 1 – energy of the train of pulses; 2 – separate pulse energy; 3 – pulse peak power; 4 – pulse repetition period in the train of pulses; 5 – the number of pulses in the train of pulses; 6 – pulse duration.

Fig.3. Dependencies of Nd: YAG laser radiation power parameters on pump pulse energy with 30 Hz frequency at 58 % PQS initial transmittance: 1, 2 – pulses train energy; 3 – free generation pulse energy; 4, 5 – peak power of pulse; 6, 7 – separate pulse energy; 1, 4, 6 – PQS was placed close to the rotary mirror; 2, 5, 7 – PQS was placed in the crossing point of the internal beams

Fig. 3 and 4 shows power and temporary parameters of Nd:YAG laser radiation depending on the total pump pulses energy at 30 Hz pulse–periodical pump and 58% PQS initial transmittance. The received data allowed us to define an optimum PQS position in the cavity. The highest peak power, energy of the separate pulses (fig. 3, a) and energy of pulse train (fig. 4, b) have been achieved in the scheme 2. Actually, at the moment of the $LiF:F_2^-$ crystal enlightenment the additional PSC–mirror (raising a total efficiency of the PSC regime in the dynamic generator) was raised that allows to improve the self–compensation of optical aberrations in AEs and reduce the diffraction losses. So, the generation efficiency was increased. Besides, $LiF:F_2^-$ crystal placement at the cavity center entails increase of interaction length of laser beams with PQS medium. It resulted in increase of the time of achievement of threshold population inversion in Aes and decrease of pulses repetition frequency and their quantity in series (fig. 4). This caused the generation of pulses with large peak power, energy of the separate pulses and pulse train (fig. 3) in comparison with the scheme 1. The pulse train energy in the scheme 2 was 1.82 J, the radiation average power – 55 W, and in the scheme 1 – 1.43 J and 43 W accordingly at the

maximal pump pulses energy of 127 J and PQS initial transmittance of 58 %. The generation efficiency in the scheme 2 grew by 12 %, and fall by 18 % in scheme 1 in comparison with the free generation regime.

The peak power of pulses (fig. 3, a), their quantity in train and period (fig. 4) was grew with increase of pump pulses energy. The peak power of a separate pulse in the scheme 2 achieves 4 MW at the maximum pump energy, that is in 2 and more times more than peak power of pulses in the scheme 1 made (1.6 MW). The growth of pulse peak power and their energy could be explained by the contribution of the hologram by F_2^- color centers in the LiF crystal at the compelled resonant dispersion to the diffraction efficiency of dynamic nonlinear mirror initially formed by refractive index gratings in AEs [9,10]. This resulted in increasing of the parametrical feedback in the dynamic generator, increase of PSC regime efficiency and hence increase of mode volume and increase of energy output in AEs.

The pulse duration within the error limits of measurements remained constant of 50±5nc and did not depend on the scheme (1 or 2), as well as on pump pulses energy. All pulses of the Q–switched radiation, which registered by high–speed oscilloscope C1–75 with the help of the avalanche photo diode LFD–2A, had a smooth temporary structure, that verified the single–mode single–frequency character of radiation [11].

The application of $LiF{:}F_2^-$ crystals under the scheme 2 for passive Q–switch of the Nd: YAG laser dynamic cavity has allowed to receive single–mode single–frequency radiation with beam quality $M^2 = 1.01$ and divergence $\theta = 0.34$ mrad (at a level of e^{-2}) at pump energy up to 127 J. The coherence length of laser radiation was determined with the help of Michelson interferometer. It was more than 18 m (oscillation spectrum width of 0.07 pm).
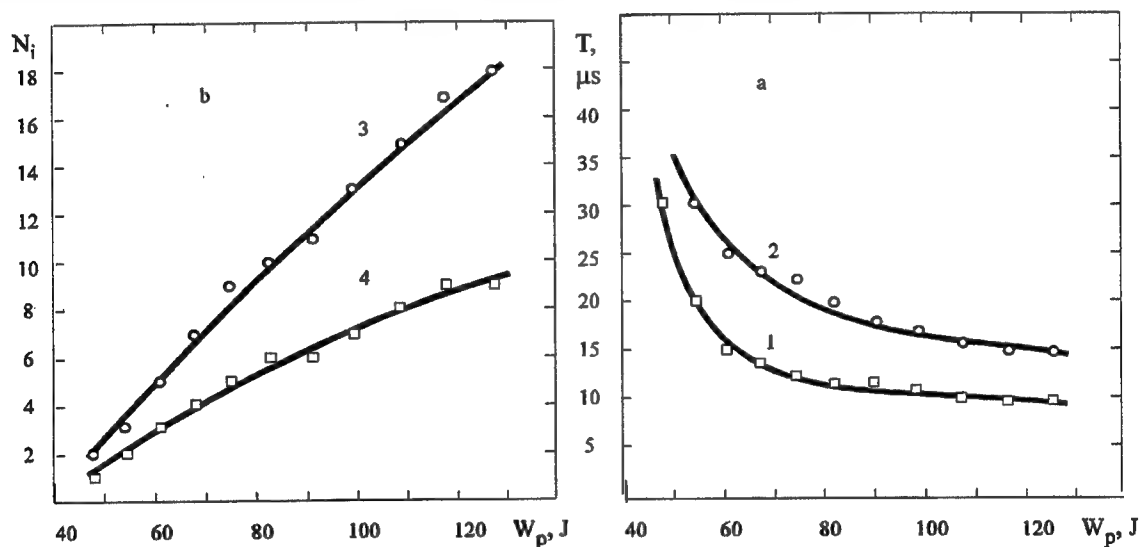
Fig.4. Dependencies of Nd: YAG laser radiation temporary parameters on pump pulse energy with 30 Hz frequency at 58 % PQS initial transmittance: 1, 2 – period of pulses occurrence in the train; 3, 4 – quantity of pulses in the train; 1, 3 – PQS was placed close to the rotary mirror; 2, 4 – PQS was placed in the intersection point of the generated beams

3. CONCLUSION

Thus, the given data testify the high efficiency of $LiF{:}F_2^-$ crystals for use as a passive Q–switch in powerful Nd:YAG lasers with dynamic cavity. It has allowed us to receive full aperture single–mode single–frequency radiation with beam quality close to unit at diffraction limited divergence and to output beam spatial brightness up to $3.8{\cdot}10^{14}$ W/sm^{2}sr. Our investigations open new potentialities of solid state lasers for applications in material processing, spectroscopy, microelectronics, medicine, science, etc.

4. ACKNOWLEDGEMENTS

5. REFERENCES

1. D. M. Roessler and M. G. Coady, "Laser systems in the *AUTOMOTIVE INDUSTRY*", Optics and Photonics News 7, p.17 1996.
2. M. J. Damzen, R. P. M. Green, G. J. Crofts, "Spatial characteristics of a laser oscillator formed by optically-written holographic gain grating", Optics Comm. 110, p.152, 1994.
3. M. J. Damzen, R. P. M. Green, and K. S. Syed, "Self-adaptive solid-state laser oscillator formed by dynamic gain-grating holograms", Optics Lett. 20, p.1704, 1995.
4. O. L. Antipov, S. I. Belyaev, A. S. Kuzhelev. "Phase conjugator of the light beams based on Nd:YAG–rod with the reciprocal feedback", OSA TOPS on Advanced Solid–State Lasers, 1, pp.411–416, 1996.
5 T. T. Basiev, A. N. Kravets, S. B. Mirov, A. V. Fedin. Patent of Russia N 1799526, 1992.
6, A. N. Kravets, T. T. Basiev, S. B. Mirov, A. V. Fedin. "Technological Nd–lasers with passive Q–switches based on crystal", SPIE, 1839, pp.2–11, 1991.
7. O.L. Antipov, A.S. Kuzhelev, A.P. Zinov'ev, V.A. Vorob'ev, "Pulse repetitive Nd:YAG laser with distributed feedback by self-induced population grating," Optics Communication, 152, issue 4-6, pp.313-318, 1998.
8. T. Zhang, L. Wan, Y. Ruan, "Nonlinear optical phase conjugate effect caused by F_2^- colour center in *LiF* crystals", Chines Phys. Lett., 2, pp.16-22, 1991.
9. O. L. Antipov, A. S. Kuzhelev, D. V. Chausov, "Nondegenerate four-wave mixing measurement of resonantly induced refractive index grating in Nd:YAG amplifier", Optics Lett., 23, p.448, 1998.
10. O. L. Antipov, S. I. Belyaev, A. S. Kuzhelev, A.P. Zinov'ev "Nd:YAG laser with cavity formed by population inversion gratings" SPIE proceeding (Edited by P. Galarneau and A.V. Kudryashov), 3267, paper 22, 1998.
11. V. V. Grabovskii, V. I. Prokhorenko, D. Ya. Yatskiv "Characteristics of single–frequency emission from a laser with a cavity based on a Sagnac interferometer." Quantum Electronics (in Russian), 22, pp.361–364, 1995.

Self-Adaptive Resonators

E. Rosas*, V. Aboites* and M. J. Damzen

The Blackett Laboratory, Imperial College,
London SW7 2BZ, UK

*Laboratorio de Láseres, Centro de Investigaciones en Óptica, A.C.,
Apdo. Postal 1-948, C.P. 37000, León, México

ABSTRACT

We present a spatial mode analysis of a self-adaptive holographic laser oscillator formed by a non-linear medium in a self-intersecting loop geometry incorporating additional intracavity elements and a feedback mirror acting as output coupler. We use an ABCD transfer matrix approach for cavity elements as well as the four-wave mixing in the nonlinear medium and demonstrate transient evolution as well as self-consistent steady-state solutions for the fundamental mode configuration. We find the transient case evolves to the self-consistent solution if one exists. We show the effects of intracavity lens focal length and position in cavity, as well as the finite transverse dimensions of the nonlinear medium, on the size of the self-consistent mode to find regimes for large mode size, good phase conjugate quality and low loss operation.
Keywords: Gaussian beams, holographic oscillators, optical phase conjugation.

1. INTRODUCTION

Almost since it was proposed in 1972,[1] the technique of optical phase conjugation, (OPC), has been used in order to correct for thermally-induced phase distortions in the gain medium, which cause degradation of beam quality and stability in conventional solid-state lasers.[2] OPC techniques have been incorporated in phase-conjugate resonators correcting dynamically for intracavity phase distortions and maintaining good output mode quality.[3] Such resonators have been constructed using photorefractive materials,[4] stimulated Brillouin scattering cells,[5] and absorbing/amplifying media.[6,7] In all these cases the resonator oscillation required input of an external beam or start-up cavities.

This work describes a transient and self-consistent analysis of the fundamental spatial mode of a self-adaptive holographic resonator[8] that is self-starting without requirement of external input beams or start-up cavities. Figure 1a shows a simplified version of the system formed by a nonlinear four-wave mixing (FWM) medium,[9] (in a self-intersecting loop geometry with interacting beams E_1 - E_4), an output coupler, an amplifier that allows the system to reach lasing threshold and possibly other intracavity elements. Much spatial mode analysis work has been performed on conventional stable/unstable resonators.[10,11] Work has also been done in phase-conjugate resonators,[12,13] however, consideration has normally been made of perfect phase conjugation or simulating the effect of spatially varying external writing beams by placing Gaussian apertures directly in front of the phase conjugation mirror (PCM).[14] A very recent work,[15] has dealt with the stationary case in a phase-conjugate resonator where the PCM is not externally prescribed by a writing beam but is self-forming from spontaneous noise,[8] which means that the spot size and radius of curvature (ROC) of the feedback beam and FWM pump beams are interdependent. In this work, we analyze the transient evolution of the fundamental mode (i.e. spatially Gaussian) of the self-adaptive resonator using the standard techniques for studying mode dynamics in conventional laser resonators, i.e. the complex q beam parameter[10] and ray transfer (ABCD) matrices,[11] and try to analyze a more general range of regimes of intracavity lens focal length and position in cavity and consideration of finite size of nonlinear medium. The primary motivation for this work was to understand the way to control the mode size of the system in order to design new adaptive laser oscillators (ALO) that exhibit a large mode size within the adaptive laser oscillator and therefore result in a high output energy due to greater utilization of the available gain volume in the amplifier together with good phase conjugation and low losses.

2. FOUR-WAVE MIXING INTERACTION AND ABCD RULE WITH GAUSSIAN BEAMS

In the FWM interaction represented in figure 1a, the electric fields of the interacting beams are written in the form:

$$E_j = \tfrac{1}{2}\tilde{A}_j \exp[i(\omega t - kz)] + c.c. \qquad j = 1..4 \qquad [1a]$$

$$\tilde{A}_j(r,z) \propto \exp[-ikr^2/2\tilde{q}_j(z)] \qquad [1b]$$

$$\frac{1}{q_j(z)} = \frac{1}{R_j(z)} - i\frac{\lambda}{\pi w_j^2(z)}$$ [1c]

where ω is the angular frequency, $k = 2\pi/\lambda$ is the magnitude of the wavevector with λ as the wavelength, the complex amplitude $\tilde{A}_j$ is taken to have a circularly-symmetric Gaussian variation as a function of the transverse radial coordinate r, q_j is the complex beam parameter for a beam with radius of curvature R_j and spot size w_j, and z is a distance in the direction of propagation. To calculate the form of the generated "conjugate" beam we use the standard result of a simple FWM interaction,[9]

$$\tilde{A}_4 \propto \tilde{A}_1 \tilde{A}_2 \tilde{A}_3^*$$ [2]

to obtain the following relations for complex q_j parameters at the FWM interaction region and its corresponding radii of curvature and spot sizes, respectively:

$$\frac{1}{q_4} = \frac{1}{q_1} + \frac{1}{q_2} - \frac{1}{q_3^*}$$ [3a]

$$\frac{1}{R_4} = \frac{1}{R_1} + \frac{1}{R_2} - \frac{1}{R_3}$$ [3b]

$$\frac{1}{w_4^2} = \frac{1}{w_1^2} + \frac{1}{w_2^2} + \frac{1}{w_3^2}.$$ [3c]

Perfect phase conjugation is achieved when $\tilde{A}_4 \propto \tilde{A}_3^*$,[5] which requires $q_4 = -q_3^*$, i.e. the spot size of A_4 is equal to the spot size of A_3 ($w_4 = w_3$), and the radius of curvature of A_4 is the reverse of A_3 ($R_4 = -R_3$). To achieve this condition requires the beams A_1 and A_2 to be large aperture waves compared to the probe beam A_3 ($w_1, w_2 \gg w_3$), and to have conjugate wavefronts or for beam A_3 to have a small radius of curvature ($R_3 \ll R_1, R_2$). However, in experiments A_1 and A_2 are finite Gaussian beams which, from equation (3c), produces a beam reduction ($w_4 < w_3$) and will result in an imperfect wavefront conjugation ($R_4 \neq -R_3$) since A_1 and A_2 will not have conjugate wavefronts.
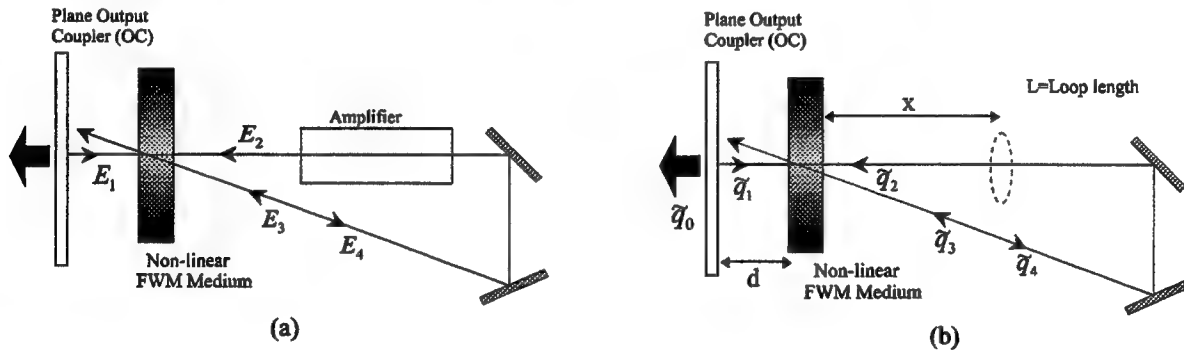
Figure 1. a) FWM interaction of beams E_1, E_2 and E_3 to produce the beam E_4 inside an adaptive laser resonator; and b) simplified schematic diagram of such an adaptive laser resonator, of loop length L and distance from the output coupler to the FWM interaction d. The 'dashed' elements represent additional (optional) optical elements.

When a Gaussian beam, initially described by the complex beam parameter q, propagates through an optical system composed of simple paraxial elements it is possible to calculate the new propagated value for the complex beam parameter (say q') by using the ABCD Rule which contains the whole of the paraxial ray optics:

$$q' = \frac{Aq + B}{Cq + D}$$ [4]

where A, B, C, and D are the elements of the total ABCD transfer matrix that is the result of the product of all the individual matrices representing each of the individual optical elements.[11]

3. SELF-CONSISTENT SOLUTIONS FOR THE EMPTY OSCILLATOR

In a recent work,[15] the self-consistency of Gaussian modes oscillating inside a self-adaptive holographic resonators was studied in the simplest case consisting of a plane output coupler, (OC), and a transversely infinite FWM medium in a self-intersecting geometry. We will summarize here the key results of this system which we will use as a *reference* for more complex cavity configurations that will be analyzed later. For this simple reference cavity it was found that there exist a self-consistent value for the complex beam parameter at the output coupler given by

$$\tilde{q}_R = L(2+i) \qquad [5a]$$

which corresponds to the self-consistent values for the output beam size (w_R) and the output beam radius of curvature (R_R):

$$w_R = \sqrt{(5L\lambda/\pi)} \qquad [5b]$$

$$R_R = 5L/2 \qquad [5c]$$

In this case it is clearly seen that the beam size from equation (5b) is finite and real for all values of cavity length L, indicating a stable cavity configuration and has a radius of curvature corresponding to a divergent output beam which does not match the curvature of the plane output coupler. For long cavity length L, the radius of curvature tends to match the plane output coupler and a large mode volume is produced. It may, however, be impractical to have a very long cavity due to space constraint and stringent alignment sensitivity. It is therefore necessary to look at more complex cavity scenarios to seek out regimes with larger mode size for a given fixed cavity length L.

4. THE LENS-IN-LOOP OSCILLATOR

We consider an oscillator that incorporates a lens in the loop, located just in front of the FWM medium (as might occur from a thermal-induced lensing in the FWM medium, for example), and for this case the self-consistent solution changes equation (5a) to

$$\tilde{q}_0 = L\left[2g + i\sqrt{(4g^2 - 4g^4 + 1)}/g\right] \qquad [6a]$$

It is informative to write the new self-consistent output solution as a ratio to the empty cavity values (with subscript R) for spot size and radius of curvature as:

$$w_0 = \frac{w_R}{\sqrt{5}}\left[\frac{(4g^2+1)^2}{g^2(4g^2-4g^4+1)}\right]^{\frac{1}{4}} \qquad [6b]$$

$$R_0 = \frac{R_R}{5}\left(\frac{4g^2+1}{g^3}\right) \qquad [6c]$$

where $g=1-L/f$ is a useful stability parameter. One feature of the result in equation (6b) is the existence of a range of confinement for the mode that defines whether the beam size is real (stable cavity) or imaginary (unstable cavity) according to the value of $4g^2-4g^4+1\geq0$. The other key feature is that there exists a range where the mode size is larger than the empty (reference) cavity mode size (w_R).

5. THE TRANSIENT DYNAMICS OF THE EMPTY ADAPTIVE LASER OSCILLATOR

The ABCD Rule of equation (4), together with the results of the preceding sections allow us to analyze the transient spatial mode dynamics of a self-starting ALO. At the beginning, we start with a simple ALO, which is shown in figure 1b. For this first case, the only optical elements are the OC and the self-pumped FWM mirror. The complex parameters, $\tilde{q}_j$ (j = 1 .. 4), of the four beams in the plane of the FWM medium, and the $\tilde{q}_0$ parameter at the output coupler (see fig. 1b) are given by boundary conditions including time-delay after each round-trip

$$\tilde{q}_0^{(n)} = \tilde{q}_2^{(n)} + d \qquad [7a]$$

$$\tilde{q}_1^{(n)} = \tilde{q}_0^{(n)} + d \qquad [7b]$$

$$\tilde{q}_3^{(n)} = \tilde{q}_1^{(n-1)} + L \qquad [7c]$$

$$\frac{1}{\tilde{q}_4^{(n)}} = \frac{1}{\tilde{q}_1^{(n)}} + \frac{1}{\tilde{q}_2^{(n)}} - \frac{1}{\tilde{q}_3^{*(n)}} \qquad [7d]$$

$$\tilde{q}_2^{(n+1)} = \tilde{q}_4^{(n)} + L \qquad \text{[7e]}$$

where d is the distance from the FWM cell to the plane OC (set to zero in this case), and L is the length of the loop and where the subscript n corresponds to the nth round-trip of the loop.

To initiate the system, we injection-seed the interaction with an initial $\tilde{q}_2^v$ value which is maintained at this value for the next two round-trips until the FWM process returns a new value of $\tilde{q}_2^n$ (n=2) via equation (7e). The initial $\tilde{q}_2^v$ sets $\tilde{q}_0$ and $\tilde{q}_1$ initially (via equations (7a) and (7b), respectively) but $\tilde{q}_3$ is undefined at n=0 until a round-trip delay later (n=1) via equation (7c). At that stage $\tilde{q}_4$ is then defined by equation (7d), and a further round-trip later $\tilde{q}_2^n$ (n=2) evolves to a new value via equation (7e). Subsequent evolution of the beam parameters is via successive iteration of equations (7a)–(7e).

We show in Figure 2 the transient evolution of the fundamental mode of the cavity, by iterating equations (7a)–(7e) with the considerations stated before. We find that although in all cases the value for the complex beam parameter at the output coupler $\tilde{q}_0$ tends to the self-consistent solution given by $\tilde{q}_R = L(2+i)$, they evolve in a different way dependent on the initial input; and also, perhaps not surprisingly, it is noticed that the closer the wavefront curvature and beam size is to the self-consistent solution, the fastest it converges to the self consistent value.

In the following sections, we show some results of the transient evolution analysis that we conducted for other more complex configurations of the ALO, finding convergence to self-consistent solutions if they existed.
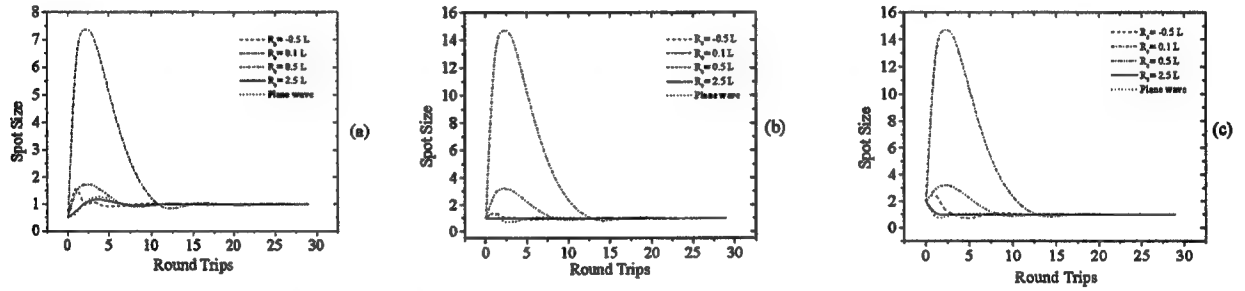
Figure 2. Transient evolution of fundamental modes with different initial radii of curvature and initial spot sizes of a) 0.5 of the reference, w_R, spot size, b) the reference value, and c) 2.0 of the reference value. The loop length, L, was taken as 1 m.

6. EFFECT OF THE LENS POSITION IN LOOP OSCILLATOR

In order to investigate mode control of the adaptive resonator and improvement in the quality of phase conjugation, the system (figure 1b) was modified to consider the incorporation of a lens in the loop located at different distances x from the FWM medium. At the same time, we keep $d=0$ (the OC placed in the position of the FWM medium). The new set of equations describing the propagation of the $\tilde{q}$ parameter around the system are given by (7a), (7b) and (7d) (with $d=0$) as before but with equations (7c) and (7e) replaced by

$$\tilde{q}_3^{(n)} = \frac{(1 - L/f + x/f)\tilde{q}_1^{(n-1)} + (L - Lx/f + x^2/f)}{(-1/f)\tilde{q}_1^{(n-1)} + (1 - x/f)} \qquad \text{[8a]}$$

$$\tilde{q}_2^{(n+1)} = \frac{(1 - x/f)\tilde{q}_4^{(n)} + (L - Lx/f + x^2/f)}{(-1/f)\tilde{q}_4^{(n)} + (1 - L/f + x/f)} \qquad \text{[8b]}$$

Figure 3 exhibits the effect of the lens position in loop on the stability ranges of the adaptive resonator. In this case we considered an adaptive resonator with loop length L, a lens inserted at the x'=x/L position, x being the distance along the loop measured from the FWM medium. For comparison we present in figure 3 the cases for the ALO with a lens located in front of the non-linear medium (x'=0); at mid-position in the loop (x'=0.5); and at three fourths of the loop path (x'=0.75). It is noticeable from figure 3 that the insertion of a lens in the loop enables us to control the size of the output mode as well as to produce a widening of the stability range and eventually suppression of the middle range singularity depicted in the x'=0 case (when the lens is located in front the FWM medium) by making the beam to be focused in the FWM medium, which can be seen in this same graph for x'=0.5 and x'=0.75 cases when L/f ratios of 2 and 4 are reached, respectively. We also notice from this graph that as the lens is separated from the nonlinear medium, an important reduction of the beam size is produced when the beam is focused half-way from the L-x distance, which means that the beam is expanding when it reaches the FWM material; this can be seen for x'=0.5 with L/f≈4 ; and for x'=0.75 with L/f≈5.35.
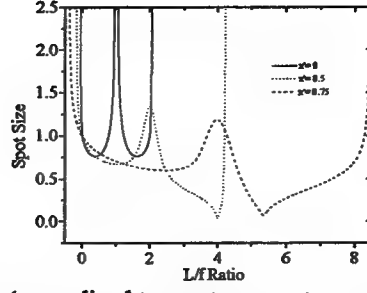
Figure 3. Variation of the output spot size (normalized to empty resonator spot size) as a function of L/f ratio. The three sets of curves correspond to the lens located at different normalized distances (x'=x/L) from the FWM medium.

7. THE FINITE TRANSVERSE SIZE EFFECT OF FWM MEDIUM

We finally study the effect of the lens position in the oscillator but also taking into account the finite transversal dimensions of the FWM medium by considering it as a Gaussian transmittance aperture with 1/e radius size equal to a. Under this new consideration, in order to describe the propagation of the $\tilde{q}$ parameter around the finite size FWM medium system, it is necessary to use equations (7a), (7b) and (7d) (with $d=0$) and modify (8a) and (8b) as follows:

$$\tilde{q}_3^{(n)} = \frac{A_T \; \tilde{q}_1^{(n-1)} + B_T}{C_T \; \tilde{q}_1^{(n-1)} + D_T} \qquad [9a]$$

$$\tilde{q}_2^{(n+1)} = \frac{D_T \; \tilde{q}_4^{(n)} + B_T}{C_T \; \tilde{q}_4^{(n)} + A_T} \qquad [9b]$$

where A_T, B_T, C_T and D_T are given by

$$A_T = \left(-i\lambda/\pi a^2\right)\left[x+(L-x)(1-x/f)\right]+(L-x)(-1/f)+1 \qquad [9c]$$

$$B_T = x+(L-x)(1-x/f) \qquad [9d]$$

$$C_T = -1/f+(2-L/f)\left(-i\lambda/\pi a^2\right)+\left[x+(L-x)(1-x/f)\right]\left(-i\lambda^2/\pi^2 a^4\right) \qquad [9e]$$

$$D_T = 1-x/f+\left(-i\lambda/\pi a^2\right)\left[x+(L-x)(1-x/f)\right] \qquad [9f]$$

Figures 4 and 5 show the intra-loop behavior of the Gaussian beam spot size as a function of the L/f parameter. In figure 4 we plot the behavior of the spot size for an ALO formed by FWM medium whose transversal radial dimension, a, is ten times that of the reference spot size value, w_R, for the loop length considered before; while figure 5 considers the case for $a/w_R=3$. Figures 4 and 5 exhibit the cases for x'=0, x=0.5 and x'=0.75. We now notice that the consideration of a finite size FWM medium together with the insertion of a mobile-lens in the loop of the ALO can lead to a good control of the size of the output mode as well as improve the phase conjugation process which means that $w_4 \approx w_3$ and $R_4 \approx R_3$. When a finite size FWM medium is considered, the output beam size tends to fit the size of the non-linear medium and the half stability range singularity disappears for the ALO where the lens is placed in front of the FWM medium.
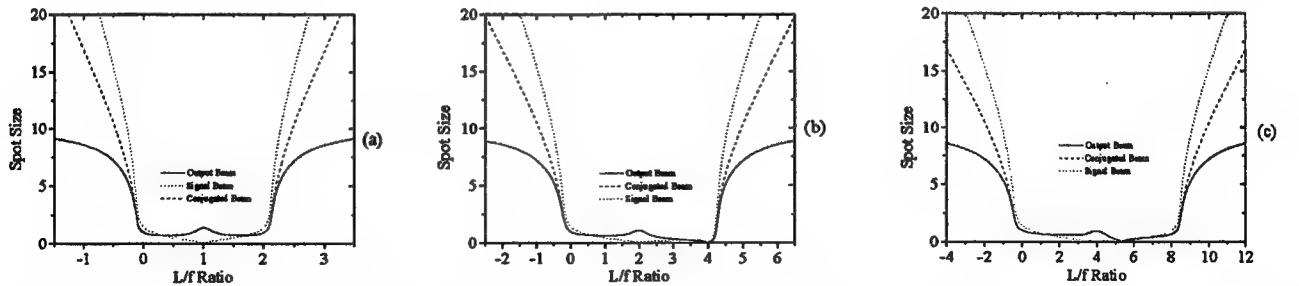
Figure 4. Spot size (normalized to empty resonator spot size) versus L/f ratio for an adaptive laser resonator whose FWM medium has a transversal radial dimension (a) of ten times reference spot size value (w_R). Different normalized lens locations (x'=x/L) are considered a) x'=0 (at FWM medium), b) x'=0.5 (at mid-point of loop) and c) x'=0.75.
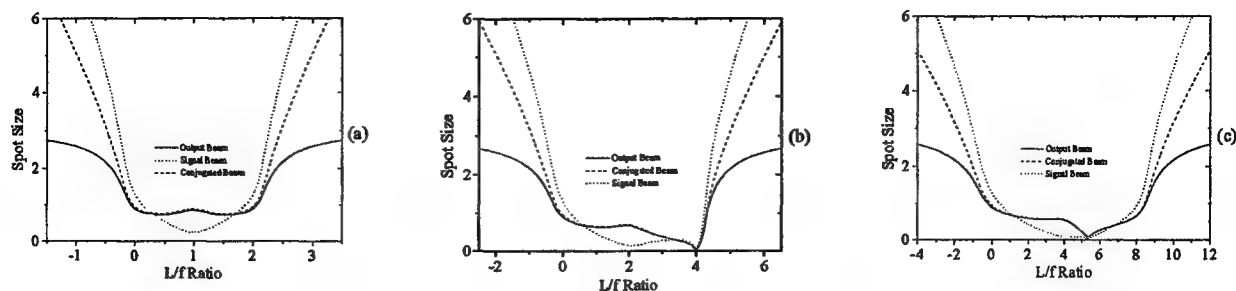
Figure 5. Same as Figure 4 but with a smaller FWM transversal radius (a) equal to 3 times reference empty cavity spot size (w_R).

8. CONCLUSION

As a conclusion we have studied the transient dynamics of fundamental spatial modes (i.e. Gaussian beams) in a self-adaptive holographic laser oscillator where the FWM medium is taken to have infinite transversal dimensions. We have demonstrated that fundamental spatial modes evolve to a self-consistent value when transient dynamics is considered. We have modified our initial system to consider a new ALO where a lens is located at several positions in the loop measured from the infinite FWM medium in order to study the effects of intracavity lens focal length and position in cavity on the spot size of output mode. We found that the insertion of a lens in the loop of the ALO enables us to control the output mode spot size. We finally have considered a finite size non-linear medium in the same last ALO configuration managing to remove the half stability range singularity presented for some lens in loop positions.

9. AKNOWLEDGMENTS

10. REFERENCES

1. B. Ya. Zel'dovich, V. I. Popvichev, V. V. Ragul'skii and F. S. Faizullov, "Connection between the Wavefronts of the Reflected and Exciting Light in Stimulated Mandel'shtam Brillouin Scattering", *JETP Lett.* **15**, 109-113 (1972).

2. W. Koechner, *Solid-State Laser Engineering*, Springer-Verlag, Berlin, 1992.

3. D. M. Pepper and Amnon Yariv, "Compensation for pase distortions in nonlinear media by phase conjugation", *Opt. Lett.* **5**, 59-60 (1980).

4. J. O. White, M. Cronin-Golomb, B. Fisher and A. Yariv, "Coherent Oscillation by Self-Induced Gratings in the Photorefractive Crystal BaTiO$_3$", *Appl. Phys. Lett.*, **40**, 450-452 (1982).

5. J. Auyeung, D. Fekete, D. M. Pepper and A. Yariv, "A theoretical and experimental investigation of the modes of optical resonators with phase-conjugate mirrors", *IEEE J. Quantum Electron.*, **QE-15**, 1180-1188 (1979).

6. P. Sillard, A. Brignon and J.-P Huignard, "Nd:YAG loop resonator with a Cr^{4+}:YAG self-pumped phase-conjugate mirror", *IEEE J. Quantum Electron.*, **QE-33**, 483 (1997).

7. I. M. Bel'dyugin, M. V. Zolotarev, S. E. Kireev and A. I. Odintsov, "Copper Vapor Laser with a Self-Pumped Wavefront Reversing Mirror", *Sov. J. Quantum Electron.*, **16**, 535-537 (1986).

8. M. J. Damzen, R. P. M. Green, and K. S. Syed, "Self-adaptive solid-state laser oscillator formed by dynamic gain-grating holograms", *Opt. Lett.* **20**, 1704-1706 (1995).

9. R. W. Hellwarth, "Generation of Time-Reversed wave fronts by nonlinear refraction", *J. Opt. Soc. Am.*, **67**, 1-3 (1977).

10. H. Kogelnik and T. Li, "Laser beams and resonators", *Appl. Optics* **5**, 1550-1567 (1966).

11. A. E. Siegman, "Unstable optical resonators" *Appl. Optics* **13**, 353-367 (1974).

12. M. G. Reznikov and A. I. Khizhnyak, "Properties of resonators with a wavefront-reversing mirror", *Sov. J. Quantum Electron.* **10**, 633-634 (1980).

13. J. F. Lam and W. P. Brown, "Optical resonators with phase-conjugate mirrors", *Opt. Lett.*, **5**, 61-63 (1980).

14. A. Yariv and P. Yeh, "Confinement and stability in optical resonators employing mirrors with Gaussian reflectivity tapers", *Opt. Comm.* **13**, 370-374 (1975).

15. D. Udaiyan, G. J. Crofts, T. Omatsu and M. J. Damzen, J. "Self-consistent spatial mode analysis of self-adaptive laser oscillators", *Opt. Soc. Am. B*, **15**, 1346-1352 (1998).

Phase conjugation of speckle-radiation from pulse-periodic YAG:Nd oscillator with holographic mirror.

V.V.Yarovoy

Institute of Applied Physics , Russian Academy of Sciences
46,Ulyanov str., 603600 Nizhny Novgorod, Russia

ABSTRACT

The role of a small-scale diffraction in resonator with holographic mirror for providing the effective selection of wave conjugated to operating speckled wave has been investigated theoretically and experimentally. Possibility of high fidelity reconstruction of complicated amplitude-phase information on spatial structure of signal radiation in the zero mode of the "holographic" resonator have been studied in the parametric space singularity satisfying the geometric-optical approximation. The reasons for some disagreement between the model conclusions and experimental data obtained in the YAG:Nd-laser with hologram of gain saturation have been discussed.

Keywords: phase-conjugation, dynamic hologram, speckle-beam, gain gratings.

1. INTRODUCTION.

Optical oscillator with holographic mirror[1] formed by external signal wave $E_1 - E_3$ (Fig.1) is considered to be one of the effective PC-correctors being used in different laser systems. The growth of interest in PC correctors of this kind is connected partly with advancement in the range of greatly high average powers of laser radiation in the diode-pumped solid-state systems (for example, in YAG:Nd systems). The cause is that, under the use of gain saturation nonlinearity[2,3] for hologram recording, distorting thermal influence of both laser radiation (because of heating on the "defect of quantum" [4]) and diode-pumping radiation on the hologram is not very large.
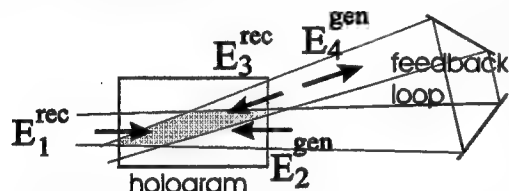
Fig.1.Optical oscillator with holographic mirror operated by external signal wave E_1-E_3.

Fig.2.The case of unsupported "short" hologram recorded by two speckle-waves.
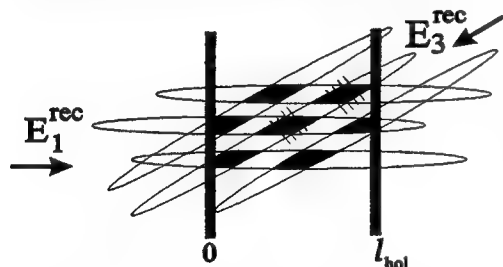
Another reason for all increasing interest in the PC-scheme is that it proves to be effective for PC of not only smooth laser beams but also of multimode and especially speckle-beams.[3,5] The latter formulation of problem is vital when one needs to reconstruct information about object wave distorted by transmission function of some random transporting medium (for instance, of multimode fiber). In this case one has to deal with the hologram recorded by two waves both of them being speckled ones. This situation is much different from the recording of the hologram by smooth beams. First of all, the traditional holography (Gabor's holography), based on principle of "supporting" (when one of the two recording waves is considered to be plane wave against the background of other, that is

$$I_1 E_3^* = constE_3^*$$

), turns out to be practically unacceptable. To satisfy the principle, it would be necessary to focus the wave E_3 in the size of a speckle-nonhomoneity of wave E_1,

but the corresponding aperture loss of the generation wave $E_2 \sim E_1^*$ on such output holographic mirror would be very considerable to realize the generation practically in this resonator.

Therefore, it needs to use in this case an "unsupported" holography. So, selective capacity of the "unsupported" hologram, concerning the separation of a conjugated component in the generation wave from noises, was originally

connected with providing of the diffractive mixing of speckles of the recording waves in the volume of a "long" hologram[6] whose length l_{hol} was much longer than those of longitudinal correlation $z_{cor1,3}$ $(z_{cor}=k\rho^2$, where ρ is radius of transverse correlation of recording speckled wave), so that $N_1 = l_{hol} / \sqrt{z_{cor1}z_{cor3}} >> 1$. Evident advantage of this hologram is that it guaranties the PC-regime in the scheme independently of the resonator features. However, there are, as a rule, certain difficulties in practical realization of this diffractive approximation. In particular, when the hologram is recorded, using the gain saturation nonlinearity, its length is limited by length of an laser rod. Therefore, to satisfy the $N_1 >> 1$ it is necessary to provide either sharp focusing of the recording beams in the nonlinear media or supplementary "speckling" of the input recording wave E_1. The former is limited by breakdown of the active element (in Q- switch regime), the latter can make it difficult guiding without aperture losses of the recording beam E_3 along the feedback loop of the optical system.

Thus, the selective capacity of "unsupported" hologram satisfying the geometrical optics approximation ($N_1 < 1$) was studied and demonstrated later[7]: providing of good mutual "geometrical mixing" of speckles of the recording beams in hologram volume is quite sufficient to give start to the selective mechanisms in such hologram (Fig.2), that is $N_2= l_{hol}/b >>1$, where $b=\rho/sin\varphi$, φ is the angle of convergence of recording waves E_1 and E_3.

In this paper, the idea of the unsupported "geometric-optical" holography, which has obvious practical advantages comparing with the diffractive case (which requires $N_1 >> 1$), further develops, since there are a number of important questions which must be cleared up. In particular, the "short" hologram ($N_1 < 1$) seems to be not selective when dealing with the waves of the $E_2 \sim F(x)E_1^*$ type, where $F(x)$ is the smooth and one-dimensional along $x_0 = \dfrac{\left[\mathbf{k_1 k_3}\right]}{\left[\left|\mathbf{k_1 k_3}\right|\right]}$ complex function: in another words, some of these waves are able to be reflected from the hologram as well as conjugated wave itself $E_{2c} \sim E_1^*$. So, it is necessary to make clear the role of optical resonator in discriminating these waves. In particular, is it necessary to compensate the absence of diffractive effects in hologram (when $N_1 < 1$ but $N_2 >> 1$) by providing the diffractive mixing of the recording speckle-waves in the feedback loop of resonator(when $N_3 = L_{eff.r} / z_{cor} >> 1$, where $L_{eff.r}$ is effective length of resonator)? Or, perhaps, are there other reasons which may provide PC-regime only within geometric-optical model and, therefore, determine selective mechanisms which have more universal character for this scheme than diffractive one? To answer these questions the analysis of average spatial parameters of base mode depending on parameters of resonator for double-Gaussian input speckled beam was carried out. It is surprising that the scheme has been revealed to avoid losing the selective capacity (respecting to the selection of the conjugated component) in the peculiar point of parametric space, which satisfied the geometry-optical approximation (when $N_3 = 0$).

2. SELECTION OF PHASE-CONJUGATED WAVE IN GEOMETRIC-OPTICAL RESONATOR WITH "SHORT" SELECTIVE HOLOGRAM

It was pointed out in a number of works[8,9], which were devoted to peculiarities of modes formed in the resonator with the unsupported hologram, that the small-scale diffraction (both in hologram and in the feedback loop of resonator) must play decisive role in providing of the effective selection of the conjugated component in the mode wave. This conclusion was made, in particular, on the ground of analysis of the solution for the zero-mode in geometric-optical resonator with transporting of the recording wave E_1 image to the recording wave E_3 by an lens system, so that

$$E_3(\mathbf{r}) = \hat{G}_{res}^+(E_1(\mathbf{r})) = M \; E_1(M\mathbf{r})e^{-i\phi_r^+(\mathbf{r})}$$

$$E_2(\mathbf{r}) = \hat{G}_{res}^-(E_4(\mathbf{r})) = M^{-1}E_4(\mathbf{r}/M)e^{-i\phi_r^-(\mathbf{r})} \qquad (1),$$

where $M = a_1 / a_3$ is the scaling factor, ϕ_r^+, ϕ_r^- ($\phi_r^+(r/M) = \phi_r^-(r)$) are the regular phases involved in image by resonator lens system. The zero-mode in such resonator with unsupported geometric-optical hologram, having the reflectivity $\hat{R} = \zeta E_1 E_3^*$ (so that $E_4(\mathbf{r}) = \hat{R} \bullet E_2(\mathbf{r})$ has the form[9]:

$$E_4(\mathbf{r}) = const E_3^*(\mathbf{r}) \prod_{i=0}^{\infty} \left| E_1(\mathbf{r}/M^i) \right|^2 \qquad (2)$$

Therefore, calculation of the mode wave projection on the conjugated wave E_3^* in accordance with the expression

$$\chi = \frac{\left| \int E_4 E_3 d^2\mathbf{r} \right|^2}{\int E_3 E_3^* d^2\mathbf{r} \int E_4 E_4^* d^2\mathbf{r}} \qquad (3)$$

gave the following estimation (when $\nu = 1/M^2 < 1$)

$$\chi \approx \frac{1-\nu^2}{2^{m_{max}}} \qquad (4).$$

The m_{max} is actually limited by the $m_{max} \approx \mathrm{int}\left\{ \ln(a_1/\rho_1)/\ln(M) \right\}$ taking into account that the terms $\left| E_1(\mathbf{r}/M^i) \right|^2_{(i > m_{max})}$ in (2) are approximately constants on the E_3 diameter. When obtaining (4) it was also taken into consideration[9] that the projection χ is approximately equal to average projection $\overline{\chi}$ in statistical ensemble of the input wave E_1 realizations having the same transverse correlation function $< E_1(r_1)E_1^*(r_2) >$.

Moreover, it was supposed that statistics in the ensemble were normal ones, the functions $I_1(\mathbf{r}/M^i)$ with different i were noncorrelated between each other on speckle scale, and the magnitudes of integrals in the (3) for each realization of the wave E_1 were approximately equal to those averaged in statistic ensemble. The latter supposition is true due to the ergoditic hypothesis which is true when functions under integrals have a lot of phase-independent nonhomoneities (speckles) on the integration area.

Therefore, if only the focusing of the beam E_3 to the size of a speckle of the beam E_1 does not take place (when $m_{max} = 0$) that would correspond to approximation of the supported Gabor's holography, the quota of conjugated component χ in the zero-mode for the unsupported (when $m_{max} \gg 1$) geometric-optical hologram has the small magnitude due to (4).

However, the mentioned above geometric-optical hologram, as it was shown later[7], is a degenerated case of more general solution for the hologram, which also satisfies the nondiffractive approximation and has the following operator $\hat{R}$:

$$E_4(\mathbf{r}) = \hat{R}[E_2] = \gamma E_3^*(\mathbf{r}) \int\limits_0^{l_h} [E_2(\mathbf{r}')]E_1(\mathbf{r}')dz \tag{5},$$

where $\mathbf{r}' = x'\mathbf{x_0}' + y'\mathbf{y_0}' = (x\cos\varphi + z\sin\varphi)\mathbf{x_0}' + y\mathbf{y_0}'$, E_i -distributions of complex amplitudes in cross-section which are orthogonal to propagation directions of corresponding waves, φ is the convergence angle of the recording waves E_1 and E_3.

This form for the $\hat{R}$ results from the equation

$$\frac{\partial E_4(\mathbf{r})}{\partial z} + \frac{i}{2k}\Delta_\perp E_4(\mathbf{r}) + \beta E_4(\mathbf{r}) = \gamma E_3^* E_1 E_2,$$

which describes the growth of weak wave E_4, which is born at scattering the wave E_2 ($E_4 \ll E_2$) on the volume gratings of hologram nonsaturated by recording waves E_1 and E_3. The term $\beta E_4(\mathbf{r})$ is responsible for change of the wave E_4 amplitude along z due to own amplification (or absorption) of holographic nonlinear medium. To simplify the consideration, the term may be omitted, since it leads only to substitution of real length of holographic medium on an effective hologram length $l_{eff.hol}$.[3]

Thus, neglect of the second diffractive term in the left part of the equation (because of $N_1 \ll 1$) results in (5).

So, taking into account the (5) and (1) ($E_2(\mathbf{r}') = \hat{G}_{res}^-(E_4(\mathbf{r}))$), the solution for the zero-mode is modified as

$$E_4 = constE_3^*(\mathbf{r}) \prod_{i=0}^{m_{max}} \int\limits_0^{l_{hol}} I_1\left\{\mathbf{r}'_{(i)}(\mathbf{r}/M^i, z_{(i)})\right\}dz_{(i)} \tag{6}.$$

Then, the analogous calculation for the χ under similar suppositions gives the following estimation

$$\chi \approx \frac{1 - v^2}{(1+g)^{m_{max}}} \tag{7},$$

where $g \approx \left(\frac{b}{l}\right)\left\{\sqrt{\pi}erf(l/b) - \left(\frac{b}{l}\right)\left[1 - \exp\left(-(l/b)^2\right)\right]\right\}$, $b = \frac{\rho_1}{\sqrt{2}\sin(\varphi)}$, $erf(x) = \frac{2}{\sqrt{\pi}}\int\limits_0^x \exp\left(-y^2\right)dy$.[7]

The well-known model of a twice-Gaussian recording beam with the following transverse correlation function

$$<E_1(r_1)E_1^*(r_2)> = \bar{I}_1(0)\exp\left(-\frac{R^2}{a_1^2} - \frac{(\delta r)^2}{\rho_1^2} - i\varepsilon R\delta r\right) \quad (R = \frac{r_1 + r_2}{2}, dr = r_1 - r_2)$$

was used in the calculations, too.

At the $N_2 = l_{hol}/b < 1$ the expression (7) is reduced to (4) because of the $g \approx 1$. On the contrary, when $N_2 = l_{hol}/b \gg 1$ and taking into account that $\sin\varphi_{max} \approx a_1/l_{hol}$, the g is the small parameter: $g \approx \sqrt{\pi/2}\delta$, where $\delta = \rho_1/a_1 \ll 1$. The expanding of the χ in a power series of the δ and the neglecting the terms above the second order gives the following estimation:

$$\chi = (1 - M^{-4})(1 + \sqrt{\pi/2}\frac{\ln\delta}{\ln(M)}\delta) \tag{8}$$

So, if the sufficient narrowing of the beam E_3 takes place ($\nu \ll 1$, in fact, $\nu \le 0.5$ is sufficient) and if the input beam E_1 has well-developed speckle-structure ($\delta \ll 1$), the scheme provides good selection of conjugated wave even when diffractive mechanisms are suppressed here (when $N_1 \ll 1$ and $L_{ef.res} = 0$). The theoretical dependencies of PC-fidelity χ on the parameters δ and ν are given on the Fig.3.

Let us make clear the received result (7-8). Parameter g has the following physical meaning, which was also in detail concidered earlier[7]. After falling on the hologram the wave $E_2 \sim E_1^*$, the reflected wave

$$E_4 = \gamma E_3^* \int_0^{l_h} I_1 dz$$ may be expressed as sum of two virtual waves which are correlated and noncorrelated (in average) to the E_3^*:

$$E_4 = E_{4c} + E_{4n} = \gamma t_{hol} \bar{I}_1 E_3^* + E_{4n},$$ where

$$< E_{4n} E_3 > \equiv 0.$$

Fig.3. Theoretical dependence of PC-fidelity on the degree of "geometrical mixing" of recording waves speckles in short hologram for different parameters of scaling M and speckling d.

It is necessary also to say here that the projection of the E_{4n} on the E_3^* in each realizations of statistic ensemble also has the small value due to ergoditic principle $\int E_{4n} E_3 d^2\mathbf{r} \approx \left\langle \int E_{4n} E_3 d^2\mathbf{r} \right\rangle \approx 0$.

Thus, the following parameters $\mathcal{R}_{cc}$ and $\mathcal{R}_{cn}$ may be introduced, where $\mathcal{R}_{cc} = \int I_{4c} d^2\mathbf{r} / \int I_{2c} d^2\mathbf{r}$, $\mathcal{R}_{cn} = \int I_{4n} d^2\mathbf{r} / \int I_{2c} d^2\mathbf{r}$ are reflectivities of the conjugated wave $E_2 \sim E_1^*$ in conjugated and nonconjugated components of wave E_4, correspondingly. Under this interpretation parameter g is ratio $\mathcal{R}_{cn} / \mathcal{R}_{cc}$.

Therefore, the selective function of "short" hologram in the above case ($N_2 \gg 1$) consists in essential reduction of the noise E_{4n}, the reason for which is the conjugated wave $E_2 \sim E_1^*$ itself. However, despite the small quota ($g \ll 1$) of that own noise appearing after each act of reflecting of the conjugated component from the unsupported hologram, the general quota of the noises is increasing fast with the growth of round trips number m, which provides the nonstationary phase of establishing the mode in the resonator and which is just limited by the m_{max}. Thus, the accumulation of the own noises in the mode and, consequently, the change of their relative quota occurs only during the nonstationary phase of mode establishment.

In fact, the estimation (7) must be considered as lowest one for the χ. It is connected with the fact that there is an intermediate range $m_{ef}(M,\delta) < i < m_{max}(M,\delta)$ within which the ground of power function in the denominator of the (7) is changed smoothly from the $(1 + g)$ to 1.
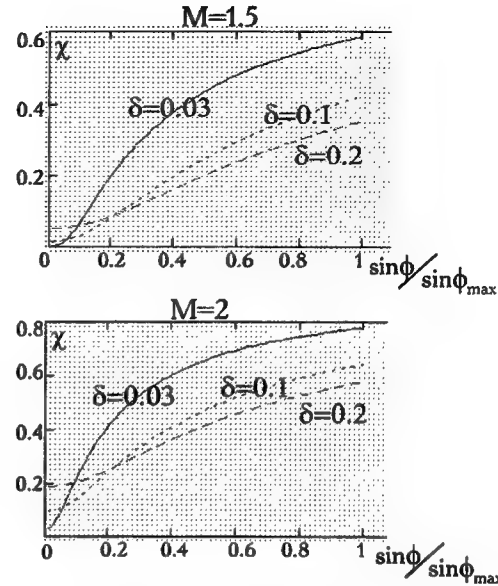
So, the above analysis gives possibility to specify the mechanisms which are responsible for the spatial structure capturing of mode wave by signal wave, when there is no diffraction in the scheme. The resonator and the hologram play joint and mutually complementary roles in supplying these mechanisms:

-first of all, the resonator together with "short" selective hologram ($N_1 \ll 1$, but $N_2 \gg 1$) guarantees the absolute convergence to the mode solution (6) independently on the initial spatial distribution in primary wave in the resonator. It means, in particular, that resonator does not allow the solutions of the following type

$$E_4 = F(\mathbf{r})E_3^* + E_{4n}, (< E_{4n}E_3 > = 0),$$

where $\int FI_3 d^2\mathbf{r} = 0$ and, therefore, $\int E_4 E_3 d^2\mathbf{r} \approx \left\langle \int E_4 E_3 d^2\mathbf{r} \right\rangle \approx 0$. The similar spatial structures are forbidden in the resonator since all of them do not satisfy the requirement of spatial resonance, which is necessary condition for mode solution, except for the case when

$$F(\mathbf{r}) = \prod_{i=0}^{\infty} \bar{I}_1(\mathbf{r} / M^i) > 0 \text{ (that is } \int FI_3 d^2\mathbf{r} > 0\text{)};$$

-second reason, connected partly with the first, is that nonconjugated (or noise) component in the zero-mode originates only from conjugated wave itself, as result of partial or distorted reconstruction of information on the wave E_3^* in the reflected wave E_4. Therefore, the relative quota of the own noises in this mode depends both on the quota of noise appearing after each act of reflecting of the conjugated component E_1^* during the nonstationary phase of establishing the mode solution and on the duration of this phase, when the accumulation of these noises occurs. That is why, the general quota of noise in zero-mode may be effectively minimized by means of hologram itself because of $\mathcal{R}_{cn} / \mathcal{R}_{cc} \ll 1$ as well as due to the necessary curtailing the nonstationary phase $m_{max}(M)$ in development of the mode wave.

There is nothing to be changed in the scheme basically after supplementary introduction of the diffraction in the feedback loop ($L_{eff.res} \neq 0$): the above statements remain the same. The influence of the diffraction leads only to faster rate of establishing of mode wave in the resonator and to the corresponding reduction of the general noise. In this case $\chi = 1 - g$.[7]

3. EXPERIMENT

3.1. Setup.

The scheme of the experimental setup is shown in Fig.4. The input speckle-wave E_1 (Fig.5.b) in the manner of Q-switch spectral-limited pulse with duration of 30 ns together with the wave E_3, in which the wave E_1 is transformed as a result of the passing along the feedback loop, records a hologram of inverted popularity in the YAG:Nd-amplifier 2 ($\varnothing 8 \div 100mm$). Polarizers 3 and 5 are nearly self-crossed, so that the recording signal wave is first greatly weakened after 5 and then, after passing the amplifiers 6, is transformed into the wave E_3, whose energy density equals approximately to the one of the wave E_1. The optical "diode" 7 (Faraday cell) provides unidirectional regime of the generation in the ring resonator. Having formed the resonator due to the holographic mirror recording, the generator is below the

Fig.4. The scheme of the experimental setup: 1-random phase plate; 2-holographic YAG:Nd amplifier; 3,5,12-Glan polarizers; 4-Pockels cell; 6-YAG:Nd-amplifiers; 7- Faraday cell; 8-lenses; 9,10-measurers of laser energy; 11-Faraday rotator.

75

generation threshold just because of the presence of self-crossed polarizers 3 and 5, in spite of the fact that the total amplification in feedback loop is approximately equal to 10^5. The opening of the resonator for generation is realized via operated delay $(1 \div 100$ *msec*) by means of electrooptical Pockels cells 4. The use of the delay unit (3,4,5) excludes any influence on mode forming process on the part of possible parasitic "seeds" from random scattering of the signal recording wave on the defects within the optical system of the resonator. Lenses 8 provide guiding without aperture losses of the recording beam and, when necessary, the transporting the image from the zero diffractive order of the hologram to its first order through the feedback loop of the resonator.

The output generation wave has linear polarization which is orthogonal to one of the E_1.

The random phase plates 1, used in the experiments for speckling of the signal wave E_1, had divergences Θ (Θ is the half-width on level e^{-1} of maximum), which were equal (in radian) to $\sim 10^{-3}$ and 2.5×10^{-3}. At the radius $a_0 = 1.5mm$ of the Gaussian beam E_0 on the phase plate entrance, the corresponding parameters

$$\delta = \rho_1 / a_1 = \frac{\Theta_{dif}}{\Theta} = \frac{2}{ka_0 \Theta}$$ were approximately equal to 1/5 and 1/12. The parameter N_1 is defined as

$$N_1 = \frac{l_{eff.hol}}{\sqrt{z_{cor1} z_{cor3}}} = \frac{l_{eff.hol} M}{z_{cor1}}, \qquad \text{where} \qquad z_{cor1} = n_{YAG} k_0 a_1^2 \delta^2 \ (n_{YAG} \approx 1.8, \qquad k_0 = \frac{2\pi}{1.06 \mu m});$$

$l_{eff.hol} \approx l_{rod} f(gl_{rod})$; $\exp(gl_{rod}) \approx 10$ is nonsaturated gain of the holographic active medium; $f(x)$ is the factor, conditioned by amplification of the recording waves E_1 and E_3 in the hologram. In particular, for weak saturation of the holographic active medium by the recording waves and for counter-geometry of these waves convergence[3], the factor $f(x)$ is equal to $\dfrac{2(\exp(x) - 1)^2}{x(\exp(2x) - 1)} \approx 0.7$. Therefore, when the amplifier 2 has length l_{rod} of 10 cm and with radius a_1 being equal 2.5 mm, the hologram corresponds to the approximation of the "short" (nondiffractive) hologram: for maximum $M \approx 2$ in the experiments, N_1 is equal to 0.05 (for $\delta \approx 1/5$) and to 0.3 (for $\delta \approx 1/12$).

The measurement of the relative quota of the conjugated component χ was provided by calorimetric measurers of laser energy 9 and 10. The measurer 9 in the near-zone measured the full energy of the generation wave, the measurer 10 in the far-zone ($\sim$10 m) registered only the energy of the conjugated component.

3.2. Results.

According to (7) the relative quota of the conjugated component χ in the mode wave in the neighborhood of the parametric space singularity, satisfying the geometric-optical approximation, depends both on the scale parameter M and on the degree δ of "speckling" of the input wave E_1. That is why the measurement of the χ was carried out in the experiments with resonator, transporting the image, for three different parameters M (0.7, 1.4 and 2) and for signal speckle-waves E_1 with two different δ (1/5 and 1/12). The experimental data and corresponding theoretical estimations are given in Table 1.

When the M was equal to 0.7 the generation wave with conjugated component was not registered in the scheme. This is in accordance with theoretical expectation, because the mode (6) comprising the nonzero conjugated component must not exist in the geometric-optical resonator if $M < 1$.

Somewhat higher values for the χ, when $M = 1.4$, are explained by above mentioned fact that estimation (7) appears really to be lowest one for the χ.

Considerable disagreement between the experiment and the theory, when $M = 2$, has apparently more principal reason. To explain this properly, it is necessary to appeal to other facts revealed in the experiments.

As a matter of fact, the generation threshold in the YAG:Nd scheme with holographic mirror turns out to be very close to the threshold of self-excitation of a loop scheme which is the same optical system except for the

Table1.

δ \ M	0.7	1.4	2	
1/5	0	0.3	0.6	χ_{theory}
	0	0.5±0.05	0.4±0.05	$\chi_{exper.}$
1/12	0	0.37	0.7	
	0	0.42±0.04	0.45±0.05	

Table1. The dependence of relative quota of conjugated component χ in generation wave on parameters of scaling M and recording wave speckling δ: χ_{theory} is quota estimated according to theoretical model; $\chi_{exper.}$ is quota measured in experiment.

hologram recorded by external signal wave. The possible explanation to the proximity of these thresholds is that the self-excitation also occurs on gain gratings, which are self-started in the amplifier 2, where optical axis of the loop system is self-crossed. It is likely that the gratings are formed initially by a weak noise radiation of some parasitic linear resonator which may occur even on slight defects of active rods under such a large amplification inside the loop. The possibility of such mechanisms in similar loop schemes based on the YAG:Nd active medium was mentioned, for example, in [2].

Therefore, after switching the Pockels cell 4, the scheme is opened for the generation of mode wave (6), which occurs on the gain saturation hologram, which has already been recorded by the signal wave E_1-E_3, as well as for the parasitic generation of self-excitation happening on self-started, supplementary gain gratings. Such joint development of "useful" mode wave (6) and of the "parasitic" wave of the self-excitation in the ring resonator may lead to their independent, additive contribution in the output radiation, as well as to the competitive effects which are able to reveal themselves during the nonlinear phase of the holographic active medium saturation by these waves. In particular, considerable nonstability of the generation wave energy in the series consisting of the 20-30 shots was observed. It took place in spite of the fixed parameters of resonator and hologram, such as M, φ, δ, and for rather stable energy, temporal, spatial and spectral properties of signal wave E_1. This energy nonstability, which was about 50-60% of average energy, may serve as an argument of the competition existence, though the physical mechanisms of this presumed competition have not been clear in detail and, therefore, should be a subject of individual consideration. Besides, it is surprising that contrary to the above-mentioned energy nonstability in the output radiation, the relative quota of the conjugated component χ, as well as the energy of self-excitation radiation measured in the loop scheme when there was no signal wave, were stable enough. Their nonstabilities were about 5% within each series of the kind.

Thus, the ratio of the thresholds of mode wave and self-exiting wave and, consequently, the relative contribution of these waves to the output radiation depends, in particular, on the scale parameter M. It is true, because the larger narrowing the beam E_3, the bigger the aperture loss on the holographic mirror and the higher, therefore, the generation threshold for mode wave (6). But at the same time the threshold for the parasitic generation remains unchangeable since it is not bound to the hologram aperture. So, when M was equal to 1.4, the energy of self-excitation measured in the loop scheme (signal wave E_1 was absent) made up only 10-15% of the full energy of the holographic generator output radiation (when signal wave E_1 was present). On the contrary, when M was equal to 2, the former was about 40-50% of the latter, giving considerable supplementary contribution to nonconjugated component of holographic generator output radiation and explaining satisfactorily the above-mentioned disagreement between the experiment and the theory.

The spatial structures of the recording and generation beams are shown in Fig.5. The maximum energy of generation wave of 25 mJ was achieved at the input signal energy of 5 mJ (for M~1.4).

It should be mentioned too that the diffractive mixing additionally in the feedback loop, when parameter N_3 exceeded 1, resulted in the growth of PC quality up to 75%.

The frequency of pulse repetition in the experiment was varied from 1 to 30 Hz. The preliminary experiment has shown that output radiation average power increased proportionally to the pulse repetition frequency and significant deterioration in the spatial structure of the output wave was not revealed, comparing with the single-pulse regime.
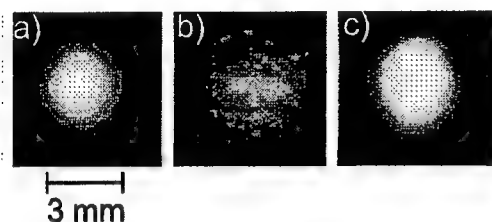

3 mm

Fig.5. The space structures of radiation- of the master oscillator E_0 (a); of the recording speckle-wave E_1 in the nonlinear medium (b); of the generation wave E_g (c) in far zone (~10m), after passing the phase plate1.

It is necessary to note in conclusion that assumptions about temporal steadiness of hologram and about its operator $\hat{R}$ independence on the generation wave parameters limit the set of possible generation regimes in the oscillator, which satisfy the above assumptions. Taking into account back influence of generation wave on the hologram is necessary, for example, for permanent generation regime. It is more important when dealing with hologram of gain saturation, since under conditions of saturation parameters identity of loop amplifiers and holographic medium, the generation wave always saturates the hologram. However, the Q-switch regime with generation of short giant pulse, realized in the holographic resonator, is quite adequate to the adopted model. Indeed, in the above regime the mode forming occurs during rather long linear phase (which is, however, much less than life-time of gain gratings) when the above back influence may be neglected. Nonhomogeneous saturation of hologram by generation wave during short nonlinear phase limits mostly the energy of output radiation, not affecting considerably the formed distribution in the mode wave.

4. CONCLUSIONS.

The above analysis has shown that "diffractive mixing" of recording speckle-waves in the hologram volume and in the feedback loop of the ring holographic resonator, being a desirable condition though, is not a necessary requirement of the above capture-regime. The absence of the diffractive mechanisms of conjugated component selection is compensated entirely by mutual acting of the hologram and resonator, which satisfy the geometric-optical approximation. On the one hand, due to the requirement of spatial resonance for mode solution, the holographic resonator does not support those spatial structures, in case of which the short hologram ($N_1 \ll 1, N_2 \gg 1$) appears to be not selective. On the other hand, the noise of the zero mode, which is always

produced after reflecting of exactly conjugated wave E_1^* from the unsupported hologram, is reduced effectively too, when $N_2 \gg 1$ and when the nonstationary phase of mode establishment m_{max} is short enough. It occurs as the result of recovery of the "quasi-supporting" in the hologram due to providing of the good mutual "geometric" mixing of recording speckle-waves in its volume, as well as under condition of sufficient focusing M of the beam E_3 to the beam E_1.

The competitive effects between mode wave and parasitic self-exiting wave may explain the observed peculiarities of generation and some disagreement between experiment and theoretical model.

5.REFERENCES.

1. I. M.Bel'dyugin, M.G.Galushkin and E.M.Zemskov, "Light radiation wavefront reversal with the use of feedback under four-wave interaction", Quantum Electronics (in Russian), Vol.11, No.5, pp.887-893, May 1984.

2. R.P.M.Green, G.J.Crofts, W.Hubbard, D.Udaiyan, D.H.Kim and M.J.Damzen, "Dynamic laser control using feedback from a gain grating" IEEE Journal of Quantum Electronics, Vol.32, No.3, 1996, p.371-377.

3. A.V.Kirsanov and V.V.Yarovoy, "Phase conjugation of a speckle-inhomogeneous beam by an Nd glass oscillator based on four-wave mixing with feedback" Quantum Electronics (in Russian), Vol.24, No.3, pp. 245-250, March 1997.

4. M.G.Galushkin, K.V.Mitin and K.A.Sviridov, "Four-wave interaction due to a thermal nonlinearity in active media of solid-state lasers", Quantum Electronics (in Russian), Vol.21, No.12, pp.1157-1159, December 1994.

5. A.A.Betin, K.V.Ergakov and O.V.Mitropolsky,"Reflection of a speckle-inhomogeneous radiation of CO_2 laser under four-wave interaction with feedback", Quantum Electronics (in Russian), Vol. 21, No.1, p.63-66, January 1994.

6. A.A.Betin and A.V.Kirsanov, "Selection of a phase-conjugate wave in an oscillator based on four-wave interaction with feedback in an extended nonlinear medium", Quantum Electronics (in Russian), Vol.21, No.3, pp.237-240, March 1994.

7. A.V.Kirsanov and V.V.Yarovoy,"Selection of a wave phase-conjugated to an speckled beam in an FWMF-oscillator with a "short" hologram", Optics Communications, Vol.138, pp.235-241, May 1997.

8. A.A.Betin and N.Yu.Rusov, "The lasing mode structure under Four-Wave Mixing with Feedback", Quantum Electronics (in Russian), Vol.15, No.5, pp.1021-1031, May 1988.

9. A.A.Betin, E.A.Jukov, O.V.Mitropolsky and N.Yu.Rusov, "PC and self-PC of CO_2 laser radiation on FWM in absorbing liquids" in Conference on PC of laser radiation in nonlinear media, , Digest (Minsk, 1987), pp. 5-21,1987.

Brillouin scatter and Faraday effect isolators / nonreciprocal rotators for high fluence multiple-pass amplifiers

S. Jackel, I. Moshe, R. Lavi, and R. Lallouz

Nonlinear Optics Group - Soreq NRC
81800 Yavne, Israel
FAX: 972-8-9434401
e-mail: drstevenjackel@yahoo.com

Abstract

A high-energy phase-conjugate mirror (PCM) / Nonlinear Isolator (NLI) based on pressurized methane was tested to the 5 J level, using 200 ns, 300 MHz bandwidth pulses from a phase conjugated multiple Nd:glass amplifier. Performance was good when a 50 cm focal length lens was employed. With a 25 cm lens, PCM performance was good except when gas breakdown occurred. In the presence of gas breakdown, reflectivity and return beam quality dropped. NLI isolation was aided by breakdown. A model was developed that shows that if breakdown occurs for a short focal length lens, then increasing the focal length raises the breakdown threshold but does not eliminate the problem at all input energies. This is a consequence of the fact that as input energy increases, the amount of energy leaking into the focal region increases faster than the breakdown threshold increase due to temporal broadening of the leaked pulse. High reflectivity (> 80%) single-cell tight-focus PCMs are feasible for use at the 10 J level, but as an NLI appears limited compared to glass based Faraday rotators.

I. Introduction

High brightness multi-joule (>3 J) lasers can be built based on Phase-Conjugated Multiple-Pass Amplifiers (PCMPAs).[1] Such lasers always have a Phase Conjugate Mirror (PCM) that reflects, with high fidelity, a greater than 1 J input pulse, and they may utilize a Nonlinear Isolator (NLI) that must reflect with high efficiency and fidelity a beam nearly or exactly equal to the laser output energy.[2]

PCMs for pulsed laser systems are generally based on stimulated Brillouin scatter (SBS) in liquids or gases.[3] In their simplest configuration, a tight focus PCM consists of a cell housing the active medium, together with a focusing lens at the cell's front and a beam dump at the cell's rear.[4] High energy PCMs often consist of a tight focus cell preceded by a Brillouin amplifier wherein a collimated beam of light propagates towards the tight focus cell and interacts with the reflected beam.[5] The BA then protects the tight focus PCM from excessive energy loads. An alternative to this two cell arrangement is to use a long focal length concentrating lens as well as an active medium suitable for high energy operation.[6] While it has been stated in the literature that a PCM should be used only within a factor of ten from its threshold if high fidelity is to be achieved,[7] we have found that if breakdown can be eliminated in a tight focus geometry, then the dynamic range can be considerably larger, in agreement with other published work.[8]

An NLI is a high reflectivity PCM fashioned as a Newtonian telescope.[2] It acts as a power limiter by reflecting pulsed laser light and reducing transmitted power to the SBS threshold level. An NLI is useful when the forward-transmitted power is less than the SBS threshold and the backward propagating power is substantially greater. Initially, we developed NLIs that used CCl_4 or CS_2 in PCMPAs where the NLI incident energy was ≤ 0.5 J. It was found to be particularly useful when moderate beam depolarization occurred or when Faraday rotator damage was a problem.

A Nd:Cr:GSGG PCMPA developed by us utilized a high energy PCM based on methane in a cell with a 50 cm focal length lens.[9] CH_4 was selected because it was found to have the best response to multiple longitudinal mode pulses as produced from etalon narrowed but unseeded oscillators. Energy into the PCM was 1.2 J.

In this work, results are presented on high energy PCMs / NLIs tested up to the 5 J level.[10] Parameters measured were the input, reflected, and transmitted energies. Also determined was the possible presence of laser induced methane breakdown. Not only does this work extend the tested range of our high energy PCMs, but it also quantifies the performance of high-energy gas NLIs. The important adjustable parameter dominating the SBS light-CH_4 interaction during NLI operation is the gas pressure, which determines the SBS threshold and thus the amount of energy that can be propagated in the forward direction together with the reflectivity of the light propagating in the backwards direction. A lower limit on pressure is imposed by breakdown. Breakdown threshold can be increased by using longer focal length lenses, thus reducing the focused intensity (while proportionally increasing the interaction length). We show here the ability to configure an NLI with sufficient forward transmission and backwards isolation to efficiently mate a Q-switched oscillator with 1 cm diameter Nd:Cr:GSGG and to provide high energy protection needed with a Nd:glass quadruple pass PCMPAs.

II.   Experimental setup

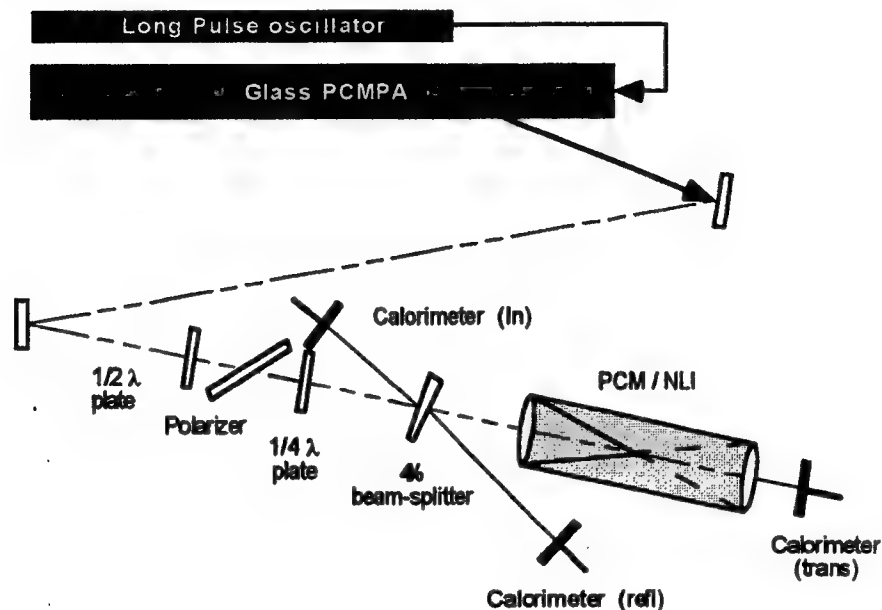Figure 1 shows a figure of the experimental setup.

Figure 1 - Setup for measurement of high energy PCM / NLI performance. Three calibrated calorimeters measured input, reflected and transmitted energies.

The laser was the same as used in previous high fluence Faraday rotator (FR) testing with the exception that Terbium Gallium Garnet FRs were replaced with high damage threshold Tb:glass FRs.[10] Particular effort was made to eliminate feedback and gain saturation effects that could substantially alter pulse duration. Thus, despite the fact that amplifier pulse forming network (PFN) voltages were varied   to   control energy, pulse duration variations were less than what would materially affect scaling of parameters with input energy. Pulse duration into the NLI was set at 200 ns.

Isolation against PCM back-reflections was provided by a polarizer and 1/4λ plate. It was confirmed that back-reflections did not affect any PCMPA output parameters, despite the fact that the pulse duration was long enough to cause the leading edge of any leakage pulse to experience unsaturated amplifier gain. Use of the 1/4λ plate resulted in circular input polarization to the PCM / NLI.

Diagnostics used were calibrated Ophir volume absorbing calorimeters. Input and reflected light calorimeters had 3-AP detector heads, and picked off 4% reflections from an uncoated BK7 2^0 wedged beam-spliter placed at a small angle to the optical axis. When necessary, calibrated neutral density filters were used. Transmitted light was measured with a 30-AP detector head. Absolute calibration accuracy was ±5%.

The PCM / NLI cells were based on stainless steel tubes to which were affixed planocovex lenses of 1 cm thickness that also acted as high pressure windows. These cells have retained integrity, up to the maximum 140 atm available, with a pressure

drop of less than 1 atm per 2 years (Full scale lifetime test being performed at the Naval Research Laboratory on a Soreq high pressure CH_4 PCM). Cell lengths were machined to match the focal lengths of the focusing and recollimating lenses used. No internal focusing mechanism was available but the NLI output was more than adequately collimated for these tests. Identical lenses were used to focus and recollimate the beam, so internal NLI magnification equaled one. Two lens sets were used with focal lengths of 25 and 50 cm. This provided a factor of four focal spot intensity difference, which was sufficient to differentiate between interactions dominated by breakdown or by stimulated Brillouin scatter. As has been shown theoretically and proved experimentally, the SBS threshold for a tight focus geometry is independent of lens focal length.[11] Breakdown, however, scales proportionally with the focal length squared, since it is an intensity dependent phenomenon.

The PCM / NLI active medium was gas phase methane (CH_4). Residual air concentration was reduced to $<2x10^{-3}$ prior to final filling by twice filling the cell and feed lines to 50 atm and then bleeding off the gas till the pressure dropped to less than 5 atm. With a final filling to 20 atm (the lowest pressure tested) the residual air concentration dropped to $<5x10^{-4}$. The purity of the bottled CH_4 was 99.9%.

III. Experimental results

The first tests confirmed that the PCM was not interacting with the pump laser and that all light was at 1053 nm. The PCMPA was fired without the oscillator and the presence of self-oscillations was sought. None were found, showing that no coupling was occurring prior to opening of the oscillator Q-switch. The entire laser was fired under high-energy conditions and the laser pulse shape was compared with and without the presence of the PCM reflection. No pulse distortion was observed so as to confirm the absence of coupling to the PCMPA 0^0 dielectric mirror and PCM. A 45^0 1053 nm high reflectivity mirror was placed between the NLI output window and the transmitted light calorimeter to check for the existence of Stimulated Raman Scatter which would shift the light wavelength to 1390 nm. A null result occurred.

What was observed early in the experiment was gas breakdown in the interaction region of the 25 cm focal length lens. Not only did reflectivity and transmission measurements behave anomalously, but also a distinct ping was heard from the cell, and after a few shots, a pile of ash could be seen on the cell floor beneath the focal region. All of these phenomena were indicative of gas breakdown.

It was thus, confirmed that the input pulse was clean, that all of the output photons were at 1053 nm, and that the interactions were SBS and gas breakdown.

Results using the 25 cm focal length lens set are shown in figures 2, 3, and 4, while results using the 50 cm lens are shown in figures 5,6, and 7. Three parameters are plotted as functions of input energy: reflectivity, transmission, and collected fraction of input energy. The collected fraction of input energy (sum of the PCM reflection and NLI transmission) is evaluated because it indicates the occurrence of other phenomena such as light scattering and absorption. These phenomena may occur with gas breakdown. While scattering and absorption may increase NLI contrast and may even surpass the isolation effectiveness of SBS, the mechanisms that cause such effects may compete with SBS and may interfere with the reflection process.
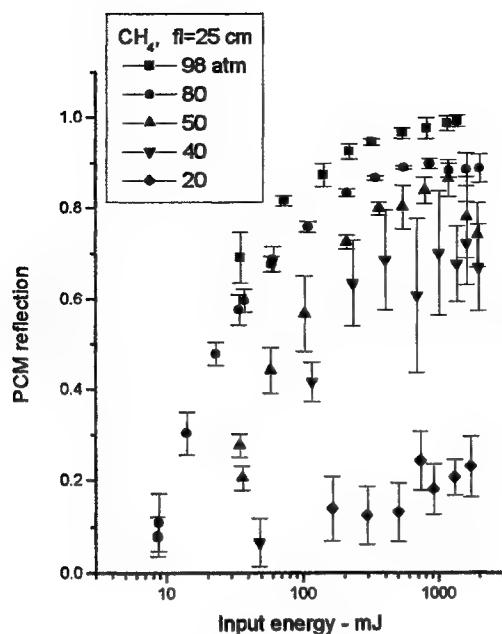
Figure 2 - Reflectivity of the CH$_4$ PCM / NLI as a function of input energy for various fill pressures. Focusing and recollimating lenses had 25 cm focal lengths.
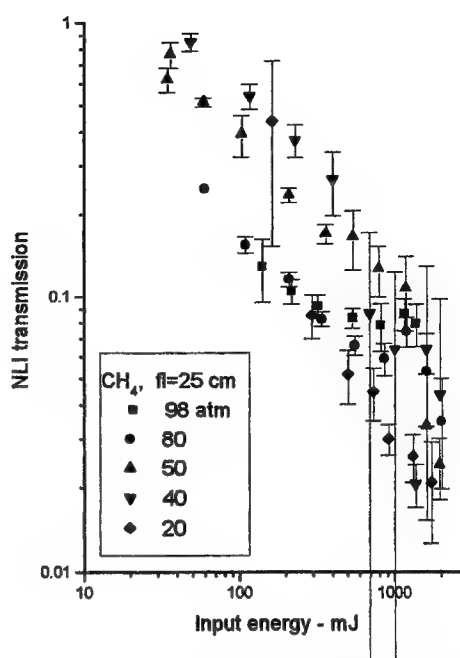
Figure 3 - Transmission through PCM / NLI as function of input energy for various fill pressures. Focusing and recollimating lenses had 25 cm focal lengths.
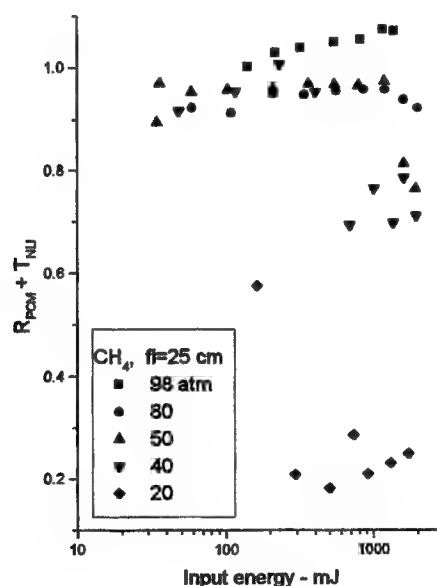
Figure 4 - Total measured energy check sum (PCM reflected plus NLI transmitted energies divided by input energy). Small values imply absorption and / or scatter.
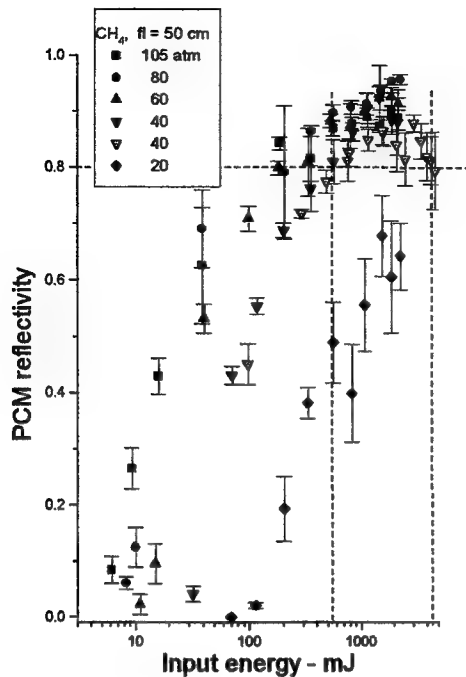
Figure 5 - Reflectivity of the CH₄ PCM. Focusing lens had 50 cm focal length.
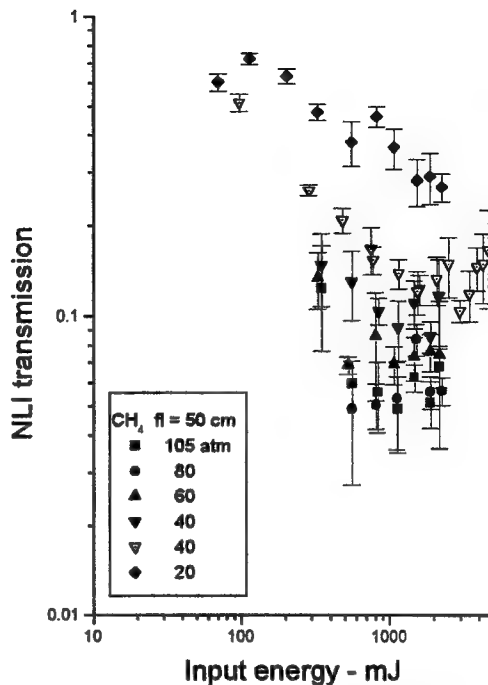
Figure 6 - Transmission through NLI. Focusing and recollimating lenses had 50 cm focal lengths.
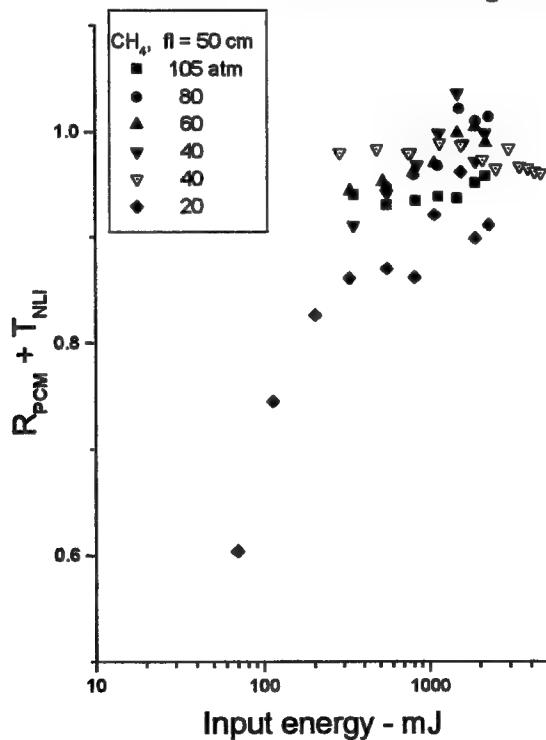
Figure 7 - Total measured energy check sum (PCM reflected plus NLI transmitted energies divided by input energy).

Breakdown was never heard in any of the 50 cm focal length experiments. In those tests a maximum of 2.3 J was input into the PCM while the CH_4 pressure was varied between 20 and 105 atm.. When using the 25 cm focal length lens, breakdown was heard above threshold input energies that varied with CH_4 pressure. The measured dependence is shown in figure 8.

If no other factors were dictating PCM / NLI fill pressure, then the results show that breakdown can be overcome by going to high enough pressure. Pressure is, however, not an independent parameter in an NLI. It determines the amount of energy that can be transmitted in the forward direction. This is seen in the PCM reflection curves. Well defined threshold values are seen in figures 2 and 5 (input energy at the 1 % reflectivity level). SBS threshold as a function of pressure is plotted in figure 9.

As an example, assume that 40 mJ must be transmitted through the NLI while 2 J of backwards propagating light must be blocked. To transmit 40 mJ, the NLI pressure must be kept at below 40 atm (figure 9). To reflect 2 J without breakdown using a 25 cm lens requires a pressure greater than 80 atm (figure 8). These two conditions are incompatible, so a 25 cm lens cannot be used. For most high energy applications, it appears that a 25 cm focal length lens is too short to avoid breakdown. A 50 cm lens appears appropriate for most of our near term applications, and the scaling appears such, that should very high energy NLIs be required, then longer focal length lenses can be used (space permitting).

Figure 8 - Dependence of breakdown threshold on CH_4 pressure for a 25 cm PCM focusing lens.

Figure 9 - Stimulated Brillouin Scatter threshold as a function of CH_4 pressure for 25 and 50 cm focal length lenses.

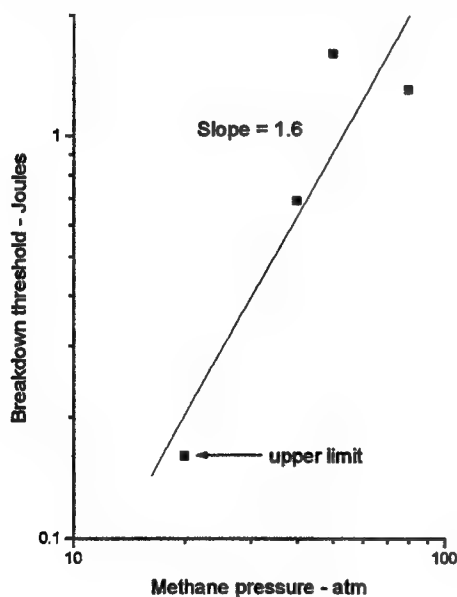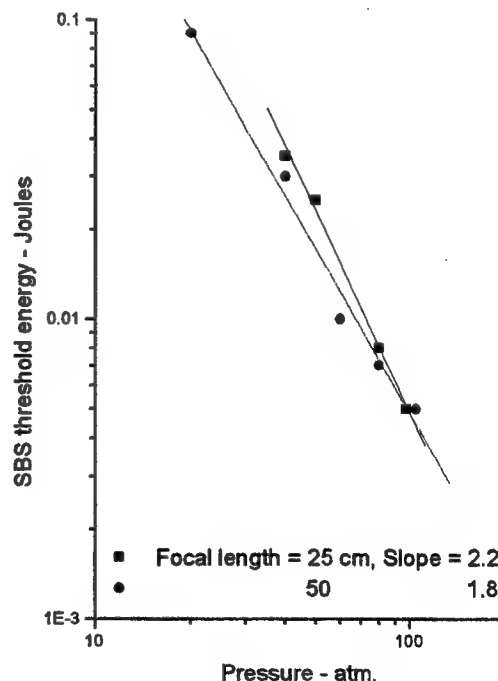It may be noted that the SBS threshold scaling with pressure is very different for these long, narrow bandwidth but multiple longitudinal mode pulses, than was observed in the past with short (17 ns) single longitudinal mode pulses. We here measured a threshold that scaled roughly with the inverse of pressure squared, while the previous conditions resulted in a linear scaling with the inverse of the pressure (as expected by steady-state theory for transform limited pulses). It appears that the scaling difference is due to pulse duration and / or laser bandwidth, and not due to breakdown, because figure 8 and 9 show that breakdown using the 25 cm lens occurred above the SBS threshold, and because the 25 and 50 cm lens SBS threshold results were very similar while breakdown did not occur with the 50 cm lens.

Despite the anomalous SBS threshold scaling with pressure, figure 9 shows, to the accuracy of the experiment, that the SBS threshold is independent of lens focal length and this is as expected by theory.

Examination of reflectivity curves show that PCM reflectivity can be high (>80 %) in the absence of breakdown. This is adequate for a PCM used in a multiple-pass amplifier if the reflected beam fidelity is good. It was found that the beam was well behaved in the absence of breakdown. When breakdown occurred, near-field beam aberrations occurred. The most dangerous of these was the generation of filaments or hot spots.

The 25 cm focal length lens results showed that despite the fact that at some fill pressures the SBS threshold was reached first, breakdown eventually occurred. With the 50 cm lens, breakdown was not observed up to the 2 J level for all pressures. It is desired to run the NLI up to10 J, so the question arises as to whether-or-not breakdown free performance can be assumed. The answer is no. To see this, consider the following idealized model. Steady-state SBS theory indicates that the peak intensity reaching the rear of the interaction region should remain constant and equal to the SBS threshold intensity, for input above threshold. In a tight focus geometry, the rear of the interaction region is the concentrating lens focal spot. The forward edge of the interaction region is determined by the instantaneous laser beam power and moves towards the lens during the laser pulse rise-time. If one compares pulses of equal full-width half-maximum duration (τ_{laser}) but of different peak powers (P_{max}), then the effective pulse width of the light reaching the focal spot (τ_{trans}) is larger for the more powerful pulse. This is because the SBS cuts the input pulse at a power level equal to the SBS threshold power (P_{th-SBS}). For a Gaussian input pulse of the form:

$$P = P_{max}e^{-2.77(t/\tau_{laser})^2} \qquad (1)$$

the width of the truncated Gaussian pulse reaching the rear of the interaction region is:

$$\tau_{trans} \approx 1.20\tau_{laser}\left[\ln|\xi|\right]^{1/2} \qquad (2)$$

where $\xi \equiv P_{max}/P_{th-SBS}$ is the number of times above SBS threshold we are working. The energy transmitted to the rear of the interaction zone (E_{trans}) is given by:

$$E_{trans} \approx P_{th-SBS}\tau_{trans} = 1.20P_{th-SBS}\tau_{laser}\left[\ln|\xi|\right]^{1/2} \qquad (3)$$

The dielectric gas energy breakdown threshold has a pulse duration dependence that scale as:

$$E_{BD-trans} \approx E_{BD-0}(\tau_{trans} / \tau_{BD-0})^{\beta}$$
$$= E_{BD-0}(1.20 P_{th-SBS})^{\beta} (\tau_{laser} / \tau_{BD-0})^{\beta} \left[\ln|\xi|\right]^{\beta/2} \quad (4)$$

where variables with a "BD-0" subscript denote measured breakdown, under conditions identical to those now investigated except for the difference in τ. $\beta \approx 1/2$. It can be seen that both E_{trans} and $E_{BD-trans}$ depend on $\ln|\xi|$, but the dependence of E_{trans} is stronger.

$$E_{trans} / E_{BD-trans} \propto \left[\ln|\xi|\right]^{(1-\beta)/2} \quad (5)$$

and for $\beta < 1$ ($\beta \approx 1/2$ in this case), $E_{trans}/E_{BD-trans}$ increases with ξ. The increase with P_{max} of energy reaching the focal spot is more rapid than the breakdown threshold increase. Thus, breakdown will eventually occur for any lens used. If, however, breakdown does occur, then a longer focal length lens will solve the problem (so long as the Raleigh range remains less than the pulse coherence length).

What level of reflectivity is required in an NLI? Saturated reflectivity of 80% is not adequate in an NLI unless accompanied by additional beam inhibiting processes. Reflectivity of 90% is required in an NLI used to retroreflect a laser beam and to protect a more effective but more damage prone isolator. Reflectivity of > 99.9% is required of a stand-alone NLI. Beam blocking processes additional to SBS include laser induced gas breakdown and Raman scattering. Gas breakdown, because it interferes with SBS is unacceptable in a PCM / NLI as required in a PCMPA. We found no evidence of Raman scatter in our experiment. (determined by inserting a narrow bandwidth 1053 nm mirror into the NLI transmitted light beam path, and checking for Raman shifted ($\lambda_{Raman}= 1380$ nm) light frequency doubled into the red by a Litton-Airtron KTP coated "Green Card".)

Figures 3 and 6 show NLI transmission. Energy transmission ($T_{NLI-energy}$) is defined as energy transmitted through the NLI divided by the input energy. The NLI is a power limiter that, when SBS is dominant and functioning properly, limits the power to the threshold power level. The normalized power transmission $T_{NLI-power}$ (defined at the peak of the input pulse) has a theoretical scaling of $T_{NLI-power} \sim P_{max}^{-1}$. $T_{NLI-energy}$ will have a somewhat weaker scaling because the width of the transmitted pulse increases as the peak power increases (Cut a Gaussian duration pulse at power levels farther below the peak, and the width of the flat-top zone increases).

$$T_{NLI-energy} \equiv \frac{E_{trans}}{E_{laser}} \approx \frac{P_{th-SBS}\tau_{trans}}{P_{max}\tau_{laser}} = 1.20 \frac{\left[\ln|\xi|\right]^{1/2}}{\xi} \quad (6)$$

Equation 6 is plotted as the points of figure 10. Also plotted is an apparent linear curve fit for the log-log plot. This is done because experimental data is usually analyzed in this way so that a scaling parameter (slope) can be extracted. A slope of

(-)0.81 is so derived. Past measurements using single longitudinal mode pulses and liquids yielded slopes of (-) 0.7-0.8. This is in excellent agreement with the "apparent" linear fit to the model.
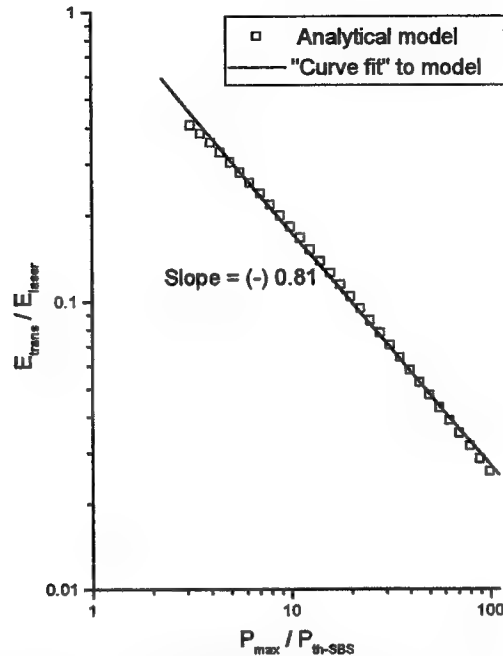
Figure 10 - Theoretical energy transmission through the NLI based on the analytical model (points) and an "apparent" linear curve fit to the model (line) in order to obtain the scaling factor (slope). The slope can be compared to time integrated experimental measurements.

In the case of the transmission data of figure 3 where a 25 cm focusing lens was used, the results are complicated by the presence of breakdown. When breakdown occurred, transmission dropped. Thus, if only isolation is required from an NLI then breakdown helps. If, as in many cases, a high quality reflected beam is also required, then breakdown is a hindrance. Over the ranges of the measurements obtained with the 50 cm focal length lens, the NLI transmission dependence on input energy appears weaker than depicted in figure 10 even when adding the 100% transmission points based on the SBS reflection measurements. Never-the-less, if we require 30 mJ of 300 MHz bandwidth oscillator energy to be injected into a PCMPA, then a 40 atm fill pressure can be used, which will result in a 10% high energy transmission. This level of transmission is sufficient to extract with reasonable efficiency the output from a four pass PCMPA producing 10 J, while protecting a 1 cm clear aperture TGG Faraday isolator.

Laser energy entering the PCM / NLI can be accounted for as transmitted, reflected, scattered, and absorbed energy. The experiments only measured forward transmission and backward reflection. Figures 4 and 7 show the sum of these two energies normalized to the input energy. In the absence of breakdown, 90 - 100 % of the input energy was accounted for. When breakdown occurred, a large fraction of the

input energy was unaccounted for. Thus, in the absence of breakdown transmission and absorption governed by SBS accounted for the NLI energy balance. When breakdown occurred, scattering and absorption were important energy channels.

IV.   Conclusions

A high energy PCM / NLI was tested to the 5 J level. The PCM / NLI was based on use of high pressure methane. It was found necessary to suppress gas breakdown in order to maintain a high fidelity reflected beam. This was accomplished by replacing a 25 cm focal length concentrating lens with one of 50 cm focal length, so as to lower the focused intensity to below the breakdown threshold. Insuring that the breakdown threshold was higher than the SBS threshold did not assure breakdown free operation at all input energies. A simple model that included the effect of transmitted pulse temporal broadening showed this effect.

Using the 50 cm lens, the SBS threshold could be raised to 30 to 40 mJ by reducing fill pressure to 40 atm. PCM reflectivity was 90 % while NLI isolation was 10 dB. This performance is sufficient for consideration of a NLI in a quadruple pass PCMPA operating at up to 10 J in order to efficiently extract the output beam and to protect a high contrast but lower damage threshold Faraday isolator.

Whether-or-not an NLI is actually used depends on the capabilities of a Faraday rotator to perform the same task. Recent improvements in raising the damage threshold of Faraday rotator materials suggests that the competition will be fierce. Figure 11 shows the damage threshold improvement obtained in switching from TGG to Tb:glass Faraday rotator material.[10]
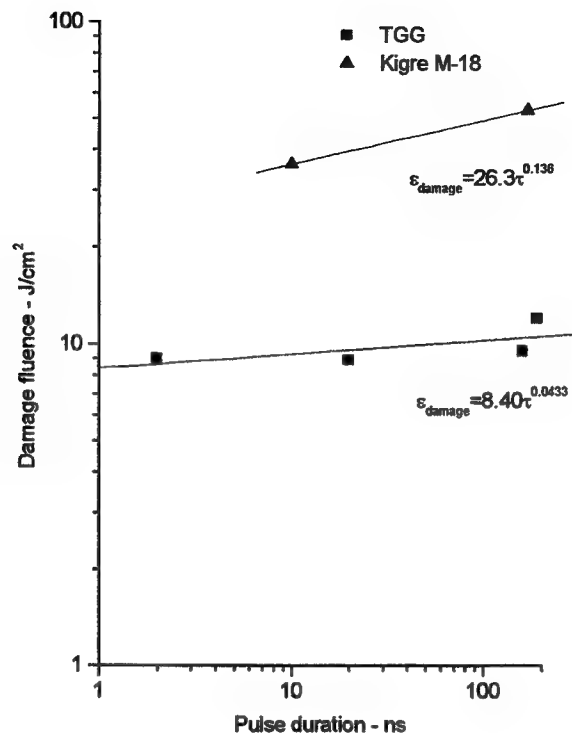
Figure 11 - Summary of Faraday rotator damage tests on Terbium Gallium Garnet (TGG) and Tb:glass (Kigre M-18), showing 4 to 5 times higher damage threshold of Tb:glass and the weak pulse duration dependence of the Tb doped materials. 200 ns points were obtained at Soreq, and the remaining data was obtained from Lawrence Livermore National Laboratory, Litton-Airtron, and Passat Enterprises.

V.   References

1. S. Jackel, R. Lallouz, and A. Ludmirsky,
   Phase-conjugated multiple-pass amplifiers for low repetition rate, high energy, pulsed Nd:glass lasers,"
   in *The Sixth Meeting in Israel on Optical Engineering*, Proc. SPIE 1038, 521-525 ((1989)
   R. St. Pierre, D. Mordaunt, H. Injeyan, J. Berg, R. Hilyard, M. Weber, M. Wickham, G. Harpole, and R. Senn,
   "Diode array pumped kilowatt lasers,"
   IEEE J. of Selected Topics in Quantum Electronics 3, 53-58 (1997)

2. S. Jackel, S. Atzmon, R. Lallouz, S. Sternklar, and P. Shalev,
   "Nonlinear optical isolators based on high-reflectivity Brillouin mirrors and their application to advanced lasers,"
   Opt. Eng. 31, 328-334 (1992)

3. D. Pepper,
"Nonlinear optical phase conjugation,"
Opt. Eng. 21, 156-183
V. Volynkin, K. Gratsianov, A. Kolensikov, Yu. Kruzhilin, V. Lyubimov, S. Markosov, V. Pankov, A. Stepanov, and S. Shklyarik,
Reflection by stimulated Brillouin scattering mirrors based on tetrachlorides of group IV elements,"
Sov. J. Quantum Electron. 15, 1641-1642 (1985)
N. Andreev, E. Khazanov, and G. Pasmanik,
"Applications of Brillouin cells to high repetition rate solid-state lasers,"
IEEE J. of Quantum Electron. 28, 330-341 (1992)

4. N. Basov, V. Efimkov, I. Zubarev, A. Kotov, A. Mironov, S. Mikhailov, and M. Smirnov,
"Influence of certain radiation parameters on wavefront reversal of a pump wave in a Brillouin mirror,"
Sov. J. of Quantum Electron. 9, 4550-458 (1979)

5. D. Hull, R. Lamb, and J. Digman,
"Efficient phase conjugation at high energies using two cells,"
Opt. Comm. 72, 104-108 (1989)
G. Crofts, M. Damzen, and R. Lamb,
"Experimental and theoretical investigation of two-cell stimulated Brillouin-scattering systems,"
J. of Opt. Soc. Am. B 8, 2282-2288 (1991)
M. Mangir and D. Rockwell,
"4.5-J Brillouin phase-conjugate mirror producing excellent near- and far-field fidelity,"
J. Opt. Soc. Am. B 10, 1396-1400 (1993)

6. R. Menzel and H. Eichler,
"Temporal and spatial reflectivity of focused beams in stimulated Brillouin scattering for phase-conjugation,"
Phys. Rev. A 46, 7139-7149 (1992)
R. Mullen and J. Matossian,
"Quenching optical breakdown with an applied electric field,"
Opt. Lett. 15, 601-603 (1990)

7. J. Ottusch and D. Rockwell,
"Stimulated Brillouin scatter phase-conjugation fidelity fluctuations,"
Opt. Lett. 16, 369-371 (1991)

8. P. Suni and J. Falk,
"Measurements of stimulated Brillouin scattering phase-conjugate fidelity,"
Opt. Lett. 12, 838-840 (1987)
C. Dane, W. Neuman, and L. Hackel,
"Pulse-shape dependence of stimulated-Brillouin-scattering phase-conjugation fidelity for high input energies,"
Opt. Lett. 17 1271-1273 (1992)

9. S. Jackel, I. Moshe, A. Kaufman, R. Lavi, and R. Lallouz,
   "High-energy, Nd:Cr:GSGG lasers based on phase and polarization conjugated
   multiple-pass amplifiers,"
   Opt. Eng. 36, 2031-2036 (1997)

10. S. Jackel, I. Moshe, A. Kaufman, R. Lavi, R. Lallouz, and Z. Jackel,
    "Faraday rotators for use in multijoule Nd:Cr:GSGG and Nd:Glass phase and
    polarization conjugated multiple-pass amplifiers,"
    in *Proceedings of the 10th Meeting on Optical Engineering in Israel* SPIE 3110
    (1997)

11. B. Ya. Zel'dovich, N. Pilipetsky, and V. Shkunov,
    "Principles of Phase Conjugation,"
    Springer-Verlag Press - Germany (1985)
    Y. Kuo, K. Choi, and J. McIver,
    "The effect of pump bandwidth, lens focal length, and lens focal point location on
    stimulated Brillouin scattering threshold and reflectivity,"
    Opt. Comm. 80, 233-238 (1991)

FOUR-WAVE MIXING OF CHIRPED SIGNAL AND SPECTRAL-LIMITED PUMPS
IN A RESONANT MEDIUM

Vladimir Kabanov

Institute of Physics, NASB
Skarina Ave. 70, Minsk 220072, Belarus

ABSTRACT

An investigation is reported of the characteristic features of a four-wave mixing of a chirped signal with bandwidth-limited pump waves in a resonant medium modelled by a two-level scheme. Analytic estimates are obtained and a numerical analysis is made of the combined influence of various mechanisms (spatial phase matching, a finite nonlinear response time, and phase cross-modulation) on the spectral composition and on the temporal behaviour of the fourth pulse. Conditions are found for achieving, with practically undetectable distortions, phase conjugation of a chirped signal accompanied by shortening of the pulse envelope and narrowing of the spectrum of the phase-conjugate wave.

1. INTRODUCTION

The practical realization of phase conjugation at four-wave mixing (FWM) of laser pulses in a nonlinear media is connected with a set of attendant effects.[1-7] In this report, we present the results of numerical modeling and analytical estimates of the transient FWM of chirped signal and band-limited pumps in a resonant medium modelled by two-level scheme. Combined influence of different attendant effects (spatial phase matching, a finite nonlinear response time, and phase cross-modulation) on spectral composition and temporal behavior of fourth wave have been analyzed.

2. THEORETICAL MODEL AND ANALYTIC ESTIMATES

We shall consider a two-level model of a nonlinear medium and describe the nonlinear susceptibility by the following equation[6]:

$$p_{21}^{-1}\partial_t \chi_{NI} + (1 + \underline{a}|\mathcal{E}|^2)\chi_{NI} = -n_0 \ae_0 \underline{\hat{a}}|\mathcal{E}|^2 / 2\pi,$$

(1)

where n_0, $\ae_0$ are, respectively, the refractive index and the extinction coefficient of an unexcited medium; $\hat{a} = a + i\alpha$ is a complex nonlinear parameter; p_{21} is the total probability of spontaneous and nonradiative transitions; $\underline{\hat{a}} = cn_0\hat{a}/8\pi$. If calculations are limited solely to large-scale K_- dynamic gratings $K_\pm = k_1 \pm k_3$, the slowly varying amplitudes $E_i = \tilde{A}_i \exp(i\varphi_i)$ obey the following system of equations[8]:

$$(v^{-1}\partial_t \pm \partial_z)E_{1,2} = -(i2\pi\omega / n_0 c)(\chi_0 E_{1,2} + \chi_{\pm 1}E_{3,4}),$$

$$(v^{-1}\partial_t \pm \partial_z)E_{3,4} = -(i2\pi\omega / n_0 c)(\chi_0 E_{3,4} + \chi_{\pm 1}E_{1,2}),$$

(2)

$$\chi_q = (2\pi)^{-1}\int_{-\pi}^{\pi}\chi_{NI}\exp(-iq K_- r)d(K_- r),\ \ (q = 0,\pm 1).$$

where v is the velocity of light in the medium. The system of integrodifferential equations (1)-(2) makes it possible to investigate FWM and to take into account the depletion of the pump fields, the nonlinear absorption of all the interacting waves, and the appearance of a finite nonlinear response time of the medium.

2.1. Spatial phase matching

The wave-vector mismatch Δk reduces the efficiency of formation of the wave E_4, the amplitude of which falls by a factor of two for $\Delta kL / 2 \approx 2$. The width of the spectrum within the limits of which the phase-conjugate pulse can reproduce effectively the spectral components of the initial signal is:

$$\Delta \omega_{4c} = 2\omega_0 / kL. \tag{3}$$

The spectral width $\Delta \omega_{4c}$ of an FWM-filter, determined by the spatial phase matching mechanism, is related to the transit time of the radiation in the medium $\tau_{fwm} = L / v$ by $\tau_{fwm} \Delta \omega_{4c} = 2$. If the radiation frequency is $v = 5 \times 10^{14}$ Hz and if $k = 1.3 \times 10^5$ cm^{-1}, $L = 1$ cm, and $n_0 = 1.25$, we find that $\tau_{fwm} \approx 4.2 \times 10^{-11}$ s and $\Delta v_{4c} = \Delta \omega_{4c} / 2\pi \approx 7.6 \times 10^9$ Hz.

2.2. Finite nonlinear response time

The finite nonlinear response time can be responsible for frequency filtering of the input signal during formation of a conjugate wave with the central frequency $\omega_3 = \omega_0$ and with the half-width

$$\Delta \omega_{4m} = 2\tau_m^{-1}, \tag{4}$$

where $\tau_m = [(1 + \alpha J_0) p_{21}]^{-1}$ is the effective relaxation time of the nonlinear response, $J_0 = \sum_{i=1}^{4} |E_i|^2$. If $p_{21} = 10^9$ s and the total intensity varies in the range $1 >> \alpha J_0 = 1$, the quantity $\Delta \omega_{4m} / 2\pi$ fluctuates within the limits $3.2 \times 10^8 \div 6 \times 10^8$ Hz.

2.3. FWM with chirped signal

If the signal is chirped in accordance with the square law $A_{30}(t) = A_{30} \exp[-(1 + im)t^2 / 2\tau_0^2]$, the width of the spectrum $\Delta \omega_{ph}$ is defined by $\tau_0 \Delta \omega_{ph} = 2[\ln 2(1 + m^2)]^{1/2}$. A phase-conjugate pulse is obtained if the spectral width of the FWM-filter does not limit effective FWM of all the spectral components of the chirped signal. It follows from the above estimates that the main constraint comes from the finite response time, i.e. it is necessary to satisfy the condition $\Delta \omega_{ph} < \Delta \omega_{4m}$. Full phase conjugation of a chirped pulse is possible if

$$\tau_0 > [\ln 2(1 + m^2)]^{1/2} \tau_m. \tag{5}$$

2.4. Phase cross-modulation

Strong pump waves give rise to phase cross-modulation of the fourth wave. A sufficiently high level of cross-modulation may distort the initial phase of the signal and may influence significantly the spectral composition of the conjugate and signal pulses.[7] The spectral broadening of a conjugate pulse as a result of cross-modulation can be estimated as

$$\Delta \omega_{cm} \approx \phi_{max} \Delta \omega_g, \quad \Delta \omega_g = 2\sqrt{\ln 2} \cdot \tau_0^{-1}, \tag{6}$$

where $\phi_{max} = \omega_0 \text{æ}_0 \underline{a} L (2A_{10}^2 + A_{20}^2) / c$ is the maximum frequency shift.

3. NUMERICAL RESULTS AND DISCUSSION

Numerical modelling of FWM of bandwidth-limited pump pulses [$\varphi_1(z = 0,t) = \varphi_2(z = L,t) = 0$] and a phase-modulated (in accordance with the square law) signal with a Gaussian envelope was based on the integrodifferential system of equations (1)-(2). The results given below apply to a nonlinear medium with coincident Gaussian profiles of the absorption and emission bands on the assumption that the optical density of the medium is described by $\hat{L} = 2\omega_0 \text{æ}_0 L / c = 1$; $n_0 = 1,25$, $p_{21} = 10^9 \text{ s}^{-1}$. The carrier frequency ω_0 of the interacting waves is detuned relative to the centre of the absorption band ω_{12} by $\eta = (\omega_0 - \omega_{12}) / \Delta = 2$. The intensity of saturation at the centre of the absorption band is $I_{sat} = \alpha^{-1}(\omega_{12}) = 1 \text{ MW cm}^{-2}$ and the signal intensity is 1% of the intensities of two identical pump waves.

3.1. Quasi-steady-state FWM regime

An analysis of the quasi-steady-state FWM regime ($\tau_0 \gg \tau_m$) makes it possible to establish the following relationships. At a low level of phase modulation of the initial signal, the temporal behaviour of the phases of the signal and of the generated fourth wave is distorted significantly by cross-modulation in the presence of strong pump waves. Figs. 1a – 1d demonstrate the characteristic temporal behaviour of the amplitude and phase of the signal and of the generated fourth wave at the exit from the nonlinear medium when $\tau_0 = 10p_{21}^{-1}$ and the intensities at the maxima of the pump pulses are $I_{1,2}^m = 0,5I_{sat}$. Phase modulation characterised by $m = \pm 2$ broadens the input signal spectrum, which in this case amounts to $\Delta\omega_{ph} / 2\pi \approx 6.7 \times 10^7$ Hz. The signal pulse spectrum at the exit from the nonlinear medium may be close to the spectrum of the bandwidth-limited signal. Narrowing of the spectrum of the fourth wave $S_4(\Omega = (\omega - \omega_0)\tau_0)$ shown in Fig. 1e ($\Delta\nu_4 \approx 3 \times 10^7$ Hz) is related to the opposite contributions of phase modulation of the input signal and of cross-modulation. These mechanisms alter the sign of the frequency deviation, the result of which is reduction in the resultant frequency deviation of the fourth pulse generated by FWM. Reversal of the sign of the phase modulation level m of the input signal reduces the width of the signal pulse, whereas the spectrum of the fourth wave becomes much wider than the initial value (Fig. 1f).

3.2. Phase conjugation

An increase in the level of phase modulation of the input signal makes the influence of cross-modulation on the phase quite negligible. The temporal behaviour of the initial phase is reproduced by the fourth pulse practically without detectable distortions, which indicates that phase conjugation takes place. The envelope of the conjugate pulse becomes shorter, which implies the presence of an FWM-filtering. In the spectral representation this is demonstrated by narrowing of the conjugate wave spectrum (Fig. 2). If the width of the input signal spectrum is $\Delta\nu_3 \approx 2.5 \times 10^8$ Hz, the spectral width of the conjugate wave is limited (Fig. 2c) to the interval $\Delta\nu_4 \approx 9 \times 10^7$ Hz.

3.3. FWM at finite nonlinear response time

A further increase in the modulation level m of the input signal has the that FWM-filtering mechanisms limit even more the reproduced spectral composition. The temporal behaviour of the fourth pulse therefore demonstrates not only shortening of the envelope, but incomplete reproduction of input signal phase. Reduction of the duration of the interacting pulses makes this behaviour dominant and, when FWM involves pulses of duration considerably less than the relaxation time of the nonlinear response ($\tau_0 \ll \tau_m$), this behaviour is observed even at low levels of modulation of the input signal, in accordance with formula (5). The temporal behaviour of the signal waves and the spectra of these waves illustrating this situation are given in Fig. 3. We can see that under the influence of the finite nonlinear response time the signal pulses

appear at the exit from the nonlinear medium after some delay (Fig. 3a), the phase is distorted (Fig. 3b), but the spectrum of the fourth wave is close to the spectrum of the bandwidth-limited signal $\Delta \nu_4 \approx 3 \times 10^9$ Hz (Fig. 3c).

Fig. 1. Temporal behaviour of the envelopes A_i (a, b) and phases φ_i (c, d), and also of the spectral densities S_i (e, f) of the signal (dashed curves) and conjugate (continuous curves) pulses calculated for a chirped signal (dotted curves) on the assumption that $\tau_0 = 10 p_{21}^{-1}$, $I_{1,2}^m = 0.5 I_{sat}$, $\hat{L} = 1$, $m = -2$ (a, c, e), and $m = 2$ (b, d, f).

Fig. 2. Temporal behaviour of the envelopes A_i (a) and phases φ_i (b) and also of the spectral densities S_i (c) of the signal (dashed curves) and conjugate (continuous curves) pulses for a chirped signal (dotted curves) on the assumption that $\tau_0 = 10 p_{21}^{-1}$, $I_{1,2}^m = 0.5 I_{sat}$, $L = 1$, $m = -10$.
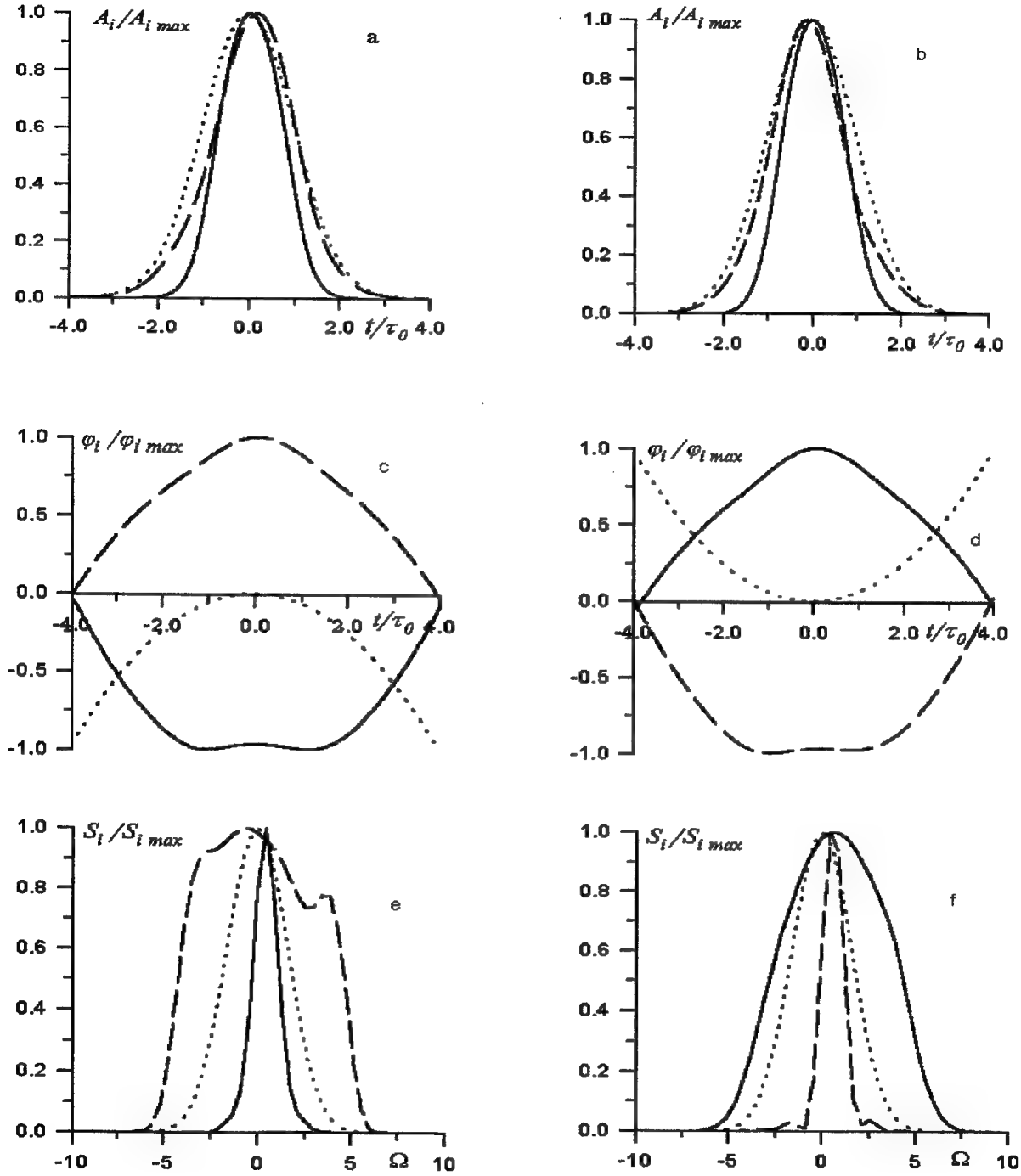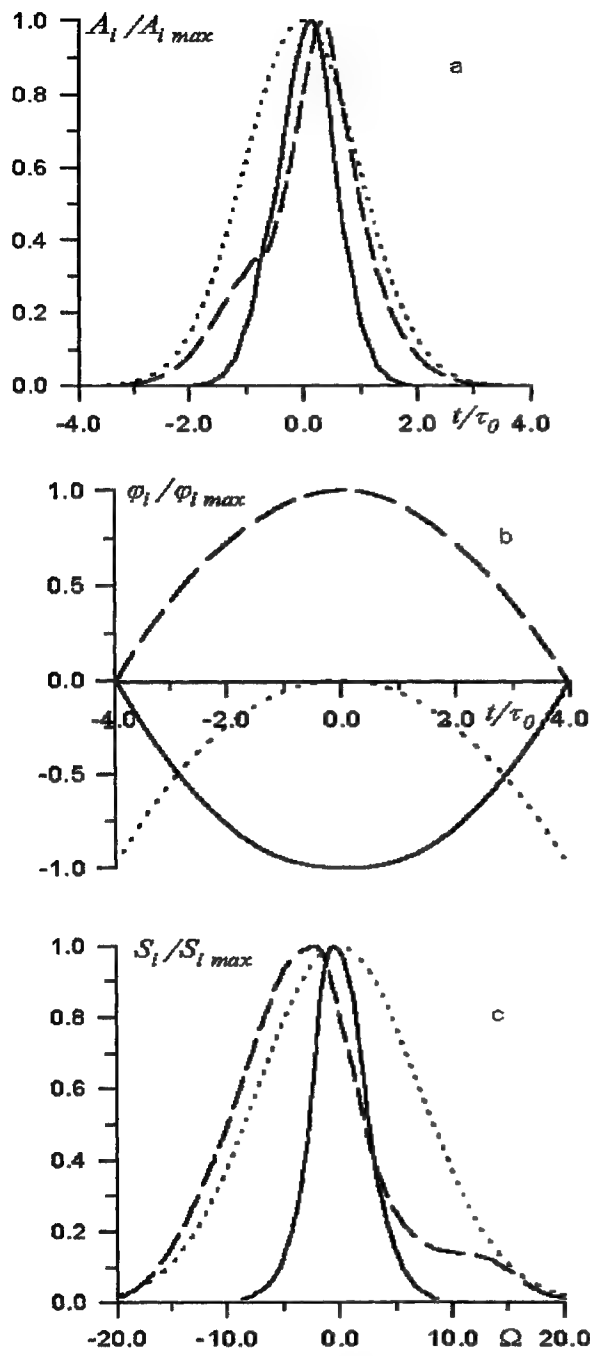
Fig. 3. Temporal behaviour of the envelopes A_i (a) and phases φ_i (b) and also of the spectral densities S_i (c) of the signal (dashed curves) and conjugate (continuous curves) pulses for a chirped signal (dotted curves) on the assumption that $\tau_0 = 0.1 p_{21}^{-1}$, $I_{1,2}^m = 0.5 I_{sat}$, $L = 1$, $m = -10$.
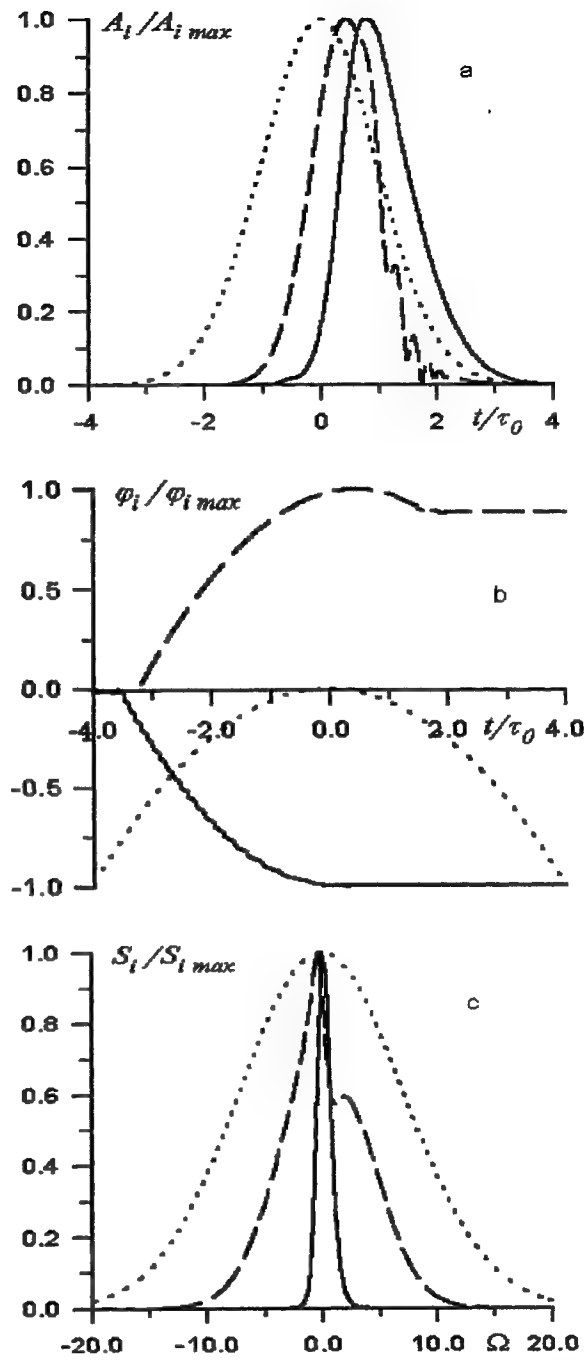
4. Conclusions

It follows that several factors may influence the formation of the fourth wave in FWM of bandwidth-limited pump waves with a chirped signal. When the level of the input signal is low, the phase of the fourth wave generated by quasi-steady-state FWM may be distorted significantly as a result of cross-modulation. An increase in the level of phase modulation results in phase conjugation with practically undetectable distortions and it is accompanied by shortening of the envelope and narrowing of the spectral composition of the conjugate wave. A further increase in the modulation level and with reduction of the pulse duration at a low modulation level increases the role of the FWM-filtering mechanisms which result from spatial phase matching and from the finite nonlinear response time. This not only shortens the envelope, but also distorts the phase and also reduces the width of the spectrum of the fourth wave right down to the width of the bandwidth-limited pulse.

5. References

1. R.A Fisher, B.R Suydam, B.J. Feldman, "Transient analysis of Kerr-like phase conjugaters using frequency-domain techniques", *Phys. Rev. A,* Vol. 23, pp. 3071-3083, 1981.

2. R.A Fisher, B.R. Suydam, "Transient response of Kerr-like phase conjugaters: a review", *Optical Eng.*, Vol. 21, pp. 184-189, 1982.

3. N. Kukhtarev, A. Borshch, M. Brodin, V. Volkov, T. Semenets, "Laser beam critical behaviour and phase conjugation in the semiconductors, resonant media and crystals", *J. Phys. (Paris),* Vol. 44, colloq. C2, pp. C2-5 - C2-14, 1983.

4. V.N. Abrashin, P.A. Apanasevich, A.A. Afanas'ev, V.V. Drits, A.I. Urbanovich, " four-wave mixing in a resonant medium", *Kvantovaya. Elektron. (Moscow),* Vol. 12, pp. 546-550, 1985; [*Sov. J. Quairtum Efecrron.*, Vol. 15, pp. 357-362, 1985].

5. V.V. Drits, V.V. Kabanov, A.S. Rubanov, "Phase conjugation by transient four-wave mixing in a resonant medium", *Litovski Frzicheski Sbornik,* Vol. 32, pp. 785-792, 1992.

6. V.V. Kabanov, A.S. Rubanov, "Dynamic of transient four-wave mixing in a resonant medium", *Proc. SPIE (Phase Conjugation and Adaptive Optics),* Vol. 2771, pp. 141-148, 1996.

7. V.V. Kabanov, "Influence of self-modulation on degenerate four-wave mixing in a resonant medium", *Kvantovaya Elektron. (Moscow),* Vol. 22, pp. 284-286, 1995; [*Quantum Eleerron.,* Vol. 25, pp. 267-269, 1995].

8. V.V. Kabanov, A.S. Rubanov, "Dynamic gratings and four-wave phase conjugation in dye solutions", *IEEE J. Quantum Electron.,* Vol. QE-26, pp. 1990-1998, 1990.

Four-wave mixing of the fundamental, Stokes, and anti-Stokes waves in a single-mode birefringent fiber: influence of initial conditions on energy exchange among the waves, optical switching.

Podoshvedov S.A.

Nonlinear Optics Laboratory, Southern Urals State University, Lenin av. 76, Chelyabinsk, Russia.

ABSTRACT

The behavior of the fundamental, Stokes, and anti-Stokes waves in a single-mode birefringent fiber is investigated. Analysis of the nonlinear dynamics of the four-wave mixing are developed using Hamiltonian representation of equations describing the process. Significant mathematical progress has been made in solving problem of the four-wave mixing, in particular, analytical solutions in the terms of Jacobian elliptic and hyperbolic functions and graphic solutions on the phase plane are obtained. The main problems addressed concern optical switching among the waves.

1. INTRODUCTION

Spatial instability is a general phenomenon that exists for a wide class of the wave processes in nonlinear optics. The existence of the spatial instability is connected with joint action of both parametric energy exchange among the waves and nonparametric interactions which are responsible for self and cross modulation. The spatial instability is found to exist in interaction of the light waves in a quadratic nonlinear medium and in the wave mixing in materials with inversion symmetry (cubic media) when the lowest-order nonlinear effects originate from the third-order susceptibility $\chi^{(3)}$. For example, spatial instabilities have been discovered in the nonlinear dynamics of the following wave processes: in two-wave parametric mixing in a quadratic nonlinear medium in the presence of self-and cross-phase modulation,[1] in mixing of the polarizations of an intense beam in a cubic crystal with birefringence and third-order nonlinearity,[2] in degenerate four-photon mixing between orthogonal polarizations in a birefringent fiber,[3-5] and in two-wave mixing of the fundamental and its third harmonic in a cubic medium.[6] Spatial instability leads to abrupt changes in the transfer of the full power among the waves. In particular, the output distribution of the power among the waves is very sensitive to the changes of both input ratio of the powers in the waves and initial difference of the phases of the waves taking part in the mixing. These effects can be used for the construction of the optical switching devices.

In the paper we consider interaction of the fundamental wave polarized along both axes of the single-mode birefringent fiber with Stokes and anti-Stokes waves with orthogonal polarizations. The four-wave mixing in the birefringent fibers has been studied by many peoples.[7,8] Most of them considered a simple model that describes the nonlinear interaction among the waves on initial stage of propagating. According to the model, fundamental waves are considered to remain constant and is much more intense than Stokes and anti-Stokes waves. Using the model it is possible to derive the linearized equations. Obviously this approach is limited to short lengths. Although the model can give some general picture of the interaction among the four waves, it is oversimplified model. The treatment with linearized equations is not appropriate, when the light waves propagate to the large distances, as depletion of the fundamental wave needs to be taken into consideration. Generally speaking, when the conversion from the fundamental wave into the Stokes and anti-Stokes waves is high, evolution equations for the amplitudes of the fields become nonlinear and must be solved in general. A general consideration for arbitrary length of the fiber and conversion efficiency of the fundamental wave into Stokes and anti-Stokes waves are of practical interest as the results can be used to derive optimum conditions for obtaining large conversion.

The aim of the present paper is to develop analytical approach to describe the nonlinear dynamics of the four-wave mixing in a birefringent fiber. Hamiltonian representation of the equations describing the four-wave mixing enables to obtain exact analytical formulae for fraction of the total power in the waves as function of the length of a medium. For better understanding the nature of the nonlinear dynamics of the four-wave mixing, it is desirable to describe the wave process on the phase-space portraits when spatial evolution of the four electric fields is presented by moving a material point on a given trajectory in the phase plane. Then, by inspecting

phase-space portraits, it is possible to find the areas in which maximum conversion is observed. Using the phase-space portraits and property varying input distribution of total power among the waves or initial difference of the phases, one obtains optical switching in the four-wave mixing.

2. GENERAL THEORY

The electric field $\vec{E}(\vec{r};z)$ traveling along a single-mode birefringent fiber can be described in the terms of the linearly polarized modes:

$$\vec{E}(\vec{r};z) = \frac{1}{2}((\vec{e}_x F_{0x}(x,y)E_{0x}(z)\exp(i\beta_{0x}z) + \vec{e}_y F_{0y}(x;y)E_{0y}(z)\exp(i\beta_{0y}z))\exp(-i\omega_0 t) +$$

$$\vec{e}_x F_1(x,y)E_1(z)\exp(-i\omega_1 t + i\beta_1 z) + \vec{e}_y F_2(x,y)E_2(z)\exp(-i\omega_2 t + i\beta_2 z) + c.c.) \tag{1}$$

where ω_0, ω_1, and ω_2 $(2\omega_0 = \omega_1 + \omega_2)$ are the mean optical frequencies of the fundamental, Stokes, and anti-Stokes waves correspondingly.

The evolution equations can be derived from wave equation in the slowly varying envelope approximation as follows[9]:

$$\frac{dE_{0x}}{dz} = \frac{i2\pi n_2}{\lambda_0 A}(\frac{2}{3}E_1 E_2 E_{0y}^* \exp(i\Delta kz) + (|E_{0x}|^2 + \frac{2}{3}|E_{0y}|^2 + 2|E_1|^2 + \frac{2}{3}|E_2|^2)E_{0x}) \tag{2}$$

$$\frac{dE_{0y}}{dz} = \frac{i2\pi n_2}{\lambda_0 A}(\frac{2}{3}E_1 E_2 E_{0x}^* \exp(i\Delta kz) + (\frac{2}{3}|E_{0x}|^2 + |E_{0y}|^2 + \frac{2}{3}|E_1|^2 + 2|E_2|^2)E_{0y}) \tag{3}$$

$$\frac{dE_1}{dz} = \frac{i2\pi n_2}{\lambda_1 A}(\frac{2}{3}E_{0x}E_{0y}E_2^* \exp(-i\Delta kz) + (2|E_{0x}|^2 + \frac{2}{3}|E_{0y}|^2 + |E_1|^2 + \frac{2}{3}|E_2|^2)E_1) \tag{4}$$

$$\frac{dE_2}{dz} = \frac{i2\pi n_2}{\lambda_2 A}(\frac{2}{3}E_{0x}E_{0y}E_1^* \exp(-i\Delta kz) + (\frac{2}{3}|E_{0x}|^2 + 2|E_{0y}|^2 + \frac{2}{3}|E_1|^2 + |E_2|^2)E_2) \tag{5}$$

where the amplitudes $E_i(z)$ are slowly varying functions of z on comparing with $\exp(i\beta_i z)$;

$\Delta k = \beta_{0x} + \beta_{0y} - \beta_1 - \beta_2 = (\omega_0(n_{0x} + n_{0y}) - \omega_1 n_1 - \omega_2 n_2)/c$ is mismatch of the wave vectors of the fundamental, Stokes, and anti-Stokes waves; n_{0x}, n_{0y}, n_1, n_2 are the linear coefficients of refraction of the modes of the fiber; $n_2 = 3.2 \cdot 10^{-16} cm^2/W$ is the Kerr coefficient; A is an effective area of core of the single-mode fiber. Note that only elements of the third-order susceptibility in tensor $\chi^{(3)}$ for which the indices are equal in pairs are nonzero. As a direct consequence of this property of an isotropic medium, waves interacting in the four-wave mixing must be also polarized in pairs (either all on one axis or two on each axis). In the case of silica fibers, for which the dominant contribution is of electronic origin, the elements of the three-component tensor have nearly the same magnitude and can be assumed to be equal.

It is possible to obtain the following integrals of moving from Eqs.(2-5):

$$|E_{0x}|^2 - |E_{0y}|^2 = D_1 \tag{6}$$

$$\frac{\lambda_1}{\lambda_0}|E_1|^2 - \frac{\lambda_2}{\lambda_0}|E_2|^2 = D_2 \tag{7}$$

$$|E_{0x}|^2 + |E_{0y}|^2 + \frac{\lambda_1}{\lambda_0}|E_1|^2 + \frac{\lambda_2}{\lambda_0}|E_2|^2 = P \tag{8}$$

Eqs.(6,7) express the fact that both photons of the fundamental and photons of the Stokes and anti-Stokes waves arise and annihilate in pairs. Eq.(9) is law of conservation of the total power.

Let us introduce the new variables q_1, q_2, q_3, q_4 as follows:

$$E_{0x} = \sqrt{P}q_1 \tag{9}$$

$$E_{0y} = \sqrt{P}q_2 \tag{10}$$

$$E_1 = \sqrt{P\frac{\lambda_0}{\lambda_1}} q_3 \qquad (11)$$

$$E_2 = \sqrt{P\frac{\lambda_0}{\lambda_2}} q_4 \qquad (12)$$

Equations(2-5) may be reduced to a two degree of freedom nonlinear oscillator equations by means of a canonical transformation from the four complex variables q_1, q_2, q_3, q_4 to the two real conjugate variables $\eta = |q_3|^2$ and $\psi = \varphi_3 + \varphi_4 - \varphi_1 - \varphi_2 + ks$, where φ_i is the phase of i wave. We obtain that η and ψ obey the coupled nonlinear equations:

$$\frac{d\eta}{ds} = \frac{2}{3}\sin\psi\sqrt{\eta(\eta - d_2)(1 + d_1 + d_2 - 2\eta)(1 + d_2 - d_1 - 2\eta)}$$

(13)

$$\frac{d\psi}{ds} = \frac{2}{3}\cos\psi(\frac{\sqrt{(\eta - d_2)(1 + d_1 + d_2 - 2\eta)(1 + d_2 - d_1 - 2\eta)}}{2\sqrt{\eta}} - \frac{\sqrt{\eta(\eta - d_2)(1 + d_2 - d_1 - 2\eta)}}{\sqrt{1 + d_1 + d_2 - 2\eta}} -$$

$$- \frac{\sqrt{\eta(\eta - d_2)(1 + d_1 + d_2 - 2\eta)}}{\sqrt{1 + d_2 - d_1 - 2\eta}} + \frac{\sqrt{\eta(1 + d_1 + d_2 - 2\eta)(1 + d_2 - d_1 - 2\eta)}}{2\sqrt{\eta - d_2}} - A\eta + B + C + D + k \quad (14)$$

where $d_1 = D_1/P$, $d_2 = D_2/P$, $s = z/L_{nl}$ is the normalized distance; $1/L_{nl} = 2\pi P/\sqrt{\lambda_1\lambda_2} A$ being the characteristic distance; $k = \Delta k L_{nl}$. The coefficients A, B, C, D have the following form:

$$A = \frac{1}{3}(16(\sqrt{\frac{\lambda_1}{\lambda_2}} + \sqrt{\frac{\lambda_2}{\lambda_1}}) - \frac{10\sqrt{\lambda_1\lambda_2}}{\lambda_0} - \frac{4\lambda_0}{\sqrt{\lambda_1\lambda_2}} - 3(\sqrt{\frac{\lambda_2}{\lambda_1}}\frac{\lambda_0}{\lambda_1} + \sqrt{\frac{\lambda_1}{\lambda_2}}\frac{\lambda_0}{\lambda_2})) \qquad (15)$$

$$B = \frac{2d_1}{3}(\sqrt{\frac{\lambda_2}{\lambda_1}} - \sqrt{\frac{\lambda_1}{\lambda_2}}) \qquad (16)$$

$$C = \frac{d_2}{3}(4(\sqrt{\frac{\lambda_2}{\lambda_1}} + 3\sqrt{\frac{\lambda_1}{\lambda_2}}) - \frac{5\sqrt{\lambda_1\lambda_2}}{\lambda_0} - \frac{3\lambda_0}{\lambda_2}\sqrt{\frac{\lambda_1}{\lambda_2}} - \frac{2\lambda_0}{\sqrt{\lambda_1\lambda_2}}) \qquad (17)$$

$$D = \frac{1}{3}(4(\sqrt{\frac{\lambda_1}{\lambda_2}} + \sqrt{\frac{\lambda_2}{\lambda_1}}) - \frac{5\sqrt{\lambda_1\lambda_2}}{\lambda_0}) \qquad (18)$$

and $|q_1|^2$, $|q_2|^2$, $|q_3|^2$, $|q_4|^2$ are connected with η as:

$$|q_1|^2 = \frac{1 + d_1 + d_2 - 2\eta}{2} \qquad (19)$$

$$|q_2|^2 = \frac{1 + d_2 - d_1 - 2\eta}{2} \qquad (20)$$

$$|q_4|^2 = \eta - d_2 \qquad (21)$$

Eqs.(13,14) are a set of the nonlinear differential equations coupling the fraction of the total power in the Stokes wave η with difference of the phases of the waves ψ. The two-dimensional dynamical system for the variables η and ψ (Eqs.(13,14)) can be described in terms of Hamiltonian mechanics where η and ψ are the canonical-conjugate variables. The Hamiltonian reads as:

$$H = \frac{2}{3}\cos\psi\sqrt{\eta(\eta - d_2)(1 + d_1 + d_2 - 2\eta)(1 + d_2 - d_1 - 2\eta)} - \frac{A\eta^2}{2} + (B + C + D + k)\eta \qquad (22)$$

and the corresponding Eqs.(13,14) can be presented as:

$$\frac{d\eta}{ds} = -\frac{\partial H}{\partial \psi} \tag{23}$$

$$\frac{d\psi}{ds} = \frac{\partial H}{\partial \eta} \tag{24}$$

Conservation of the Hamiltonian (Eq.(22)) and the variables d_1 and d_2 leads to the possibility to solve the Eqs.(13,14) in terms of Jacobian elliptic and hyperbolic functions. In order to make it let us reduce Eqs.(13,14) to a one-degree-of-freedom nonlinear oscillator equation. To obtain the equation it is necessary to express $\sin\psi$ from the Eq.(22) and to set it into Eq.(13). Using the procedure, one obtains the following integral representation of the initial problem:

$$s = \int_{\eta_0}^{\eta(s)} (\frac{\partial H(\eta,\psi)}{\partial \psi})^{-1} d\eta = \frac{1}{\sqrt{G}} \int_{\eta_0}^{\eta(s)} \frac{dx}{\sqrt{f(x)}} \tag{25}$$

where $\eta_0 = \eta(s=0)$, $H_0 = H(\eta_0,\psi_0)$, $f(\eta) = -\eta^4 + a_3\eta^3 + a_2\eta^2 + a_1\eta + a_0$, $G = A^2/4 - 16/9$, and the coefficients a_i are the following:

$$a_3 = \frac{1}{G}(-\frac{16}{9}(1+2d_2) + Aa) \tag{26}$$

$$a_2 = \frac{1}{G}(\frac{4}{9}(1+5d_2^2 - d_1^2 + 6d_2) - a^2 - AH_0) \tag{27}$$

$$a_1 = \frac{1}{G}(\frac{4}{9}d_2(d_1^2 - 2d_2 - d_2^2 - 1) + 2aH_0) \tag{28}$$

$$a_0 = -\frac{H_0^2}{G} \tag{29}$$

where $a = B + C + D + k$. In example investigated below, we use the following wavelengths of the fundamental, Stokes, and anti-Stokes light waves $1.319\mu m$, $1.338\mu m$, $1.3\mu m$ correspondingly. Also, we shall deal with such values of d_1 and d_2 which can be obtained in the case of using the following initial distribution of the total power among the waves $P_1 = P_2 = 10W$, $P_3 = 10mW$, $P_4 = 1\mu W$. Let us consider perfect phase-matching case. Then it is necessary for us have a single-mode fiber with birefringence $\delta n \approx 3 \cdot 10^{-5}$.

It is desirable to be able to obtain exact solutions of the Eqs.(13,14) by means of analytical tools. Before we find analytical solutions of the Eqs.(13,14), let us consider graphic solutions of the equations (13,14). Nonlinear dynamics of the four-wave mixing essentially depends on number of the fixed points of the Hamiltonian, their stability and location on the phase plane. The fixed points of the two dimensional system, say, (η_e, ψ_e) represent the nonlinear eigenmodes of the four-wave mixing. They are defined by setting $d\eta/ds = d\psi/ds = 0$ in the Eqs.(13,14). These points are the extreme of the Hamiltonian (Eq.(22)). A simple condition for vanishing the right hand side of the Eqs.(13,14) is that $\psi_e = 0$ or $\psi_e = \pi$. From the Eqs.(13,14), one obtains dependence of the eigenmodes on mismatch k. As bifurcation diagram of the four-wave mixing is equivalent to the them have been earlier obtained[1-6], we do not show it here.

Let us briefly discuss the phase trajectories that represent the solutions of the Eqs.(13,14) on the phase plane $(\eta\cos\psi, \eta\sin\psi)$. Since the Hamiltonian H in the Eq.(22) is a conserved quality along s, the trajectories in Fig.1 are also the constant level curves of H. The phase space for η is a ring with large and small radii $\eta = (1 + d_2 - d_1)/2$ and $\eta = d_2$ correspondingly. As can be seen from Fig.1, three stable eigenmodes are the stable centers on the phase plane. Away from each of three elliptic fixed points, the representative point of the

Stokes wave moves on stable periodic trajectories. The circle of radius d_2 is forbidden zone for moving the point η. Because of small size of the zone it is impossible to see the third eigenmode located near circle of radius of d_2. The unstable eigenmode with $\psi_e = \pi$ (which is indicated by the letter A in the figure) is the origin of the double-loop separatrix that divides the phase space into three domains of periodic evolutions. Moreover, the spatial period of the conversion diverges to infinity on the double-loop separatrix. Considering phase-space portrait, it is worth noting significant exchange among the waves is observed near double-loop separatrix.

Let us solve Eqs.(13,14) by employing mathematical methods. To obtain the analytical solutions, it is necessary to find all roots η_i of the equation $f(\eta_i) = 0$. As $f(\eta)$ is multinomial of fourth order, it is possible to obtain the roots using analytical methods. But in the way, one obtains complex and long expressions which turn out not to be useful for them analyzing. Instead of seeking the roots using mathematical methods we present dependence of $f(\eta)$ on η in Fig.2,3. Figures 2,3 show the potential field in which moves the material point as function of η for different values of H (Eq.22). So Fig.2(a,b) is obtained for the following values of
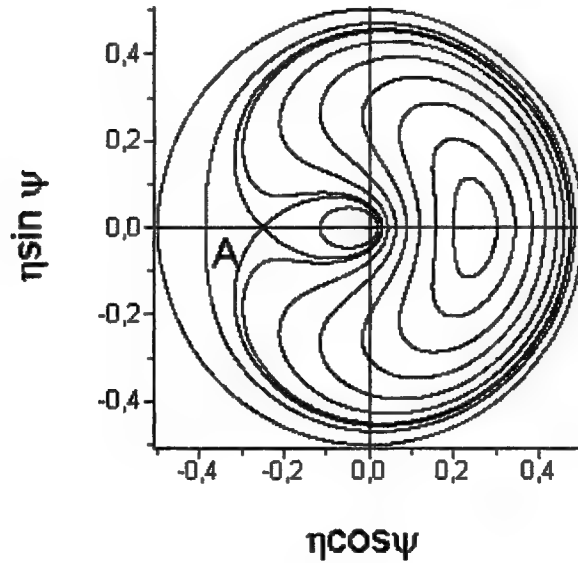

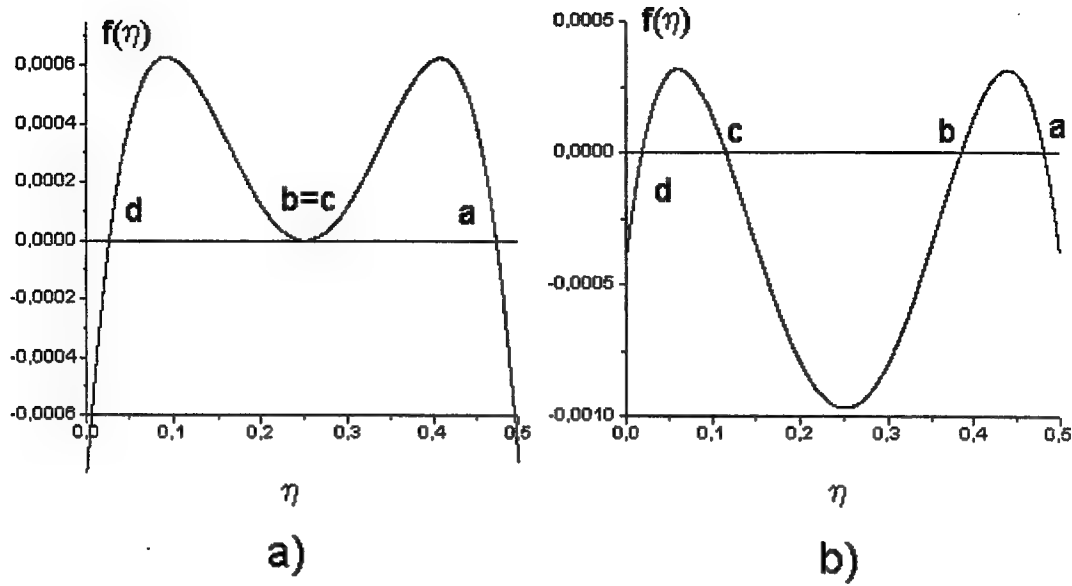Fig.1 Phase-space portrait for perfect phase-matching case.

Fig.2 Dependence of the function $f(\eta)$ on η for a) $H = H_{ins}$ and b) $H < H_{ins}$.
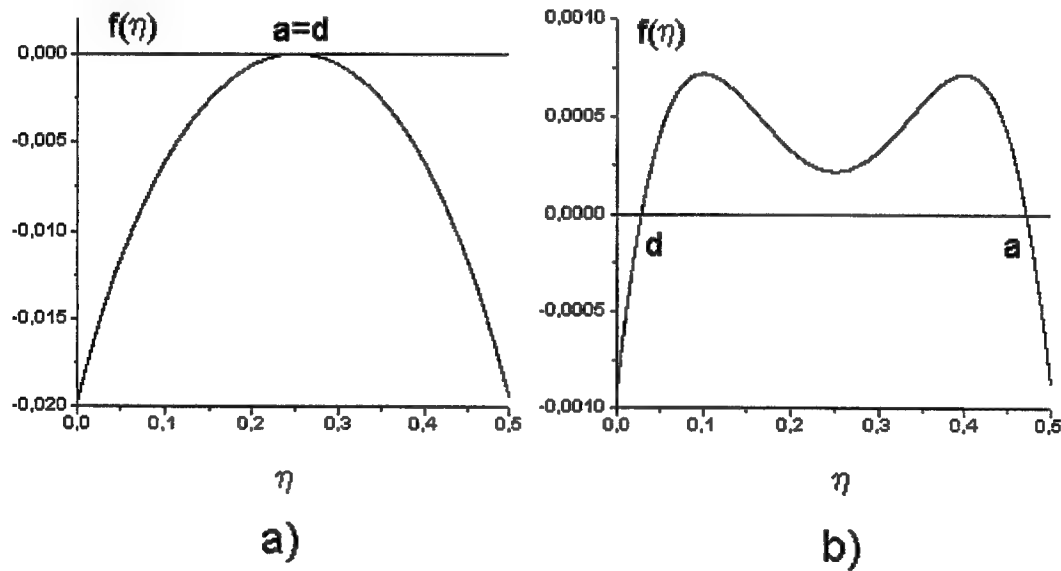
Fig.3 Dependence of the function $f(\eta)$ on η for a) $H = H_{st}$ b) $H_{ins} < H < H_{st}$

the Hamiltonian: Fig.2(a) is for $H = H_{ins} \approx 0.0420254$ (one obtains the value substituting value of the unstable eigenmode with $\psi_e = \pi$ and $\eta_e \approx 0.2505$ into the Hamiltonian (Eq.(22)); Fig.2(b) is for $H = 0.03 < H_{ins}$. The case in Fig.2(a) corresponds to the phase trajectories which constitute double-loop separatrix on the phase-space portrait in Fig.1. Here we present expansion of the $f(\eta)$ on multipliers for the case:

$f(\eta) = (a - \eta)(b - \eta)^2(\eta - d)$ where $d \approx 0.0267$, $c = b \approx 0.2508$, $a \approx 0.4739$. Then, by integrating Eq.(25), one obtains solution of the Eqs.(13,14) as follows:

$$\eta = b + \frac{2(b-d)(a-b)}{(a-d)chU_1 + 2b - a - d} \approx 0.2 + \frac{0.1}{0.4472 \cdot chU_1 + 0.001} \tag{30}$$

105

for large loop of the double-loop separatrix (Fig.1) and

$$\eta = b - \frac{2(a-b)(b-d)}{(a-d)chU_2 + a + d - 2b} \approx 0.2508 - \frac{0.1}{0.4472 \cdot chU_2 - 0.001} \tag{31}$$

for small loop of the double-loop separatrix, where

$$U_1 = \pm arch((\eta_0(a+d-2b) + b(a+d) - 2ad)/((a-d)(\eta_0 - b)))) - \sqrt{(a-b)(b-d)} \cdot \sqrt{A^2/4 - 16/9} \cdot s \approx$$
$$\pm arch((0.1 - 0.001\eta_0)/(0.4472(\eta_0 - 0.2508)) - 0.333 \cdot s$$

$$U_2 = \pm arch((\eta_0(a+d-2b) + b(a+d) - 2ad)/((a-d)(b-\eta_0))) - \sqrt{(a-b)(b-d)} \cdot \sqrt{A^2/4 - 16/9} \cdot s \approx$$
$$\pm arch((0.1 - 0.001\eta_0)/(0.4472(0.2508 - \eta_0)) - 0.333 \cdot s.$$

We must write sign + in U_1 and U_2 in the case if initial point on the phase-plane portrait (Fig.1) is located in top of the phase plane $(\sin\psi > 0)$ for U_1 and in bottom of the phase plane $(\sin\psi < 0)$ for U_2.

Considering Fig.2(b), we see two areas of moving the material point η where $f(\eta) \geq 0$. One of them has been restricted by the points d and c, and the other is located between the points b and a. The value of the H corresponds to trajectories on the phase-plane portrait in the Fig.1 which are located inside small loop of the double-loop separatrix and outside the separatrix. $f(\eta)$ has four different material roots. Expansion of the $f(\eta)$ can be presented as follows: $f(\eta) = (\eta - d)(c - \eta)(b - \eta)(a - \eta)$ where $d \approx 0.0018$, $c \approx 0.162$, $b \approx 0.3848$, $a \approx 0.4818$. Let us now consider solution of the Eqs.(13,14) located inside the small loop of the double-loop separatrix. Doing substitution of the variables as follows $y = \arcsin(\sqrt{((a-c)(x-d))/((c-d)(a-x))})$ and inverting the new integral, one obtains the following solution of the promlem:

$$\eta = \frac{a(c-d)sn^2(U,r) + d(a-c)}{(c-d)sn^2(U,r) + a - c} \approx \frac{0.07715 \cdot sn^2(U,r) + 0.0006}{0.16012 \cdot sn^2(U,r) + 0.3198} \tag{32}$$

where $r = \sqrt{((a-b)(c-d))/(a-c)(b-d))} \approx 0.3561$ is the modulus of the elliptic sine function sn;

$U = \sqrt{(a-c)(b-d)}\sqrt{A^2/4 - 16/9} \cdot s/2 \pm F(\beta_0, r) \approx 0.2609 \cdot s \pm F(\beta_0, r)$; $F(\beta_0, r)$ is the elliptic integral of the first kind;

$$\beta_0 = \arcsin\sqrt{((a-c)(\eta_0 - d))/((c-d)(a-\eta_0))} \approx \arcsin\sqrt{0.3198(\eta_0 - 0.00188)/(0.16012(0.4818 - \eta_0))}$$

Function $sn(x)$ is periodic in x with a period equal to $4K(k)$, where $K(k)$ is the complete elliptic integral of the first kind.

The phase trajectories located outside double-loop separatrix in the $(\eta\cos\psi, \eta\sin\psi)$ plane have another interpretation in the terms of periodic functions of sn. Using the new variable y connected with the x as: $y = \arcsin(\sqrt{((b-d)(a-x))/((a-b)(x-d))})$, we find the function $\eta(s)$ evolve according to:

$$\eta = \frac{d(a-b)sn^2(U,r) + a(b-d)}{(a-b)sn^2(U,r) + b - d} \approx \frac{0.00018 \cdot sn^2(U,r) + 0.0006}{0.16012 \cdot sn^2(U,r) + 0.3198} \tag{33}$$

where $U = \pm F(\mu_0, r) - \sqrt{(a-c)(b-d)}\sqrt{A^2/4 - 16/9} \cdot s/2 \approx \pm F(\mu_0, r) - 0.2609 \cdot s$,

$r = \sqrt{((a-b)(c-d))/(a-c)(b-d))} \approx 0.3561$ is the modulus of the elliptic sine function; $F(\mu_0, r)$ is the elliptic integral of the first kind;

$$\mu_0 = \arcsin(\sqrt{((b-d)(b-\eta_0))/((a-b)(\eta_0 - d))}) \approx \arcsin(\sqrt{0.38292(0.3848 - \eta_0)/0.097(\eta_0 - 0.00188)})$$

We must write +or − in the dependence on location of the initial point in the phase-space portrait (Fig.1). Analyzing Eqs.(32,33), it is possible to show the expressions (32,33) for the case $H < H_{ins}$ will be transformed to Eqs.(30,31) when $H \to H_{ins} - 0$. The behavior of the Eqs.(32,33) under

$H \rightarrow H_{ins} - 0$ may be immediately understood by looking at the phase-plane portrait in the Fig.1.

Consider now the case when $H > H_{ins}$. In Fig.3(a),3(b) we plot the function $f(\eta)$ for the case $H = H_{st} \approx 0.20869$ and $H_{ins} < H = 0.045 < H_{st}$ correspondingly. There are the trivial solution $\eta(s) = const$ in the case $H = H_{st}$. One obtains the value of the Hamiltonian inserting the value of the stable eigenmode with $\psi_e = 0$ and $\eta_e \approx 0.25$ into Eq.(22). As a result, the light waves propagate unchanged and the nonlinearity introduces only a progressive phase shift in them. More interesting situation arises in the case $H < H < H_{st}$. The values of the Hamiltonian correspond to the phase trajectories which are located inside large loop of the double-loop separatrix in the Fig.1. Considering the phase-space portrait and the Fig.3(b), it is worth noting area of moving the material point η is extended for the values of the H for which are carried out condition $H - H_{ins} \approx 0 +$. The values of the Hamiltonian are of practical interest as large conversion among the waves is observed in the cases. Analysis of the function $f(\eta)$ shows that there is only two real roots and two complex-conjugate roots. One presents expansion of the $f(\eta)$ on multipliers as (Fig.3(b)):

$$f(\eta) = (0.4717 - \eta)(\eta - 0.0287)(\eta^2 - 0.5011072\eta + 0.067266337).$$ Then, by introducing the new variable y as $y = 2arcctg(\sqrt{(q(a-x))/(p(x-b))})$ in the Eq.(25), one obtains the following solution:

$$\eta = \frac{(p+q)(qa+pd)sn^2(U,r) + 2pq(a+d)cn^2(U,r) \pm 2pq(a-d)cn(U,r)}{(p+q)^2 sn^2(U,r) + 4pq \cdot cn^2(U,r)} \tag{34}$$

where $U = \sqrt{pq}\sqrt{A^2/4 - 16/9} \cdot s \pm F(\alpha_0, r)$; $p^2 = (b'-a)^2 + b''^2$; $q^2 = (b'-d)^2 + b''^2$; $b = b' + ib''$ is the complex root; $\alpha_0 = 2arcctg(\sqrt{(q(d-\eta_0))/(p(a-\eta_0))})$;

$r = 0.5\sqrt{((p+q)^2 + (a-d)^2)/pq}$ is the modulus of the elliptic functions sn and cn. Consider Eq.(34) with + under function of cn. If the initial point on the phase plane is located in top of the phase-plane portrait $(\sin\psi > 0)$, then $U = \sqrt{pq}\sqrt{A^2/4 - 16/9} \cdot s - F(\alpha_0, r)$ and if the initial point is located in bottom of the phase plane $(\sin\psi < 0)$, then $U = \sqrt{pq}\sqrt{A^2/4 - 16/9} \cdot s + F(\alpha_0, r)$. Contrary picture takes place for Eq.(34) with sign – under function of cn.

3. APPLICATIONS AND CONCLUSIONS

In this section we briefly discuss one example of optical switching and the conditions for the experimental observability of the large wave conversion by means of changing initial difference of the phases of the waves. For that, consider the following distributions of initial total power among the waves:
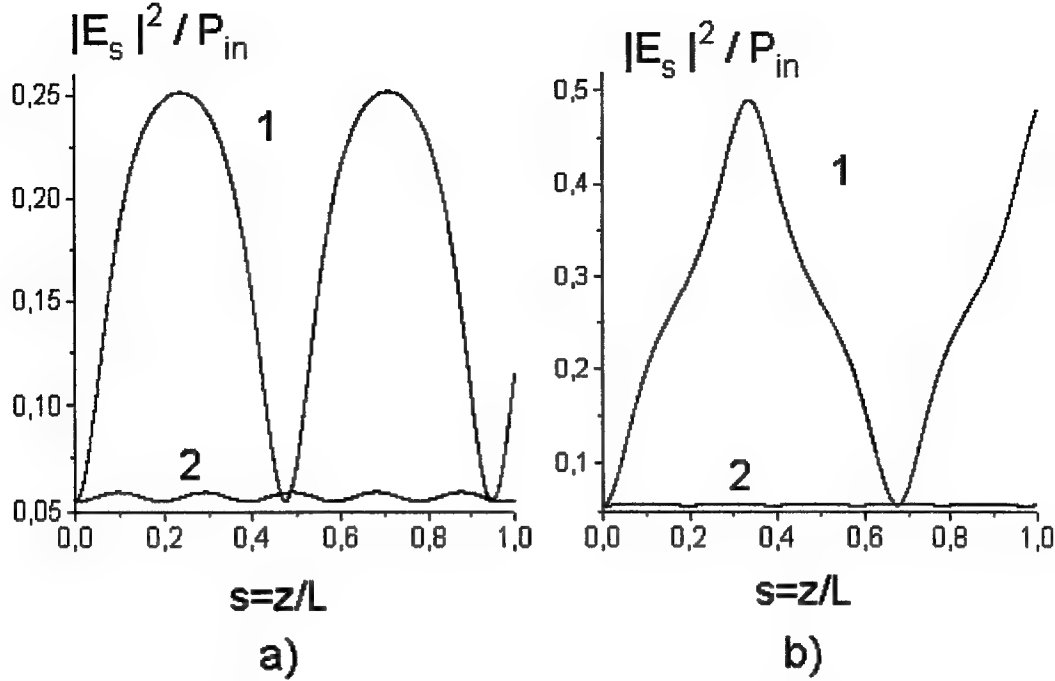
Fig.4(a,b) Fraction of the Stokes power versus the propagation distance z/L for different values of the initial difference of the phases.

$P_1 = P_2 \approx 9.86mW$, $P_3 \approx 1.136mW$, $P_4 \approx 0.137mW$ is for the Fig.4(a); $P_1 = P_2 \approx 9.847mW$, $P_3 \approx 1.151mW$, $P_4 \approx 0.157mW$ is for the Fig.4(b).

The solid lines in the Fig.4(a,b) show the dependencies of the fraction of the total power in the Stokes wave $|E_1|^2/P_{in}$, $(P_{in} = |E_{0x0}|^2 + |E_{0y0}|^2 + |E_{10}|^2 + |E_{20}|^2$, where $E_{i0} = E_i(s=0))$ on the dimensionless distance $s = z/L$ for the case $L/L_{nl} = 50$ where L is the total length of the fiber. For both the Fig.4(a) and the Fig.4(b) initial distributions of the power among the waves are equal but initial differences of the phases $\psi_0 = \psi(s=0)$ distinguish on π. Curves 1 in the Fig.4(a,b) are obtained for the case $\psi_0 = \pi$, while the curves 2 in Fig.4(a,b) are obtained for the case $\psi_0 = \pi$. As can be seen from the figures, it is possible to observe optical switching by changing the initial difference of the phases. Let us translate the graphic results to real physical units in order to be able to use them in experimental situation. An important parameter that may be extracted from our analysis is the distance S_m, where maximum conversion from the fundamental wave into the Stokes and anti-Stokes waves first occurs. This distance may be easily obtained from the exact and graphic solutions. The results for above mentioned distributions of the total power among the waves are the following: $S_m \approx 185343m$ is for the Fig.4(a) and $S_m \approx 305940m$ is for the Fig.4(b).

We have studied the exactly integrable nonlinear dynamics of the nonlinear four-wave mixing among the waves. We found that our analysis may provide a good description of the wave process in any regimes even in the strong depletion regime of the fundamental wave. Whenever the absolute value of the linear mismatch $|k|$ is small, the dynamics of the four-mode equations exhibits bifurcation and instability phenomena. As consequence of existing instability in the four-wave mixing, great sensitivity of the output fields with respect to small variations of the initial conditions in the proximity of the separatrix is observed. We have also briefly discussed the conditions for experimental observation of strong conversion in the four-wave mixing in fiber with birefringence, with particular relevance to applications in optical switching devices.

4. REFERENCES

1. S. Trillo, S. Wabnitz, Opt. Lett. **17**, pp. 1572-1574, 1992.
2. G. Gregori, S. Wabnitz, Phys. Rev. Lett. **56**, pp. 600-604, 1986.
3. G. Cappellini, S. Trillo, Opt. Lett., **16**, pp. 895-897, 1991.
4. G. Cappelini, S. Trillo, Phys. Rev. **A44**, pp. 7509-7516, 1991.
5. S. Trillo, S. Wabnitz, Phys. Lett. **A159**, pp. 252-255, 1991.
6. S.A. Podoshvedov, Opt. Commun. **142**, pp. 79-83, 1997.
7. R.H. Stolen, J.E. Bjorkholm, A. Ashkin, Appl. Phys. Lett **24**, pp.308-314, 1997.
8. R.H. Stolen, IEEE J. Quantum Electron., **QE-11**, pp.100-105, 1975.

Wave front transformation by nonlinear formed dynamic holograms

Alexei L. Tolstik

Department of Laser Physics and Spectroscopy, Belarusian State University,
220050 Minsk, Belarus

ABSTRACT

Conversion of light beams by the dynamic volume holograms in resonant media revealing the fifth- and higher-order nonlinearities has been analyzed. The experimental results on the energy and angular characteristics of laser radiation diffracted from a dynamic transmission grating in the solution of Rhodamine 6J dye and polymethine dye 3274U are considered. A theoretical model that allows for the calculation of the energy efficiency of light-beam conversion at different propagation directions of a reconstructing wave has been proposed.

Keywords: dynamic holograms, multiwave mixing, phase conjugation, resonant media, higher-order nonlinearities.

1. INTRODUCTION

Dynamic diffraction structures show promise as the elements of optical data processing systems owing to their ability to realize real-time control and conversion of complex light fields. So far practically all the investigations into the information capacity of diffraction methods have been concerned only with the linearity approximation for holographic recording of the wave front. However, a number of materials (semiconductor glasses, dyes, atomic media) are characterized by a high level of the fifth- or higher-order nonlinearity leading to distortion of the holographic-grating groove profile. Such a nonlinear recording of holograms has been traditionally considered as a negative factor resulting in the emergence of noise components in the diffracted radiation.[1] At the same time, high priority of the investigations associated with the development of control elements for laser fluxes stimulate the researchers to analyze new means of information processing on the basis of nonlinear holographic elements (spatial filtration, associative memory; double phase conjugation among other things allowing for visualization of complex phase portraits[2,3]). Due to the effect of absorption saturation, in resonant media these nonlinearities manifest themselves together with the cubic nonlinearity providing a means for realizing N-wave mixing. In this case, as a result of expanding the medium susceptibility into a series of dynamic grating components, new components emerge, which determine the possibility of the Bragg reading-beam diffraction of the second and higher orders.

Dynamic gratings are recorded by signal E_S and reference E_1 waves having the same frequency ω. Condition of the Mth-order Bragg diffraction (M=N/2-1) is satisfied through an increase of the reading angle or through the change in the recording-wave frequency. The experiments performed for measurement of the higher-order susceptibilities (using gases,[4,5] semiconductor glasses,[6,7] dyes[7,8] as nonlinear media) were based on recording and reading of dynamic gratings at the same frequency, and the fulfillment of the Bragg condition was achieved by changing an incidence angle of the reading beam. In the second case the reading wave E_2 has a frequency $M\omega$ and is counter-propagating relative to the reference one. This resulted in phase conjugation with simultaneous conversion of the radiation frequencies.[9-12] Both parametric scattering schemes have been illustrated in Fig. 1 for the case of six-wave mixing (N=6, M=2).

In this report we give an analysis of the schemes for multiwave mixing realized in media with saturable (resonance, thermal) nonlinearity in conditions revealing the nonlinearity of the fifth- and higher-order. Let us consider both cases of dynamic hologram reconstruction (at frequencies ω and 2ω). A dynamic hologram was formed by signal $E_S=A_S \exp[i(k_S \mathbf{r} - \omega t + \varphi_S)]$ and reference $E_1=A_1 \exp[i(k_1 \mathbf{r} - \omega t + \varphi_1)]$ waves; it was reconstructed by a wave $E_2=A_2 \exp[i(k_2 \mathbf{r} - 2\omega t + \varphi_2)]$ or $E_2=A_2 \exp[i(k_2 \mathbf{r} - \omega t + \varphi_2)]$ counter-propagating relative to the reference one. Under the conditions of quadratic

formation of a dynamic grating, when the diffraction was determined by the second components of the medium susceptibility expansion in a series of space harmonics of the dynamic grating, the induced nonlinear polarization $P \sim \left(E_1 E_s{}^*\right)^2 E_2$ was responsible for the wave E_D generation. The wave E_D direction is determined by the phase synchronism condition $k_D = 2k_1 - 2k_S + k_2$ (Fig. 1). And in conditions of the hologram reconstruction at a double frequency with opposite propagation directions of the plane reference and reading waves $k_2 + 2k_1 = 0$, the induced wave E_D propagates counter to the signal one E_S.
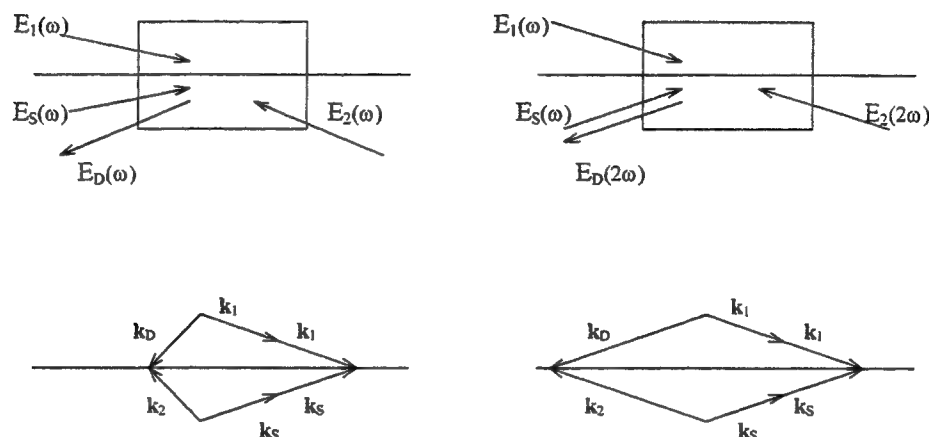

Fig.1. Mixing geometry and phase-matching diagrams.

In the experiments these methods of wave front transformation have been realized using the polymethine dye 3274U and Rhodamine 6J dye.

2. SIX-WAVE MIXING IN POLYMETHINE DYE 3274U

A theoretical study of the efficiency of six-wave mixing will be carried out for resonant media simulated with three-level schemes taking into account transitions in the ground singlet $S_0 - S_1$ as well as in the excited singlet $S_1 - S_2$ channels. Such a scheme may be used to describe the energy states of polymethine dye 3274U molecules.[13] A medium is assumed to absorb radiation at a frequency ω and be transparent at a double frequency. In this case, the formation of the diffracted wave is determined by the diffraction of the reading wave E_2 from thermal dynamic grating formed by the signal and reference waves. In the given approximation, the nonlinear susceptibilities $\chi(\omega)$ and $\chi(2\omega)$ determining the recording and reconstruction of a dynamic hologram have the form[14]

$$\chi(\omega) = \frac{n_0 \kappa_0}{2\pi} \left(\frac{\hat{\Theta}_{12}}{B_{12}} - \frac{\hat{\alpha}I + \hat{\beta}I^2}{1 + JI + \beta I^2} \right), \tag{1}$$

$$\chi(2\omega) = \frac{n_0 \kappa_0}{2\pi} \frac{a_t I + b_t I^2}{1 + JI + \beta I^2}, \tag{2}$$

where $a_t = \sigma\left(1 - \mu_{21}\right)$ and

$$\hat{\alpha} = a + i\alpha = \left(\hat{\Theta}_{12} + \hat{\Theta}_{21} - \hat{\Theta}_{23}\right)/vP_{21} - \sigma(1 - \mu_{21}),$$

$$\hat{\beta} = b + i\beta = \left[B_{23}\left(\hat{\Theta}_{12} + \hat{\Theta}_{32}\right) + B_{32}\left(\hat{\Theta}_{12} + \hat{\Theta}_{21} - \hat{\Theta}_{23}\right)\right]/v^2 P_{21} P_{32} -$$
$$- \sigma\left[B_{32}\left(1 - \mu_{21}\right)/vP_{32} + B_{23}\left(1 - \mu_{32}\right)/vP_{21}\right],$$

$$J = \left(B_{12} + B_{21}\right)/vP_{21} + B_{32}/vP_{32},$$

$$b_t = \sigma \cdot \left[B_{32}\left(1 - \mu_{21}\right)/vP_{32} + B_{23}\left(1 - \mu_{32}\right)/vP_{21}\right].$$

Here, $\sigma = 2\omega \cdot \left(dn/dT\right) \cdot t / cC_\rho$, dn/dT is the thermo-optical coefficient; C_ρ is the specific heat capacity; t is the time; P_{21} and P_{32} are the summary probabilities of spontaneous and nonradiative transitions in the channels 2-1 ($S_1 - S_0$), 3-2 ($S_2 - S_1$) channels; μ_{ij} is the quantum yield of luminescence in the $i - j$ channel; $v = c/n_0$ is the speed of light in a medium; n_0 is the nonresonant component of the refractive index; κ_0 is the linear coefficient of extinction; and $\hat{\Theta}_{ij}(\omega) = \Theta_{ij}(\omega) + iB_{ij}(\omega)$ is a complex function describing the spectral properties of the resonant transition $i - j$, where $\Theta_{ij}(\omega)$ is related to Einstein's coefficient $B_{ij}(\omega)$ by dispersion relations.

A system of equations describing six wave mixing for nonlinear polarization $P \sim \left(E_1 E_S^*\right)^2 E_2$ has the form

$$\frac{\partial E_{1,S}}{\partial z} = i\frac{2\pi\omega}{cn_0}\left(E_{1,S}\chi_0(\omega) + E_{S,1}\chi_{\pm1}(\omega)\right),$$

(3)

$$\frac{\partial E_{2,D}}{\partial z} = -i\frac{4\pi\omega}{cn_0}\left(E_{2,D}\chi_0(2\omega) + E_{D,2}\chi_{\pm2}(2\omega)\right),$$

where $\chi_m = \frac{1}{2\pi}\int\limits_{-\pi}^{\pi}\chi(\zeta)\exp\left(-im\zeta\right)d\zeta$ are the components of expansion of nonlinear medium susceptibility χ in the Fourier series in terms of the grating harmonics with $\zeta = (\mathbf{k}_1 - \mathbf{k}_S)\mathbf{r}$. The term with $\chi_0(\omega)$ takes into account the modulation of both the absorption coefficient and refractive index through a medium bleaching in the interference field formed by the reference and signal waves and $\chi_{\pm1}(\omega)$ determines to rescattering of waves from the amplitude-phase grating written by these same waves, $\chi_0(2\omega)$ describes phase-shift, and $\chi_{\pm2}(2\omega)$ describes the parametric coupling of reading and diffracted waves.

For the intensities of reference and signal waves $I_{1,S}$ lower than or of the order of the saturation intensity of the principal singlet-singlet transition the spectroscopic properties of a resonant medium are determined by bleaching of the $S_0 - S_1$ transition and linear absorption from the excited singlet S_1 level. In view of (1) and (2), the expression for the parametric coupling coefficient of waves $\chi_{\pm2}(2\omega)$ virtually determining the diffraction efficiency of a dynamic hologram can be represented in the form

$$\chi_{\pm2}(2\omega) = \frac{a_t - b_{t0}/\alpha}{\alpha}\left(1/A - 2(1 + \alpha(I_1 + I_S))/A(1 + \alpha(I_1 + I_S) + A)\exp(\pm i2(\varphi_1 - \varphi_S)),\right. \quad (4)$$

where $A = \overline{\left(1 + 2\alpha(I_1 + I_S) + \alpha^2(I_1 - I_S)^2\right)}$ and $b_{t0} = \sigma B_{23}(1 - \mu_{32})/\nu P_{21}$. The factor $a_t - b_{t0}/\alpha$ entering into the expression for $\chi_{\pm 2}(2\omega)$ describes the dependence of the diffracted-wave formation efficiency on the spectral characteristics of a medium:

$$a_t - b_{t0}/\alpha = \sigma\left[(1 - \mu_{21}) - k_p(1 - \mu_{32})/k_0\right]. \tag{5}$$

Here, $k_p = k_0 B_{23}/(B_{12} + B_{21})$ is the coefficient of residual absorption, $k_0 = 2\omega\kappa_0/c$ is the initial absorption coefficient.

The above formulae make possible the determination of conditions for the efficient light-field conversion. Specifically, from (5) it is obvious that on condition $k_p(1 - \mu_{32}) = k_0(1 - \mu_{21})$ is satisfied, diffraction is absent since in this case the medium is a linearly absorbing one: $\chi(2\omega) \sim I, \chi_{\pm 2}(2\omega) = 0$.

For experimental realization of phase conjugation with simultaneous frequency doubling of the signal wave we used the experimental setup shown in Fig. 2. A dynamic hologram was recorded at the generation frequency of an yttrium aluminate garnet laser (emission frequency $\lambda = 1.06\mu m$, pulse duration $\tau = 9ns$), corresponding to the absorption band maximum of a solution of polymethine dye 3274U in isobutyl alcohol (bleaching intensity $\sim 13MW\ cm^{-2}$, lifetime of molecules in an excited state $\sim 10ps$).[15] A hologram was reconstructed by the second harmonic ($\lambda = 0.532\mu m$) of the same laser radiation, which was not actually absorbed by the dye solution. An aperture 3 mm in diameter selected the spatially homogeneous part of the radiation. A spectral splitter (3) and mirrors (8) formed the signal and reference waves. A mirror (4) directed the reconstructing wave opposite to the reference wave. The mirror (4) was movable enabling the read-out angle to be variable. Filters (6) made it possible to alter the total intensity of the recording radiation. The angle (~ 90 mrad) between the directions of the co-propagating pump wave and signal beam ensured in practice an overlap of the interacting waves over the whole length of the cell (L=0.5 cm) containing the dye solution. The intensity of the reference wave was monitored with a laser energy meter (9). The energy efficiency of the radiation conversion (i.e. the intensity ratio of the diffracted and reconstructing beams) was determined by a recording system based on photodiodes (5) and pulse digital voltmeters.
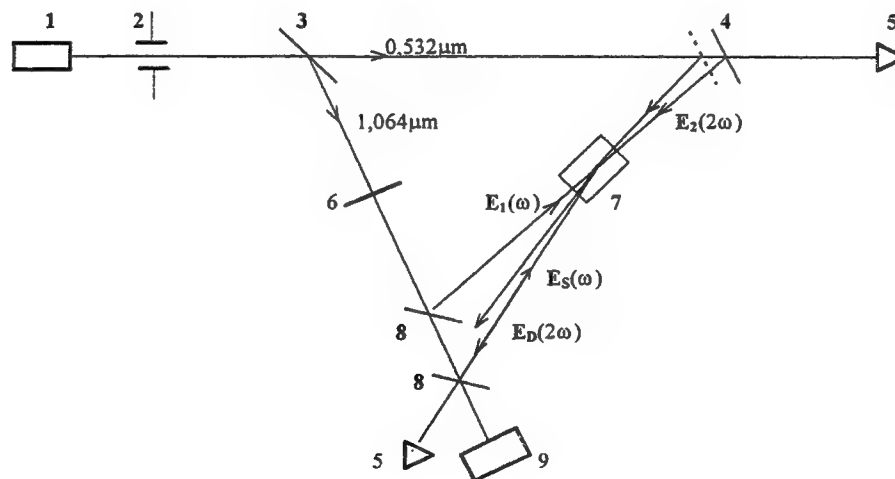

Fig. 2. Experimental setup: (1) laser; (2) aperture; (3) spectral splitter; (4,8) mirrors; (5) recording system; (6) optical filters; (7) cell with dye solution; (9) meter measuring the laser radiation energy.

113

Fig. 3 shows the diffraction efficiency of conversion $\xi = I_D / I_2$ as a function of the angle β between reading and recording waves (and $\beta=0$ in case of counter-propagating waves). The first maximum ($\beta=23$ mrad) is due to linear recording of dynamic holograms with the polarization $P \sim E_1 E_2 E_S^*$ responsible for generation of the wave E_D at a double frequency 2ω. The value of $\beta=23$ mrad is associated with phase synchronism $k_1+k_2=k_S+k_D$ leading to a decrease in the angle between the diffracted and reading waves as compared to the angle between the hologram recording beams.
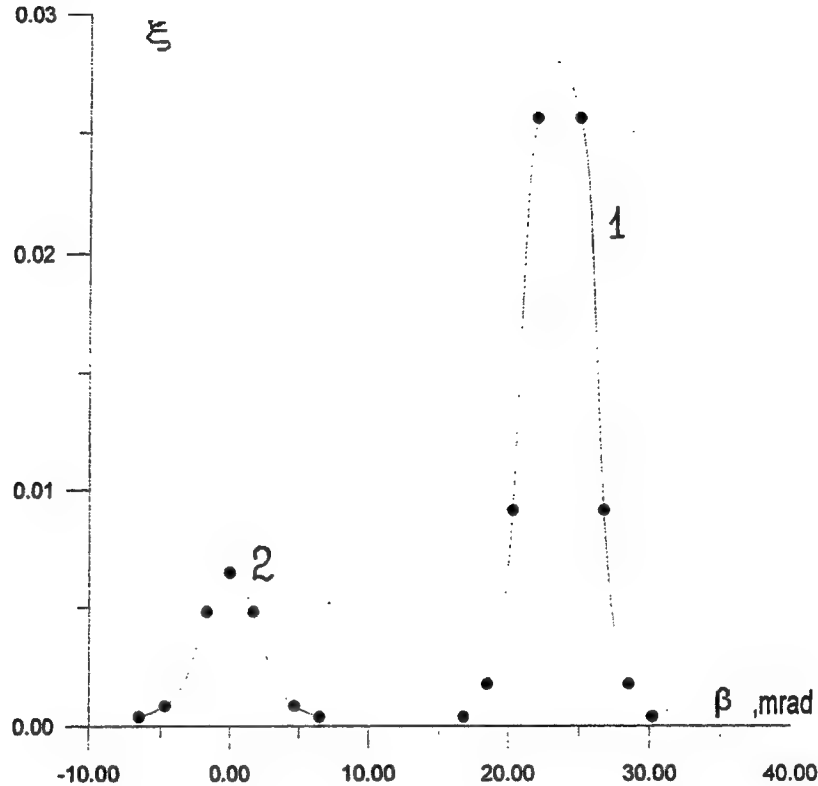

Fig. 3. Diffraction efficiency ξ as a function of the incidence angle of reading beam for $k_0 L = 3$ and $I_1=I_S=8\text{MWcm}^{-2}$. An X10 magnification was used for the diffraction efficiency values associated with the curve 2.

The presence of the second maximum in $\xi(\beta)$ in case of $\beta=0$ is due to the quadratic recording method of dynamic holograms, when the diffraction is determined by the second components in the medium susceptibility expansion into harmonics of the dynamic grating and the induced nonlinear polarization $P \sim \left(E_1 E_S^*\right)^2 E_2$ is responsible for generation of the wave E_D at a double frequency. As has been demonstrated previously, in this case the induced wave E_D is propagating in the counter direction to the signal one E_S ($k_D=-2k_S$) and has a double conjugate phase $\varphi_D = -2\varphi_S$. In such a manner the waves E_S and E_D have coincident surfaces of wave front at counter propagation directions, i.e. these waves possess the features of phase-conjugate waves

The dependence of the diffraction efficiency $\xi = I_D / I_2$ of a dynamic hologram on the intensity of the reference wave I_1 (in our experiments $I_1=I_S$) is plotted in Fig. 4. The conversion efficiency $\xi=10^{-3}$ was three orders of magnitude higher than the formation efficiency of dynamic holograms in polymers by resonant two-photon absorption.[2]

The solid line in Fig. 4 gives the calculated function of the diffraction efficiency. The parameters of the medium and radiation correspond to the experimental conditions (n_0=1.36, τ=9ns, $(dn/dT)C_\rho^{-1} = -1.5*10^{-4}J^{-1}cm^3$, $B_{23}/B_{12} = 0.43$) and the quantum efficiency of luminescence in the ground and excited channels is close to zero μ_{21}=0.003, μ_{32}=0.0001.[13-16] The dependence of the diffraction efficiency on the intensity of the waves used to form a hologram at the entry to the nonlinear medium $I_1=I_S$ is plotted in Fig. 4 with a normalization factor 1/3 taking account of the fact that the solution of this system of equations gives the diffraction efficiency at the end of a pulse, whereas the experimental results give the efficiency averaged over the whole pulse.[17] A good quantitative agreement is observed between the experimental and theoretical data.
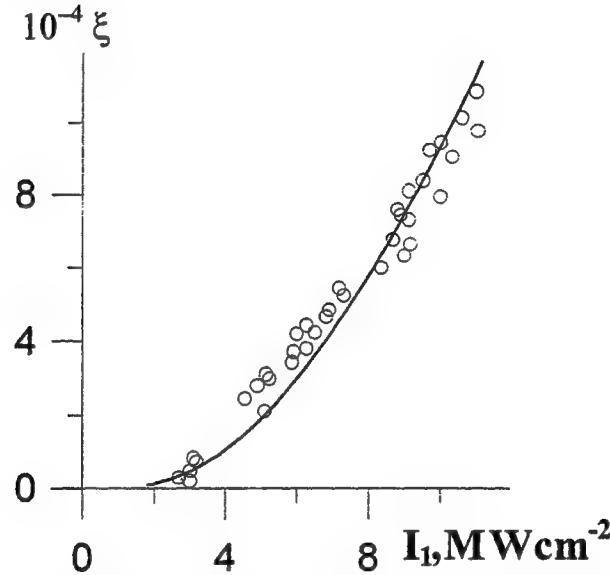

Fig. 4. Experimental (circles) and calculated (continuous curve) dependencies of the diffraction efficiency ξ on the intensity of the hologram-recording waves.

3. MULTIWAVE MIXING IN RHODAMINE 6J DYE

An analysis for the efficiency of light-field conversion upon diffraction from the nonlinearly formed holograms and in case of the frequency-degenerate multiwave mixing may be performed taking as an example the dynamic hologram recording in ethanol solution of the Rhodamine 6J dye. A theoretical description of such an interaction may be conducted with the use of coupled equations similar to the system (3). The first equation in this new system describing the hologram-recording waves remains the same, and the second one is of the form:

$$\frac{\partial E_{2,D}}{\partial z} = -i\frac{2\pi\omega}{cn_0}\left(E_{2,D}\chi_0(\omega) + E_{D,2}\chi_{\neq M}(\omega)\right),$$

where M=N/2-1 is a diffraction order realized within the medium with the (N-1)th-order nonlinearity. Diffraction of different orders from a volume holographic grating has been realized at different propagation directions of a reconstructing wave conforming to the condition of Bragg diffraction from different spatial components of the grating.

The diffraction efficiency of conversion $\xi = I_D/I_2$ as a function of the angle β between reading and recording waves is given in Fig. 5. Experimental setup was the same, as in the previous case (Fig. 2), but with a semitransparent mirror instead of beamsplitter 3. In the process, the second harmonic of YAG-laser was used both for the recording and reconstruction of dynamic holograms. The angle between the recording waves was $\alpha = 30mrad$. With counter propagation direction of the reading wave ($\beta=0$) the classical case of phase conjugation upon four-wave mixing has been realized. The second maximum in the dependence of diffraction efficiency on the reading angle was observed with

$\beta \approx \alpha / 2$ and conformed to the phase synchronism condition $k_D = 2k_1 - 2k_S + k_2$ (Fig. 1). As previously stated, it is attributed to the fifth-order nonlinearity ($P \sim \left(E_1 E_S^*\right)^2 E_2$). The third maximum in the region of $\beta \approx \alpha$ conforms to the condition of phase synchronism $k_D = 3k_1 - 3k_S + k_2$. In this case the eight-wave mixing is registered at a seventh-order nonlinearity $P \sim \left(E_1 E_S^*\right)^3 E_2$.

It should be noted that diffracted beams in the afore-mentioned cases are differing not only in the propagation direction, but also in the wave phase making it possible to rely on simultaneous realization of various operations of the wave front transformations.
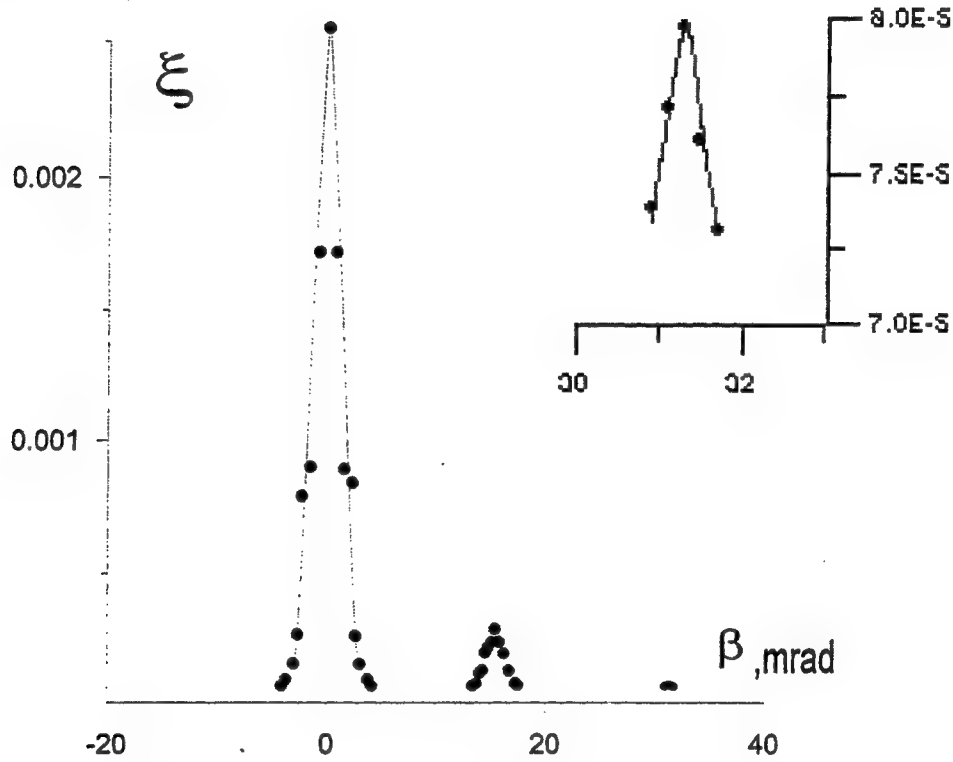

Fig. 5. Diffraction efficiency ξ as a function of the incidence angle of reading beam for Rhodamine 6J dye for $k_0 L = 0.5$ and $I_1 = 2I_S = 0.2 \text{MWcm}^{-2}$.

4. CONCLUSION

Theoretical and experimental studies into the light-beam conversion in conditions of multiwave mixing have made it possible to develop the diffraction method for wave-front transformation. It has been proposed to use the above schemes of interaction for conversion of wave fronts of the laser beams with a developed transversal structure. Considering the fact that reconstruction of diffracted beams in different directions may be realized concurrently, the proposed approach could be used when developing multi-functional elements for the optical data processing systems. Specifically, it should be noted that the use of the proposed scheme for recording and reconstruction of dynamic holograms opens new possibilities for real-time frequency conversion of laser radiation (both for plane waves and composite images). In the process, frequency conversion may be combined with the phase-conjugation effect thus allowing for compensation of distortions when radiation is propagating in the phase-inhomogeneous media.

5. REFERENCES

1. R.J.Collier, C.B.Burckhardt, L.H.Lin, Optical Holography, Academic Press, 1971.

2. F. Charra and J-M. Nunzi, "Nondegenerate multiwave mixing in polydiacetylene. Phase conjugation with frequency conversion", J.Opt.Soc.Am.(B), **8**(3), pp. 570-577, 1991.

3. S.M. Karpuk, A.S. Rubanov, A.L. Tolstik and A.V. Chaley, "Double phase conjugation upon nondegenerate four-wave mixing", Proc. SPIE, **2771**, pp. 149-155, 1995.

4. R.K. Raj, Q.F. Gao, D. Bloch and M. Ducloy, "Direct observation of high-order optical susceptibilities via angularly-resolved multiwave mixing", Opt. Commun., **51**(2), pp. 117-120, 1984.

5. J.W.R. Tabosa, C.L. Cesar, M. Ducloy and J.R. Rios Leite, "Degenerate multiwave mixing in SF_6", Opt. Commun., **67**(3), pp. 240-244, 1988.

6. A. Blouin, P. Galarneau and M-M. Denariez-Roberge, "Degenerated six-wave-mixing using high order Bragg diffraction in semiconductor-doped glass", Opt. Commun., **72**(3,4), pp. 249-252, 1989.

7. A. Blouin, M-M. Denariez-Roberge and P. Galarneau, "Degenerate N-wave mixing in a saturable absorber", J.Opt.Soc.Am.(B), **8**(3), pp. 578-583, 1991.

8. A. Blouin and M-M. Denariez-Roberge, "Theory and experiment of degenerate six-wave mixing in both isotropic and anisotropic saturable absorbers", IEEE J. Quantum Electron., **29**(1), pp. 227-235, 1993.

9. V.V.Ivakhnic and V.I.Nikonov, "Double wave-front conjugation with frequency conversion upon nondegenerate six-wave mixing", Opt. Spektrosk., **75** (2), pp. 385-391, 1993.

10. S.M. Karpuk, A.S. Rubanov, A.L. Tolstik and A.V. Chaley, "Quadratic recording of dynamic holograms in resonance media", Pis'ma Zh. Tekh. Fiz., **20**(12), pp. 4-8, 1994 [Technical Physics Letters, **20**(6), pp. 475-476, 1994].

11. S.M. Karpuk, A.S. Rubanov and A.L. Tolstik, "Double phase conjugation in quadratic recording of dynamic holograms in resonance media", Opt. Spektrosk., **80**(2), pp. 313-318, 1996 [Optics and Spectroscopy, **80**(2), pp. 276-280, 1996].

12. S.M. Karpuk, A.S. Rubanov and A.L. Tolstik, "Nonlinear formation of dynamic holograms in a dye solution", Kvantovaya Elektron., **24**(1), pp. 52-54, 1997 [Sov. J. Quantum Electron., **27**(1), pp. 49-51, 1997].

13. V.I. Prokhorenko, M.V. Melishchuk and E.A. Tikhonov, "Nonlinear absorption spectroscopy of polymethine dyes in the spectral range of 1.064 μm", Ukr.Fiz.Zh., **30**(10), pp. 1480-1488, 1985.

14. V.V. Kabanov, A.S. Rubanov and A.L. Tolstik, "An influence of transitions between excited singlet and triplet states upon phase response of dye solutions", Kvantovaya Elektron., **15**(8), pp. 1681-1686, 1988 [Sov. J. Quantum Electron., **18**, p. 1047, 1988].

15. A.V. Masalov, V.A. Petukhov, N.V. Timokhovich, L.B. Vodovatov and M.V. Gorbunkov, "Measurements of excited state lifetimes in dye molecules by the curves of solution bleaching by the polarized light", Kvantovaya Elektron., **18**(6), pp. 749-757, 1991 [Sov. J. Quantum Electron., **21**, p. 680, 1991].

16. M.A. Vasil'eva, V.B. Gul'binas, V.I. Kabelka, A. V. Masalov and V. P. Syrus, "Measurements of picosecond times of bleachable dyes relaxation using crossed polarizers technique" Kvantovaya Elektron., **10**(2), pp. 415-419, 1983 [Sov. J. Quantum Electron., **13**, p. 233, 1983].

17. M.H. Garrett and H.J. Hoffman, "Thermally induced phase-conjugation efficiency and beam-quality studies", J.Opt.Soc.Am., **73**(5), pp. 617-623, 1983.

Experimental study of heating optical materials by pulsed CO_2 laser radiation

E.I.Dmitriev, A.S.Sakyan, A.N.Starchenko, D.A.Goryachkin[a]

Institute for Testing Optoelectronic Devices, Sience Centre " S.I.Vavilov State Optical Institute",
Sosnovii Bor, Leningrad region, Russia
Research Institute for Laser Physics Sience Centre[a] " S.I.Vavilov State Optical Institute",
St.Petersburg, 199034, Russia

ABSTRACT

The results are presented on experimental investigations of action onto an optical glass BK-7 and some other materials of a CO_2 laser radiation with the pulse duration of 20-70 µs and the energy density of 0.1-3 J/cm^2. The dynamics of a thermal response, temperature of heating and emissivity of irradiated glass samples are under consideration. The results obtained can be used in imaging techniques for objects selection.

1. EXPERIMENTAL SET-UP AND METHODICS OF MEASURING

An optical scheme of the experimental set-up is shown in Fig.1. The radiation of a pulse CO_2-laser, after passing wedge 2, which splitted a part of the beam for measuring the output energy and temporal pulse shape of the radiation, was reflected by wedges-attenuators 7, 8 and focused by lens objective 9 onto the surface of a sample under study. The focal spot diameter could be varied from 1mm to 1cm. At distance l from the sample, variable from 75 to 225 mm, high-sensitive detector 11 with renewable filter 12 was placed.
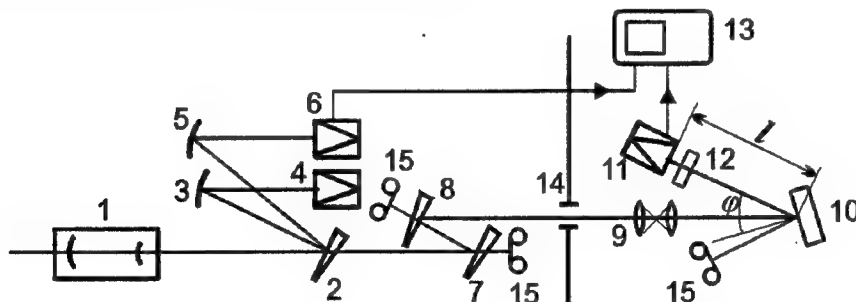

Fig.1. Optical schematic of the experimental set-up. 1-pulse CO_2-laser; 2,7,8-wedges; 3,5-focusing mirrors; 4-calorimeter; 6-photon-drag detector; 9-objective; 10-irradiated glass sample; 11-HgCdTe-photodetector; 12-renewable filter; 13-oscilloscope; 14-shielding screen; 15-radiation absorbers.

A cooled photoresistor with a sensitive element (0.6mm-in size) on the base of a trial composition HgCdTe was used as the thermal emission detector. Its signal was recorded by a two-channel storing oscilloscope (one of the sweep traces). The second trace was used to record currently a temporal profile of the laser radiation pulse. Angle φ between the observation line and a normal to the sample surface (see Fig. 1) was changed from 10 to 40 degrees depending on a distance between the sample and detector. Because of slight dependence of a scattering indicatrix of dielectric materials on an observation angle up to 60 degrees (see[1], for example), this change in angular orientation of the detector resulted only in variation of the effective irradiated area of the sample (area of the thermal emission source) by the expression: $A_{eff} =A_s \times cos(\varphi)$, where A_s -is the laser radiation focal spot diameter.

The information on a temperature of heating the sample by laser radiation can be derived from the temperature dependence of its spectral radiant intensity (or brightness) $L(\lambda,T)$. In the classic optical pyrometry temperature evaluations are typically based on determining the ratio between the spectral radiant intensities of an emitter measured in two quasi-monochromatic spectral bands[2]. In our research, at operation in the middle-infrared the possibility of performing high-sensitive measurements in a wide wavelength band (that is necessary to enlarge the signal/noise ratio)

was not evident. By this reason for evaluating the irradiated sample temperature we had to use the methodics based on measuring the thermal fluxe intensities, which passed through filters with various spectral transmissivities $\tau_i(\lambda)$, and on determining ratios between the intensities, obtained for various pairs of the filters.

At carrying-out the experiments the following set of filters was used:
- made of glass IKS-5 with the thickness of 2 mm (transparent up to 4.4 μm);
- made of glass BS-14 with the thickness of 2 mm (to 5.2 μm);
- made of crystal LiF with the thickness of 4.4mm (to 7.3 μm);
- made of crystal NaF with the thickness of 27mm (to 8 μm).

All these materials have a strong absorption in 10.6 μm-region, so the filters were used additionally to suppress the reflected and scattered radiation of the "heating" CO_2 laser. In the opposite case the background level of 10.6 μm radiation was high, that made it impossible to obtain the low-intensity thermal response under study.

Radiant temperature T of the heated sample with emissivity ε can be, as usually, accepted equal to the temperature of the heated black-body emitter, which is characterised by the same fluxe intensities ratio. By this reason, to interpret correctly the data obtained and to determine the sample temperature and «blackness» we needed previously to calibrate our detector in a set of separate experiments. At this calibration the black-body model was heated in a step-wise manner and intensities of fluxes, emitted by it, were measured with various spectral filters. In the considered temperature interval the dependence of detecting signal U for i-th filter on a temperature for the both black-body model and sample under investigation can be well approximated by the expression:

$$U_i \ (T) = a_i \times (T)^{bi} \tag{1},$$

where a_i, b_i - are coefficients, which can be calculated when calibrating the detector by the black-body model for the corresponding filter. From approximation (1) the temperature can be determined by ratio R of signals for each two filters from the expression:

$$T^{b1-b2} = R \times (a_2/a_1) \tag{2},$$

where $R = U_1/U_2$, and the signals for two various filters are measured at the same irradiation energy density. The sample emissivity and true temperature T_{true} can be estimated for several filters by the radiant temperature from the expression:

$$\varepsilon = (T/T_{true})^{bi} \tag{3}.$$

2. EXPERIMENTAL RESULTS

At carrying-out the experiments the most attention has been concentrated on the study of BK-7 glass (polished and roughly-burnished samples of 8-10 mm-thickness). Besides, samples, made of crystals Si and Ge, as well as of painted metals were under investigation in a few tests. An effective energy density of the laser radiation on the sample surface (an exposure), which was calculated with taking into account an effective area of irradiation A_{eff}, was varied within $H_{eff} = 0.1$-3 J/cm^2. At the densities exceeding about 0.8-1 J/cm^2 a light-induced breakdown (little sparks or a flame) occurred on the polished glass surface, that disturbed a purely thermal nature of the beam action. Hereinafter, the flame-free mode of action will be named as a below-threshold mode, and an interaction followed by the flame occurrence - as an above-threshold mode.

Fig. 2a represents oscillograms of temporal profiles of the laser radiation pulse (about 20μs in duration) and of the thermal response (the detector signal) from the irradiated sample which was typical for the above-threshold interaction mode. Fig. 2b represents similar oscillograms but obtained in the below-threshold mode. It is worth to note, that in the presence of a near-surface flame the purely thermal flux intensity became less than in the below-threshold mode, due to blocking the laser radiation by the light-induced plasma flame.

Fig. 3 shows the below-threshold thermal responses recorded at various energy densities of the "heating" radiation. The results of studying the dynamics of the thermal responses have demonstrated, that in the both below- and above-threshold interaction mode the signal rise during irradiation pulse was almost linear. The signal (and the sample temperature), as it is seen from the shown oscillograms, peaked till the end of the laser radiation pulse. The maximum temperature rise of the sample surface at $H_{eff} = 0.7$ J/cm^2 (the below-threshold mode) was evaluated by using the methodics described above, as about 100 K. As this takes place, the glass sample emissivity was appeared to be close to 1, that is in a satisfactory agreement with results of theoretical thermal physics calculations[2]. In the above-threshold mode

at H_{eff} = 2.7 J/cm² the peak flame temperature was estimated not less than 1200K, with the radiant temperature of 900K, that gives the value of the flame emissivity ε = 0.3.
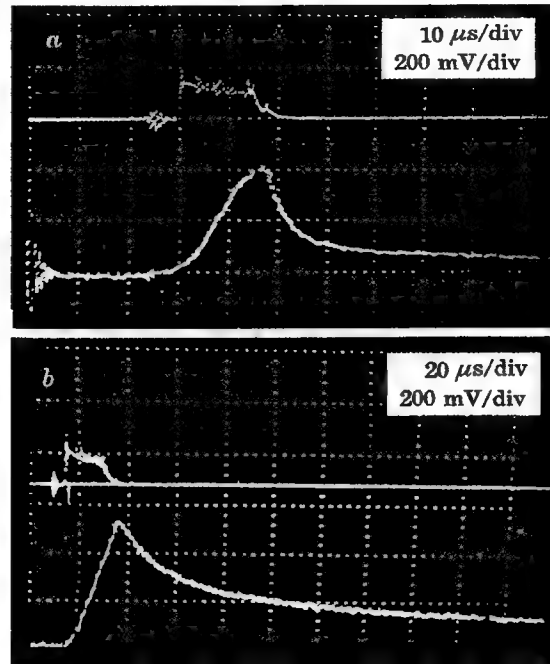

Fig.2. Oscillograms of the laser radiation pulse (the upper) and thermal response (in the bottom) in the above-threshold, at H_{eff}=2.7 J/cm² (a) and below-threshold, at 0.5 J/cm² (b) mode of interaction
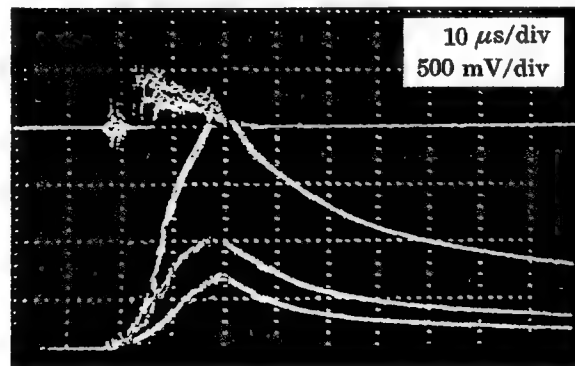

Fig.3. Oscillograms of the laser radiation pulse (the upper) and thermal response (in the bottom) obtained at laser energy densities of 0.26, 0.36 and 0.66 J/cm² respectively.

Fig.4 illustrates the dependence of maximum temperature on the sample surface (obtained by processing peak values in oscillograms) on the effective energy density in the laser beam spot in the below-threshold mode of irradiation. The dependence is close to linear that corresponds to theoretical predictions[2]. Note, that when a roughly burnished glass surface was irradiated, the below-threshold thermal flux from the sample has not been recorded, since an optical breakdown occurred even at exposures of about 0.1 J/cm².

Temperature relaxation periods (decay time of a thermal response pulse at 0.5-intensity level) were considerably different in below- and above-threshold modes and equal to 40-70 and 7-10 μs, respectively (compare oscillograms in

Fig. 2a and b). After the first "fast" stage of the temperature relaxation the slowly decreasing signal at all exposures was observed with the decay time of 6-8 ms. Most likely this signal corresponded to cooling process of the sample internal layer. In accordance with the data of[3], a depth of the heated layer for glasses may exceed 30 μm and it is thinner, when the surface temperature is higher.
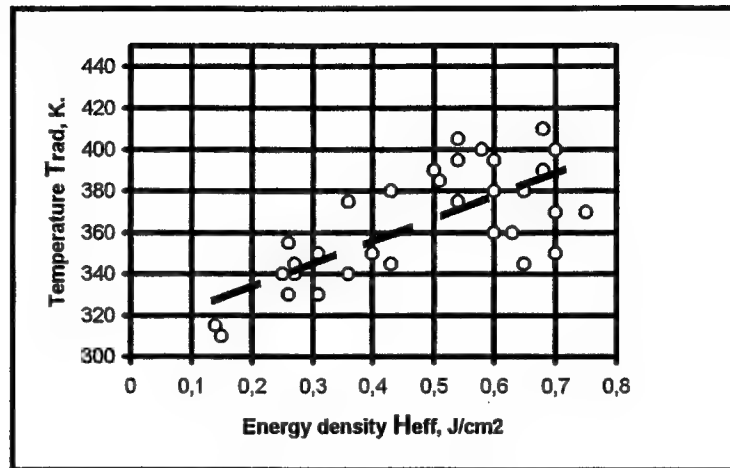

Fig.4. The calculated dependence of maximum temperatures on the sample surface on laser energy density in the below-threshold mode of irradiation.

3. CONCLUSION

The main results of our research can be formulated as follows:
- below-threshold illumination of a BK-7 glass surface by a pulse CO_2 laser radiation with a 20-70 μs-duration leads to a temperature rise of 100-200 K within about 30 μm-in deep surface layer;
- maximum temperature of the surface in the below-threshold mode of irradiation increases linearly when the laser radiation energy density rises;
- temperature relaxation of the heated layer in the below-threshold mode of irradiation can be divided into two stages: the "fast" relaxation which lasts for 40-70 μs and results from emission processes on the surface, and the "slow" stage with the duration up to ten milliseconds resulted from diffusion cooling of internal glass layers;
- decay time of the response obtained from a light-induced flame is an order of magnitude shorter than the flame-free one, the sample temperature in the above-threshold mode is lower due to blocking the laser radiation by the flame.

4. ACKNOWLEDGMENTS

5. REFERENCE

1. L.Z. Kriksunov, Reference-book on the infrared technics , Moskwa.: Sov.radio, 1978, 400 p., (in Russian).

2. D.Ya. Svet, Optical methods of measuring real temperatures , Moskwa.: Nauka, 1982, 296 p., (in Russian).

3. A..D. McLachlan, F.P. Meyer, "Temperature dependence of the extinction coefficient of fused silica for CO_2 laser wavelengths", *Applied Optics,* vol. 26, No. 9, .pp.1728-1731, 1987.

Laser-induced two-dimensional submicron periodical structures on the high-reflectance surface

Vasily V. Valyavko, Vladimir P. Osipov

Stepanov Institute of Physics, National Academy of Sciences of Belarus,
70 F.Scaryna Ave., 220072, Minsk, Belarus E-mail: ifanbel@ifanbel.bas-net.minsk.by

ABSTRACT

There are discussed physical aspects of one-pulse laser forming of two-dimensional periodical surface microstructures with the characteristic sizes about 30 times less than the used laser radiation wavelength. It is experimentally shown that by means of TEA carbon dioxide laser treatment of the 800 A°-aluminium film, evaporated on the K8-glass substrate, the periodical system of microhollows with the diameter about 0.5 micron can be formed. The proposed method may be useful for surface microstructures producing in microelectronics or precise filters fabrication.

Keywords: periodical surface structures, laser processing of the solid-state surface, intracavity laser treatment.

1. INTRODUCTION

In preceding works [1,2] it was theoretically and experimentally shown the possibility of the submicron equidistant parallel grooves forming on thin metallic film surface by the single pulse laser processing. It was achieved by means of the original intracavity laser treatment method. The main feature of this method is that the processed surface plays the role of the laser cavity mirror, turning the intracavity laser beam, as shown at the Fig.1. This situation is followed by the multibeam interference picture forming on the mirror, turning the laser beam. When the laser radiation intensity in the interference maxima overcomes the damage threshold of the mirror surface, on the processed areas of the mirror there are formed periodical surface structures (which period may be evaluated according to the Fig.2), corresponding to the general view of the interference picture (Fig.3).
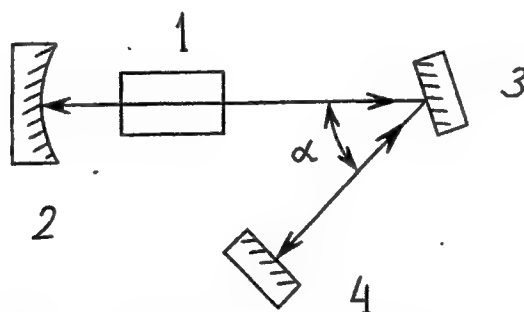

Fig.1. The basic optical scheme of the periodical structures forming on the solid-state surface: 1 - active medium; 2 - 100%-reflectivity concave mirror; 3 - turning mirror (processed sample); 4 - 100%-reflectivity mirror; α - turn angle.

Firstly, it was experimentally demonstrated [1], that TEA CO_2-laser (150-ns pulse duration, 0.2-Joule pulse energy, 10.6-micron radiation wavelength) processing of the aluminium film (800 A°-thickness, 98%-reflectivity coefficient), evaporated on the optical glass K8 substrate, allowed to form the system of the extremely narrow parallel grooves on the surface of the sample by one laser pulse treatment.
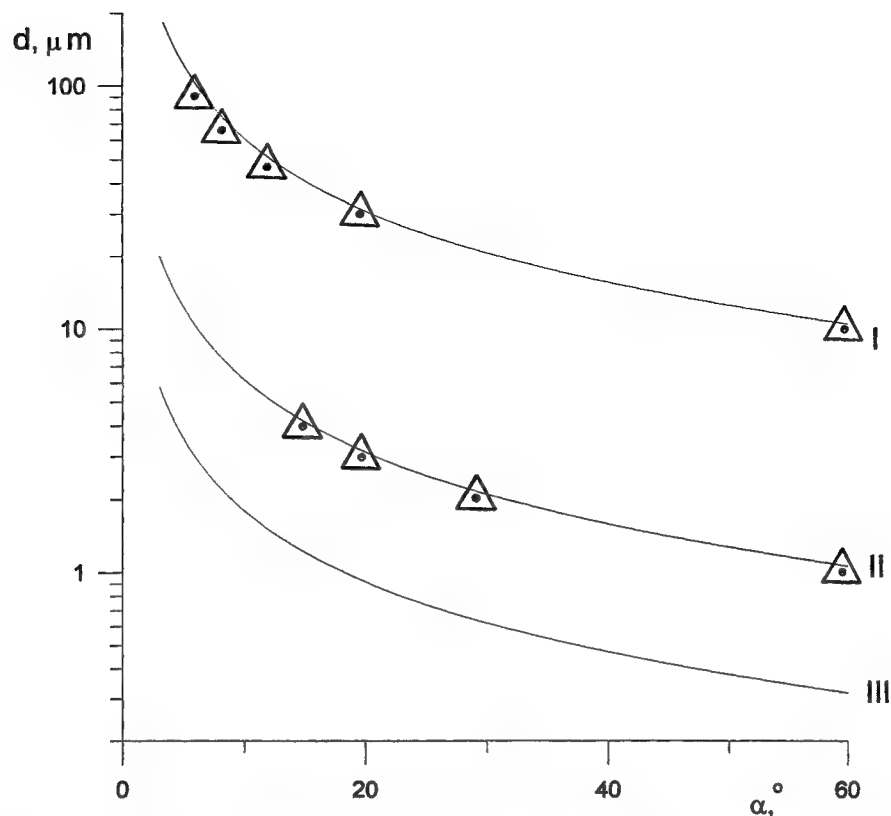
Fig.2. The calculated dependencies of the distance d between the grooves on the laser beam turn angle α:
I - CO_2-laser, λ=10.6 μm; II - Nd-glass laser, λ=1.06 μm; III - XeCl-laser, λ=0.308 μm, Δ - the experimental data.

a)   b)   c)
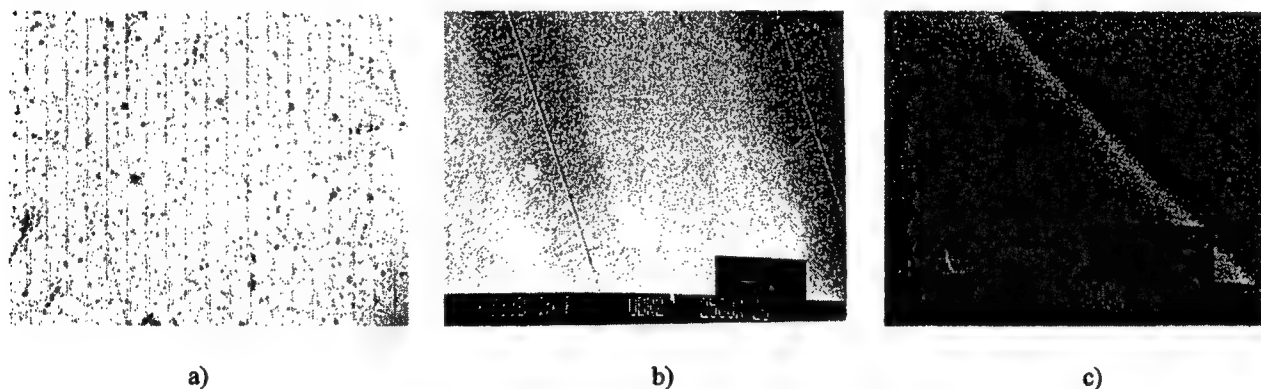
Fig.3. The microphotographs of the 800 A°-Al-film surface, processed by the intracavity method (laser wavelength 10.6 μm, α=8.7°: a) [250X] magnification, optical microscope; b) [2500X] magnification, SEM; c) [25000X], SEM.

    The investigation of the treated zones by means of the scanning electron microscopy showed that the groove width is about 0.3 micron. The period of the grooves - distance between the grooves (depending on the beam turn angle and laser wavelength) may be changed from 7 to 500 microns. Therefore, this method has enabled to obtain one-dimensional submicron structures (namely, parallel narrow grooves) with the width about 30 times less than the wavelength of the used laser radiation.

    The aim of this work is the development of the intracavity laser treatment approach on the base of special laser cavity and the application of 1.06-μ laser in addition to 10.6-μ laser.

123

2. PHYSICAL ASPECTS OF THE TWO-DIMENSIONAL SUBMICRON STRUCTURES FABRICATION

It was shown [2], that the picture of the grooves, formed on the treated sample, is essentially determined by the mode structure of the laser beam, generated in the concrete laser cavity. The width of the grooves, formed on the treated surface, is determined by the cavity parameters and the longitudinal mode structure of the laser beam. However, the contrast of the groove picture (the ratio between the grooves period and the groove width) depends, in first turn, on the laser radiation spectrum width, the cavity length and the mirrors reflectance.

On the base of the developed intracavity approach it is proposed two new methods of periodical surface structures fabrication:

2.1. Subsequent processing.

The sample is processed by the first laser pulse. Then the sample is rotated to the 90° (or other angle) around the axis, which is perpendicular to its treated surface. After that, the second laser pulse processes the same area of the sample and forms another system of the parallel grooves, so the resulting picture looks as a grid. The elementary site of the grid may have a form of square, rectangle or parallelogram, depending on the grooves period and the magnitude of the angle of the mirror rotation.

2.2 Simultaneous processing.

Two additional cavity mirrors are introduced into the standard laser cavity scheme for intracavity processing in such way that laser beam is turned by the processed sample twice: firstly, in one plane and, secondly, in another plane, as it is shown in the Fig.4.
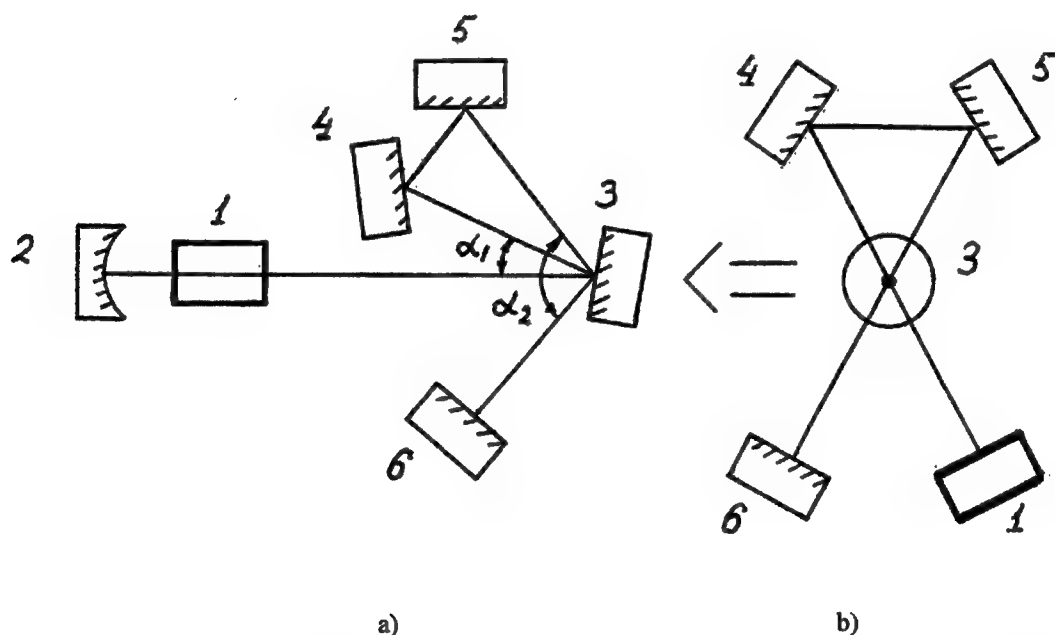

a)   b)

Fig.4. The cavity scheme for the simultaneous intracavity fabrication of two-dimensional submicron structures:
a) the projection to the plane of the paper; b) the view of the same cavity from the right side: 1 - active medium;
b) 2 - 100%-concave mirror; 3 - turn mirror (processed sample); 4,5,6 - 100%-reflectance mirrors; α_1, α_2 - turn angles of the laser beam.

During the laser pulse on the turn mirror (processed sample) there is formed an interference picture looking as a superposition of two systems of parallel narrow interference bands, that is in the form of a grid. Naturally, when in the sites of this grid the intensity of the laser radiation reaches the threshold of the optical strength of the surface material, there are formed periodical submicron surface structures, corresponding to the proper interference picture.
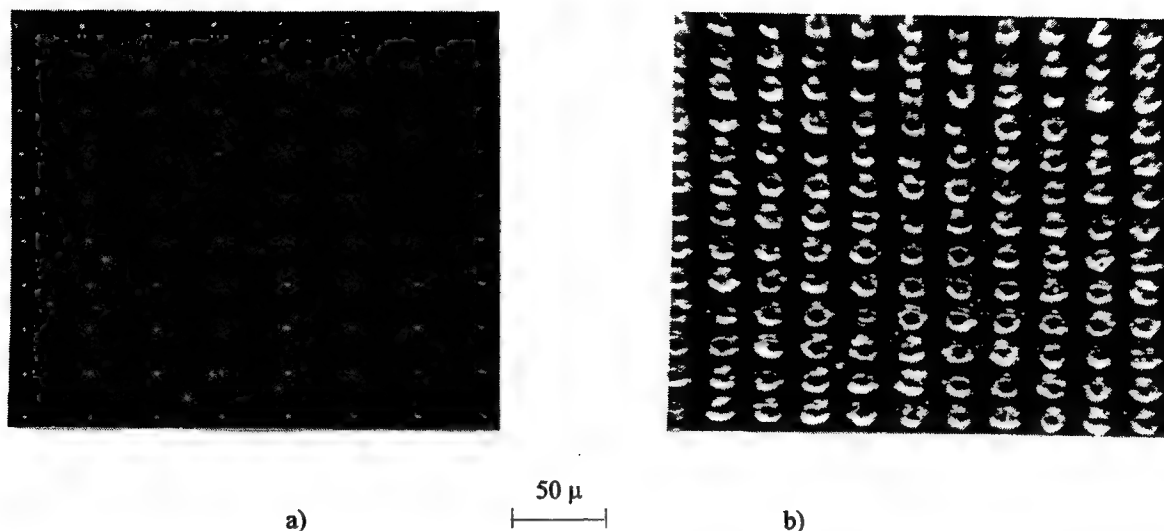
50 μ

a)   b)

Fig.5. The micrographs of the Al-film surface, processed by the one-pulse intracavity laser treatment (at 10.6-μ wavelength): the laser radiation intensity is a) near to the threshold; b) 10% over the threshold.

3. EXPERIMENTAL CASES

3.1. 10.6-μ laser treatment.

The optical scheme, shown in Fig.1, is used for a microfabrication of the submicron-size grids by the two subsequent laser pulses with the intermediate rotating of the processed sample, along the axis, which is perpendicular to the mirror plane. Earlier described [1] active element of the pulsed TEA CO_2-laser is used as an active medium 1. The main parameters of the laser are: pulse duration is equal to 150 ns, 0.2-Joule energy in TEM_{00}-mode, the diameter of the laser beam is about 6 mm; 10.6-micron radiation wavelength. The concave mirror 2, made of stainless steel 12X18H9T has the curvature radius 10 m. The optical glass substrates (having the diameter 40 mm and the thickness 10 mm) with evaporated aluminium film (800A° thickness) are used as the mirrors 3 - 6.

The system of micron and submicron periodical microhollows is fabricated by means of the optical scheme, shown in Fig.4. A treated sample 3 is installed at the distance 200 cm from the mirror 2, which is installed at the back end of the active element 1 (with the length of 50 cm). The distances between mirrors 4-5 and 1-6 are of 5 cm; 4-6 and 1-5 - 7 cm; 3-4 and 3-5 - 23 cm; 3-6 - 28 cm.

In the Fig.5a,b there are shown the micrographs of the sample surface, processed by the simultaneous method, according to the optical scheme, shown in the Fig.4.

When the summary laser radiation intensity is near to the threshold of the surface damage, on the processed sample area (with the diameter of about 3 mm) there is fabricated the periodical system of microhollows, which diameter is about 0.5 micron. The horizontal and vertical periods of the microhollows system are 48 and 33 microns, correspondingly. At the small increasing of the laser radiation intensity it is observed the rapid rising of the hollow diameter. For an example, 10%-increasing of the intensity results in the microhollows system with the size of the hollows about 15×20 microns (as shown in the Fig .5b).

3.2. 1.06-μ laser treatment.

Another series of experiments was carried out with the Nd-glass laser, working at free generation regime. The main parameters of the laser are: pulse duration is equal to 0.5 ms, 0.03-Joule energy in TEM_{00}-mode, the diameter of the laser beam is about 4 mm; 1.06-micron radiation wavelength. The concave interference mirror 2 has the curvature radius 6.8 m. The optical glass substrates (having the diameter 40 mm and the thickness 10 mm) with evaporated aluminium film (800A° thickness) are used as the mirrors 3 - 6. A treated sample 3 is installed at the distance 27 cm from the mirror 2, which is installed at the back end of the active element 1 (with the length of 16 cm). The distances between mirrors 4-5 and 1-6 are of 10 cm; 4-6 and 1-5 - 10 cm; 3-4 and 3-5 - 19 cm; 3-6 - 22 cm.

The resulting microhollows systems with the different periods (about 2 microns at less than 0.3-μ hollow width) are shown in the Fig.6a,b.

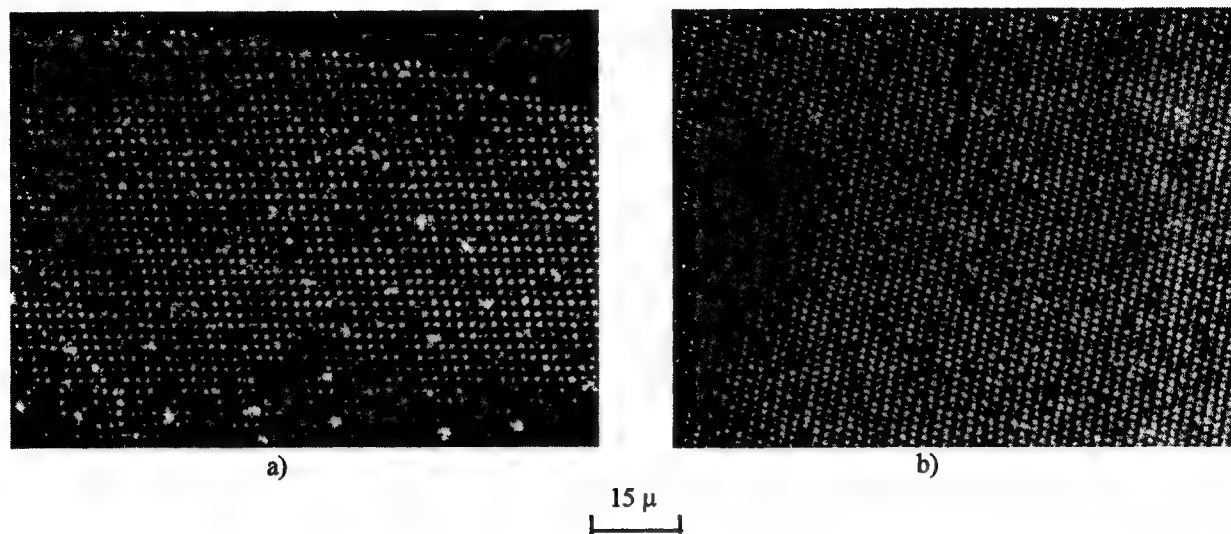a)   b)

15 μ

Fig.6. The micrographs of the Al-film, processed by the 1.06-μ intracavity two-pass laser treatment. The relation between structures periods is equal to: a) 1 : 1; b) 1 : 1.5.

The introduction of the round diaphragm with the diameter of several millimeters into the laser cavity (in case of one-way optical scheme similar to Fig.1) results in the formation of the concentric areas, covered with the periodic submicron structures, as shown in the Fig.7. The form and the amount of the circles depend on the place of the diaphragm in the cavity.
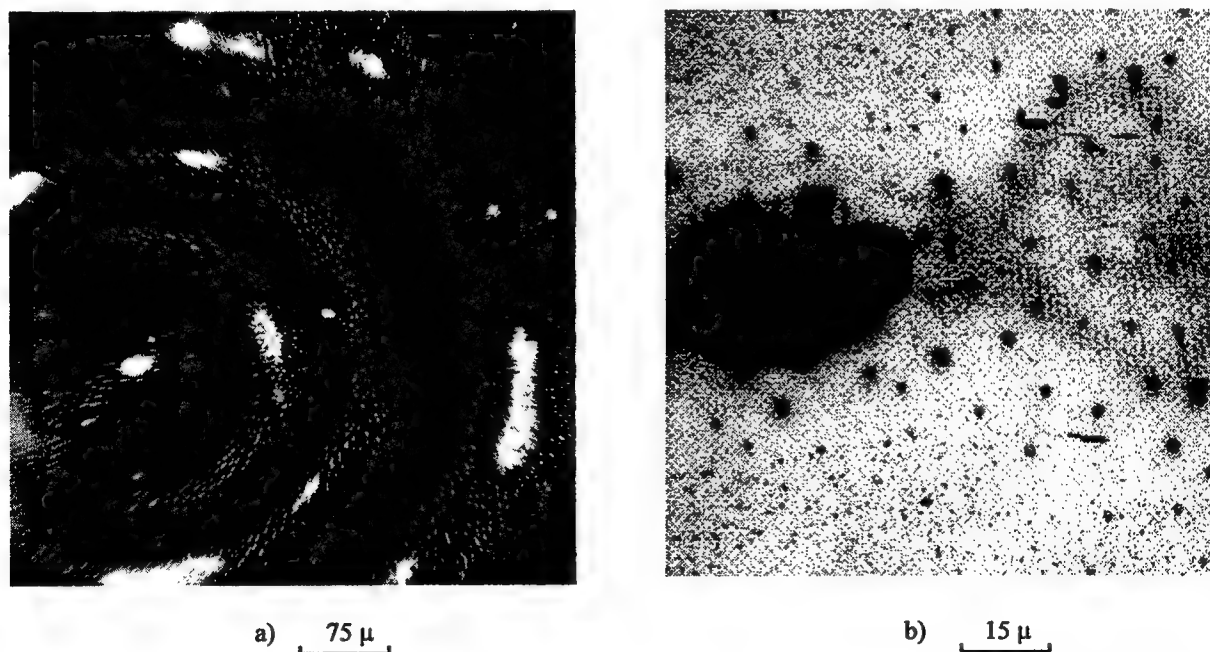

a)   75 μ   b)   15 μ

Fig.7. Microphotograph of the Al-film, processed by the 1.06-μ laser pulse: a) the general view of the processed area; b) the view of the central part of the processed area.

4. CONCLUSIONS

1. The proposed development of the intracavity method makes it possible to fabricate two-dimensional periodical surface structures in micron and submicron range without any contamination of the processed solid-state surface.

2. The application of two subsequent pulses technique can be used to fabricate surface microgrids, the elementary site of which looks as a square, rectangle or parallelogram. The period of the grid can be changed from 7 to 500 microns, if 10.6-micron laser radiation is used. The width of the grid grooves is about 0.3 micron.

3. In case of the simultaneous processing of the sample surface by the one-pulse 10.6-μ laser beam in two different planes of incidence, there is fabricated a periodical system of microhollows, which diameter is about 0.5 micron and the periods of the system can be varied in the same range from 7 to 500 microns. In case of 1.06-μ laser treatment the periods of the system can varied from 0.8 to 100 microns at the width of the hollows less than 0.3 micron.

This method can be applied to:
- microelectronics for periodical micron and submicron structures fabrication at electron device production;
- precise filters production in chemical and biochemical industry.

5. REFERENCES

1. V.Valyavko, V.Osipov, «Submicron-size laser treatment of the solid state surface», Proc. of the Conf. «Microelectronic Manufacturing'94», Austin, USA: SPIE, Vol.2335-34, pp.130-133, Sept.1994.

2. V.Valyavko, A.Mozgo, V.Osipov, «Intracavity forming of submicron periodical structures», J.Appl.Spectoscopy, Vol.62, N 1, pp.111-116, 1995.

3. V.Valyavko, V.Osipov, «Mode structure laser radiation influence on the surface submicron-size periodical structures producing», Proc. of the Conf. «Microelectronic Manufacturing'96», Austin, USA: SPIE, Vol.2877-20, pp.160-165, Sept.1996.

Adaptive system for phasing large composite telescope mirrors for CO_2-lasers radiation transportation

Inna M. Belousova, Vladimir A. Grigoryev, Oleg O. Stepanov

Institute for Laser Physics, Birzhevaya 12, St.Petersburg, 199034, Russia

Vladislav Ya. Telkunov

All-Russia Research Center "S.I.Vavilov State Optical Institute",
Birzhevaya 12, St.Petersburg, 199034, Russia

ABSTRACT

Adaptive phasing system for large-sized composite telescope mirrors intended for transportation of high-power CO_2-lasers radiation by long distances are presented. The phasing system consists of a wave-front censor and a unit for controlling drives. A heterodyne side-shift interferometer with a rotated radial diffraction grating was used as the wave-front censor. The grating can operate both in visible and IR spectral ranges. The phasing system allows to monitor and control automatically the correct form of the composite mirror in conditions of mechanical vibrations and thermal effects with the error not greater than $\lambda/40$. At external perturbing factors, whose phase variations may reach $100°$ to $120°$, the (Strehl) phasing efficiency is 0.977. The phasing system can be also applied in astronomical telescopes and other systems for observation of remote objects.

1. INTRODUCTION

The phasing system is intended for automatic phasing and maintaining in the phased state the composite telescope mirrors used for transportation of high-power CO_2-laser radiation by long distances.

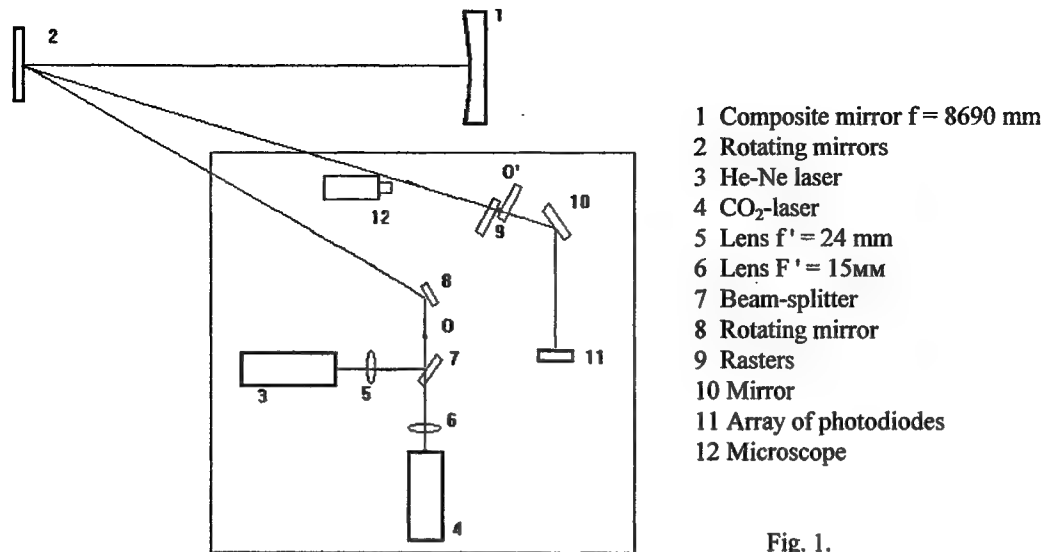## 2. DESCRIPTION OF PHASING SYSTEM FOR COMPOSITE TELESCOPE MIRROR

Phasing of a composite telescope mirror is reached by illumination of a composite mirror (CM) from the center of its curvature, measurement of wave-front phases of signals reflected by segments of the composite mirror, and generation of signals for controlling the drives.

The phasing control system (Fig. 1) consists of three hexahedron segments 360 mm in size. The lower (fixed) element is the reference one. Two upper (mobile) elements are provided with electromechanical drives with the moving range $\pm$ 0.5 mm and error (hysteresis) ≤ 0.1 μm.

To study the phasing control device (PCD), we used a mockup of interference-shadow device. The PCD shadow channel operates in the visible band and is intended for preliminary adjustment of the whole system and of CM segments as to the angle and the focal point with errors ensuring unambiguous response of the interference channel ($\leq 10"$ as to the angle and ≤ 50 μm as to the focal point).

The shadow channel consists of the He-Ne laser (3) and the objective (5) focusing laser radiation near the center of CM curvature. Being reflected from the CM, the radiation is concentrated in the conjugated point O', in which the working surface of one of the rotated rasters (9) is located. The pattern of the rasters is alternating transparent and opaque stripes of equal width, intersecting at the angle of $120°$.

The opaque stripes are Foucault knifes in the shadow method. Since the data are frequency-separated, the rasters are rotated with different speeds, or are two-frequency ones.

1 Composite mirror f = 8690 mm
2 Rotating mirrors
3 He-Ne laser
4 CO_2-laser
5 Lens f' = 24 mm
6 Lens F' = 15ᴍᴍ
7 Beam-splitter
8 Rotating mirror
9 Rasters
10 Mirror
11 Array of photodiodes
12 Microscope

Fig. 1.

The rotating rasters form moving shadow images of CM segments in the focal plane (2) of the objective. The images are recorded by the array of photodiodes (11). The direction and phase of motion of shadow images of adjusted elements with respect to the reference one depend on their angular and axial misalignment. The values of angular misalignments of adjusted elements with respect to the reference one are determined by the difference of signal phases from the photodiodes.

The axial misalignment (offset of the curvature center of a raster working surface) was determined by the difference of phases of signals from photodiodes located at the edges of segments shadow images. When the rasters drive is switched on, preliminary adjustment may be carried out using the static shadow image by turning the raster with hand.

The phase difference is related to misalignment in the angle and focal point:

$$\Delta\varphi_\alpha = \alpha F/b , \tag{1}$$

where $\Delta\varphi_\alpha$ is the phase difference in degrees, α is the misalignment in the angle in degrees, b is the raster period.

$$\Delta\varphi = 360 \cdot D_c^2/R^2 \cdot \Delta f/\lambda , \tag{2}$$

where D_c^2 is the transverse segment dimension, R is the curvature radius of the segment in mm, Δf is the misalignment along the axis in mm.

The interference channel is intended for controlling the phasing, i. e., for matching focal points (centers of curvature) with errors in the angle $\alpha \leq \lambda/mD_c$, and in the focal point $\Delta f = n\lambda + \lambda/m$, where m and n are integers determined by the required quality of phasing.

The interference channel uses the principle of an infrared heterodyne side-shift interferometer to reduce the influence of perturbing factors (vibrations, atmospheric turbulence etc.). The interference channel consists of the CO_2-laser (4), whose radiation axis coincides with the axis of the He-Ne laser of the shadow channel, and the objective (6) focusing laser radiation to the center of the CM curvature O.

Being reflected from the CM, the infrared radiation is focused on working zones of the rotated rasters. For infrared

radiation, the period of raster stripes is less than the diameter of the diffraction circle, and the rasters operate as diffraction gratings creating the image of the CM of the zero and higher (odd) orders. The rasters periods are chosen so that the first orders are shifted by the value of the image diameter. Thus, the first orders of the adjusted elements from each segment of each raster are overlapped over the zero order of the reference element, and vice versa.

When rasters are rotated, the frequencies of the first orders are shifted by the value:

$$\Omega = 2\pi Nr/b, \qquad (3)$$

where N is the number of revolutions of the raster per second, r is the radius of the working zone, b is the period of the raster.

To perform heterodyne detection of signals produced as the result of overlapping of the first orders of the adjusted elements on the zero order of the reference element, we used three receivers located in the plane of the objective image (2) in places of images of the drives, or one receiver located in the image center.

The frequency of the heterodyne signal is determined by relation (3), and the phases depend on linear misalignment of the adjusted and the reference elements. To measure the linear misalignment, the phases of signals from infrared receivers of the channel are compared to a signal phase from one of photodiodes of the reference element executing the role of the reference signal.

The difference of phases of signals from the reference and adjusted elements is:

$$\Delta\varphi_i = 2\pi\Delta i/\lambda, \qquad (4)$$

where Δi is the linear misalignment between the adjusted and reference elements in the point i.

The CM segments could be phased both manually by means of the control panel, and automatically, by means of automatic feed-back consisting of laser sources, photoreceivers, amplifiers and phase detectors connected to drives. The quality of phasing as to the angle was checked by means of the micrometer microscope (12) by the value of misalignment of diffraction circles created by the segments. The quality of phasing as to the focal point was checked by the static shadow picture and the value of residual step between edges of adjacent segments, using a translation meter with the reading error of 0.1 μm, in the range ± 10 μm.

The measurement results have shown that the root-mean-square deviation of phasing as to the angle was 2" (0.1 of the angular size of the diffraction circle at the wavelength 10.6 μm). The root-mean-square deviation of phasing as to the focal point was 0.25 μm ($\lambda/40$ at $\lambda = 10.6$ μm), the Strehl number corresponding to the given errors being equal to 0.977.

4. CONCLUSIONS

The performed experimental research have confirmed serviceability of the considered phasing system and possibility to reach high accuracy of composite mirror phasing, permitting to transport and focus effectively high-power laser radiation on remote objects.

5. REFERENCES

1. I.M.Belousova, A.V.Bukanov, V.A.Grigoryev, N.A.Gryaznov, V.M.Kisilev, S.N.Leonov, A.L.Melkonyan, N.A.Novoselov, A.G.Skepko, M.B.Stolbov, "Wave-front analyzers for adaptive optical systems," Opticheskiy Zhurnal, № 3, pp. 33-45, 1992.
2. N.V.Ryabova, V.F.Zaharenko, "Active and adaptive optics in large-sized telescopes," Opticheskiy Zhurnal, № 6, pp. 5-44, 1992.

Phase plate of double action in oblique incidence heterodyne laser interferometer.

A.G. Seregin, D.A. Seregin, A.I. Stepanov.
Research Center "Vavilov State Optical Institute", 199034, St.Petersburg, Russia

V.N. Shekhtman
Engineering-Physics Laboratory,189620 St.Petersburg, Russia

ABSTRACT

It is extraordinary useful to conserve the advantages of the heterodyne Interferometry with high sensitivity of straight phase measurements in oblique incidence interferometer. In our case the directions of test and referent beams are made by the diffraction gratings. The special-property phase plate is located in collimated beam path between the diffraction gratings and test mirror, and incidence test and referent beams pass through this plate twice. The particularity of the phase plate is that one creates the path difference $\lambda/4$ at reference beam direction, and $\lambda/2$ at test beam direction. Initial polarization vector of reference beam is rotated on $90°$ and polarization vector of test beam on $180°$. Such two beams with different frequency interfere at the exit. It has been found optimum decision of polarization frequency component dividing and combining.

1. INTRODUCTION.

It is extraordinary useful to conserve the advantages of the heterodyne interferometry [1,2], with high sensitivity of straight phases measurements and possibilities of determination of the straight phase variation in oblique incidence interferometer [3]. Using of interference circuits with heterodyne processing allows compensating inevitable decrease of sensitivity.

Change of the order interference δN and respective alteration of phase's difference $\delta\varphi$ between the interfering wave fronts are connected by a known ratio

$$\delta N = \delta\varphi/2\pi \tag{1}$$

One is necessary in our case to connect with the test sensitivity of a deviation of a surface with oblique incidence light beam collimated on it.

For concrete methods there are concepts of a limit of sensitivity $\delta\varphi_{min}$, or minimum significance of a difference of phases, which can be registered, and threshold sensitivity, under which by analogy to a photo-electric term in [4] it is offered to understand magnitude, return to $\delta\varphi_{mi}$ i.e. $1/\delta\varphi_{min}$. In a general view of analysis the interferometry information sensitivity function is depended from many parameters numbers and attempt to receive its expression is very difficult. The concept of sensitivity is used for comparison of various methods of the interference test in reality. The possibilities of realization of heterodyne method influencing on a parameter of sensitivity function for oblique incidence interferometers are considered in this work.

2. SENSITIVITY CONCEPTION

So the measurements of the deviation of the testing surface (ST) are discussed in this work we shall formulate some necessary concepts using the known approaches to a problem of interferometric methods sensitivity.

The sensitivity S is expedient to tie with fringe contour interval. Fringe contour interval is the deviation of the ST form according to the change of the path difference Δ between testing and reference interactive wave fronts (WF) equal to length of a wave of used radiation λ with the certain angle of oblique incidence on ST of the testing WF - ε. We shall designate the fringe contour interval value as H_λ account for ST deformation $H = H_\lambda$ with change of the order N per unit between the next-fringe, against [5]. With counting number of testing beam reflections M from ST in multipass interferometers the expression for H_λ will look like

$$H_\lambda = \lambda/2M\cos\varepsilon, \quad \text{where } M = 1,2... \tag{2}$$

The complete deformation ST H in the given point (x, y) with account (2) and size increase of the order N in a point (x', y') of interferogram in relation to reference WF is

$$H(x,y) = H_\lambda [N(x', y') + \delta N(x', y')], \tag{3}$$

where $N(x',y')$ - integer, and $\delta N(x',y') <1$, $\Delta=(N+\Delta N)\ \lambda$

The strict sense of fringe contour interval value H_λ is assigned scale of a topographical card ST, connected linearly with λ, and also with geometry of the interferometer circuit (M and $\cos\varepsilon$) according to expression (2) in this case. Let's introduce the concept appropriate to the minimal limit of a registered error of the topographical relief $h_{\delta Nmin}$ and connected with minimal registered increment of the interference order δN_{min} expressed through $\delta\varphi_{min}$[4] from (1)

$$h_{\delta Nmin} / H_\lambda = \delta N_{min} = \delta\varphi_{min}\ /2\pi, \tag{4}$$

here $\delta\varphi_{min}$ - appropriate minimal registered meaning increment of a phase of testing WF $W_p(x',y')$, reflected from ST in comparison with reference WF $W_o(x',y')$, reflected, for example, from an ST. We shall name as coefficient C of threshold sensitivity as inverse value to ratio $h_{\delta Nmin} / H_\lambda$ from [4]

$$C = H_\lambda/h_{\delta Nmin} = 2\pi/\delta\varphi_{min} = 1/\delta N_{min}, \qquad C>>1 \tag{5}$$

Number of the minimal increments δN_{min} registered and according to the increment order ΔN in the given point (x',y'), or $\Delta N/ \delta N_{min}$ we shall designate n_d by analogy with (3) but within the limits of one fringe

$$\Delta H(x,y)=h_{\delta Nmin}\ n_d, \tag{6}$$

Obviously from (5) and (6) follows, that

$$\Delta H(x,y)= H_\lambda\ \Delta N/ C\ \delta N_{min}. \tag{7}$$

By analogy to conception of threshold sensitivity for a phases difference [4] we shall enter concept of threshold sensitivity for deformation ST as a size which is inverse to the minimal limit of a registered level of a topographical relief $h_{\delta Nmin}$, and with the account (5)

$$S =1/ h_{\delta Nmin}=C/ H_\lambda. \tag{8}$$

Then, substituting (2) in (8), we receive

$$S =(2MC \cos \varepsilon)/\lambda, \tag{9}$$

where C by definition is equal $H_\lambda/h_{\delta Nmin}$ [7].

The received expression (9) allows to compare the various interferometers circuits with reference WF for the control of form TS deviations with variations of M, C, ε and λ. Changing parameters M, C, ε and λ it is possible to find optimum of their combinations with the interferometric control at various stages of form-making optical and nonoptical TS.

Any phasemeter is known not to be capable directly to register a phase on frequency of a light (10^{14} Hz).. Therefore, as a rule, with the analysis of interference pattern in a plane X', Y' the intensity change $\delta I(\varphi)$ or extreme position of distribution of intensity of fringes is a registered size.

Carrying of a working spectrum to a radio range with the help of optical heterodyning [1,2] allows successfully deciding tasks of phase of a light wave measurement on appropriate radio frequency.

Nowadays optical heterodyning is carried out with using of modulators which have a rotating phase plates and diffraction gratings, two-frequency laser with Zeemane splitting in a magnetic field, acoustooptical and electrooptical modulators, ring laser, and also modulators on the base of two-frequency modulations of a basic mirror in interferometer [8]. A choice of that or other type of the modulator, each has its own advantages and lucks, depends on the different subjective factors unconnected to the general optimization sometimes.

Accounting the experience of our work using the heterodyne interferometer with two-frequency modulator is proposed to be most perspective occasion for metrology of surface [8]. Using of the similar circuits allows to compensate reduce of sensitivity with oblique incidence on account the special heterodyne processing method of interference pattern, i.e. increases of factor C in expression (9) with $M = 2$ is

$$S=(4C \cos \varepsilon)/ \lambda$$

Irrespective of a type of the modulator the important factor in heterodyne interferometers with reference WF is the optimum division frequency component in testing and reference beams. The most widespread reception of the decision of this task served a quarter-wave outcome with using a polarizing cube-prism [2].

3. THE SCHEME WITH A QUARTER-WAVE OUTCOME.

The basic scheme of oblique incidence heterodyne interferometer for testing of surface deviations is on the fig.1a. One is built on the basis of the circuit Twiman-Green with a quarter-wave outcome. Reference and testing WF W_r and W_t with valid amplitudes a_r and a_t in a point of interference field $P'(x'_p,y'_p)$, accordingly are determined by expressions

$$W_r(x_p,y_p,t) = a_r\ exp\ i(\ \omega_r\ t +\ \varphi_r),$$
$$W_t(x_p,y_p,t) = a_t\ exp\ i(\ \omega_t\ t + \varphi_t), \tag{10}$$

where ω_r, ω_t - optical frequencies WF W_r and WF W_t,

$$\varphi_r = 4\pi L_r / \square \lambda,$$
$$\varphi_t = [2\pi/\lambda][2L_t + \Delta],$$

where

$2L_r$ - length of a reference optical path WF (W_r),

$2L_t + \Delta$- length of a testing optical path WF (W_t).

Δ for φ_t in (10) in our situation describing the increment of testing optical path length because of the surface form deviations $H(x_p, y_p)$ in any determined point P on a ST is

$$\Delta = 4H(x_p, y_p)\cos \varepsilon \square \tag{11}$$
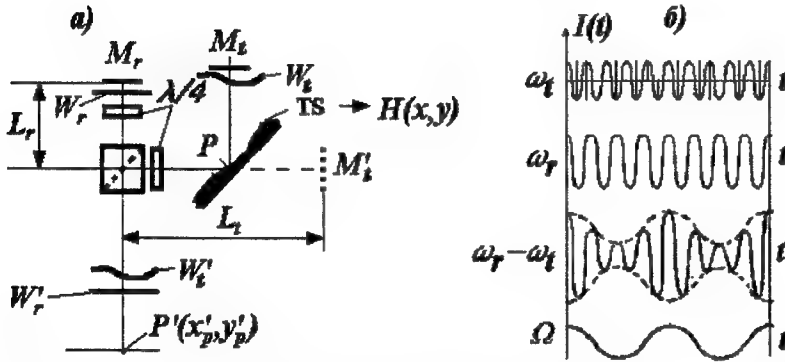
Fig.1.
a) - scheme of oblique incidence heterodyne interferometer;
b) - result of a superposition W_r' and W_t': $\Omega = \omega_r - \omega_t$

The intensity beating on output of the oblique incidence heterodyne laser interferometer in a point $P(x_p y_p)$ as a result of a superposition W_r' and W_t' is registered instantly by the phasemeter. This result is according Fig.1b

$I(t) = |W_r' + W_t'|^2 = (a_r^2 + a_t^2)[1 + \gamma \cos(\Omega_t + \Phi)]$,

Where γ - the factor of contrasting interference pattern, Ω - the frequency of intensity fluctuation $I(t)$, Φ- the phase of intensity fluctuation with frequency Ω, $\gamma = 2a_r a_t/(a_r^2 + a_t^2)$, $\Omega = \omega_r - \omega_t$

$\Phi = \varphi_r - \varphi_t = 4\pi l_r/\lambda - [2\pi/\lambda][2l_t + \Delta] = 4\pi(l_r - l_t)/\lambda - 2\pi\Delta/\lambda$. With the account (11)

$$\Phi = 4\pi(l_r - l_t)/\lambda - [8\pi H(x_a y_a)\cos \varepsilon]/\lambda. \tag{12}$$

The first member of a difference (12) represents constant shift of phases and characterizes the tuning of interferometer, and second contains the information about TS. The signal $U(t)$ on an output of the photodetector for the given point P interference field is proportional to intensity $I(t)$. From expression (12) it follows, that as a result of mixture on the photodetector two mutually - coherent optical signals with various frequencies and phases, spectrum of electrical signal on the output of the photodetector is fluctuations with intermediate frequency Ω and phase Φ. Φ is equal to phase shift of light waves in testing and reference shoulders of oblique incidence heterodyne laser interferometer.

As the concept of a phase is determined just to within constant size, it is meaningful to consider only variable part

$$\Delta\Phi = [8\pi H(x_a, y_a)\cos \varepsilon \square]/\lambda, \tag{13}$$

which depends on variable deviations H with constant ε and λ.

4. THE SCHEME WITH A PHASE PLATE OF DOUBLE ACTION

For oblique incidence laser interferometer on diffraction gratings the problem of division of beams with different frequencies is limited by the sizes of the first passing grating, on which the division and overlapping of testing and reference beams is carried out.

Successful application of a thin quarter-waved plate of the large size placed at 45° angles to polarization vertical plane of the laser in Zygo interferometer allows turning a polarization plane of beams. After the opposite passage through the polarizing beam splitter it allows to direct beams with the minimal losses to CCD array. In our original decision the phase plate is established simultaneously in both beams after passing of the first transparent grating.

On Fig.2. the heterodyne interferometer scheme is shown which build on the base of interferometer with diffraction gratings IT-293. One is used in the experiences on the investigation of adaptive mirror form. The laser beam 1 is directed on the modulator of optical frequency 2, on which output two components with orthogonal polarization P_s and P_p and shift of frequency Ω will be formed. After passage of beams through elements 3 - 7 will be formed the wide collimated beam, which is divided by a transparent grating 8 into testing and reference beams. The reference beams incidents on a thin crystal plate 9 - on normal, and reference one - under diffraction angle.

As a result of double passage of testing and reference beams through a plate 9, after reflections from TS 20 and grating 10, the vectors of polarization of both beams appear parallel. And each of beams has the own frequency, and the difference between frequencies is equal Ω.
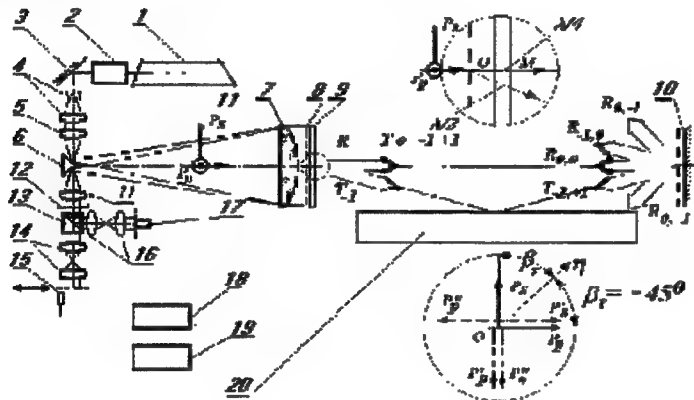

Fig.2. Scheme with a phase plate of double action

On an exit of interferometer for cutting parasitic components is established polarizator 12. The beam splitter 13 provides presence of testing and reference channels with photodetectors 15 and 17 The photodetector 17 is motionless and gives out a reference signal for comparison with a signal, taking from the photodetectors 15, which scans on a field of interference.

The phase meter block 18 gives out the initial data for the computer 19. With a conclusion from the circuit of a plate 9 and switched-off modulator 2 interferometer works in a usual mode. Lenses 11, 14 and 16 serve for conjugation of center of a TS 20 with the analysis plane.
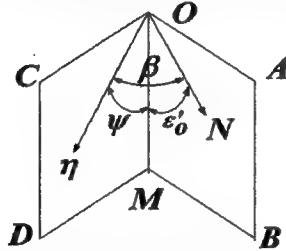

Fig.3. Common case of optical axis Oη and perpendicular OM to plate 9 dislocations.

According to designations on fig.3 the dependence of a difference of phases between ordinary and unusual beams in a phase plate by thickness d from a angle of incidence of beams has a kind [9]:

$$\Delta\Phi = [2\pi\,d/\,\lambda]\,\{(A^2\text{-}B^2)sin2\psi\,cos\,\beta\,sin\,\varepsilon\,/2C^2 +$$
$$+[1/C]\sqrt{1\text{-}A^2\,sin^2\beta\;\,sin\,^2\varepsilon}\,\text{-}[A^2\,B^2\,/C^2\,]cos^2\beta\;\,sin\,^2\varepsilon\;\,\text{-}[1/B]\sqrt{1\text{-}\,B^2sin^2\varepsilon}\,\},\qquad(14)$$

where $A = 1/n_e$ and $B = 1/n_o$ accordingly for unusual and ordinary ray,

ψ - the angle between normal line OM to the surface plate and optical axis $O\eta$ crystal,

β - the angle between axis crystal $O\eta$ and plane $OABM$ of incidence of the ray polarizing in the incidence plate,

ε - the angle of incidence of the beam on the plate.

In our case $\psi=90°$, then C = A = $1/n_e$, $\beta_r=45°$ and $\varepsilon_r=0$ for a reference beam, $\beta_t = -45°$ and $\varepsilon_t \sim 11°$, $n_o=1,542$ and $n_e=1,551$ for a testing beam with using of a quartz plate. For the decision of a task of maintenance of simultaneous double action of a phase plate $\lambda/4$ and $\lambda/2$ the joint performance of two conditions for reference and testing of beams is necessary carry out the next:

$$d(n_{er} - n_o) = (2k_{1/4} + 1)0,25\,\lambda \qquad\qquad \text{for reference (r) beam,} \qquad (15)$$

$$d(n_{et} - n_o{}') = (k_{1/2} + 0,5)\lambda \qquad\qquad \text{for testing (t) beam,} \qquad (16)$$

where $n_{er}\,(\,\varepsilon\,)$, $n_{et}\,(\,\varepsilon)$ and $n_o{}'\,(\varepsilon)$ - function ε according to expression (14), $k_{1/4}$ и $k_{1/2}$ - integers of half-waves $(0,5\lambda)$ and lengths of waves (λ) accordingly, or orders of quarter wave and half-wave plates.

In our case for the reference beam $\varepsilon_r = 0$ and the members containing $\sin\varepsilon$ in expression (14) become 0 and in (15) $n_{er} = n_e = 1,551$.

Multiplier in braces of expression (14) is the appropriate differences from (15) and (16), which for given ψ and β look like

$$n_{er} - n_o = 1/C - 1/B, \qquad (17)$$
$$n_{et} - n_o =$$
$$= [1/C]\sqrt{1 - A^2\sin^2\beta\ \sin^2\varepsilon - [A^2\,B^2\,/C^2]\cos^2\beta\ \sin^2\varepsilon} - [1/B]\sqrt{1 - B^2\sin^2\varepsilon}, \qquad (18)$$

By substituting (17) and (18) accordingly in (15) and (16), we shall receive

$$d(1/C - 1/B) = (2k+1)0,25\,\lambda$$
$$d\{[1/C]\sqrt{1 - A^2\sin^2 45^\circ \sin^2 11^\circ - [A^2 B^2/C^2]\cos^2 45^\circ \sin^2 11^\circ} - [1/B]\sqrt{1 - B^2\sin^2 11^\circ}\} =$$
$$= (k+0,5)\lambda.$$

Let's define numerical meaning

$$n_{et} - n_o{}' =$$
$$= [1/C]\sqrt{1 - A^2\sin^2 45^\circ \sin^2 11^\circ - [A^2 B^2/C^2]\cos^2 45^\circ \sin^2 11^\circ} - [1/B]\sqrt{1 - B^2\sin^2 11^\circ},$$

where $A = 1/n_e$ and $B = 1/n_o$ accordingly for unusual and ordinary rays, $C^2 = A^2\,\sin^2\psi + B^2\,\cos^2\psi$, $n_o = 1,542$ and $n_e = 1,551$, $\psi = 90^0$, $C = A = 1/n_e$.

In view of our case feasible significance (18) is

$$n_{et} - n_o{}' = 0.01$$

By substituting meanings in expression (15) and (16), we shall receive

$$d = (k_{1/4} + 0.5)\ 35,15,$$
$$d = (k_{1/2} + 0,5)\ 63,28$$

By equalizing the right parts of the received expressions, we shall deduce a required ratio of the orders

$$(k_{1/4} + 0.5) = (k_{1/2} + 0,5)\ 1,8 \text{ or } k_{1/4} = 1,8k_{1/2} + 0,4 \qquad (19)$$

The ratio (19) satisfies to simultaneous performance of conditions (15) and (16). Since in (19) k should be whole it is obviously that the result of $1,8k_{1/2}$ has the six tenth after of a point. For example $k_{1/2} = 7$, $1,8k_{1/2} = 12,6$ and $k_{1/4} = 13$. Thus for a half-wave mode of a testing beam and for a quarter wave mode of a reference beam the thickness of a plate is identical and according to the conditions (15) and (16)

$$d = 0,48\text{мм}$$

The carried out analysis shows an opportunity of frequency divisions of testing and reference beams with the help of a phase plate 9, creating difference $\lambda/4$ at reference beam direction and $\lambda/2$ at testing beam direction. As a result of application of such plate the initial polarization vector with frequency ω_r in a reference beam turned on 90°, and polarization vector with frequency $\omega_t = \omega_r - \Omega$ of a testing beam turned on 180°. Such two beams with different frequency interfere at the exit.

Thus the modulation of intensity with frequency Ω is in each point interference field. The phase of the modulated signal determines deviation of the TS from the plane. The error of measurement of a phase in modern phasemeter does not exceed 1-3°, hence, the accuracy of decoding interferograms can be increased up to 0,01 fringe. For maintenance of such accuracy it is necessary to increase the requirements to interferometer elements and its tuning. The similar decision suits compact variant of interferometer with a concave grating with installation of a phase plate of double action in testing and reference beams near to a flat reflective grating.

5. CONCLUSION

In the numerous publications in the literature the important problems connected with practical using of heterodyning in optical range are analyzed. They are the signal/noise ratio with a choice of the optimum size diaphragm cutting out the real size of the interference field by the photodetector of instant action and optimum number of analyzing points, etc. In our work the decision of optimum dividing and combining of a frequency component in heterodyne variants is found. Scheme of oblique incidence interferometer with the help of a phase plate of double action is offered.

6. REFERENCES

1.R.K. Crane,"Interference Phase Measurement" Appl. Opt., Vol.8, № 3, pp.538-542, 1969.

2. N.A Massie, "Digital Heterodyne Interferometry" SPIE Proc., Vol.816, pp.40-48, 1987.

3. A.L Duncan. et al.,"Precision Surface Figure Measurements of Large Mirrors Using Grazing Incidence Interferometry"Proc. Of SPIE, 1987, Vol.818, pp.373-380.

4.V.A. Seleznev, " Increasing of hologram interferometry method sensitivity. Researching and development. Authoref. of thesis. State Inst. of Appl. Opt, Kazan, 1973.

5. J. Wilson, "The double-pass oblique-incidence interferometer for the inspection of nonoptical surfaces ". Appl. Opt., Vol.22,№ 8, pp.1144-1148, 1983.

6. P. Langenbeck, "Multipass interferometry", Appl. Opt., Vol.8,№ 3, pp.543-552, 1969.

7. V.V Anistchenko, S.N Koreshev., V.A Parfenov., V.I Podoba., A.G Seregin., V.I Sidorov. "Laser interferometric control problems in adaptive astronomical telescope" SPIE Proc., Vol.2200,pp.591-592, 1994.

8. I. Sh. Etsin, M.G. Arkipov, A. G. Seregin, "Interferometer with two-frequency phase modulation" SPIE Proc., Vol.816, pp.40-48, 1994.

9 .V.A. Maskalev "Theoretic Foundation of Opto-physical Researching" Leningrad, Mashinostroenie, pp 194-197,1987(In Russian).

Author Index